

ABSTRACT

LIANG, JUNKAI. Addressing Challenges of Uncertainty and Non-convexity toward Future Power Systems with High Renewable Penetration. (Under the direction of Wenyuan Tang).

Driven by the societal goals of zero carbon emission and 100% renewable future, the world has witnessed a rapid growth of variable generation, such as solar photovoltaic and wind power. The output of variable generation changes with time and is not known with perfect accuracy, which stimulates tremendous research on the renewable energy integration. The variability and uncertainty introduced by variable generation can impose new challenges on the power system planning, operation, and economics. For example, supply-demand balancing and maintaining voltage limits becomes more difficult. When it comes to the long-term planning, planners are facing more significant uncertainties. The increase in uncertainty poses new challenges for the implementation of state-of-the-art algorithms. On the other hand, the increased renewable penetration makes the non-convexity in the power system problems non-trivial. In this dissertation, we study some methods from the perspective of energy data analytics, optimization, and control that can potentially improve the renewable energy integration.

To ensure the efficient and reliable operation of electric grid, an accurate and general short-term forecasting algorithm with interpretability is desired. Theoretically speaking, if accurate predictions of variable generation are available, the uncertainties will be eliminated. Furthermore, driven by the complexity of the related decision-making task which calls for the forecast uncertainty, the main interest of forecasting turns from point to probabilistic or scenario forecasting. From the perspective of decision making and risk assessment, the optimal solution is directly linked to a set of uncertain realizations instead of the expectation of the future outcome. Therefore, it is desirable to make probabilistic or scenario forecasting. In Chapter 2, we leverage the recent advances in deep learning architectures and propose four models to enhance the accuracy of short-term forecasting in power systems.

Gas-fired units are widely used nowadays not only for the generation but also for the operating reserves because of the low natural gas price, fast start-up flexibility, and fast ramp rates. The gas and power systems become deeply coupled. In this regard, the uncertainties and constraints in the gas network may have a huge impact on the power system planning, operation, and economics. Hence, it is worth investigating the operation and planning of an integrated energy system. In chapter 3, we focus on two specific problems of integrated energy systems. The two problems investigate the long-term planning and short-term scheduling.

In Chapter 4, we focus on energy trading. We study trading strategies under two types of trading markets. First, an energy hub, which is considered as a unit where multiple energy carriers can be converted, conditioned, and stored, is trading between different energy sectors. Second, we propose a continuous double auction mechanism and study the peer-to-peer trading of electricity. Establishing local and distribution-level electricity markets provides an effective

solution to managing large amounts of small-scale distributed energy resources.

Besides the peer-to-peer trading, we develop a new business model to manage customer-sited solar in Chapter 5. The proposed business model assumes that the utility and the households within a community cooperatively deploy solar and storage. The invested solar and storage are shared by all the participants. The case studies shed light on the future customer-utility relationship. Moreover, we observe that increased penetration of distributed energy resources, especially solar at a community level, can provide additional resiliency and improve the reliability of the distribution system. With the adaptive system topology, dynamic microgrids featured by different boundaries can be formed, in which distributed generation serves one or more critical service facilities.

© Copyright 2021 by Junkai Liang

All Rights Reserved

Addressing Challenges of Uncertainty and Non-convexity toward Future Power Systems with
High Renewable Penetration

by
Junkai Liang

A dissertation submitted to the Graduate Faculty of
North Carolina State University
in partial fulfillment of the
requirements for the Degree of
Doctor of Philosophy

Electrical Engineering

Raleigh, North Carolina

2021

APPROVED BY:

Mesut Baran

Ning Lu

Osman Ozaltin

Wenyuan Tang
Chair of Advisory Committee

BIOGRAPHY

The author received the B.Eng. degree in electrical engineering and automation from Southeast University, Nanjing, China, in 2015, and the M.S. degree in electric power systems engineering from North Carolina State University, Raleigh, NC, USA, in 2016, where he is currently pursuing the Ph.D. degree in electrical engineering.

His research interests include power system operations and planning, integrated energy systems, and renewable energy integration.

ACKNOWLEDGEMENTS

I would like to express the deepest appreciation to my supervisor Dr. Wenyuan Tang for his unwavering support of my Ph.D study and research, for his patience, enthusiasm, understanding, and guidance. Besides, I would like to express my sincere gratitude to the rest of my committee members: Dr. Mesut Baran, Dr. Ning Lu, and Dr. Osman Ozaltin, for their great help, encouragement, and insightful comments. My sincere thanks also goes to all the colleagues and friends. Last but not least, I would like to thank my parents for love and understanding.

TABLE OF CONTENTS

LIST OF TABLES	vi
LIST OF FIGURES	viii
Chapter 1 Introduction	1
1.1 Forecasting Tasks in Power Systems	1
1.1.1 Spatio-Temporal Renewable Forecasting	1
1.1.2 Spatio-Temporal Net-Load Forecasting	3
1.1.3 Scenario Generation	3
1.1.4 Scenario Reduction	5
1.2 Uncertainty and Non-convexity in Integrated Energy Systems	6
1.3 Energy Trading	9
1.4 Sustainable Community and Critical Service Restoration	11
Chapter 2 Deep Learning for Forecasting Tasks in Power Systems	14
2.1 Attention Temporal Convolutional Network	15
2.1.1 Problem Statement	16
2.1.2 Model Specifications	16
2.1.3 Case Studies	21
2.2 Graph Transformer Network	29
2.2.1 Problem Statement and Training Methodology	30
2.2.2 Model Specifications	30
2.2.3 Case Studies	37
2.3 Sequence Generative Adversarial Network	42
2.3.1 Problem Statement	42
2.3.2 Model Specifications	43
2.3.3 Case Studies	45
2.4 Mixed Autoencoder Based Fuzzy Clustering	53
2.4.1 Problem Statement	53
2.4.2 Model Specifications	54
2.4.3 Case Studies	58
2.5 Conclusion and Discussion	69
Chapter 3 Integrated Gas and Power Systems	72
3.1 Multistage Stochastic Co-planning of Integrated Energy Systems	73
3.1.1 Modeling Integrated Energy Systems Expansion Co-planning	73
3.1.2 Multistage Stochastic Program With Recourse	78
3.1.3 Multistage Stochastic Expansion Co-planning	80
3.1.4 Case Studies	84
3.2 Interval Based Transmission Contingency-Constrained Unit Commitment	90
3.2.1 Contingency-Constrained Unit Commitment Model	90
3.2.2 Interval Based Uncertainty Representation	93
3.2.3 Reformulation of Interval Based Constraints	96
3.2.4 Fuzzy Preference between Interval Numbers	98
3.2.5 Case Studies	100
3.3 Conclusion and Discussion	107

Chapter 4 Energy Trading Paradigms	109
4.1 Optimal Trading Strategies for Trading between Gas and Electricity Markets . .	110
4.1.1 Uncertainties and Variables	110
4.1.2 Problem Formulation	112
4.1.3 Optimal Policies	113
4.1.4 An Illustrative Example	119
4.2 Optimal Trading Strategies for Transactive Energy	120
4.2.1 Continuous Double Auction Model	120
4.2.2 Optimal Trading Strategies	122
4.2.3 An Illustrative Example	127
4.3 Conclusion and Existing Technical Challenges	130
Chapter 5 Sustainable Community and Dynamic Microgrid	132
5.1 Sustainable Community Based PV-Storage Planning	133
5.1.1 Non-cooperative Benchmark	133
5.1.2 Cooperative Planning Framework	135
5.1.3 Solution Methodology	137
5.1.4 Scenario Generation	139
5.1.5 Case Studies	140
5.1.6 Conclusion	145
5.2 Critical Service Restoration via Dynamic Microgrids	146
5.2.1 Problem Formulation	146
5.2.2 Solution Methodology	149
5.2.3 Case Studies	156
5.2.4 Conclusion	160
BIBLIOGRAPHY	161
APPENDIX	172
Appendix A Parameters and Topologies for the Expansion Co-planning Problem .	173
A.1 Parameters of the Small System	173
A.2 Parameters of the Large System	175

LIST OF TABLES

Table 2.1	Comparison of Aggregated Point Predictions for the Renewable Forecasting.	27
Table 2.2	Comparison of Summation of Forecast Errors for the Renewable Forecasting.	27
Table 2.3	Comparison of Winkler Scores for the Renewable Forecasting.	28
Table 2.4	Comparison of Point Predictions for the Net-Load Forecasting.	39
Table 2.5	Comparison of Pinball Scores for the Net-Load Forecasting.	41
Table 2.6	Comparison of Models for the Scenario Generation Using the Brier Score. .	50
Table 2.7	Comparison of Models for the Scenario Generation Using the Variogram Score.	51
Table 2.8	Topology of Networks Used in the Mixed Autoencoder Based Fuzzy Clus- tering.	58
Table 2.9	Comparison of Methods for the Scenario Reduction Using the Cosine Dis- tance Score.	59
Table 2.10	Comparison of Methods for the Scenario Reduction Using the Brier Score.	63
Table 2.11	Computational Time of Scenario Reduction Methods.	64
Table 2.12	Illustration of Load Shedding Blocks Used in the Empirical Analysis. . . .	65
Table 2.13	Comparison of Methods for the Scenario Reduction Using the Policy Sta- bility.	68
Table 2.14	Comparison of Realized Costs under Different Penalties for the Scenario Reduction.	68
Table 2.15	Comparison of Different Selections of the Number of Preserved Scenarios. .	69
Table 3.1	Investment Decisions for the 6-Bus Test System.	85
Table 3.2	Sensitivity Analysis of Economic Value of P2G.	86
Table 3.3	Performance of Different Approaches under the 20-Scenario Case.	88
Table 3.4	Performance of Different Approaches under the 60-Scenario Case.	88
Table 3.5	Realized Cost for Unit Commitment Decisions Obtained by the Proposed Model.	103
Table 3.6	CPU Time for 24-Bus System and 118-Bus System.	103
Table 3.7	The Lower and Upper Bounds Produced by Selecting Different Slack Nodes.	104
Table 3.8	Sensitivity Analysis of the Optimistic Degree.	105
Table 3.9	Comparison of Operation Cost with and without the Use of P2G.	106
Table 3.10	Change in Cost with Different Wind Penetration Levels	107
Table 4.1	An Illustrative Example of Continuous Double Auction.	121
Table 4.2	Information Available to Each Prosumer.	122
Table 5.1	Payoffs of Each Player without Uncertainty.	143
Table 5.2	Investment Decisions for Different Selections of γ	143
Table 5.3	Payoffs (\$) for Different Selections of γ	144
Table 5.4	Comparison of Outcomes under Fixed γ and Bargaining Dependent γ . . .	144
Table 5.5	Parameters of Critical Loads.	156
Table 5.6	Parameters of Community-Level Solar.	157
Table 5.7	Comparison between the Proposed Method and the Centralized Optimiza- tion.	158
Table 5.8	Comparison between Three Methods	159
Table A.1	Candidate Sets of Generators and P2Gs.	173
Table A.2	Candidate Sets of Lines.	174
Table A.3	Evolution of Random Variables.	174
Table A.4	4-Block Load Duration Curve and Wind Profile.	174

Table A.5	The Coupling Buses/Nodes in the Test System.	176
Table A.6	Candidate Set of Gas Generators.	176
Table A.7	Candidate Set of P2Gs.	177
Table A.8	Candidate Set of Transmission Lines.	177
Table A.9	Candidate Set of Pipelines.	178

LIST OF FIGURES

Figure 2.1	Illustration of the temporal convolutional layer on encoding spatial information.	17
Figure 2.2	An example of the stacked dilated convolutional network.	19
Figure 2.3	Architecture of the attention temporal convolutional network.	20
Figure 2.4	The locations of renewable sites used.	22
Figure 2.5	The attention scores for the 2-hour ahead point forecasting of wind speed. Two time windows are shown.	23
Figure 2.6	The 2-hour ahead point predictions and corresponding base sequences at wind sites 5 and 8 during two time windows.	23
Figure 2.7	The attention scores for the 2-hour ahead point forecasting of solar generation. Two time windows are shown.	24
Figure 2.8	The 2-hour ahead point predictions and corresponding base sequences at solar site 18 during two time windows.	25
Figure 2.9	The forecast error of wind speed, in terms of the MAE and the RMSE.	25
Figure 2.10	The forecast error of solar generation, in terms of the MAE and the RMSE.	26
Figure 2.11	The Pinball scores of wind speed and solar generation forecasting.	28
Figure 2.12	An illustration of the multi-headed attention in the graph attention network.	32
Figure 2.13	An illustration of positional encoding.	33
Figure 2.14	Architecture of the transformer.	34
Figure 2.15	Architecture of the graph transformer network.	37
Figure 2.16	Attention scores of Zone 3 in the graph attention network.	39
Figure 2.17	Attention scores of Zone 3 in the first sublayer of the transformer.	40
Figure 2.18	Probabilistic net-load forecasting results on a summer day and a winter day.	40
Figure 2.19	The comparison of probabilistic net-load forecasts, in terms of the Winkler score.	41
Figure 2.20	The structure of the sequence generative adversarial network.	44
Figure 2.21	Sample paths of forecast error generated by models for the scenario generation on April 29, 2019.	47
Figure 2.22	Sample paths of wind generation generated by models for the scenario generation on December 25, 2012.	48
Figure 2.23	Comparison of models for the scenario generation, in terms of the MSE and the Energy score.	49
Figure 2.24	Comparison of scenarios generated by models for the scenario generation based on the expected and the actual costs.	52
Figure 2.25	Comparison of scenarios generated by models for the scenario generation based on standard deviations of the actual costs.	53
Figure 2.26	The mixed autoencoder based fuzzy clustering architecture.	55
Figure 2.27	The value of each individual element in the sample-wise entropy.	57
Figure 2.28	Comparison of methods for the scenario reduction using the Euclidean distance score.	60
Figure 2.29	Box plots of values in scenarios generated by different methods for the scenario reduction, compared with the realized values in the original scenario set.	61
Figure 2.30	Comparison of methods for the scenario reduction using the Energy score.	62

Figure 2.31	Comparison of different methods for the scenario reduction, in terms of the objective error and the policy error.	66
Figure 2.32	Comparison of the original scenario set and the preserved scenario sets generated by scenario reduction methods, in terms of the standard deviation of the realized cost.	67
Figure 2.33	Comparison of the performance of different methods for the scenario reduction on four new scenario sets, in terms of the realized cost.	69
Figure 3.1	An example of scenario tree.	78
Figure 3.2	An illustration of nonanticipativity constraints.	81
Figure 3.3	6-bus power system coupled with a 6-node gas system.	85
Figure 3.4	The savings contributed by the selected P2G in each stage.	86
Figure 3.5	The evolution of all the uncertainties for the 20-scenario case.	87
Figure 3.6	CPU time and bound versus iterations for branch-and-price and progressive hedging.	89
Figure 3.7	Illustration of piecewise linearized gas flow.	95
Figure 3.8	9-node natural gas network.	101
Figure 3.9	System demand and wind generation profile.	101
Figure 3.10	Interval based power transfer distribution factor of the pipeline from node 1 to 2.	102
Figure 3.11	Number of different unit commitment decisions by selecting different slack nodes.	104
Figure 3.12	Illustration of the reduced cost.	107
Figure 4.1	The feasible region of each operation in the normal case.	120
Figure 4.2	Timeline of CDA trading and physical delivery.	122
Figure 4.3	The optimal submitted price under different stages and quantities of excess electricity.	128
Figure 4.4	The total payoff and the optimal submitted price under different market trends.	128
Figure 4.5	The total payoff and the optimal submitted price under different loss allocation coefficients.	129
Figure 4.6	An illustrative example of auction process.	130
Figure 5.1	Probability density function for forecast errors.	140
Figure 5.2	Expected consumption for each household.	141
Figure 5.3	Expected LMP, insolation, and TOU rate.	142
Figure 5.4	Investment decisions without uncertainty.	142
Figure 5.5	Comparison of payoffs for cases with and without investment of power rating.	145
Figure 5.6	IEEE 123-node distribution system with 11 critical loads and 5 community PVs.	157
Figure 5.7	Modified European low voltage test feeder.	159
Figure A.1	Topology of 118-bus power system.	175
Figure A.2	Topology of 40-node gas system.	175

CHAPTER

1

INTRODUCTION

The rapid penetration of distributed energy resources (DERs) characterized by high variability and uncertainty is bringing new challenges to power systems, from analytical and computational perspectives. In this dissertation, we will study some methods that can potentially improve the DER integration by relieving uncertainty and non-convexity brought by DERs. First, we develop four models that generate effective probabilistic or trajectory forecasts. More accurate forecasts with information of uncertainty can improve the short-term scheduling. Second, we show that the risk introduced by DERs can be hedged by integrated energy systems (IESs). Third, we examine two energy trading paradigms that help the DER integration. Fourth, we propose a new business model wherein the utility and customers within a community optimally deploy the PV-storage in a cooperative manner. Finally, we observe that DERs can improve the resiliency and reliability of the distribution system.

1.1 Forecasting Tasks in Power Systems

1.1.1 Spatio-Temporal Renewable Forecasting

Traditionally, the short-term prediction of a variable generation (VG) mainly relies on its local information, and the corresponding methods do not address the potential of off-site information on enhancing the accuracy. The reader can refer to [1] and references therein for more on conventional forecasting approaches. In recent years, due to the availability of geographically distributed time-series data over a large number of sites, there exists a surge of interest in improving the accuracy of the VG short-term forecasting using information from neigh-

boring sites as features, i.e., spatio-temporal forecasting. Spatio-temporal forecasting models are first developed for the forecasting of wind resources. For example, parametric models and quantile regression are used to obtain parametric and non-parametric predictive densities, respectively [2], in which geographically dispersed information is used. The dependency structure of prediction errors for distant wind farms is characterized in [3]. Following the same spirits, the spatio-temporal forecasting techniques are also used for the solar forecasting. For example, linear models are developed for the forecasting of solar generation [4]. Similarly, a vector autoregressive with exogenous input model for the solar forecasting is presented to utilize neighboring meteorological information [5].

In the context of spatio-temporal forecasting, the large amount of explanatory variables increases the dimensionality dramatically, which requires the model to handle complex optimization problems. Great efforts have been made to tackle the issue. A correlation-constrained and sparsity-controlled vector autoregressive model is presented, in which the incorporation of expert knowledge reduces the complexity of the underlying mixed integer nonlinear programming problem [6]. Quantile regression is adopted in [7], where the exogenous variables are selected by mutual information and LASSO. An autoregressive based compressive spatio-temporal forecasting model exploits the sparsity of correlations between time series and predicts the solar power [8]. Most of the aforementioned works are parametric models, which may be ineffective in capturing the complex dynamics of renewable resources. Furthermore, the feature selection process highly relies on the domain knowledge, and hence, the models are without high generalization.

Another alternative is deep learning models. In deep learning structures, the input features will be first mapped into data representations. Given the high capability, this process can be regarded as feature selection. In this regard, a combination of long short-term memory (LSTM) and graph convolutional network (GCN) is used for the short-term wind speed forecasting [9]. A GCN coupled with autoencoder performs the spatio-temporal solar irradiance forecasting [10]. GCN is a spectral domain based model, and the selection of weighted adjacency matrix depends on the expert knowledge as well as the target forecasting task. A group of bidirectional LSTMs and stacked dilated convolutional LSTMs predict the spatio-temporal distribution locational marginal prices and wind generation in [11, 12], respectively. However, a common issue of deep learning models is the lack of interpretability.

To tackle the issue, we propose an attention temporal convolutional network (ATCN). The main contributions are given as follows [13]: 1) A spatio-temporal forecasting architecture is proposed for the ultra-short-term forecasting of renewable resources, which shows state-of-the-art performance; 2) Spatial and temporal information is extracted by dilated convolution networks, which allows us to process all the time steps simultaneously. In addition, the model introduces attention mechanisms to improve the interpretability; 3) The model does not require any expert knowledge or feature selection. Therefore, it can be used for different kinds of renewable resources forecasting tasks.

1.1.2 Spatio-Temporal Net-Load Forecasting

Earlier research on the short-term load forecasting also ignores information from other zones. The reader can refer to [14] and references therein for traditional load forecasting methods. Although works of load forecasting can be applied to net-load forecasting tasks directly, their performance may be deteriorated. Unlike the actual load, which is highly correlated with exogenous variables, the volatile nature of solar generation poses a challenge in terms of increased net-load variability [15]. Moreover, characteristics such as average daily shapes and hourly ramp events of net loads will change dramatically, compared with those of the actual load [16]. Amongst literature that studies net-load forecasting, Bayesian LSTM is used in [17] to capture epistemic and aleatoric uncertainties. In [18], the net load is decomposed into three parts: PV output, actual load, and residuals. The overall forecast is then obtained by the convolution of individual forecasts of each part. The decomposition is based on expert knowledge. In [19], the information of some locations is assumed to be visible, and dimensionality reduction is used to select useful information from those sites. Based on what is preserved by the dimensionality reduction, some base learners are used to forecast the net load of the entire system. Moreover, complex-valued neural network is adopted for very short-term load forecasting on systems with a high PV penetration in [20].

Net loads in different zones are geographically distributed time series, and hence, information from neighboring zones may improve the forecast accuracy as well. It is worth investigating the potential of using neighboring information on improving the accuracy of net-load forecasting. Limited literature to date studies this problem. An artificial neural network model and a graph dictionary learning architecture for spatio-temporal net-load forecasting are proposed in [21] and [22], respectively. However, two models are designed for point forecasting and require historical solar generation data.

In this dissertation, a new probability distribution learning model, named graph transformer network (GTrans), is developed for the probabilistic net-load forecasting with behind-the-meter solar penetration. The GTrans is built on three state-of-the-art architectures: a graph attention network (GAT), variational autoencoders (VAEs), and transformers. The main contributions of this model are given as follows [23]: 1) The model is based on attention mechanisms that can improve the interpretability of the model. The model is able to generate quantiles, prediction intervals, and scenarios; 2) A GAT is designed to extract spatial information from neighboring zones. It allows feature selection for a complete graph, which is more appropriate for the net-load forecasting task in consideration; 3) Transformers are adopted to address temporal correlations, which ensure long-range persistence. It would be useful for forecasting tasks with long forecasting horizon and high time resolution.

1.1.3 Scenario Generation

In some cases, the operator only has access to its own information. For example, loads within a microgrid are served by a single wind farm. Furthermore, the effectiveness of stochas-

tic formulations will highly depend on the selection of uncertainty representations. From the perspective of decision making and risk assessment, probabilistic forecasts such as probabilistic intervals, quantiles, or sample paths, fit the stochastic formulation better. We focus on predicting sample paths, and the process of generating scenarios is referred to as scenario generation (or scenario forecasting). The generated scenarios can be regarded as a discrete approximation of the underlying distribution.

Traditionally, scenario generation for such cases follows a two-step approach: 1) Obtaining the probabilistic distribution of wind speed or forecast error; 2) Sampling the scenarios from the statistical distribution, where Monte Carlo simulation is the prevailing method. When the number of samples is large enough, the propagated uncertainties tend to be the ground truth. In regard to the first step, parametric models are widely used to fit the data. An empirical cumulative distribution function is used to characterize the forecast error [24]. Gaussian distributions, beta distributions, and bootstrap methods are applied in [25], [26], and [27], respectively. To capture the temporal correlation, several time dependent models have been proposed. Multiple univariate autoregressive moving average processes are adopted to transform the correlated noise into statistically dependent wind speeds [28]. Generalized dynamic factor model [29] is used to derive the correlated movements of multiple time series of load and wind power scenarios. However, the statistical assumptions may not be applicable to all kinds of wind farms. In fact, it would be difficult to capture the complex temporal dynamics of wind speed using the first few statistical moments.

To tackle the issue, nonparametric (or ensemble) models have been extensively studied. Sparse Bayesian learning, kernel density estimation, and their combination are examined in [30]. Bayesian learning, as a distribution-free approach, provides good adaptive ability and robustness. Kernel density estimation gives a smoother ensemble forecasting. Combination of kernel density estimation and regular vine copulas is also used to capture the spatial correlations among wind farms [31]. Fuzzy inference is used to ensure the robustness of intra-day operations in microgrids by selecting fuzzy prediction intervals [32]. A nonparametric time series model called infinite Markov switching autoregressive process is introduced to quantify the forecasting uncertainty [33].

In spite of the aforementioned recent advances, there are two main issues in scenario generation for microgrid day-ahead scheduling: 1) Nonparametric, supervised models may capture complex dynamics among the look-ahead times, but require sufficient prior knowledge to select the input features and are difficult to tune and implement; 2) Most of the previous methods are for the main grid and use information at multiple sites within a region to improve the accuracy. However, it can be difficult to obtain such information for microgrids as small-scale centralized grids. The adaptability of those methods to a single time series process has not been carefully examined. Moreover, the economic values of generated scenarios in power system analysis are rarely evaluated.

In this work, we adapt the sequence generative adversarial network (SeqGAN) [34] for

scenario generation in the day-ahead scheduling problem of microgrids. We utilize the long short-term memory (LSTM) architecture to fulfill the task of time-series sequence generation. To guide the learning of the LSTM units, we adopt generative adversarial network (GAN) coupled with reinforcement learning. The GAN sets up a minimax two-player game between a discriminative net D and a generative net G , where D learns to distinguish whether a given data instance is real or not, and G learns to confuse D by generating high quality data. We consider the sequence generation procedure as a stochastic sequential decision making process. The generative model G is regarded as an agent of reinforcement learning, with the state to be the previous wind generation and the action to be the wind generation in the current time slot. Our main contributions include the following [35]: 1) The SeqGAN integrates the concepts of LSTM, GAN, and reinforcement learning. This method is distribution-free, and can generate both intervals with confidence and sample paths; 2) The rewards returned by the discriminative model are used to guide the learning process. To incorporate the time-dependent physical constraints in power systems, we consider the overall reward as well as the fitness in each time slot, which is more reliable for the intra-hour operation in the next day; 3) In contrast to the previous supervised methods, SeqGAN does not need the selection of features. Moreover, it is not prone to overfitting or misidentification of patterns. Hence, the generated scenarios can explore the overall variability of VGs.

1.1.4 Scenario Reduction

Scenarios already exist in some circumstances. For example, historical forecast errors coupled with point forecasts can be regarded as scenarios. Most of the scenario generation methods cannot control the number of generated scenarios with guaranteed performance. Only when the number of samples is large enough, the propagated uncertainties tend to be the ground truth. Most of the day-ahead decision-making processes, such as unit commitment, are formulated as mixed integer programming problems. Due to the presence of integer variables, the problems are proven to be NP-hard and intractable on a large scale. Dimensionality reduction techniques, known as scenario reduction, are needed to reduce the number of scenarios. In general, the essence of scenario reduction lies in finding a new scenario set with fewer number of scenarios that can keep the solution close to that generated by the original scenario set. However, two questions remain open for scenario reduction, i.e., how to perform scenario reduction, and how to tell which scenario reduction method provides scenarios with the best quality for a given problem.

Traditionally, scenario reduction is implemented by minimizing a probability distance function between two scenario sets. On the basis of Fortet-Mourier probability metric, the concept of scenario reduction is first introduced in [36], where forward selection and backward reduction methods are included. Motivated by that work, some heuristics, the combination of forward and backward methods, and many variants using Fortet-Mourier metric are presented in [37, 38] and the references therein. However, such probability metric based methods are designed for

multi-stage scenario trees, i.e., planning problems. A time series in day-ahead scheduling cannot be simply regarded as such a multi-dimensional vector due to high heterogeneity of time series. On the other hand, there are many time-dependent constraints in optimization problems for power systems, such as the minimum down time. It is crucial to preserve irregular patterns and time correlations in the original scenario set.

To tackle the issue, scenario reduction techniques for short-term time series have been extensively studied. The idea is to define a new similarity measure that captures the characteristics of time series, and then reduces the dimensionality by solving an optimization problem. A major subset of similarity based methods includes the solution sensitivity in the measure. Solution sensitivity indices of scenarios are computed by solving deterministic scheduling problems, and scenarios are clustered into clusters via k -means in [39]. The error between the expected objective values obtained by the original and preserved scenario sets is minimized by solving a probability mass transportation problem in [40]. The differences between the expected, best, and worst performance of both scenario sets are considered in [41]. However, such methods involve the optimal objective values of deterministic scheduling problems, which may be hard to scale. The space and moment distances are minimized simultaneously by particle swarm optimization in [42]. Similarity matrices between time series are computed by a radial basis kernel function and maximized by submodular optimization [43]. Probability metrics and correlations between random variables are both considered in [44].

We observe that the scenario reduction problem is indeed a time-series clustering problem. We adopt the concept “mixed autoencoders” in [45, 46], and propose a mixed autoencoder based fuzzy clustering (MAFC) architecture. First, several deep autoencoders map time series in consideration to latent representations. Using the representations, another deep neural network (DNN) gives the degree of each time-series being in different patterns. Deep hypothesis spaces in autoencoders provide high generalization capability and capture the complex temporal dynamics. With membership functions, conventional methods of constructing centroids in c -means are extended to fuzzy time-series clustering. The architecture simultaneously learns feature representations and adjusts cluster assignments. The novelties are summarized as follows [47]: 1) The MAFC leverages recent advances in deep learning and fuzzy logic on time-series clustering tasks; 2) Time series are embedded into latent spaces, driven by which, cluster assignment may implicitly consider the correlations between time steps; 3) Three different empirical criteria are designed to evaluate the quality of renewable energy scenario reduction techniques for stochastic day-ahead scheduling.

1.2 Uncertainty and Non-convexity in Integrated Energy Systems

Over the last several decades, the world has witnessed a dramatic increase in penetration of renewable energy, especially wind and solar energy, and installation of gas fired generators.

It is reported that most of the new generation capacity will be renewable and nature gas in the United States due to the low fuel price and supportive policies, according to the U.S. Energy Information Administration (EIA) [48]. Driven by an increasing share of natural gas generation, power and natural gas systems are deeply interdependent. The operational constraints and uncertainties in the gas network have a huge impact on the power system operation, planning, and economics.

When it comes to the long-term planning, planners are facing more significant uncertainties, such as the gas price and the annual increase in load. The coupling of the aforementioned energy systems complicates the planning of an IES where the coupled operation of the entire energy system should be taken into account. In addition, the increase in uncertainty poses new challenges from the perspective of the implementation of state-of-the-art algorithms.

In literature, an extensive amount of models has been proposed for IES expansion co-planning problems. A multistage stochastic programming model is presented to study the sequential investment decision with the uncertainties revealed gradually over time, where constraints in power and gas systems are both considered [49]. A two-stage chance-constrained paradigm is proposed in [50], which highlights the role of natural gas storage in managing short time uncertainties in developing long-term planning. A combined electricity and gas expansion planning model with analysis of gas-price volatility is developed [51]. However, there are two major issues in the existing models for the IES expansion planning. First, the existing models overlook the potential contribution of an IES in some worldwide societal goals such as decarbonized economy and 100% renewable penetration. Second, those models exclude uncertainties or limit the number of scenarios that represent the possible evolution of random variables. Unlike the expansion planning for power systems where only the renewable generation and the increase in electrical load are considered as uncertainties, the uncertainties in gas price and gas load also play an important role in the co-expansion planning problem. Fewer scenarios in consideration will decrease the performance of the investment decision.

To take environmental costs into account, we adopt cap-and-trade, which is a market based program to constrain the emission of pollutants by imposing tariffs. According to the data published by the United States Environmental Protection Agency (EPA) [52], the social cost of carbon is not trivial since it increases the production cost by around \$10/MW. Hence, the planner should consider cap-and-trade market in the co-expansion planning and increase the renewable utilization as much as possible. We observe that power-to-gas (P2G) is a solution to the low carbon oriented expansion planning. P2G starts with converting electricity to hydrogen through water electrolysis, and it can further react with carbon dioxide that is captured from air to produce synthetic natural gas. Comprehensive environmental benefits of P2G are listed in [53]. Due to the seasonal characteristic of renewable energy and load, P2G can absorb excess renewable generation in peak seasons, which can be then supplied to meet natural gas loads or stored to serve electric load in off seasons using gas fired generator. The feasibility of this feature is evaluated in [54].

To hedge the risk of uncertainties, we adopt the multistage stochastic programming technique. The stochastic programming method encapsulates all possible realizations and hence is less conservative. Most importantly, investment decisions should be derived on a comprehensive what-if-analysis where the optimal recourse decisions are considered for the minimum cost adjustment to the disclosure of uncertainties [55]. Given this insight, a multistage stochastic programming model where the planner can make “wait-and-see” decisions is the most appropriate one for the expansion planning. Multistage stochastic programming models are widely adopted in the field of power system expansion planning or even IES expansion planning [49, 56]. However, as the number of stages, variables, and uncertainties increases, the problem becomes computationally demanding and intractable due to the existence of integer variables. We use branch-and-price algorithm, adopted from [57], to solve the multistage stochastic program. The branch-and-price algorithm consists of Dantzig-Wolfe decomposition, column generation, and branch-and-bound [58]. It is proven to be an efficient exact algorithm for multistage stochastic mixed integer programming problems [59].

The main contributions of this work are given as follows [60]: 1) A comprehensive stochastic IES co-planning framework that accommodates cap-and-trade market and P2G investment options is presented; The case study shows that the enforcement of P2G can reduce the environmental and operational costs in long term; 2) Branch-and-price algorithm is used to solve the problem. The numerical results highlight the advantage of the algorithm; 3) To guarantee that the scenarios in consideration can encapsulate the possible evolution of uncertainties, we discuss the method for scenario generation and the selection of the number of scenarios.

Regarding the short-term operation of an IES, the high share of renewable energy requires more flexibility to follow the unpredictable variations, both in loads and renewable energy sources. In order to follow the realizations of uncertainties in real time, system operators use operating reserves, which are usually scheduled through the unit commitment [61]. Nowadays, gas-fired units are widely used not only for the generation but also for the operating reserves because of the low natural gas price, their fast start-up flexibility, and fast ramp rates [62]. The operational constraints and uncertainties in the gas network have a huge impact on the power system operation and economics. For example, when one pipeline suffers a contingency, it will influence the generation of gas-fired units. With the goal of developing renewable energy systems, the integration of power and gas systems becomes necessary to realize efficient and secure operation of future renewable-based energy systems.

Again, the rapid development of P2G technology is promoting the integration of DERs. Due to the intermittent nature of renewable energy, curtailment happens in systems with high share of renewable energy. For example, this happens when solar power peaks during the day in California, or at night when wind power is greatest in Midwest. While those curtailments do not cause reliability issues, flexible balancing tools such as utility scale energy storage are needed to increase renewable utilization. The combination of gas-fired units and P2G can act as storage and serve as a potential solution to renewable curtailment. Moreover, by means of

the rapid response of polymer electrolyte membrane electrolysis, P2G can also offer auxiliary and regulatory power services of high value.

Reliability is an overriding concern for power systems. An $N - 1$ contingency criteria is the most well-known security criteria in practice to guarantee that the system survives when any single component suffers a contingency. There is a widespread study about contingency-constrained unit commitment (CCUC) for power systems with high renewable penetration. A common approach used to study CCUC is robust optimization [63, 64]. However, robust optimization raises concerns of over-conservatism. Another important direction of the researches on CCUC incorporates the probability of contingencies such as [65]. However, the computational efficiency is not guaranteed. Moreover, the exact probability distribution of contingencies is difficult to obtain. To alleviate the computational burden, methods considering post-contingency analysis are used as the current practice to manage transmission contingencies. For example, [66] proposes an $N - 1$ security constrained formulation based on the line outage distribution factors. Unfortunately, a report from NERC indicates that as the reliance on natural gas to meet electric generation requirements increases, additional measures and risks must be considered to better understand the implications of the complex interdependency between the natural gas system and the power system [67]. Limited literature to date studies the impacts of natural gas facility disruptions on the power systems.

In this dissertation, the uncertainty in DERs and contingencies are modeled by interval numbers, and we present an interval based CCUC model for an IES with high penetration of renewable energy. Unlike the scenario based methods where each scenario is associated with its probability, interval numbers assume a vague uncertain set, which is easier to obtain. The model also considers the contribution of P2G in achieving high share of renewable energy. The main contributions of the work are given as follows [68]: 1) An interval based CCUC problem for IESs with high renewable penetration is presented, and contingencies in both transmission lines and pipelines are considered; 2) Risk preference of the decision maker is considered via preference ordering of interval numbers in the objective values; 3) We examine that the P2G can reduce renewable curtailment as well as offer auxiliary services.

1.3 Energy Trading

A key element in the vision of future energy networks is the so-called energy hub. An energy hub is considered as a unit where multiple energy carriers can be converted, conditioned, and stored. It represents an interface between different energy infrastructures and loads. The flexible combination of different energy carriers using the conversion and storage technology offers a powerful approach for various system improvements. Due to the deep coupling between the power and gas systems, we consider an energy hub acting as retailers in both electricity and gas markets. Optimizing the trading decisions for energy hubs aims to obtain the optimal involvement in electricity and other energy markets, and to maximize the expected profit.

Allowing trading between different energy sectors via energy hubs, excess power produced by a VG can be sold to energy hubs, and the operator can buy electricity from energy hubs when the realization of a VG is lower than it is expected. A few studies have discussed the operation of energy hubs. A bilevel stochastic programming model of the decision making of an energy hub manager is presented in [69]. The planning of energy hubs systems considering the uncertainty has been discussed in [70]. However, the role of P2G is not analyzed in the two works.

On the above premises, we construct a dynamic programming framework to study the trading decision making problem faced by the manager of energy hubs equipped with P2G who seeks to optimally operate the energy hubs and trade electricity as well as natural gas in the wholesale markets. The proposed trading strategy helps the managers of energy hubs to optimize their trading decisions and assists them to optimally determine the energy conversion between electricity and natural gas as well as the operation of the storage. The main contributions of the proposed trading strategy are given as follows [71]: 1) We study the optimal operation of a profit-maximizing energy hub equipped with the energy conversion and the energy storage through a dynamic programming formulation; 2) We establish a two-threshold policy for the optimal operation of the energy conversion devices; 3) We show that the expected net benefit is a concave function of the state of charge of storage, which leads to a stationary policy for the operation of the energy storage.

The current power distribution system is undergoing a transition from centralized markets to decentralized markets. Increased choice and information in transactive energy will give the prosumers greater personal utility by changing their energy use patterns. Increased use of DERs will achieve larger societal environmental goals. That being said, the National Institute of Standards and Technology indicates that the markets of transactive energy must be developed in a way that ensures transparency, choice, privacy, and ease of use to the consumers [72]. The requirements can be met by the blockchain technology, and the feasibility of applying blockchain based platform to peer-to-peer energy trading has been demonstrated in a pilot project in Brooklyn [73].

Over the past few years, there has been a significant interest in the economic mechanisms for transactive energy such as [74, 75]. Including drawbacks mentioned in [76], we believe that there are three gaps: 1) Each prosumer does not have complete information because the prosumers are typically selfish profit maximizers; 2) There exists no negotiation in the bidding process; 3) The price is cleared in spot markets. Some works address the gaps. For example, reinforcement learning is used to estimate private information [77], and an iteration based algorithm partly captures the negotiation process [76]. However, a spot market, which the current wholesale market belongs to, implies a high degree of synchronization between the prosumers without negotiating mutually acceptable terms of business. These two factors discourage the participation of prosumers. The discrete double auction is not suitable for a large-scale trading market as well.

To fill the gaps, we adopt the framework of continuous double auction (CDA). In a CDA,

the prosumers can submit bids or asks sequentially, and transactions occur upon the detection of compatible bids. The prosumers can utilize the existing information in the order book and adjust their strategies accordingly, which is essentially a negotiation process. This allows auction participants to learn about others' preferences. Even with a small number of traders who have imperfect information on supply and demand, the CDA consistently produces very efficient allocations [78]. In addition, CDA based allocation mechanisms eliminate the need for a centralized control and suit the decentralized nature of transactive energy [79], which enables the trading on a large scale. The main contributions of the developed peer-to-peer trading mechanism are given as follows [80]: 1) We propose an economic mechanism based on CDA in detail, which provides an open and democratic architecture that facilitates the prosumers' participation; 2) The proposed mechanism implicitly allocates the loss of implementing each transaction to the buyer and seller; 3) We derive an efficient trading strategy based on the dynamic programming formulation for the proposed mechanism.

1.4 Sustainable Community and Critical Service Restoration

The desire for a green, efficient, and sustainable energy supply paves the way for the rapid growth of solar energy in the world. Customer-sited solar photovoltaic systems portend a potentially disruptive change in the customer-utility relationship. We observe that a zero-energy community (ZEC) is a good solution to the PV development planning in a deregulated environment. A ZEC, which offsets all of its energy use from renewables available within the community environment, reduces the transmission line losses, is more independent and self-sufficient, and has more controls over energy decisions. Already many utility companies are making strides toward helping ZECs become a reality. For example, Texas, California, and Minnesota have been at the forefront of renewable energy advocacy, and their municipal utilities have played a key role in supporting it via net metering. However, the increasing penetration of customer-owned PV has intensified the concerns over utility revenues and the recovery of grid infrastructure cost.

Given the prevalence of net metering for U.S. residential PV system owners, there is an extensive discussion on customer economics. It is shown in [81, 82] that this setting significantly enhances the end users' bill savings, even if the reverse power flow is penalized. Unfortunately, utilities are mandated to offer net metering, but view these programs with hostility as they influence the utility's revenue and the equity of deployment subsidies. Evidence of the "action plan" can be seen in states across the country [83], such as placing an annual cap, increasing installation fee, or even abandoning the net metering policies. The conflict resolution inspires a negotiation process for finding a win-win solution, including the installation of shared PV-storage systems for risk hedging, and the allocation of surplus. Although there is a sharp increase in the number of studies investigating the benefits of ZECs, such as [84, 85], most of them focus on benefits in the short-term operation.

Some works discuss the planning for microgrids, which may potentially be extended to the ZEC planning problem. For example, a theoretical framework for the cooperative planning in a system of interconnected microgrids is presented [86], in which self-interested behavior of microgrids is considered. Such frameworks are not directly applicable to ZEC planning. For example, as an important player in the process of ZEC planning, the load-serving entity (LSE) is not included in clustered microgrid work. Another related research track is sharing economy, wherein the customers within a ZEC and the LSE share the usage of storage. A non-cooperative storage investment game is studied in which the consumers can trade their unused storage capacity [87]. A similar transaction-based Stackelberg game is presented in [88]. Regarding the cooperative framework, a coalitional game that focuses on the efficient cost allocation is developed in [89]. However, the discussion on sharing frameworks, including both PV and storage, is limited. Most importantly, uncertainties are not addressed in the above works. ZEC planning is influenced by local geography and resources. Therefore, location-specific data analytics is preferred.

We apply the Nash bargaining solution (NBS) to the cooperative planning problem for a ZEC and leverage deep learning to generate multiple realistic scenario paths as well as to factor in the meteorological and geographical aspects of the random parameters. The main contributions are as follows [90]: 1) A new business framework is proposed, wherein the load serving entity (LSE) and households within a community finish the planning phase of PV-storage system in a cooperative manner; 2) NBS is employed to derive the optimal investment strategies. Numerical results demonstrate that cooperation is beneficial for all the players and may improve the integration of PV; 3) A convolutional neural network approach for point forecasting coupled with sampling multivariate Gaussian distribution for obtaining forecasting error sample paths is used for the scenario generation of the stochastic optimization problem in consideration.

During grid outages, it is desirable for DERs to participate in effective and efficient critical service restoration to enhance grid resiliency, especially when power support from the upstream transmission system is not available. Dynamic microgrids with adaptive boundaries can be formed, in which distributed generation serves critical service facilities. In this dissertation, we will investigate such a critical service restoration problem for a single-phase distribution system.

Although there are remarkable ongoing efforts in grid resiliency enhancement using dynamic microgrids and DERs, most of the works solve the underlying problems in a centralized manner. For example, the problem can be formulated as a centralized mixed binary second-order cone programming problem as in [91, 92] or a centralized mixed binary linear program as in [93, 94]. Centralized optimization may sacrifice the privacy of DER owners. Moreover, it requires that the operator is able to solve a complicated problem promptly, which is not always the case under emergencies. Mixed binary second-order cone programs on a large scale can be computationally prohibitive, while linear models may not characterize the physical dynamics adequately.

In this regard, distributed optimization approaches are widely adopted to tackle problems in

the distribution system. For example, alternating direction method of multiplier (ADMM) technique and dual decomposition are used for optimal power flow and voltage regulation problems in distribution systems in [95, 96], respectively. However, binary variables representing on/off statuses of switches may change the structure of problems in the works mentioned above. The methods therein are not directly applicable to critical service restoration problems with dynamic microgrids. The problem in consideration needs a distributed optimization technique that is compatible with binary variables. Some works formulate the critical service restoration problem based on multi-agent systems, where the problem with binary variables can be solved in a decentralized manner. Different zones are considered as different agents in [97], which requires expert knowledge. Meanwhile, different devices such as DERs and switches are regarded as different agents in [98], where the likelihood of the number of nodes to be restored is maximized. Convergence and optimality gaps are not discussed in most of the multi-agent system based works. Distributed optimization techniques that have been applied to DC unit commitment, such as analytical target cascading in [99] and auxiliary problem principle in [100], may be extended to address the problem in consideration. The DC power flow model is generally not appropriate for distribution systems, and hence, a more realistic power flow model is needed.

In this work, we investigate a distributed optimization based solution with guaranteed performance. The main contributions of the proposed algorithm are given as follows [101]: 1) The critical service restoration problem is formulated as a mixed integer second-order cone program. A heuristic distributed optimization approach that is based on column generation is proposed to enhance computational efficiency; 2) The heuristic method is shown to converge after finite iterations with a bounded optimality gap; 3) Numerical results highlight the necessity of distributed optimization and effectiveness of the proposed approach.

CHAPTER

2

DEEP LEARNING FOR FORECASTING TASKS IN POWER SYSTEMS

Forecasting is a long-lasting research area in power systems. Driven by the complexity of the related decision making task which calls for the forecast uncertainty, today the main interest of forecasting turns from point to probabilistic or scenario forecasting. From the perspective of decision making and risk assessment, the optimal solution is directly linked to a set of uncertain realizations instead of the expectation of the future outcome. In this regard, it is desirable to make probabilistic and scenario forecasts. Nowadays, stochastic day-ahead scheduling has drawn a tremendous amount of interests worldwide in tackling the uncertainty and accounting for risks. As one of the most important streams in stochastic optimization, scenario based methods have been widely adopted to deal with the decision-making process in the short-term operation. The stochastic formulation helps decision makers hedge the risk of producing power with high cost and avoid the infeasibility of the day-ahead decisions when applied to the intra-day operations. The effectiveness of those methods will highly depend on the selection of uncertainty representation. In this regard, scenario generation (or trajectory forecasting) representing the future evolution of renewable resources is as important as probabilistic forecasting which predicts the values at quantiles. On the other hand, most of the day-ahead decision-making processes, such as unit commitment, are formulated as mixed integer programming problems. Due to the presence of integer variables, the problems on a large scale are proven to be NP-hard and intractable. It is a must to control the number of scenarios.

In this chapter, we first propose a deep learning (DL) model for renewable resources probabilistic forecasting, in which the target renewable resources at different site are regarded as

geographically distributed time series. Moreover, behind-the-meter (BTM) solar-plus-storage that is normally invisible to system operators has deteriorated the accuracy of the legacy load forecasting due to the volatile nature of solar generation. We then develop a model that can explore spatio-temporal information and be used for net-load probabilistic forecasting. Furthermore, we consider a standalone renewable site where no off-site information is available, and develop an efficient and effective algorithm for the scenario generation. Finally, we discuss how to find a new scenario set with fewer number of scenarios that yet can keep the solution close to that generated by the original scenario set, i.e., scenario reduction.

2.1 Attention Temporal Convolutional Network

Attention temporal convolutional network (ATCN) is proposed for the ultra-short-term forecasting of renewable resources. The developed ATCN is a deterministic mapping. With the use of Pinball loss function, the ATCN can obtain probabilistic forecasts as well. The model is mainly built on convolutional neural network (CNNs), which are power tools for feature extraction. Although CNN is more popular in processing spatial data, it has been shown to be a good alternative for handling sequential data recently. For example, temporal convolutional networks (TCNs) achieves state-of-the-art performance on action segmentation [102]. Compared with variants of recurrent neural networks, TCN based structures allow us to process all the time steps simultaneously. Moreover, it eliminates some common issues in recurrent neural networks such as gradient exploding. To find an efficient data representation of the extensive inputs, we utilize the idea in TCNs. Information at each site is considered as channels in convolutional layers, and the dot production during the convolution encodes spatial information. The parameters will be optimized by the training process, and therefore, it gets rid of expert knowledge and feature selection. Moreover, dilated causal convolution, which changes the spacing between kernel elements, allows us to extract information between different time steps [103]. Dilated causal convolution has been shown to successfully capture temporal dependencies in applications of probabilistic traffic and load forecasting [104]. We construct stacked dilated convolutional networks (DCN), in which each layer has a different dilation value, to capture the temporal relationship within the series. To ensure the original features for each site are preserved, we use residual connections.

On the other hand, a target time series can be regarded as a convex combination of several base time series. A convex combination is a linear combination of vectors where all coefficients are non-negative and sum to 1. The geographically distributed time series of renewable resources are expected to be spatially correlated, and some of their base sequences should show similar trends. Therefore, we want to produce a set of time series, and the predictions at different sites can be obtained by taking different convex combinations of series in the base set. To make the selection of weights data-driven, we adopt the attention mechanism [105]. Attention mechanism mimics cognitive attention, and it enhances important inputs and fades out trivial ones. The

attention scores associated with every site sum to 1 and can represent the weights of convex combination. In our case, the attention scores represent the contribution of each base sequence to the target time series. We train several DCNs simultaneously for the base time series. The weights of the convex combination for each site are determined by a dot-production attention mechanism. In the attention mechanism, the attention scores (i.e., weights) depend on both the original features and sequences in the base set. With the use of attention mechanisms, we can understand how the predictions are derived from the base sequences, which improves the interpretability.

2.1.1 Problem Statement

Let the number of sites of renewable resources we are interested in be N . Given a spatio-temporal forecasting problem, we want to predict a set of vectors $\hat{\mathbf{y}} = \{\hat{\mathbf{y}}_1, \dots, \hat{\mathbf{y}}_T\}$, where T is the forecasting horizon determined by the specific task in consideration. Let $\mathcal{T} = \{1, \dots, T\}$, we have $\hat{\mathbf{y}}_t \in \mathbb{R}^N, \forall t \in \mathcal{T}$. We have a series of fully observed time-series signals $\bar{\mathbf{y}} = \{\mathbf{y}_{-T'}, \dots, \mathbf{y}_{-1}\}$. In practice, we have all the historical observations. However, we adopt a fixed look-back window size T' , and assume that there is no useful information before the window. For simplicity, we set $T' = T$. Therefore, $\bar{\mathbf{y}} \in \mathbb{R}^{N \times T}$ is considered as input features. For all the spatio-temporal forecasting tasks of renewable resources, we always have a set of features shared by all the sites, for example, date and hour. Let the shared features be $\mathbf{X}_s \in \mathbb{R}^{F_s \times T}$. In some tasks, the operator may have extra information for each site. Let the dimension of unique features at each site in each step be F_u , we have another set of features $\mathbf{X}_u \in \mathbb{R}^{NF_u \times T}$. Finally, the features available consist of historical observations, shared features, and unique features. Denote $\mathbf{X} = (\bar{\mathbf{y}}, \mathbf{X}_s, \mathbf{X}_u) \in \mathbb{R}^{F \times T}$, where $F = N + F_s + NF_u$. Let the set of vectors representing the true realizations be $\mathbf{y} = \{\mathbf{y}_1, \dots, \mathbf{y}_T\} \in \mathbb{R}^{N \times T}$. Regarding the point forecasting tasks, we want to find a mapping $\mathbb{R}^{F \times T} \rightarrow \mathbb{R}^{N \times T}$, which makes $\hat{\mathbf{y}}$ close to \mathbf{y} . When it comes to the probabilistic forecasting, we want to predict the values of some quantiles. Let the set of quantiles of interest be $\{\tau_q | \forall q \in \{1, \dots, Q\}\}$, where Q is the number of quantiles we want to forecast. We want to find a mapping $\mathbb{R}^{F \times T} \rightarrow \mathbb{R}^{QN \times T}$, which minimizes the quantile losses.

2.1.2 Model Specifications

Preliminaries of Dilated Convolutional Network

We consider each feature dimension as an input channel, and the dot production during the convolution is expected to encode spatial information. For example, assume the input to a vanilla convolutional layer is \mathbf{X} . We have F input channels, and we apply a set of 1D filters sliding across the time steps. In a convolution, a convolution filter slides over all the features taking their dot product. The filter duration is the size of the filter, and let the filter duration be ω , the filters for the convolutional layer are parameterized by a tensor $\mathbf{W} \in \mathbb{R}^{F_{\text{out}} \times \omega \times F}$ and

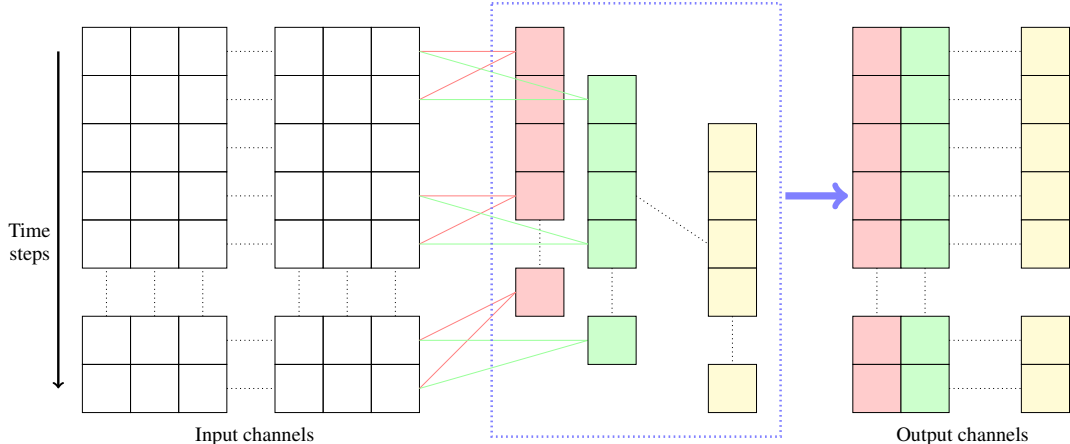


Figure 2.1: Illustration of the temporal convolutional layer on encoding spatial information.

a vector $\mathbf{b} \in \mathbb{R}^{F_{\text{out}}}$. The unnormalized output is given by

$$H_{i,t} = \text{ReLU} \left(b_i + \sum_{t'=1}^{\omega} \mathbf{W}_{i,t'} \cdot \mathbf{X}_{\cdot, t+\omega-t'} \right), \forall t \in \mathcal{T}, \quad (2.1)$$

where $i \in \{1, \dots, F_{\text{out}}\}$ and \mathbf{H}_i is i -th row of $\mathbf{H} \in \mathbb{R}^{F_{\text{out}} \times T}$. Zero padding, which extends the sequence with zeros, is used to keep the length of the output the same with that of the input. An illustration is shown in Fig. 2.1, in which each color represents a unique filter. Each cell encodes all the spatial information for two time steps. The data in this example have two dimensions: forecasting horizon and features at each time step. The kernel is sliding across the time steps. The filter duration is set to 2. Each convolution encapsulates spatial information of two time steps with lag one.

Such a convolutional layer is only able to look back at a history with size linear in the depth of the network. When the time resolution is high, the forecasting horizon may be long. For example, we need to make 60-step ahead forecasting when 1-hour ahead predictions with 1-minute resolution are required. Therefore, we employ dilated convolutions that enable an exponentially large receptive field [103]. Formally, let the dilation be d , and the output of a dilated convolution layer is given by

$$H_{i,t} = \text{ReLU} \left(b_i + \sum_{t'=1}^{\omega} \mathbf{W}_{i,t'} \cdot \mathbf{X}_{\cdot, t+d(\omega-t')} \right), \quad (2.2)$$

where $i \in \{1, \dots, F_{\text{out}}\}$ and $t \in \mathcal{T}$. The value of dilation controls the spacing between kernel elements. The temporal convolutional layer is equivalent to a dilated convolutional layer with dilation 1. Moreover, to improve the convergence during training, we apply weight normalization to the dilated convolutional layers in our experiments [106].

Stacked Dilated Convolutional Networks

We employ stacked dilated convolutional layers with different dilation values to capture temporal dependencies and make predictions for the base time series. Let the set of dilated convolutional layers be $l \in \{1, \dots, L\}$ and the corresponding dilation for layer l be $d^{(l)}$. The filters for each layer l are parametrized by a set of tensors $\mathbf{W}^{(l)} \in \mathbb{R}^{F^{(l)} \times \omega^{(l)} \times F^{(l-1)}}$ and biases $\mathbf{b}^{(l)} \in \mathbb{R}^{F^{(l)}}$. We set $F^{(0)} = F^{(L)} = F$ and $\omega^{(l)} = 2, \forall l$. Let the normalized output of layer l be $\mathbf{H}^{(l)} \in \mathbb{R}^{F^{(l)} \times T}$ and $H_{i,t}^{(l)}$ represent the element in the i -th row and the t -th column. Recall that our input features are \mathbf{X} , we have

$$H_{i,t}^{(1)} = \text{ReLU} \left(b_i^{(1)} + \sum_{t'=1}^{\omega} \mathbf{W}_{i,t'}^{(1)} \cdot \mathbf{X}_{\cdot, t+d^{(1)}(\omega-t')} \right), \forall t, \quad (2.3)$$

where $i \in \{1, \dots, F^{(1)}\}$. For the remaining layers $l \in \{2, \dots, L\}$, we have

$$H_{i,t}^{(l)} = \text{ReLU} \left(b_i^{(l)} + \sum_{t'=1}^{\omega} \mathbf{W}_{i,t'}^{(l)} \cdot \mathbf{H}_{\cdot, t+d^{(l)}(\omega-t')}^{(l-1)} \right), \forall t, \quad (2.4)$$

where $i \in \{1, \dots, F^{(l)}\}$. Since we set $F^{(L)} = F$, the dimension of data representations $\mathbf{H}^{(L)}$ extracted by the DCN is the same with that of \mathbf{X} . It allows us to perform residual connections. Post the summation, the new representations are given by

$$\mathbf{h} = \mathbf{H}^{(L)} + \mathbf{X}. \quad (2.5)$$

Residual connections address degradation problems in deep neural networks. We also want the original features to be retained. In this way, we actually add some spatial and temporal signals to the input features.

Finally, the output will be calculated by a fully connected feed forward network, which consists of two linear transformations. The transformations are parametrized by two weight matrices $\mathbf{W}_1 \in \mathbb{R}^{F \times 4F}$, $\mathbf{W}_2 \in \mathbb{R}^{4F \times 1}$ and a bias vector $\mathbf{b}_1 \in \mathbb{R}^{4F}$. The output of the feed forward network is given by

$$\hat{\mathbf{Y}} = \text{ReLU} \left(\mathbf{h}^\top \cdot \mathbf{W}_1 + \mathbf{b}_1 \right) \cdot \mathbf{W}_2, \quad (2.6)$$

where $\hat{\mathbf{Y}} \in \mathbb{R}^{T \times 1}$. An illustration on how DCN extracts the temporal information is shown in Fig. 2.2. The values of the dilation in each layer are set to 1, 2, 4, 8, and 10, respectively. Zero padding is applied to keep the length of the output sequences identical. The receptive field of the DCN is increased by controlling the spacing between kernel points. For example, the first step in the second hidden layer incorporates the information of \mathbf{X}_1 to \mathbf{X}_4 . However, in a TCN, it will only receive information of \mathbf{X}_1 to \mathbf{X}_3 . The number of layers in a DCN and the dilation values are hyper-parameters. Our selection criteria is quite intuitive: the information extracted

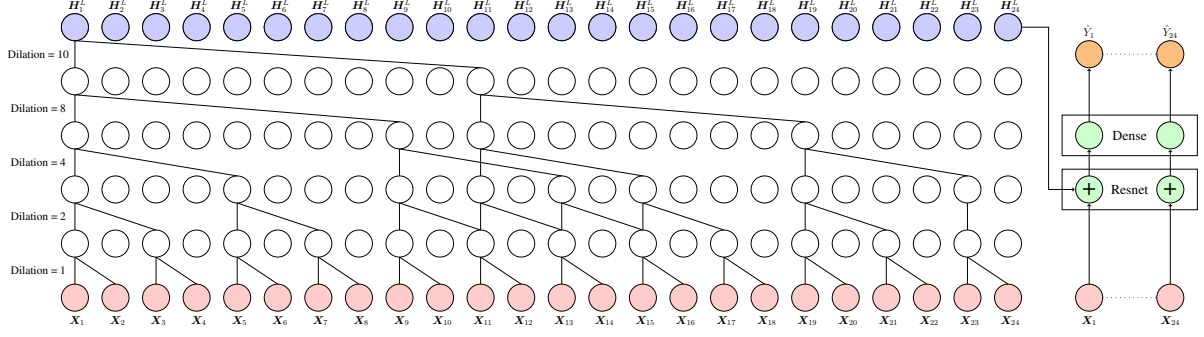


Figure 2.2: An example of the stacked dilated convolutional network.

for each step should include all the features available.

Dot-Product Attention and Point Forecasting

The DCN can be used to predict the individual time series of renewable resources directly. However, it cannot leverage the fact that the sequences may be spatially correlated, and the mapping cannot be adjusted. We train several DCNs to produce some base sequences. The prediction of time series at each site is a convex combination of the sequences in the base set. The weights of the convex combination should be self-adaptive and are determined by the current input features and the sequences in the base set. It motivates us to apply attention mechanism. Attention scores produced by the attention mechanism represent a weighted approximation of the importance of each base sequence. The summation of attention scores associated with each site is 1, which establishes the convex combination. Besides, the attention scores can be adjusted by inputs, which makes it self-adaptive.

Let the set of DCNs be $k \in \{1, \dots, K\}$. We define the base sequence generated by k -th DCN as $\hat{Y}^{(k)}$, and let $\hat{Y} \in \mathbb{R}^{T \times K}$ collect all the base sequences. We define two linear transformations parametrized by matrices $\mathbf{W}_R \in \mathbb{R}^{F \times N}$ and $\mathbf{W}_E \in \mathbb{R}^{T \times T}$. Post the transformation for \mathbf{X} and \hat{Y} , we obtain two new representations characterized by

$$\mathbf{R} = \mathbf{X}^\top \cdot \mathbf{W}_R, \quad (2.7)$$

$$\mathbf{E} = \hat{Y}^\top \cdot \mathbf{W}_E, \quad (2.8)$$

where $\mathbf{R} \in \mathbb{R}^{T \times N}$ and $\mathbf{E} \in \mathbb{R}^{K \times T}$. The final predictions are computed by

$$\hat{y} = \text{softmax}(\mathbf{R}^\top \cdot \mathbf{E}^\top) \cdot \hat{Y}^\top, \quad (2.9)$$

where the elements of $\text{softmax}(\mathbf{R}^\top \cdot \mathbf{E}^\top) \in \mathbb{R}^{N \times K}$ are the attention scores, which serve as weights of convex combinations. The n -th row characterizes the contribution of each base sequence to the predictions of site n . The complete ATCN model is shown in Fig. 2.3. K independent DCNs are constructed and generate the base sequences. The base set and the input

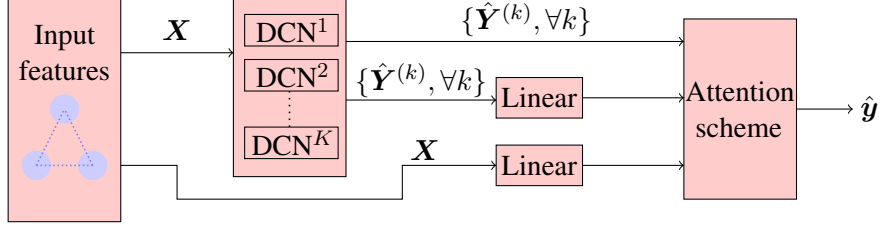


Figure 2.3: Architecture of the attention temporal convolutional network.

features are further used to determine the weights of the convex combinations via the attention scheme. Finally, the predictions of each site can be obtained by taking the corresponding convex combination. It is a deterministic mapping $\mathbb{R}^{F \times T} \rightarrow \mathbb{R}^{N \times T}$, which can be used for the point forecasting.

To guide the learning of parameters in the ATCN, we minimize the mean absolute error between the true realizations and predictions. Let $\|\cdot\|_1$ be the ℓ_1 norm. The loss function is defined as

$$\mathcal{L} = \|\hat{\mathbf{y}} - \mathbf{y}\|_1. \quad (2.10)$$

Probabilistic Forecasting

Recall that the set of quantiles of interest is $\{\tau_q, \forall q\}$. When probabilistic forecasts are desired, we want a mapping $\mathbb{R}^{F \times T} \rightarrow \mathbb{R}^{Q \times N \times T}$. Namely, we need to derive Q sets of point predictions, among which each set corresponds to a quantile τ_q . We also use K DCNs to generate the base sequences and obtain $\hat{\mathbf{Y}}$. However, we train a multi-headed attention mechanism here, in which each head predicts a corresponding quantile. Moreover, we transform the base sequences into higher-level dimensions to obtain sufficient expressive power. Since the number of quantiles we need is Q , we build a Q -headed attention mechanism. For each head q , we define three linear transformations parametrized by matrices $\mathbf{W}_R^{(q)} \in \mathbb{R}^{F \times N}$, $\mathbf{W}_E^{(q)} \in \mathbb{R}^{T \times T}$, and $\mathbf{W}_V^{(q)} \in \mathbb{R}^{T \times T}$. Post the transformations, we have

$$\mathbf{R}^{(q)} = \mathbf{X}^\top \cdot \mathbf{W}_R^{(q)}, \forall q \in \{1, \dots, Q\}, \quad (2.11)$$

$$\mathbf{E}^{(q)} = \hat{\mathbf{Y}}^\top \cdot \mathbf{W}_E^{(q)}, \forall q \in \{1, \dots, Q\}, \quad (2.12)$$

$$\mathbf{V}^{(q)} = \hat{\mathbf{Y}}^\top \cdot \mathbf{W}_V^{(q)}, \forall q \in \{1, \dots, Q\}, \quad (2.13)$$

where $\mathbf{R}^{(q)} \in \mathbb{R}^{T \times N}$ and $\mathbf{E}^{(q)}, \mathbf{V}^{(q)} \in \mathbb{R}^{K \times T}$.

The values of each quantile τ_q are computed by

$$\hat{\mathbf{y}}^{(q)} = \text{softmax} \left(\mathbf{R}^{(q)\top} \cdot \mathbf{E}^{(q)\top} \right) \cdot \mathbf{V}^{(q)}, \forall q \in \{1, \dots, Q\}, \quad (2.14)$$

where $\hat{\mathbf{y}}^{(q)} \in \mathbb{R}^{N \times T}$. We want to minimize the quantile losses, and the loss function for the

probabilistic forecasting is defined as

$$\mathcal{L} = \sum_{q=1}^Q \left[\tau_q \text{ReLU}(\mathbf{y} - \hat{\mathbf{y}}^{(q)}) + (1 - \tau_q) \text{ReLU}(\hat{\mathbf{y}}^{(q)} - \mathbf{y}) \right], \quad (2.15)$$

in which the quantile values of each site are assigned with equal importance. To ensure the predicted quantiles are not crossing, we penalize the loss function if the value of a previous quantile is large than the later ones. Therefore, we define another term to minimize, which is given by

$$\mathcal{L}' = \sum_{q=1}^{Q-1} \text{ReLU}(\hat{\mathbf{y}}^{(q)} - \hat{\mathbf{y}}^{(q+1)}). \quad (2.16)$$

The rationale is that the loss will increase when quantile crossing happens. Let the penalty of quantile crossing be ρ , the final loss function we are minimizing is $\mathcal{L} + \rho\mathcal{L}'$. In our experiment, ρ is set to 1. It is worth mentioning that penalizing (2.16) cannot make the $(q+1)$ -th quantile strictly greater than the q -th quantile. However, it can ensure that the $(q+1)$ -th quantile at least equals to the q -th quantile with some tolerances.

2.1.3 Case Studies

The proposed ACTN model is evaluated on the data sets from National Renewable Energy Laboratory (NREL). Two different renewable resources are tested: wind speed and solar generation. Our model is a mapping from the feature space to the space of the target sequences. Therefore, it is general and can be used to forecast both renewable attributes (e.g., wind speed or solar irradiance) and renewable generation (e.g., wind generation and solar generation). For example, when wind generation is desired, the system operator can replace the labels of target sequences with wind generation. We first describe the data used for training and testing, and then compare the point and probabilistic predictions made by the ATCN with those produced by the baselines.

For the point forecasting, we compare the ATCN with k -nearest neighbors based regression (k -NN), decision tree based regression (DT), LSTM based autoencoder, GRU based autoencoder, and attention based graph neural network (AGNN) [107]. The baselines are able to make multi-variate predictions. Regarding the probabilistic forecasting, we compare with quantile regression (QR), conditional kernel density estimation (KDE), LSTM coupled with Pinball loss based autoencoder, GRU coupled with Pinball loss based autoencoder, and AGNN. We also test GCN [108] in which a complete graph with identical weights is considered. Its performance is much worse, and hence, we do not select it as a baseline.

Data Description

The wind speed data are from the wind integration national data set toolkit [109], and the solar generation data are from the solar integration data sets [110]. Time resolutions for both

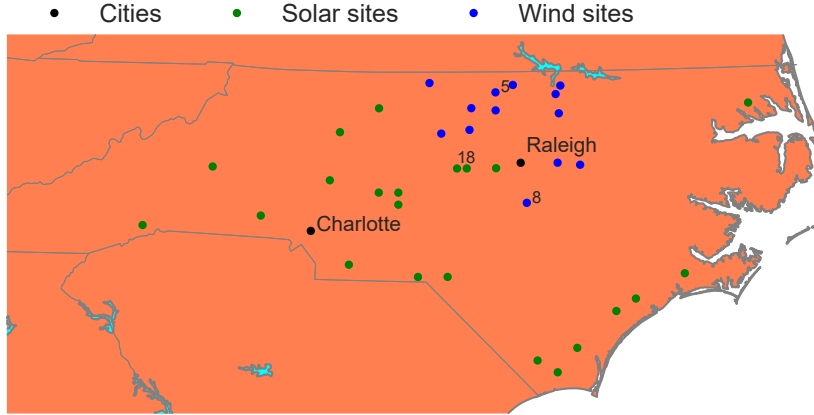


Figure 2.4: The locations of renewable sites used.

data sets are 5 minutes. The solar data set only provides the solar generation in 2006, and we select 1-year data in 2012 from the wind data set. Therefore, we have 105,120 time steps in total. The first 10 months are used for training, and the remaining two months are used for testing. The quantities of energy resources at each site are normalized to $[0, 1]$. It is worth noting that this normalization is important since the predictions of each site are computed based on the same base sequences. For the point forecasting, we test 12-step, 24-step, and 48-step ahead forecasting, i.e., 1-hour, 2-hour, 4-hour ahead forecasting. For the probabilistic forecasting, we only consider 24-step ahead forecasting, in which decimals are of interest. Therefore, τ 's are from $\{0.1, \dots, 0.9\}$. We select 13 wind sites and 22 utility-scale solar farms located in North Carolina, USA. The locations are shown in Fig. 2.4. Wind sites 5, 8 and solar site 18 are marked out for the later analysis. For the solar forecasting, historical observations and time are used as features, whereas historical observations, pressure, and time serve as features in the wind forecasting task.

We first show how the attention mechanism works and why it can improve the interpretability. For the wind speed forecasting task, we use the 2-hour ahead point forecasting as an example. We consider 4 sequences in the base set, and hence, the number of DCNs is set to 4. The attention scores of two selected time windows, which represent the importance of each base sequence to the predictions of each site, are shown in Fig. 2.5. We observe that all the sites pay more attention to the second and third sequences on November 1, whereas the importance of base sequences is more similar on December 1. It shows that the weights of convex combinations are self-adaptive, and the weights are jointly determined by both the base sequences and input features.

To give more insights, the corresponding base sequences and the predictions of wind sites 5 and 8 are shown in Fig. 2.6. We observe that the second and third base sequences (i.e., DCN 2 and DCN 3) are the dominant sequences. Their quantities are higher, and the predictions of each site are mainly adjusted by changing the weights of those two sequences. For the first

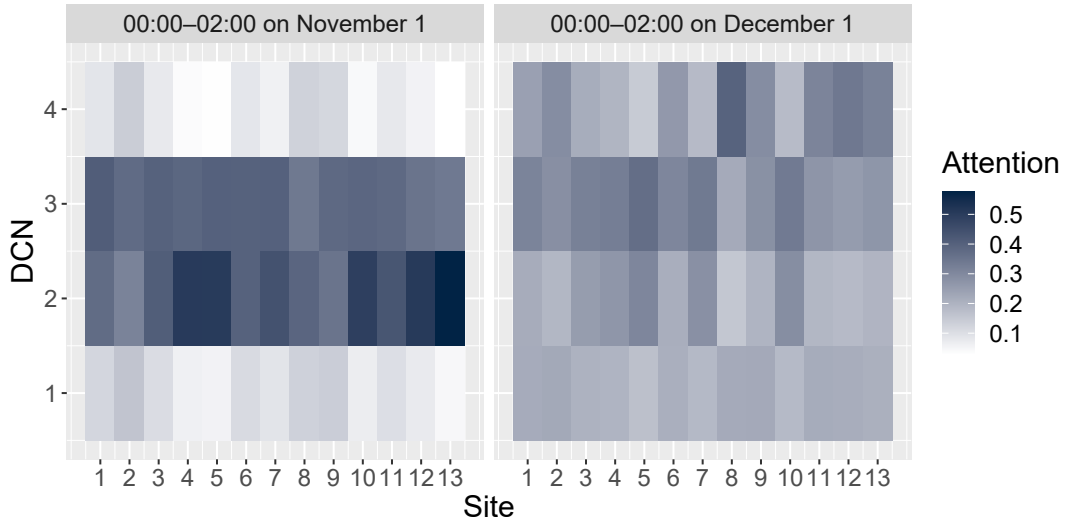


Figure 2.5: The attention scores for the 2-hour ahead point forecasting of wind speed. Two time windows are shown.

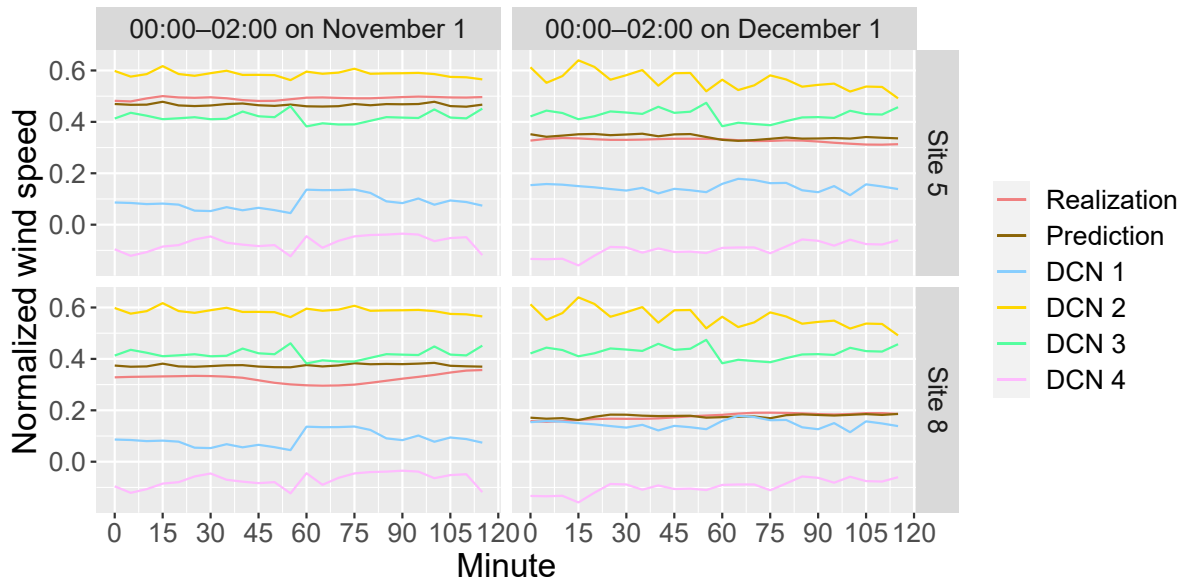


Figure 2.6: The 2-hour ahead point predictions and corresponding base sequences at wind sites 5 and 8 during two time windows.

and fourth base sequences, they are with similar magnitude but opposite signs. We interpret those two sequences as error terms which make some small adjustments to the final predictions. Moreover, we observe that the predictions of site 5 is larger than those of site 8, which coincides with the fact that site 5 pays more attention to the dominant sequences as shown in Fig. 2.5. It verifies that different weights are chosen for different sites to make the individual predictions more accurate.

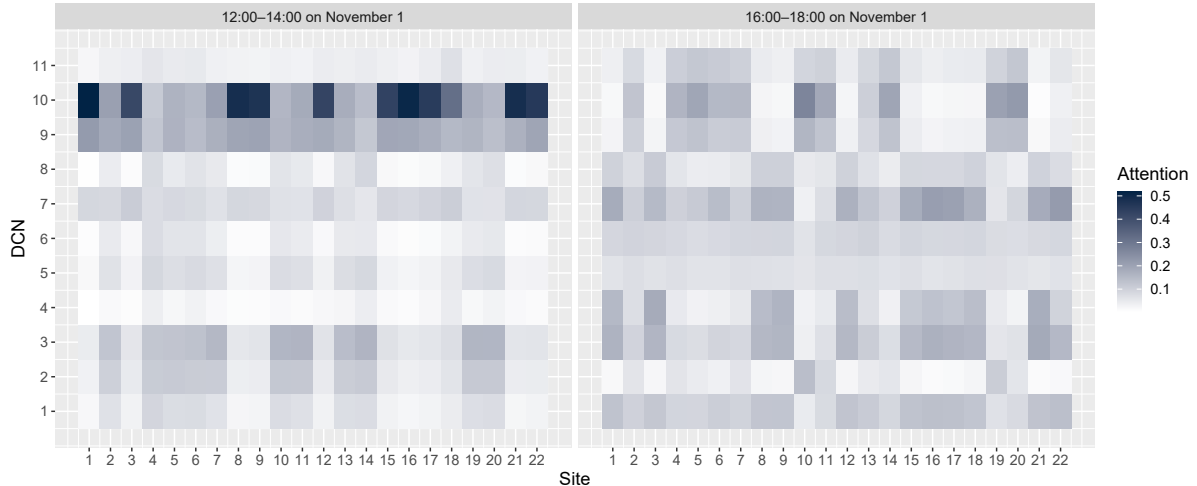


Figure 2.7: The attention scores for the 2-hour ahead point forecasting of solar generation. Two time windows are shown.

For the solar generation forecasting task, we also use the 2-hour ahead point forecasting for illustrations. Since the number of sites in consideration increases, we use 11 DCNs in this case. The attention scores of two time windows on November 1 are shown in Fig. 2.7. The corresponding base sequences and the predictions of solar sites 18 are shown in Fig. 2.8. Again, for different time windows of interest, the attention scores are self-adaptive. In the solar forecasting, we also observe dominant base sequences such as DCN 9 and DCN 10. Similarly, we have error terms for small adjustments such as DCN 4. Solar generation highly depends on the hour we are predicting. For example, we observe that the importance of DCN 9 and DCN 10 is higher between 12:00-14:00 than that between 16:00-18:00, which leads to higher predictions in the first two hours. On the other hand, the importance of DCN 9 and DCN 10 almost decreases to 0 for the selected site in the second two hours. Instead, the contributions of DCN 1, 3, and 4 are raised. According to Fig. 2.8, those three sequences are much lower. The value of DCN 4 is negative, which is actually decreasing the predictions. Since the attention scores are computed by both the base sequences and the input features, the attention mechanism should capture the change of predicting hours. Moreover, we discover that the order of the darkness of each DCN is similar for all the sites in Figs. 2.5 and 2.7. It highlights that there some potential spatial correlations between each geographically distributed time series. With the use of attention mechanisms and taking the convex combination of base sequences, we can understand what is happening in the layers that are close to the output layer. Therefore, the interpretability of the model is improved.

Results on Point Forecasting

The mean absolute error (MAE) and the root mean square error (RMSE) are selected as evaluation metrics. We do not use the mean absolute percentage error because some observa-

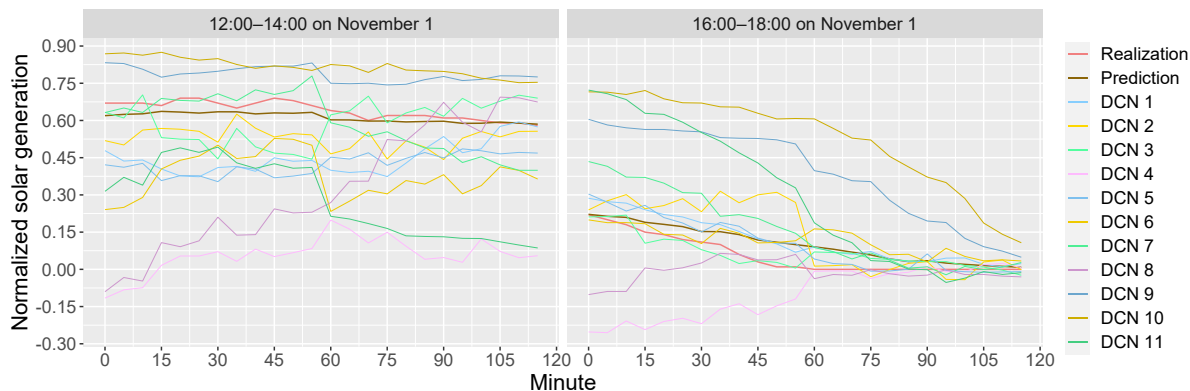


Figure 2.8: The 2-hour ahead point predictions and corresponding base sequences at solar site 18 during two time windows.

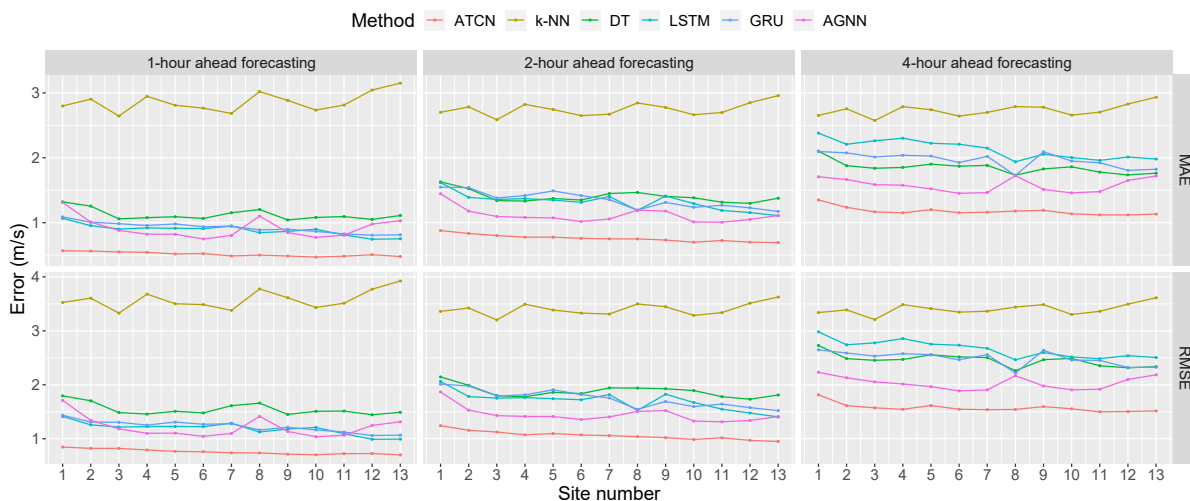


Figure 2.9: The forecast error of wind speed, in terms of the MAE and the RMSE.

tions are zero and the metric becomes inadequate. The forecast errors of wind speed and solar generation for each site are shown in Figs. 2.9 and 2.10, respectively. The predictions produced by the ATCN outperforms those predicted by baselines for all the sites, in terms of both the MAE and the RMSE. The magnitudes of wind speeds at each site are close, and hence, the errors are close. However, the capacities of solar plants are different, which leads to the differences in errors. For example, the maximum observation of site 5 is 8.7 MW and that of site 6 is 26.4 MW. Moreover, the errors are increasing with respect to the increase of forecasting horizon. This is a common issue for the multi-step forecasting. The historical observations cannot provide much information for the predictions of later steps. k -NN is taking the average of the values of k nearest neighbors, which is different with other baselines. It could be the reason of its poor performance.

From the perspective of system operators, they may be more interested in the accuracy of

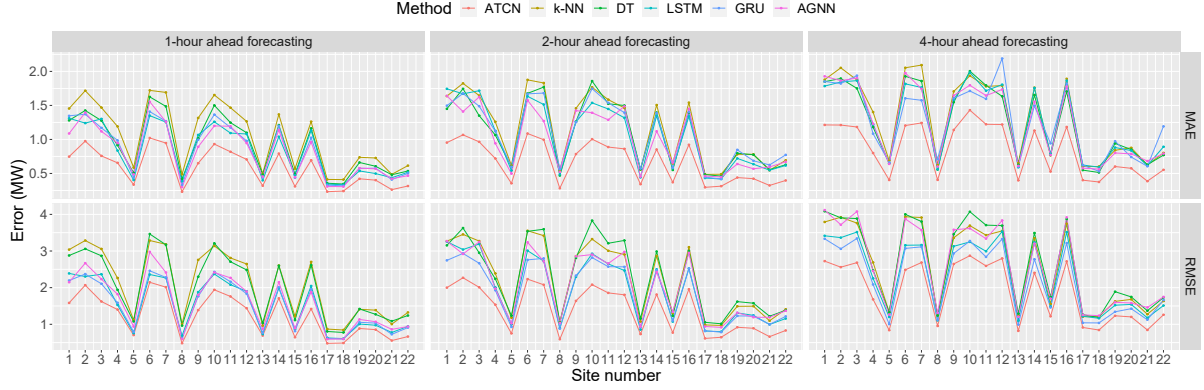


Figure 2.10: The forecast error of solar generation, in terms of the MAE and the RMSE.

predicting aggregated resources, i.e., the summation of individual sites. We report the accuracy of the point predictions in m/s and MW for the aggregated resources in Table 2.1. The errors are in m/s and MW, respectively. The performance of the ATCN is the best, and the ATCN is also effective in predicting the aggregated resources. Moreover, we observe that forecast errors of individual sites are offset. The summations of forecast errors are listed in Table 2.2. The errors of aggregated predictions are smaller than the summation of the individual errors. For example, the summation of the MAE and RMSE of the ATCN are 12.76 MW and 29.73 MW in the 1-hour ahead solar forecasting. However, those of aggregated predictions are 7.73 MW and 16.71 MW, respectively. Such offsets are more effective when the forecasting horizon is shorter. The observation aligns with the rationale of hierarchical forecasting. The comparison in Table 2.2 also shows the effectiveness of the ATCN.

Results on Probabilistic Forecasting

There are 17,568 test samples in the test set in total, and the performance of probabilistic forecasts will be evaluated over all the test samples. Two measures are used to evaluate the 2-hour ahead probabilistic predictions generated by different methods: the Pinball and Winkler scores [111]. The Pinball score provides a comprehensive evaluation for calibration, sharpness, and reliability. For site n and step t , the prediction of the τ -th quantile is $\hat{y}_{n,t}^\tau$, and the Pinball score is calculated by

$$\text{Pinball}(\hat{y}_{n,t}^\tau, y_{n,t}, \tau) = \tau \max(y_{n,t} - \hat{y}_{n,t}^\tau, 0) + (1 - \tau) \max(\hat{y}_{n,t}^\tau - y_{n,t}, 0). \quad (2.17)$$

We consider $\tau \in \{0.1, 0.2, \dots, 0.8, 0.9\}$ over the 17,568 time steps, and we evaluate the average of all the sites. The new measure we used is given by

$$\frac{1}{9 \cdot 17568 \cdot N} \sum_{\forall \tau} \sum_{t=1}^{17568} \sum_{n=1}^N \text{Pinball}(\hat{y}_{n,t}^\tau, y_{n,t}, \tau). \quad (2.18)$$

Table 2.1: Comparison of Aggregated Point Predictions for the Renewable Forecasting.

Task	Criterion	Horizon	ATCN	k -NN	DT	LSTM	GRU	AGNN
Wind (m/s)	MAE	1-hour	3.88	34.83	7.86	7.36	7.84	5.00
		2-hour	6.38	33.45	11.56	13.15	14.22	9.08
		4-hour	11.72	33.13	18.55	24.70	22.76	17.15
	RMSE	1-hour	5.75	43.45	11.02	9.84	10.50	6.75
		2-hour	9.16	41.19	15.90	16.89	18.02	12.09
		4-hour	15.84	41.25	24.98	30.74	28.82	21.66
Solar (MW)	MAE	1-hour	7.73	17.33	10.18	11.81	12.28	10.01
		2-hour	9.35	20.57	14.15	16.81	17.43	13.56
		4-hour	14.08	25.39	18.50	23.18	21.25	22.04
	RMSE	1-hour	16.71	32.53	21.50	21.61	21.43	20.97
		2-hour	19.94	38.11	29.96	31.00	29.63	31.79
		4-hour	31.22	47.01	38.36	41.80	36.87	49.38

The best scores are highlighted in bold.

Table 2.2: Comparison of Summation of Forecast Errors for the Renewable Forecasting.

Task	Criterion	Horizon	ATCN	k -NN	DT	LSTM	GRU	AGNN
Wind (m/s)	MAE	1-hour	6.67	37.20	14.60	11.53	12.00	11.94
		2-hour	9.88	35.75	18.24	17.15	17.56	14.50
		4-hour	15.29	35.54	24.02	27.68	25.52	20.51
	RMSE	1-hour	9.87	46.58	20.15	15.51	16.00	15.97
		2-hour	13.84	44.23	24.47	22.20	22.74	18.92
		4-hour	20.48	44.26	31.97	34.68	32.38	26.48
Solar (MW)	MAE	1-hour	12.76	23.10	20.13	18.29	18.64	18.02
		2-hour	14.64	25.52	23.86	23.06	23.97	22.14
		4-hour	18.80	29.29	27.65	28.02	27.87	27.62
	RMSE	1-hour	29.73	50.23	48.37	36.76	36.36	38.74
		2-hour	33.59	54.05	55.50	47.05	44.98	49.54
		4-hour	44.72	62.30	64.52	55.95	52.86	62.86

The scores of all the methods are shown in Fig. 2.11. Predictions made by the ATCN show superiority for both tasks.

Quantile predictions can be used to form interval predictions, and the Winkler score is a comprehensive metric that simultaneously measures the unconditional coverage and sharpness. The scoring rule is intuitive: narrow prediction intervals are preferred, and it incurs a penalty

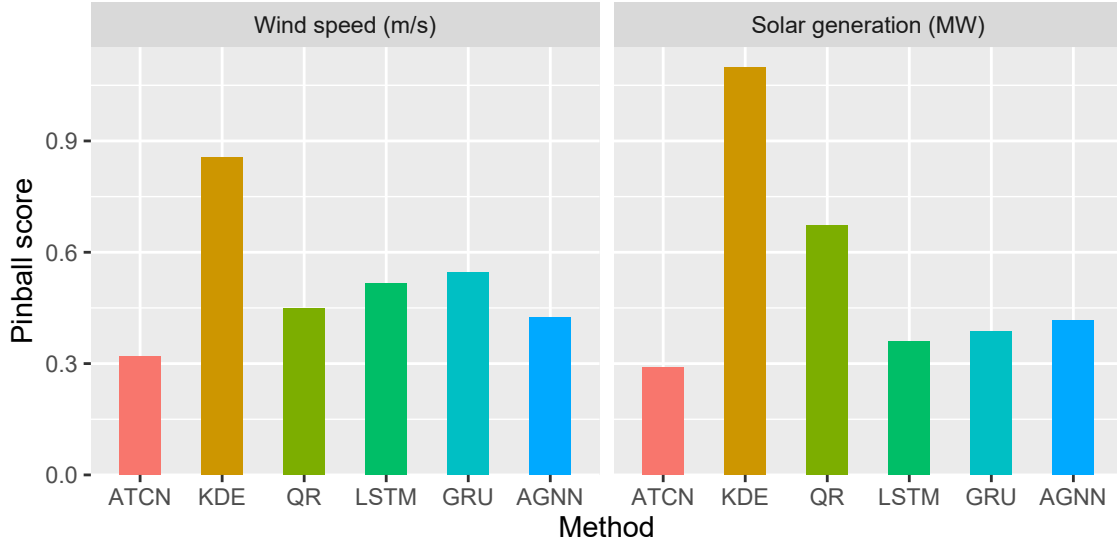


Figure 2.11: The Pinball scores of wind speed and solar generation forecasting.

Table 2.3: Comparison of Winkler Scores for the Renewable Forecasting.

Task	α	ATCN	KDE	QR	LSTM	GRU	AGNN
Wind (m/s)	0.1	3.97	10.06	5.48	6.06	5.75	5.03
	0.2	2.94	7.82	4.13	4.50	4.40	3.76
	0.3	2.35	6.41	3.33	3.67	3.65	3.19
Solar (WM)	0.1	3.61	14.27	9.38	3.87	3.91	5.69
	0.2	2.68	10.18	6.36	3.52	3.70	3.87
	0.3	1.77	6.42	3.90	2.04	2.40	2.49

if the observations are outside the intervals. We consider the classical case of the central $(1-2\alpha) \times 100\%$ prediction interval, with lower and upper endpoints that are the predictive quantiles at α and $1-\alpha$. Let the central interval be $\mathcal{C}_{n,t}^\alpha = [l^\alpha, u^\alpha]$. The score is computed by

$$\text{Winkler}(\mathcal{C}_{n,t}^\alpha, y_{n,t}) = (u^\alpha - l^\alpha) + \frac{1}{\alpha} \min_{c \in \mathcal{C}_{n,t}^\alpha} (|y_{n,t} - c|), \quad (2.19)$$

Scores for $\alpha \in \{10\%, 20\%, 30\%\}$ are tested. The scores are averaged, and the new metric is given by

$$\frac{1}{17568N} \sum_{t=1}^{17568} \sum_{n=1}^N \text{Winkler}(\mathcal{C}_{n,t}^\alpha, y_{n,t}). \quad (2.20)$$

The Winkler scores in m/s and MW are listed in Table 2.3. The scores of the ATCN outperform those of baselines, indicating that the intervals obtained by the ATCN are narrow

while with a reasonable coverage. Sequence modeling techniques perform better than the QR in the solar forecasting, since the solar data used show more complex temporal patterns.

2.2 Graph Transformer Network

As mentioned earlier, net loads in different zones are geographically distributed time series, and hence, information from neighboring zones may improve the forecast accuracy. It is worth investigating the potential of using neighboring information on improving the accuracy of net-load forecasting. A new model, named graph transformer network (GTrans), is developed for probabilistic day-ahead net-load forecasting with BTM Solar penetration. That being said, unlike the assumption in the previous model, it is not necessary for net loads in different areas to be spatially correlated. In this model, we want to extract useful off-site information and perform forecasting for each area independently. Attention mechanism based models have shown state-of-the-art performance in many fields such as natural language processing [112] and computer vision [113]. The GTrans is built on three state-of-the-art architectures: a graph attention network (GAT), variational autoencoders (VAEs), and transformers. GAT and transformers are two attention based models that are developed for graph and sequence modeling, respectively.

Information from neighboring zones may improve the forecast accuracy. Without feature selection, the improvement may be trivial, or the spatial information may even deteriorate the accuracy. In the existing literature, the selection is based on expert knowledge or spectral-based graph neural networks such as GCN. In this work, we adopt GAT from [114] to exploit useful spatial information. The GAT is a space domain based model. Compared with spectral domain based models, it does not require weights on each edge. For the forecasting problems in power systems, each site can be regarded as a node in a graph, while the edge is not well defined. In the existing works, the edges and their associated weights are defined based on expert knowledge. The GAT allows us to consider a fully connected graph and useful information from neighboring zones is extracted by attention scores. We first input the features of all the zones to the GAT, and the GAT is expected to output useful information for each zone. With outputs of the GAT, we build a transformer for each zone to make day-ahead predictions. Multi-headed attention schemes in transformers enable each time step to attend over all the time steps in the input sequence [105]. Traditionally, temporal correlations are mainly captured by variants of recurrent neural networks, e.g., LSTM, which only allows the current step to attend hidden states passed by the previous step. Moreover, LSTM mitigates the gradient vanishing problem but not the exploding one.

To make the prediction probabilistic, we adopt the spirits in the VAE [115]. We assume that the distribution of net load is conditioned on a latent space, which follows a random distribution. The mapping from a sample in the latent space to the net-load prediction is deterministic, and we obtain different predictions given different samples from the latent distribution. In the inference phase, a sample from latent distribution will be concatenated with features of all the

zones, and the concatenation will be inputted to the GAT and transformers. When the number of samples is large, we construct a discrete approximation for the distribution of net load, and hence, quantiles, intervals or scenarios can be obtained.

2.2.1 Problem Statement and Training Methodology

Consider a set of weather zones $\mathcal{I} = \{1, \dots, I\}$, where I is the number of weather zones, and a set of forecast zones $\mathcal{J} = \{1, \dots, J\} \subseteq \mathcal{I}$, where J is the number of forecast zones. We call nodes in a graph as zones. It is worth mentioning that a zone can also be a residential house, an aggregated node, a feeder, or a substation. Let T be the forecasting time horizon, which is 24 for the day-ahead forecasting in consideration, and denote $\mathcal{T} = \{1, \dots, T\}$. Each weather zone $i \in \mathcal{I}$ is associated with a set of unique features $\mathbf{x}_i^u \in \mathbb{R}^{T \times F^u}$, where F^u is the number of unique features in each time step, such as temperature and humidity. Let $\mathbf{x}^u = \{\mathbf{x}_i^u, \forall i \in \mathcal{I}\}$. Moreover, all the weather zones should have some shared features such as date and hour. We denote the shared features by $\mathbf{x}^s \in \mathbb{R}^{T \times F^s}$, where F^s is the number of shared features in each time step. For each forecast zone $j \in \mathcal{J}$, we want to forecast the net load in the next day, which is denoted by $\hat{\mathbf{y}}_j \in \mathbb{R}^T$. Let $\hat{\mathbf{y}} = \{\hat{\mathbf{y}}_j, \forall j \in \mathcal{J}\}$, and let $\mathbf{y} \in \mathbb{R}^{J \times T}$ be the measurements. In this work, we assume that we only have measurements of the net load. For the point forecasting, we want to find the mapping from \mathbf{x}^u and \mathbf{x}^s to $\hat{\mathbf{y}}$, which makes $\hat{\mathbf{y}}$ close to \mathbf{y} . Regarding the probabilistic forecasting, we aim at creating a model $P(\hat{\mathbf{y}}|\mathbf{x}^u, \mathbf{x}^s)$, which maximizes the probability of the ground truth.

In this work, we apply two training tricks: residual connections [116] and layer normalization [117]. Residual connections are to connect the output of previous layers to the output of a new layers. Let vectors \mathbf{r} and \mathbf{R} be the input and output of a hidden layer, respectively. In the standard deep learning models, the input to the next hidden layer is \mathbf{R} . However, if residual connections are applied, the input to the next hidden layer is $\mathbf{r} + \mathbf{R}$. Residual connections address degradation problems in deep neural networks. Layer normalization standardizes the inputs to a layer across the features. It allows us to use much higher learning rates and be less careful about initialization, and in some cases eliminates the need for dropout. Let ζ_r and σ_r be the mean and standard deviation of \mathbf{r} , the layer normalization is given by

$$\text{Norm}(\mathbf{r}) = (\mathbf{r} - \zeta_r) / (\sigma_r + 10^{-5}), \quad (2.21)$$

where the math operation is performed element-wisely. We use $\cdot\|\cdot$ to represent the concatenation operation throughout this section.

2.2.2 Model Specifications

Graph Attention Network

The input to the GAT is \mathbf{x}^u . It will produce a new set of features $\mathbf{G} \in \mathbb{R}^{J \times T \times F^g}$, which is the input to transformers. To transform \mathbf{x}^u into higher-level dimensions to obtain sufficient

expressive power, we apply a shared linear transformation, parametrized by a weight matrix, $\mathbf{W} \in \mathbb{R}^{F^u \times F^h}$. Post the transformation for every zone, we obtain a set of embeddings $\mathbf{h} = \{\mathbf{h}_i, \forall i \in \mathcal{I}\}$ as follows

$$\mathbf{h}_i = \mathbf{x}_i^u \cdot \mathbf{W}, \forall i \in \mathcal{I}, \quad (2.22)$$

where $\mathbf{h}_i \in \mathbb{R}^{T \times F^h}$. Let \mathbf{h}_i^t be t -th row of \mathbf{h}_i , and the rest transformations are applied to every time step. Regarding the forecasting task in consideration, the edges are not well defined. Therefore, we allow every zone to attend all the zones, drop the structural information (i.e., consider a complete graph), and use attention score $a_{i,i'}^t$ to indicate the importance of information in zone $i' \in \mathcal{I}$ to zone i in time step t .

For a zone $i \in \mathcal{I}$, the attention mechanism is designed to be a single-layer feed forward neural network, which is parametrized by a unique weight vector $\mathbf{w}_i \in \mathbb{R}^{2F^h}$. The attention score $a_{i,i'}^t, \forall t \in \mathcal{T}$ produced by the attention mechanism is given by

$$a_{i,i'}^t = \frac{\exp(\text{LeakyReLU}([\mathbf{h}_i^t \parallel \mathbf{h}_{i'}^t] \cdot \mathbf{w}_i))}{\sum_{\bar{i} \in \mathcal{I}} \exp(\text{LeakyReLU}([\mathbf{h}_i^t \parallel \mathbf{h}_{\bar{i}}^t] \cdot \mathbf{w}_i))} \quad (2.23)$$

where LeakyReLU function adds nonlinearity, and the coefficient of the LeakyReLU function is set to 0.2. We have obtained the normalized attention scores for each zone, and they are used to gather useful information from other zones. Specifically, a linear combination of all the features for all the zones serves as the output for each zone, which is given by

$$\mathbf{H}_i^t = \text{ReLU} \left(\sum_{i' \in \mathcal{I}} a_{i,i'}^t \cdot \mathbf{h}_{i'}^t \right), \forall t \in \mathcal{T}, \quad (2.24)$$

where ReLU function applies nonlinearity, and multiplication is operated element-wisely. Feature representation given by (2.24) is generated by one attention mechanism. To explore more combinations of features, we extend it to a multi-headed attention mechanism, i.e., employ many attention mechanisms. Let the number of attention mechanisms applied in the GAT be K . Each single head should execute the transformation defined by (2.24), and K different feature representations are concatenated, which leads to the following new feature representations:

$$\mathbf{H}_i^t = \left\| \right\|_k^K \text{ReLU} \left(\sum_{i' \in \mathcal{I}} a_{i,i'}^{t(k)} \cdot \mathbf{h}_{i'}^{t(k)} \right), \forall t \in \mathcal{T}, \quad (2.25)$$

where $a_{i,i'}^{t(k)}$ and $\mathbf{h}_{i'}^{t(k)}$ are attention scores and embeddings in the k -th attention mechanism, respectively. The dimension of \mathbf{H}_i^t produced by K -headed attention mechanisms is $K \cdot F^h$.

Let $\mathbf{H}_i = \{\mathbf{H}_i^t, \forall t \in \mathcal{T}\}$ and $\mathbf{H} = \{\mathbf{H}_i, \forall i \in \mathcal{I}\}$. We define another 1-headed attention mechanism to indicate importance of new information for each zone. That is, we define a new weight matrix with dimension $K \cdot F^h \times F^g$ and a new set of weight vectors to redo (2.22), (2.23), and (2.24). The input to the 1-headed attention mechanism is \mathbf{H} . Let the new feature representa-

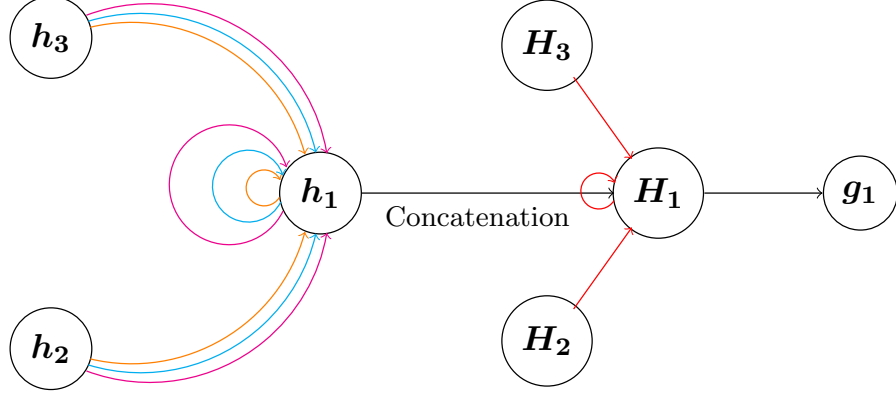


Figure 2.12: An illustration of the multi-headed attention in the graph attention network.

tions produced by the 1-headed attention mechanism be $\mathbf{g} \in \mathbb{R}^{I \times T \times F^g}$. Fig. 2.12 illustrates how zone 1 explores useful information from itself and other zones. This is a 3-zone example with a 3-headed attention mechanism. Different colors denote independent attention mechanisms. The input features are first processed by a 3-headed attention mechanism, and then the concatenation is passed to a new 1-headed attention to obtain final feature representations. The output of the GAT is considered as the input to transformers, denoted by $\mathbf{G} = \{\text{Norm}(\mathbf{g}_j), \forall j \in \mathcal{J}\}$. We consider the GAT as a mapping $\mathbf{G} = \mathbb{G}(\mathbf{x}^u)$, where $\mathbb{G} : \mathbb{R}^{I \times T \times F^u} \rightarrow \mathbb{R}^{J \times T \times F^g}$.

Transformer

For each forecast zone $j \in \mathcal{J}$, we need an independent transformer. For zone j , the input to its associated transformer is \mathbf{G}_j . Moreover, there is a set of shared features \mathbf{x}^s for all the transformers. Most shared features are categorical ones, e.g., hour and month. Therefore, we first perform embedding for \mathbf{x}^s . Moreover, we take a concatenation of \mathbf{G}_j and embeddings, resulting a new matrix of features $\mathbf{e}_j \in \mathbb{R}^{T \times F^e}$. Note that F^e is determined by F^g and the size of the embedding layers used. For notation convenience, we omit subscript j since the structures of J transformers are identical.

Unlike recurrent neural networks, the transformer includes no recurrence. However, we are making time series forecasting and want to make use of the order of the time steps. To do so, we apply positional encoding for \mathbf{e} , which injects some information about the relative or absolute position of the time step in the time series. Consider a matrix of time signals $\mathbf{PE} \in \mathbb{R}^{T \times F^e}$, which is specified by

$$PE_{t,f^e} = \begin{cases} \sin(t/(20F^e)^{(f^e/F^e)}), \forall t \in \mathcal{T}, \forall f^e \in \{1, \dots, F^e\}, \text{ if } f^e \text{ is even,} \\ \cos(t/(20F^e)^{(f^e/F^e)}), \forall t \in \mathcal{T}, \forall f^e \in \{1, \dots, F^e\}, \text{ if } f^e \text{ is odd,} \end{cases} \quad (2.26)$$

where each feature corresponds to a sinusoid. Combining the input and the positional encoding,

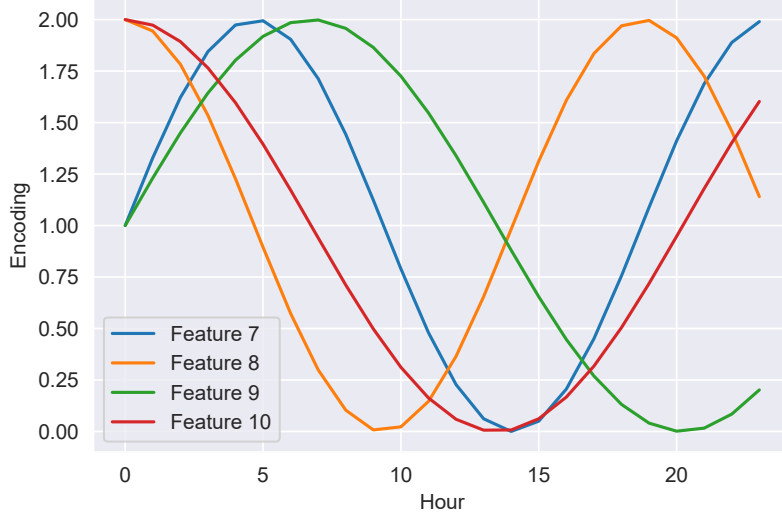


Figure 2.13: An illustration of positional encoding.

we obtain a new set of representations \mathbf{E} , which is given by

$$\mathbf{E} = \mathbf{e} + \mathbf{PE}. \quad (2.27)$$

An illustration of positional encoding is given in Fig. 2.13. The input is a matrix of ones, and 4 dimensions of the resulting representations are shown in the figure. Positional encoding adds time signals to the input. In our work, since we process all the time steps at the same time by attention mechanisms, it is necessary to add information about the order of time steps.

Current representation \mathbf{E} includes the information of positions. We use attention mechanisms to indicate the importance between time steps. Unlike the GAT, in which attention scores are calculated by a single-layer feed forward neural network, we adopt scaled dot-product attention from [105] to process the time series. Similarly, we apply a multi-headed attention scheme to allow the model to jointly attend information produced by different heads. Let the number of heads be K' , and we define three linear transformations for each head k' , parametrized by matrices $\mathbf{W}_q^{(k')} \in \mathbb{R}^{F^e \times F^d}$, $\mathbf{W}_Y^{(k')} \in \mathbb{R}^{F^e \times F^d}$, and $\mathbf{W}_V^{(k')} \in \mathbb{R}^{F^e \times F^d}$, respectively. Post the transformations, the representations are given by

$$\mathbf{q}^{(k')} = \mathbf{E} \cdot \mathbf{W}_q^{(k')}, \forall k' \in \{1, \dots, K'\}, \quad (2.28)$$

$$\mathbf{Y}^{(k')} = \mathbf{E} \cdot \mathbf{W}_Y^{(k')}, \forall k' \in \{1, \dots, K'\}, \quad (2.29)$$

$$\mathbf{V}^{(k')} = \mathbf{E} \cdot \mathbf{W}_V^{(k')}, \forall k' \in \{1, \dots, K'\}, \quad (2.30)$$

where $\mathbf{q}^{(k')}$, $\mathbf{Y}^{(k')}$, and $\mathbf{V}^{(k')} \in \mathbb{R}^{T \times F^d}$. The attention matrix $\mathbf{A}^{(k')} \in \mathbb{R}^{T \times T}$ for head k' is given

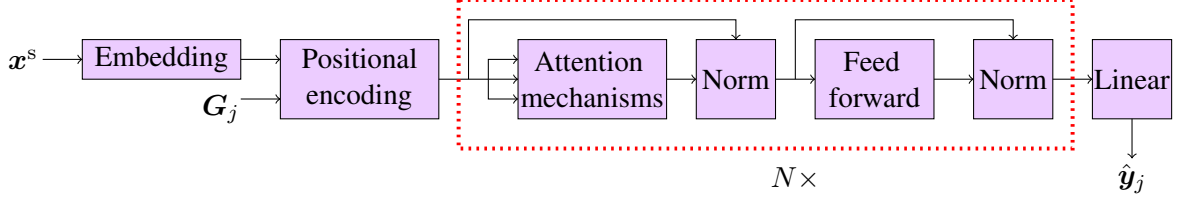


Figure 2.14: Architecture of the transformer.

by

$$\mathbf{A}^{(k')} = \text{softmax} \left(\frac{\mathbf{q}^{(k')} \cdot \mathbf{Y}^{(k')\top}}{\sqrt{F^d}} \right), \forall k'. \quad (2.31)$$

The representations extracted by head k' are then computed by $\mathbf{A}^{(k')} \cdot \mathbf{V}^{(k')}$. The representations produced by all the heads are concatenated and further processed by a single-layer feed forward neural network, which is parametrized by $\mathbf{W}_O \in \mathbb{R}^{K'F^d \times F^e}$. The calculation is given by

$$\mathbf{m}' = \left(\parallel_{k'}^{K'} \mathbf{A}^{(k')} \cdot \mathbf{V}^{(k')} \right) \cdot \mathbf{W}_O, \quad (2.32)$$

where $\mathbf{m}' \in \mathbb{R}^{T \times F^e}$. Before we pass the representations generated by the multi-headed attention mechanism to the next layer, we perform layer normalization and residual connections. The representation \mathbf{m} passed to the next layer is given by

$$\mathbf{m} = \text{Norm}(\mathbf{m}') + \mathbf{E}. \quad (2.33)$$

After the multi-headed attention layer, the representations are inputted to a fully connected feed forward network, which consists of two linear transformations. The linear transformations are parametrized by two weight matrices $\mathbf{W}_1 \in \mathbb{R}^{F^e \times 4F^e}$ and $\mathbf{W}_2 \in \mathbb{R}^{4F^e \times F^e}$, respectively. The output of the feed forward network is given by

$$\mathbf{M} = \text{Norm}(\text{ReLU}(\mathbf{m} \cdot \mathbf{W}_1) \cdot \mathbf{W}_2) + \mathbf{m}. \quad (2.34)$$

We consider a combination of a multi-headed attention layer and a fully connected feed forward layer as a sublayer, and we use N stacked sublayers before making the predictions. For example, the output of the fully connected feed forward layer in the first sublayer is the input to the multi-headed attention layer in the second sublayer. N is set to 6. Finally, we use another linear layer to map the output of the last sublayer to $\hat{\mathbf{y}}$. The complete scheme of transformers is shown in Fig. 2.14. The embeddings of shared features are concatenated with nodal features extracted by the GAT. Moreover, they are passed to N stacked sublayers. A linear combination of the output of the last sublayer is used to obtain predictions.

We consider each transformer as a mapping from \mathbf{G}_j and \mathbf{x}^s to $\hat{\mathbf{y}}_j$. Since GAT is a mapping characterized by $\mathbf{G} = \mathbb{G}(\mathbf{x}^u)$, the combination of GAT and transformers is regarded as a map-

ping $\hat{\mathbf{y}} = \mathbb{T}(\mathbf{x}^s, \mathbf{x}^u)$, where $\mathbb{T} : \mathbb{R}^{I \times T \times F^u + T \times F^s} \rightarrow \mathbb{R}^{J \times T}$. When point forecasts are desired, we can use loss functions that minimize the distance between $\hat{\mathbf{y}}$ and \mathbf{y} , e.g., mean absolute error.

Variational Autoencoders

When it comes to the probabilistic forecasting, we want to learn a mapping of distribution $P(\hat{\mathbf{y}}|\mathbf{x}^u, \mathbf{x}^s)$, which is close to the true distribution, i.e., to train a generative model. The mapping \mathbb{T} is deterministic, and we augment the model with conditional VAEs [118] to make the mapping generative. Say, we have a vector of latent variables $\mathbf{z} \in \mathbb{R}^Z$, which we can easily sample out according to the probability density function $P(\mathbf{z}|\mathbf{x}^u, \mathbf{x}^s)$. For notation convenience, we let $\mathbf{x} = (\mathbf{x}^u, \mathbf{x}^s)$. We consider a deterministic mapping $f_\theta(\mathbf{z}; \mathbf{x})$ parameterized by a set of parameters θ . After the training, θ is fixed and \mathbf{z} is random, then $f_\theta(\mathbf{z}; \mathbf{x})$ is expected to produce random variables in the space of $\hat{\mathbf{y}}$. We wish to optimize θ , and $f_\theta(\mathbf{z}; \mathbf{x})$ will be like \mathbf{y} , with samples from $P(\mathbf{z}|\mathbf{x})$. We want to maximize the probability of every generated sample $\hat{\mathbf{y}}$ by

$$P(\hat{\mathbf{y}}|\mathbf{x}) = \int P(\hat{\mathbf{y}}|\mathbf{z}; \mathbf{x})P(\mathbf{z}|\mathbf{x})d\mathbf{z}, \quad (2.35)$$

where f_θ is replaced by a distribution $P(\hat{\mathbf{y}}|\mathbf{z}; \mathbf{x})$. To compute (2.35), we introduce a new function $Q(\mathbf{z}|\hat{\mathbf{y}}; \mathbf{x})$, which takes a value of $\hat{\mathbf{y}}$ and gives us a distribution over values of \mathbf{z} 's that are likely to produce $\hat{\mathbf{y}}$. The Kullback-Leibler (KL) divergence between $Q(\mathbf{z}|\hat{\mathbf{y}}; \mathbf{x})$ and $P(\mathbf{z}|\hat{\mathbf{y}}; \mathbf{x})$ is given by

$$\mathcal{D}[Q(\mathbf{z}|\hat{\mathbf{y}}; \mathbf{x}), P(\mathbf{z}|\hat{\mathbf{y}}; \mathbf{x})] = \mathbb{E}_{\mathbf{z} \sim Q}[\log Q(\mathbf{z}|\hat{\mathbf{y}}; \mathbf{x}) - \log P(\mathbf{z}|\hat{\mathbf{y}}; \mathbf{x})]. \quad (2.36)$$

By applying Bayes rule to $P(\mathbf{z}|\hat{\mathbf{y}}; \mathbf{x})$, we obtain

$$\mathcal{D}[Q(\mathbf{z}|\hat{\mathbf{y}}; \mathbf{x}), P(\mathbf{z}|\hat{\mathbf{y}}; \mathbf{x})] = \mathbb{E}_{\mathbf{z} \sim Q}[\log Q(\mathbf{z}|\hat{\mathbf{y}}; \mathbf{x}) - \log P(\hat{\mathbf{y}}|\mathbf{z}; \mathbf{x}) - \log P(\mathbf{z}|\mathbf{x})] + \log P(\hat{\mathbf{y}}|\mathbf{x}), \quad (2.37)$$

which leads to

$$\log P(\hat{\mathbf{y}}|\mathbf{x}) - \mathcal{D}[Q(\mathbf{z}|\hat{\mathbf{y}}; \mathbf{x}), P(\mathbf{z}|\hat{\mathbf{y}}; \mathbf{x})] = \mathbb{E}_{\mathbf{z} \sim Q}[\log P(\hat{\mathbf{y}}|\mathbf{z}; \mathbf{x})] - \mathcal{D}[Q(\mathbf{z}|\hat{\mathbf{y}}; \mathbf{x}), P(\mathbf{z}|\mathbf{x})]. \quad (2.38)$$

The left hand side includes the term we want to maximize and an error term. We can maximize $\log P(\hat{\mathbf{y}}|\mathbf{x})$ while simultaneously minimizing $\mathcal{D}[Q(\mathbf{z}|\hat{\mathbf{y}}; \mathbf{x}), P(\mathbf{z}|\hat{\mathbf{y}}; \mathbf{x})]$. If the function $Q(\mathbf{z}|\hat{\mathbf{y}}; \mathbf{x})$ has high-capacity and can match $P(\mathbf{z}|\hat{\mathbf{y}}; \mathbf{x})$, then the KL divergence is zero. We are optimizing $\log P(\hat{\mathbf{y}}|\mathbf{x})$. Therefore, we minimize the following term directly:

$$\mathbb{E}_{\mathbf{z} \sim Q}[-\log P(\hat{\mathbf{y}}|\mathbf{z}; \mathbf{x})] + \mathcal{D}[Q(\mathbf{z}|\hat{\mathbf{y}}; \mathbf{x}), P(\mathbf{z}|\mathbf{x})]. \quad (2.39)$$

The first and second terms in (2.39) are named reconstruction error and KL divergence distance, respectively.

To make the computation tractable, we impose some specifications on $Q(\mathbf{z}|\hat{\mathbf{y}}; \mathbf{x})$ and $P(\mathbf{z}|\mathbf{x})$. We assume $Q(\mathbf{z}|\hat{\mathbf{y}}; \mathbf{x}) = \mathcal{N}(\mathbf{z}|\mu(\hat{\mathbf{y}}, \mathbf{x}), \Sigma(\hat{\mathbf{y}}, \mathbf{x}))$ where μ and Σ are two deterministic functions

that can be learned from data, and $P(\mathbf{z}|\mathbf{x}) = \mathcal{N}(0, \mathbb{I})$, where \mathbb{I} is an identity matrix with dimension $|\mathbb{I}|$. μ and Σ are replaced by two deep neural networks. Now, the KL divergence distance can be computed in closed form by

$$\mathcal{D}[\mathcal{N}(\mathbf{z}|\mu(\hat{\mathbf{y}}, \mathbf{x}), \Sigma(\hat{\mathbf{y}}, \mathbf{x})), \mathcal{N}(0, \mathbb{I})] = \frac{1}{2} \left(\text{tr}(\Sigma(\hat{\mathbf{y}}, \mathbf{x})) + \mu(\hat{\mathbf{y}}, \mathbf{x})^\top \mu(\hat{\mathbf{y}}, \mathbf{x}) - |\mathbb{I}| - \log \det(\Sigma(\hat{\mathbf{y}}, \mathbf{x})) \right). \quad (2.40)$$

Regarding the reconstruction loss, it also depends on the parameters of Q , which cannot be handled during backpropagation [118]. we adopt the reparameterization trick in [115], which moves the sampling to an input layer. Given $\mu(\hat{\mathbf{y}}, \mathbf{x})$ and $\Sigma(\hat{\mathbf{y}}, \mathbf{x})$, we can sample $\mathcal{N}(\mu(\hat{\mathbf{y}}, \mathbf{x}), \Sigma(\hat{\mathbf{y}}, \mathbf{x}))$ by sampling $\epsilon \sim \mathcal{N}(0, \mathbb{I})$, and then computing $\mathbf{z} = \mu(\hat{\mathbf{y}}, \mathbf{x}) + \Sigma^{1/2}(\hat{\mathbf{y}}, \mathbf{x}) \cdot \epsilon$. Moreover, we consider an unbiased estimator for the reconstruction loss using S samples as the following:

$$\mathbb{E}_{\mathbf{z} \sim Q} [-\log P(\hat{\mathbf{y}}|\mathbf{z}; \mathbf{x})] = \frac{1}{S} \sum_{s=1}^S (-\log P(\hat{\mathbf{y}}|\mathbf{z}^{(s)} = \mu(\hat{\mathbf{y}}, \mathbf{x}) + \Sigma^{1/2}(\hat{\mathbf{y}}, \mathbf{x}) \cdot \epsilon^{(s)}; \mathbf{x})), \quad (2.41)$$

where $\epsilon^{(s)}$ is s -th sample from $\mathcal{N}(0, \mathbb{I})$.

Probabilistic Forecasting

For each weather zone $i \in \mathcal{I}$, we assign it two neural networks to obtain $\mu_i(\mathbf{y}_i, \mathbf{x}_i)$ and $\Sigma_i(\mathbf{y}_i, \mathbf{x}_i)$. Note that predictions are replaced by true values during training, and if historical observations \mathbf{y}_i are not available for some $i \in \mathcal{I} \setminus \mathcal{J}$, we only consider $\mu_i(\mathbf{x}_i)$ and $\Sigma_i(\mathbf{x}_i)$. Following the reparameterization trick, we obtain a vector of latent variables \mathbf{z}_i for each zone. Let $\mathbf{z} = \{\mathbf{z}_i, \forall i \in \mathcal{I}\} \in \mathbb{R}^{I \times T \times Z}$. We concatenate \mathbf{z} with \mathbf{x}^u , and use the concatenation as the input of GAT. Recall that GAT and transformers can be regarded as a mapping $\hat{\mathbf{y}} = \mathbb{T}(\mathbf{x}^s, \mathbf{x}^u)$. Now, we have a new mapping $\hat{\mathbf{y}} = \mathbb{G}\mathbb{T}(\mathbf{x}^s, \mathbf{x}^u, \mathbf{z})$. During the inference phase, we want to generate new samples, we simply input values of \mathbf{z} from I Gaussian distributions into $\mathbb{G}\mathbb{T}$. The complete GTrans model is shown in Fig. 2.15. In the training, features and true measurements are used to obtain latent variables in VAEs. Using latent variables and unique features, the GAT outputs representations with neighboring information extracted, which is further inputted to J transformers to make predictions. During the testing, latent variables are sampled from Gaussian distributions.

We can calculate KL divergence distance using (2.40). However, we also need to calculate the reconstruction loss. In a standard VAE structure, $P(\hat{\mathbf{y}}|\mathbf{z}; \mathbf{x})$ is assumed to be an isotropic Gaussian, and the negative log probability of it is proportional to the squared Euclidean distance between \mathbf{y} and $\hat{\mathbf{y}}$, i.e., loss function is mean squared error. For any given loss function, we can assume that it is proportional to the negative log probability of a distribution after dropping constants and an error term. It allows us to define our own loss function. Without loss of generality, we assume two predictions $\hat{\mathbf{y}}_j^{(s_1)}$ and $\hat{\mathbf{y}}_j^{(s_2)}$ generated by $\mathbb{G}\mathbb{T}$ follow $\hat{\mathbf{y}}_j^{(s_1)} \leq \hat{\mathbf{y}}_j^{(s_2)}$ and $1 \leq s_1 \leq s_2 \leq S$, which can be achieved by sorting the samples in the experiments. Let $\|\cdot\|_1$ be

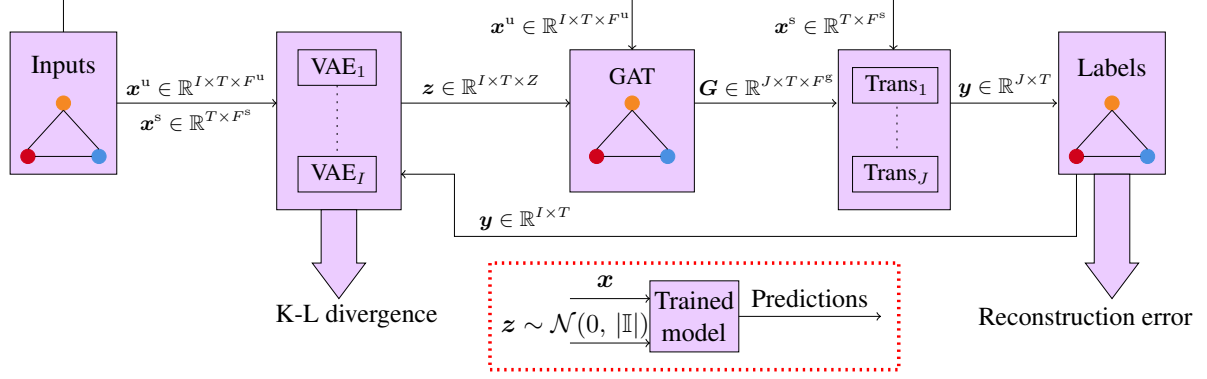


Figure 2.15: Architecture of the graph transformer network.

the ℓ_1 norm. The loss function representing the reconstruction loss is given by

$$\begin{aligned}
 \mathcal{L}_j = & \sum_{s=1}^S \left[\frac{s}{S} \text{ReLU}(\mathbf{y}_j - \hat{\mathbf{y}}_j^{(s)}) + (1 - \frac{s}{S}) \text{ReLU}(\hat{\mathbf{y}}_j^{(s)} - \mathbf{y}_j) \right] + \frac{\beta_j}{S} \sum_{s=1}^S \|\mathbf{y}_j - \hat{\mathbf{y}}_j^{(s)}\|_1 \\
 & - \frac{\beta_j}{2S^2} \sum_{s=1}^S \sum_{s'=1}^S \|\hat{\mathbf{y}}_j^{(s)} - \hat{\mathbf{y}}_j^{(s')}\|_1, \forall j \in \mathcal{J},
 \end{aligned} \tag{2.42}$$

where β_j is adjusted every epoch and depends on the magnitudes of the three terms. The first term reduces the quantile loss whereas the last two improve accuracy and diversity. Let the KL divergence distance for zone j be \mathcal{L}_j^D . We minimize $\mathcal{L}_j^D + \mathcal{L}_j$. The model can be built to forecast each zone independently or to forecast all the zones simultaneously. If the latter case is chosen, losses for all the zones should be summed up. The parameters are then updated by *Adam*.

2.2.3 Case Studies

In this section, the proposed GTrans model is evaluated on the Open Power System Data (OPSD) data set [119]. For the point forecasting, we compare GTrans with DT, support vector regression (SVR), LSTM, GRU, GCN, and AGNN. Regarding the probabilistic forecasting, baselines include quantile regression (QR), support vector machine based quantile regression (SVQR), LSTM, GRU, GCN, and AGNN. Except QR, which predicts values of quantiles, we predict the probability of intervals for the remaining baselines. We do not use DT as a baseline for the probabilistic forecasting because it always predicts an interval with probability 1.

Data Description

We use data from 3 zones from 2015 to 2019 for verification. Each zone is associated with hourly weather data. Besides the weather data, net loads in the previous day and week are also used as features. Although we have both net load and visible solar data in hourly resolution, we reconstruct the net load, i.e., current net load minus visible solar generation. The net load

in each zone is scaled to that of a typical distribution feeder, and we assume the net load of a feeder has identical heterogeneity. Data in the first 4 years and in the last year are used for training and testing, respectively.

Results on Point Forecasting

Three measures are used to evaluate the point predictions generated by different methods: the mean absolute percentage error (MAPE), the mean absolute error (MAE), and the temporal autocorrelation loss (Corr). For a 24-hour time series, we can calculate the autocorrelation for the t -hour lag, where $t \in \{0, \dots, 23\}$. Given the mapping $AR : \mathbb{R}^{24} \rightarrow \mathbb{R}^{24}$, the Corr is calculated by

$$\text{Corr} = \frac{1}{365} \sum_{d=1}^{365} \|AR(\mathbf{y}^d) - AR(\hat{\mathbf{y}}^d)\|_1, \quad (2.43)$$

where 365 is the number of days in the testing set, and \mathbf{y}^d and $\hat{\mathbf{y}}^d$ are observations and predictions on the d -th day. The comparison between different methods, in terms of 3 criteria, is listed in Table 2.4. GCN is trained on a complete graph where edges are with identical weights. The performance of GCN is worse than that of AGNN, which shows that spectral-based graph neural networks are not appropriate for forecasting tasks in power systems, without the design of edges and weights. The GTrans outperforms all the other baselines, in terms of three measures. Aggregated net load is the summation of all the 3 zones. The MAPE and the MAE of the aggregated net load are lower than the average of those of different zones, which follows the intuition behind hierarchical forecasting. We observe that a better performance on the MAPE and the MAE is not always associated with a better Corr, e.g., measures of DT and LSTM. However, predictions made by the GTrans give high accuracy while following the pattern of the time series.

Illustration of Attention Mechanisms

To illustrate how the attention mechanism works, we show two examples of attention scores in Fig. 2.16 and Fig. 2.17. Fig. 2.16 illustrates the attention scores of Zone 3 in the GAT, at three selected hours. There are 8 heads, and each cell indicates the importance of zone information to Zone 3. Intuitively, Zone 3 pays more attention to its own features for all the times. Recall that different heads represent different combinations of features. The focus will be changed at different hours. For example, Zone 3 extracts information in head 7 from Zone 2 at 18:00 while extracts nothing at 12:00. Fig. 2.17 describes the attention scores of Zone 3 in the transformer. There are 4 heads, and each cell indicates the importance of information at different time steps to the time step in consideration. Each head tends to focus on a specific time window. For example, head 4 addresses the features in the morning. Residual connections make the self-information always be maintained, and therefore, reduce self-attention.

Table 2.4: Comparison of Point Predictions for the Net-Load Forecasting.

Zone	Criterion	GTrans	SVR	DT	LSTM	GRU	GCN	AGNN
Zone 1	MAPE	3.34	10.37	4.86	6.03	5.49	7.88	6.03
	MAE (kW)	124.95	380.99	184.94	234.43	209.28	290.02	221.27
	Corr	0.1249	0.2801	0.1575	0.1546	0.1466	0.1767	0.1606
Zone 2	MAPE	2.92	9.04	4.39	5.28	4.42	6.86	6.91
	MAE (kW)	120.14	364.14	180.62	217.28	180.23	284.08	293.77
	Corr	0.0741	0.3296	0.1416	0.1221	0.1021	0.1543	0.1243
Zone 3	MAPE	4.46	12.15	5.25	5.87	6.15	22.89	15.03
	MAE (kW)	173.58	448.40	197.25	225.90	236.93	947.23	602.43
	Corr	0.1197	0.3409	0.1637	0.1572	0.1698	0.2861	0.3500
Aggregated	MAPE	2.35	9.36	3.35	5.19	3.82	8.27	6.65
	MAE (kW)	275.89	1065.0	392.15	616.19	440.59	1022.5	803.48

The best scores are highlighted in bold.

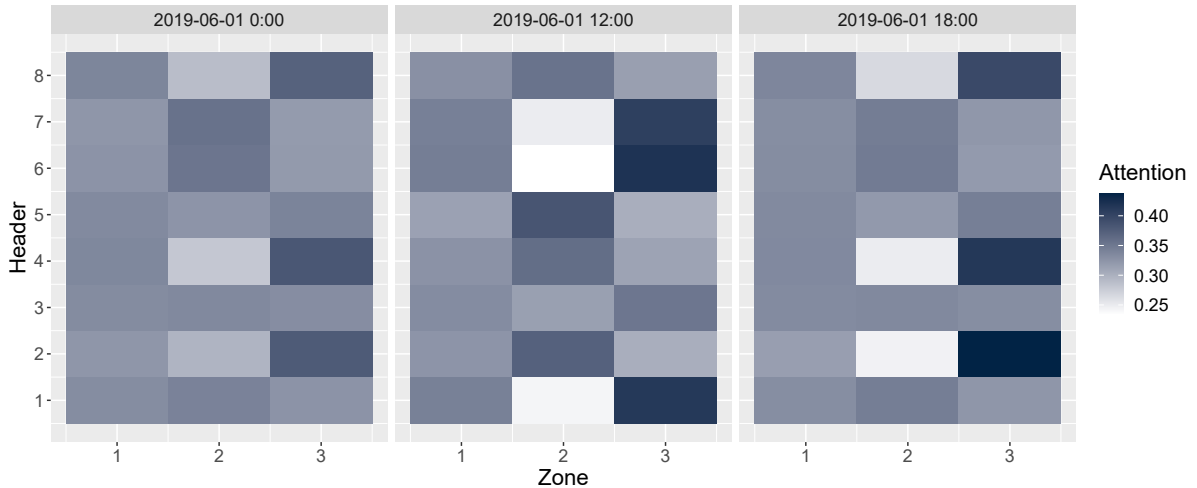


Figure 2.16: Attention scores of Zone 3 in the graph attention network.

Results on Probabilistic Forecasting

We then show the probabilistic net-load predictions produced by the GTrans for two days in Fig. 2.18. Two central prediction intervals are given. We notice that the installation of BTM solar is larger in Zone 1 and Zone 3, compared to that of Zone 2, since we observe valleys for Zone 1 and Zone 3 at noon in June. That could be the reason why the accuracy of Zone 2 is better in Table 2.4. Most of the realizations are within the 95% prediction interval, and the time series patterns are followed.

Again, we adopt the Pinball and Winkler scores to evaluate probabilistic forecasting. We

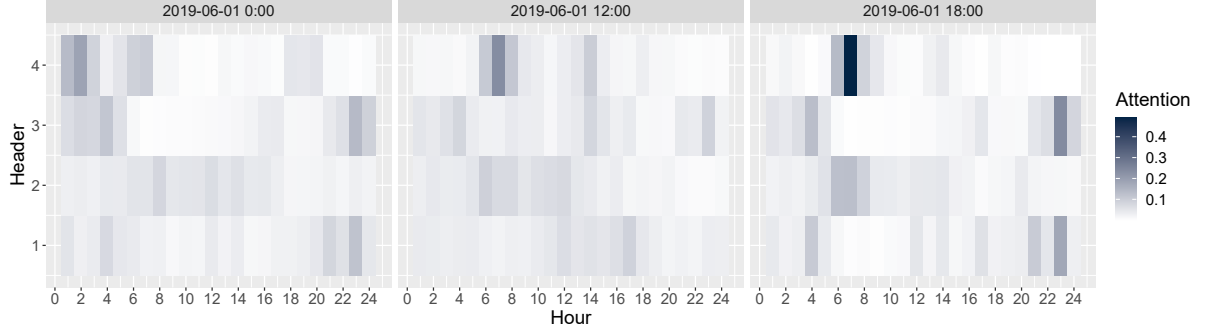


Figure 2.17: Attention scores of Zone 3 in the first sublayer of the transformer.

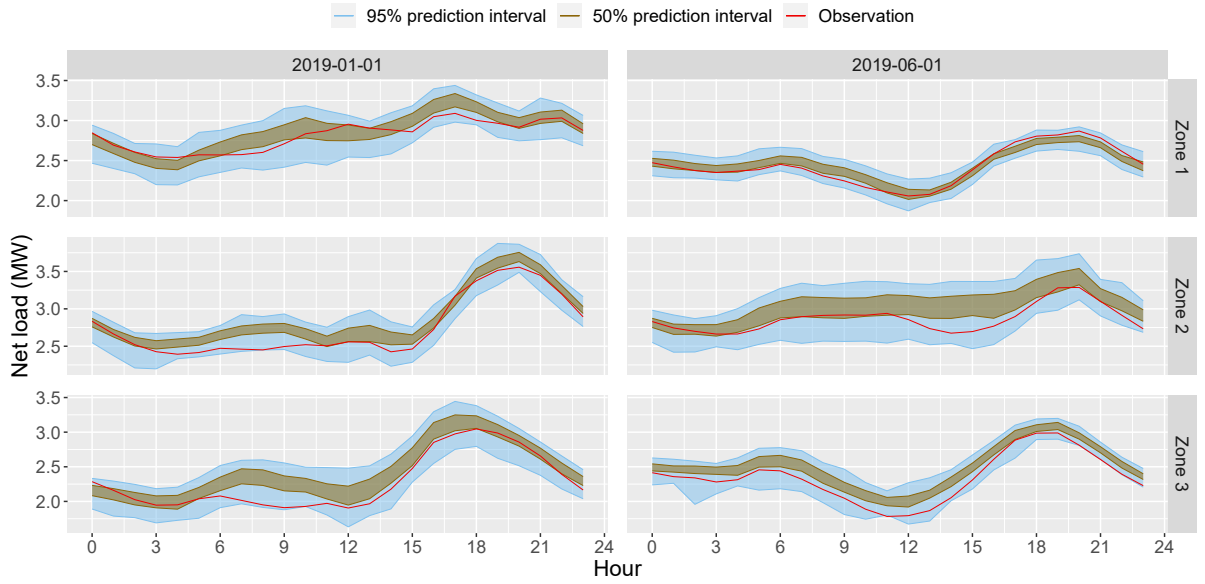


Figure 2.18: Probabilistic net-load forecasting results on a summer day and a winter day.

rewrite the equations since we report scores for each zone and the number of days in the testing set has changed.

For the τ -th quantile of the prediction \hat{y}_t^τ in time step t , the score is calculated by

$$\text{Pinball}(\hat{y}_t^\tau, y_t, \tau) = \tau \max(y_t - \hat{y}_t^\tau, 0) + (1 - \tau) \max(\hat{y}_t^\tau - y_t, 0). \quad (2.44)$$

We evaluate $\tau \in \{0.1, 0.2, \dots, 0.8, 0.9\}$ over all the 8760 hours in the testing set, which leads to a new measure

$$\frac{1}{9 \times 8760} \sum_{\forall \tau} \sum_{t=1}^{8760} \text{Pinball}(\hat{y}_t^\tau, y_t, \tau). \quad (2.45)$$

The scores in kW of all the methods are listed in Table 2.5. Predictions made by the GTrans show superiority.

Regarding the Winkler score, we also consider the case of the central $(1-2\alpha) \times 100\%$ pre-

Table 2.5: Comparison of Pinball Scores for the Net-Load Forecasting.

Zone	GTrans	QR	SVQR	LSTM	GRU	GCN	AGNN
Zone 1	47.18	58.07	84.25	67.50	52.86	105.3	67.92
Zone 2	48.79	64.90	91.28	72.74	63.45	135.7	89.55
Zone 3	52.48	85.88	128.0	77.01	66.50	174.0	91.81

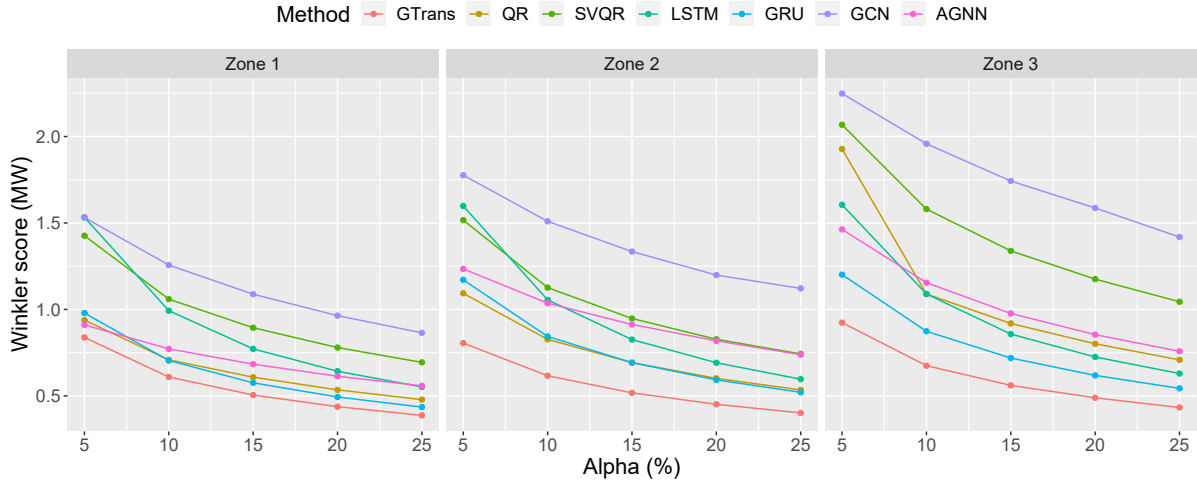


Figure 2.19: The comparison of probabilistic net-load forecasts, in terms of the Winkler score.

diction interval. Let the central interval be $\mathcal{C}_t^\alpha = [l^\alpha, u^\alpha]$. The score is computed by

$$\text{Winkler}(\mathcal{C}_t^\alpha, y_t) = (u^\alpha - l^\alpha) + \frac{1}{\alpha} \min_{c \in \mathcal{C}_t^\alpha} (|y_t - c|), \quad (2.46)$$

in which the first term calculates the width, and the second term penalizes the score if the realization is not in the interval. Again, we consider an overall performance over the entire testing set for a selected α , which leads to a new measure

$$\frac{1}{8760} \sum_{t=1}^{8760} \text{Winkler}(\mathcal{C}_t^\alpha, y_t). \quad (2.47)$$

Scores for $\alpha \in \{5\%, 10\%, 15\%, 20\%, 25\%\}$ are tested. The comparison between different methods is shown in Fig. 2.19. The predictions generated by the GTrans are the best for all the 3 zones. Moreover, we observe that deep learning models such as GRU tend to achieve a comparably better performance in Zone 1 and Zone 3. The reason could be that the capacities of BTM solar in those two zones are higher than that in Zone 2, which leads to more viability. High generalization capability in deep learning models ensures the model to approximate more complex patterns.

2.3 Sequence Generative Adversarial Network

We adapt the sequence generative adversarial network (SeqGAN) [34] for scenario generation for a single renewable site. The scenarios can be used for the short-term scheduling. We utilize the LSTM architecture to fulfill the task of time series sequence generation. To guide the learning of the LSTM units, we adopt GANs coupled with reinforcement learning. The GAN sets up a minimax two-player game between a discriminative net D and a generative net G , where D learns to distinguish whether a given data instance is real or not, and G learns to confuse D by generating high quality data. We consider the sequence generation procedure as a stochastic sequential decision making process. The generative model G is regarded as an agent of reinforcement learning, with the state to be the previous wind generation and the action to be the wind generation in the current time slot. We will examine the effectiveness of the SeqGAN based method in terms of both statistical metrics and performance of microgrid operations. For comparison, Gaussian distribution, vanilla LSTM, and multivariate KDE will be used as the benchmark methods.

2.3.1 Problem Statement

Consider a data set of real-world structured sequences for the forecast error of a wind farm. Let $\mathbf{x} = (x_1, \dots, x_T)$ be the vector of a historical sequence indexed by time $t = 1, \dots, T$, where T is the scheduling horizon. We aim to train a model to produce several new sequences $\mathbf{y} = (y_1, \dots, y_T)$ for the next day. The generated sequences are expected to take into account temporal correlations among the slots. In some situations, the weather predictions are not available for point forecasts, or there is no historical data of forecast error. The scenario generation method should produce the scenarios of wind generation by utilizing the historical sequences as training samples.

Wind power does not follow a regular pattern. The complex dynamic nature of weather, the nonlinear power conversion process of wind turbines, and successional risk in time series forecasting motivate us to use the LSTM architecture. The deep hypothesis spaces provide high generalization capability, and capture the complex dynamics and nonlinear conversion process. The hidden and internal states address the impact of previous wind generation. In practice, the training of LSTM is based on the current states of the model and wind generation in previous time slots. However, during inference, true previous wind generations are not available, and thus replaced by values generated by the model itself, yielding a discrepancy between how the model is used in training and inference. When the model is used to generate scenarios for the next day, mistakes made in early hours are fed as input to the model and can be quickly amplified. Moreover, the generated sequences are fed to conduct the day-ahead scheduling, where a task specific loss may not be directly available to complete the training of LSTM

GANs can alleviate the problem, where the loss is returned by D . However, GANs cannot be applied directly to time series scenario generation. First, GANs can only give the loss for

a complete sequence. For the day-ahead scheduling, we need to make a tradeoff between the fitness of wind generation in each time slot and the score of the entire time series sequence. For example, an irregular point may require one generator to be online for several hours due to the minimum start-up time. Second, we need to sample a sequence of random variables. It is hard to select the distribution considering the temporal relationship. For example, investigating the impact of selecting a joint Gaussian distribution or i.i.d. can be difficult and problem specific.

To overcome the first challenge, we adopt the concept of reinforcement learning. We utilize LSTM units in the generative model G . In time slot t , the state s_t is composed of the partially generated sequence $\mathbf{y}_{1:t} = (y_1, \dots, y_{t-1})$, the hidden state h_t , and the internal state c_t . The action a_t is the generated value of y_t . Let the parameters in G and D be θ and ϕ , respectively. We want to update $G_\theta(y_t|s_t)$ toward increasing the probability of selecting y_t that produces the highest reward considering the intermediate fitness in t and its future impact on the remaining time slots. While $G_\theta(y_t|s_t)$ is stochastic, the state transition is deterministic given the selected action. In time slot $t < T$, we use Monte Carlo search (i.e., sample average approximation) to generate several sample outcomes and regard the average as the expectation of the future reward.

Regarding the second difficulty, we use the forecast errors or wind generation of the previous day as inputs. The input in each time slot is rounded to its nearest integer (or any given number of decimal places) and then one hot encoded. Softmax is selected as the activation function of the output y_t to obtain the underlying distribution for each integer. By doing so, the distribution is discrete in nature. The decision maker can then choose to produce intervals with confidence or sample paths.

The proposed model is shown in Fig. 2.20. Green nodes are real wind generation, and red nodes are generated values. Wind generation in the previous day is embedded and then inputted into LSTM. For a partially generated scenario, Monte Carlo search is used to sample N complete scenarios. D gives a score for each complete scenario, which is returned to G to guide the learning process. D is trained by scenarios generated by G and real sequences from datasets. In time slot t , action of selecting y_t is assigned an action-value function by Monte Carlo search, which is used to update the parameters of the LSTM units.

2.3.2 Model Specifications

The SeqGAN is specified as follows. The end reward of each sequence is returned by D , which scores the entire sequence. To address the intermediate reward, we define the reward to go in time slot t as

$$R_t(s_t, \theta, \phi) = \mathbb{E}_{y_t \sim G_\theta(y_t|s_t)} R_{t+1}(s_{t+1}, \theta, \phi). \quad (2.48)$$

Since each $y_t \in \{0, 1, \dots, C\}$ has been rounded up to the nearest integer (where C is the wind power capacity), the distribution $G_\theta(y_t|s_t)$ can be seen as discrete. It is totally feasible to round it to any desired number of decimal places. The expectation in (2.48) can be transformed into

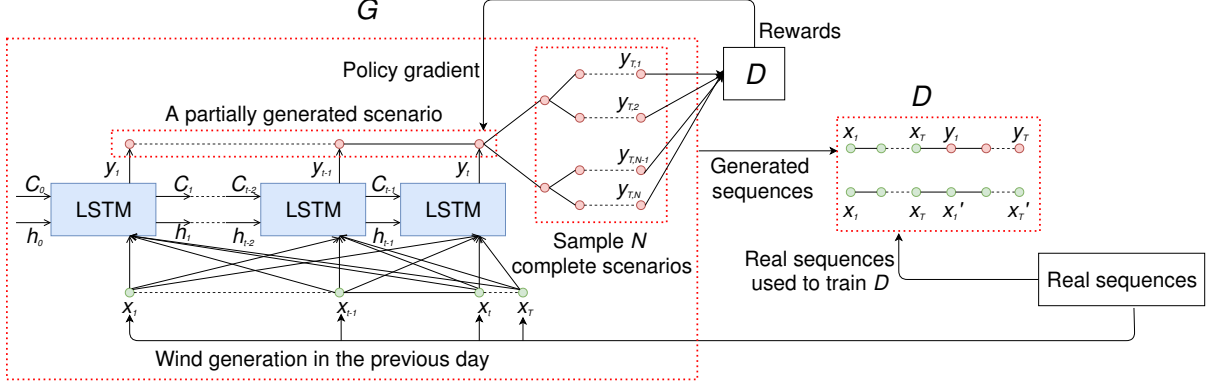


Figure 2.20: The structure of the sequence generative adversarial network.

the extensive form:

$$R_t(s_t, \theta, \phi) = \sum_{y_t=0}^C G_\theta(y_t|s_t) Q_{\theta, \phi}(s_t, y_t), \quad (2.49)$$

where $Q_{\theta, \phi}(s_t, y_t)$ is an action-value function, representing the expected accumulative reward based on the state s_t , the action y_t , and the models G and D . The discriminative model D will give the likelihood that an input sequence $\mathbf{y}_{1:T}$ is true. Since the goal of G is to fool D , we regard the likelihood as the reward for G . As for the action-value function at the boundary $t = T$, we have

$$Q_{\theta, \phi}(s_T, y_T) = D_\phi(\mathbf{y}_{1:T}). \quad (2.50)$$

However, D cannot score an incomplete sequence. In time slot $t < T$, we also want to evaluate $Q_{\theta, \phi}(s_t, y_t)$. Therefore, we use Monte Carlo to sample the remaining unknown $T - t$ time slots using G . Let N denote the total number of samples. Then the n th complete sequence is denoted by $\mathbf{y}_{1:T}^n = (\mathbf{y}_{1:t}, \mathbf{y}_{t+1:T}^n)$, for $n = 1, \dots, N$. We take the average reward of the N samples:

$$Q_{\theta, \phi}(s_t, y_t) = \begin{cases} (1/N) \sum_{n=1}^N D_\phi(\mathbf{y}_{1:T}^n), & t < T, \\ D_\phi(\mathbf{y}_{1:T}), & t = T. \end{cases} \quad (2.51)$$

To provide useful guidance for the training of G , D should be updated dynamically in an iterative manner. The loss function L_D is given by

$$L_D = - \sum_{\mathbf{x} \in \mathcal{X}} \log D_\phi(\mathbf{x}) - \sum_{\mathbf{y} \in \mathcal{Y}} \log(1 - D_\phi(\mathbf{y})), \quad (2.52)$$

where \mathcal{X} is the set of real sequences, and \mathcal{Y} is the set of generated sequences. The goal of G is to generate a sequence that looks real. Therefore, we use the negative reward to go in $t = 1$ to

be the loss function for training, which leads to

$$L_G = - \sum_{y_1=0}^C G_\theta(y_1|s_1) Q_{\theta,\phi}(s_1, y_1). \quad (2.53)$$

Unlike the conventional GANs where the inputs are random variables, the input in our model is the initial state s_1 . When $t = 1$, there is no partially generated sequence. Hence, we only need to provide the hidden and internal states. The simplest way is to set them equal to zero. In this work, we use the sequence of the previous day to initialize the states. The rationale is that there could be some time dependencies between those two days. For example, the last few hours of the previous day will have some impact on the first few hours of the next day, especially when the decision maker wants to generate wind generation scenarios directly. It can be easily extended to the case where the decision maker needs to finalize the scheduling hours ahead of the next day.

The reward returned by D is used to update the parameters θ of G . The gradient of L_G with respect to θ is given by

$$\nabla_\theta L_G = -\mathbb{E}_{s_t \sim G_\theta} \left[\sum_{y_t=0}^C \nabla_\theta G_\theta(y_t|s_t) \cdot Q_{\theta,\phi}(s_t, y_t) \right]. \quad (2.54)$$

The reader can refer to [34] for the details. For the learning purpose, an approximated direction is good enough. Therefore, we consider an unbiased estimator for (2.54):

$$\begin{aligned} \nabla_\theta L_G &= - \sum_{t=1}^T \sum_{y_t=0}^C \nabla_\theta G_\theta(y_t|s_t) \cdot Q_{\theta,\phi}(s_t, y_t) \\ &= - \sum_{t=1}^T \sum_{y_t=0}^C G_\theta(y_t|s_t) [\nabla_\theta \log G_\theta(y_t|s_t) \cdot Q_{\theta,\phi}(s_t, y_t)] \\ &= - \sum_{t=1}^T \mathbb{E}_{s_{t+1} \sim G_\theta(s_t)} [\nabla_\theta \log G_\theta(y_t|s_t) \cdot Q_{\theta,\phi}(s_t, y_t)]. \end{aligned} \quad (2.55)$$

Again, the expectation term can be approximated by sampling.

By (2.55), we have the gradient of the loss function (2.53). The parameters are then updated by an advanced gradient algorithm *Adam*. Algorithm 1 shows the process for training.

2.3.3 Case Studies

Data Description

Wind power data from the Bonneville Power Administration (BPA) [120], which provides day-ahead forecasts, is used to generate scenarios for forecast error. Moreover, we use the wind data from the NREL to generate day-ahead wind generation scenarios directly [109]. The

Algorithm 1 Algorithm for training of SeqGAN

Require:

generator G , discriminator D , number of iterations for discriminator d , number of iterations for generator g , learning rate for *Adam*.

- 1: Initialize G and D with random parameters θ and ϕ
- 2: **while** D has not converged **do**
- 3: **for** g -steps **do**
- 4: Generate a sequence $\mathbf{y}_{1:T} \sim G_\theta$
- 5: **for** t in $1 : T$ **do**
- 6: Compute $Q_{\theta,\phi}(s_t, y_t)$ by (2.51)
- 7: **end for**
- 8: Obtain the gradient of generator loss by (2.55)
- 9: Update generator network using *Adam*
- 10: **end for**
- 11: **for** d -steps **do**
- 12: Use current G to generate samples, and combine them with real sequences in \mathcal{X}
- 13: **for** k epochs **do**
- 14: Train discriminator D by (2.52)
- 15: **end for**
- 16: **end for**
- 17: **end while**

original data in both data sets has a resolution of 5 minutes. We use the average power in each hour for our study. We use two-year data for training and one-week data for testing. It is worth mentioning that SeqGAN does not need the selection of features.

Sample Paths

We use the data from April 28 to May 4, 2019 in the BPA data set to test the proposed method. Two-year data before April 28, 2019 is used for training. The total wind capacity is 4450 MW. The goal of scenario generation is to generate representative sample paths. For illustration, we only generate 20 sample paths with equal probability. We use the difference of real generation and forecasted value to be our observation. We compare the paths generated by the SeqGAN based model with those sampled from fitting Gaussian distribution and multivariate KDE. As shown in Fig. 2.21, the proposed model generates diverse realizations such as large peaks and fast ramp events. Moreover, we are more interested in the lower bound when we conduct power system analysis. The least safe margin of the scenarios generated by our method is larger than those produced by the other two methods, which helps make more robust day-ahead decisions. In addition to the potential of increasing robustness, the scenarios generated by our method follow the actual trends better, for example, the ramping from hour 21 to hour 23.

In some situations, the numerical weather predictions are not available for a point forecast, or there is no historical forecast error. Our model can be easily extended to generate scenarios for wind generation. We use the data from December 25 to December 31, 2012 at site #34804 in

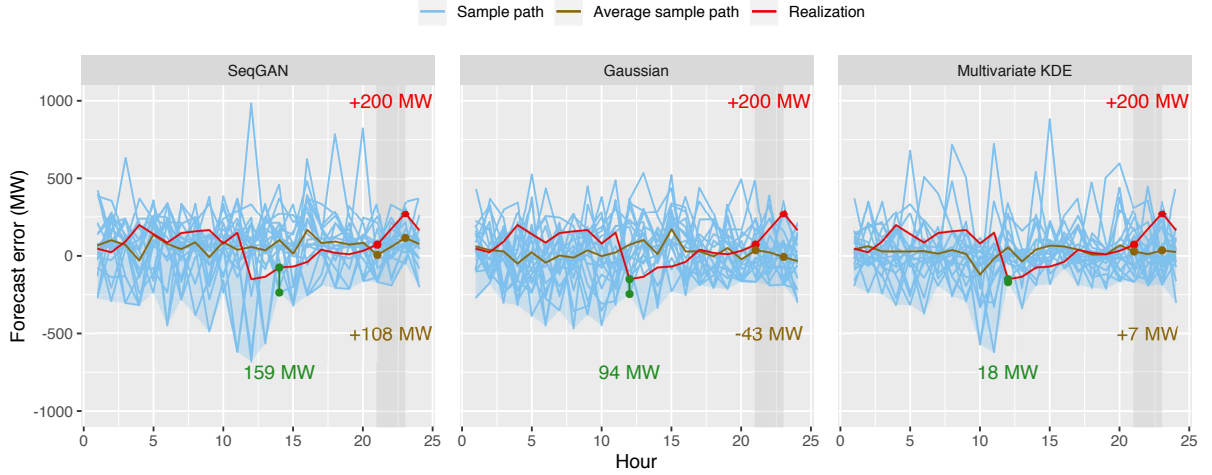


Figure 2.21: Sample paths of forecast error generated by models for the scenario generation on April 29, 2019.

the NREL data set for testing. The wind capacity is 14 MW. Two-year data before December 25, 2012 is used for training. In Fig. 2.22, we show 20 scenarios corresponding to December 25, 2012. We compare SeqGAN with vanilla LSTM and multivariate KDE. Softmax is used to be the activation function of the output layer of LSTM, which maps the output into a probability distribution. The LSTM is trained by maximum likelihood estimation. The scenarios generated by three methods are visually very different from each other. We observe that the vanilla LSTM tends to be overfitting for the last few hours. As for the scenarios produced by the multivariate KDE, they are prone to misidentification of the pattern. Moreover, schedule decisions determined by the vanilla LSTM will give a poor performance due to the resulting load shedding. The scenarios generated by the KDE based method are too conservative because the lower bound is always zero.

Statistical Analysis of Scenarios for Forecast Error

We apply two statistical metrics proposed in [121, 122] to evaluate our scenarios. For this purpose, we generate 100 scenarios with equal probability. Note that the number of scenarios is constrained by the complexity of scheduling problems.

First, we consider the mean square error (MSE) of the generated scenarios:

$$S_{\text{MSE}} = \frac{1}{T} \sum_{t=1}^T (\mathbb{E}[\mathbf{1}^T \mathbf{Y}_t] - x_t)^2, \quad (2.56)$$

where $\mathbf{Y} \in \mathbb{R}^{N \times T}$ is the matrix of N generated scenarios, \mathbf{Y}_t is the t th column vector in \mathbf{Y} , and x_t is the observation in time slot t . The rationale comes from the fact that the decisions driven by such scenarios can yield an objective value that is close to the real cost for the actual

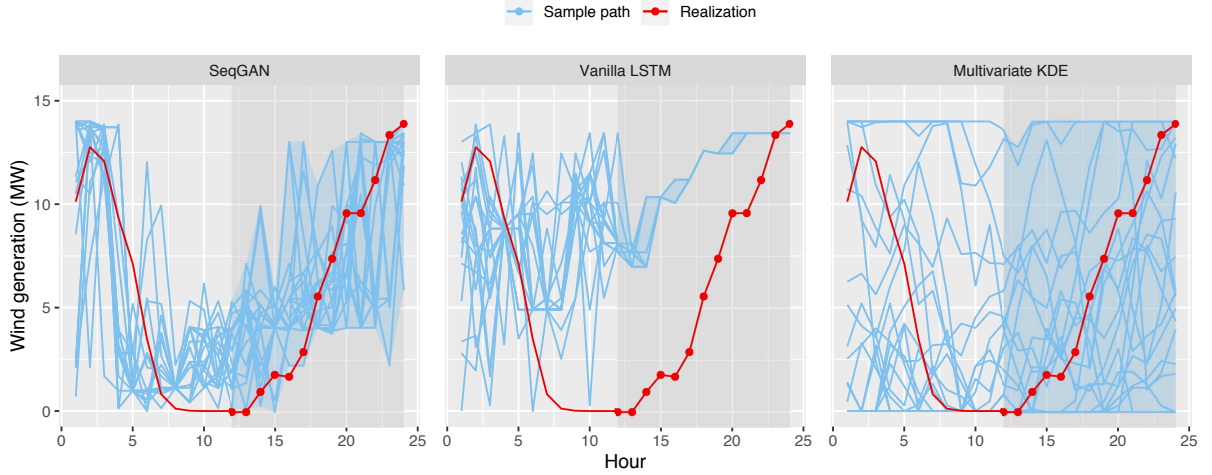


Figure 2.22: Sample paths of wind generation generated by models for the scenario generation on December 25, 2012.

realization. The score is negatively oriented since less quadratic deviation is preferred.

The second score is a multivariate skill score called the Energy score. It is proper (i.e., a perfect forecast will result in the best score) score that quantifies both the skill (accuracy) and sharpness (spread) of a scenario set. The Energy score is defined as

$$S_{\text{Energy}} = \frac{1}{T} \sum_{t=1}^T \left[\frac{1}{N} \sum_{n=1}^N \|x_t - Y_{n,t}\|_2 - \frac{1}{2N^2} \sum_{n=1}^N \sum_{m=1}^N \|Y_{n,t} - Y_{m,t}\|_2 \right]. \quad (2.57)$$

The intuition behind the Energy score is to generate diverse yet representative scenarios. Similar to the MSE, a lower score is preferred.

As shown in Fig. 2.23, our method outperforms the other two for all the days, in terms of MSE. Our methods can capture more complex temporal dynamics between the evolution of the forecast error in each time slot and generate more realistic paths. SeqGAN is an improvement over the other two approaches, which will improve the quality of the scheduling decisions. Regarding the Energy score, our method generates some scenarios that are characterized by extreme variations. The score is worse when the realization does not show many uncertainties. In such cases, the distance between the scenarios and realization deteriorates the overall score of our method. With the increasing penetration of renewable energy, microgrids are more sensitive to variations and require more robustness. Our method shows superiority when the realization exhibits hallmark characteristics of renewable generation profiles.

Statistical Analysis of Scenarios for Wind Generation

Similar to the previous assessment, we adopt two scores to evaluate the quality of produced scenarios for wind generation. When generating scenarios for wind generation directly, we are

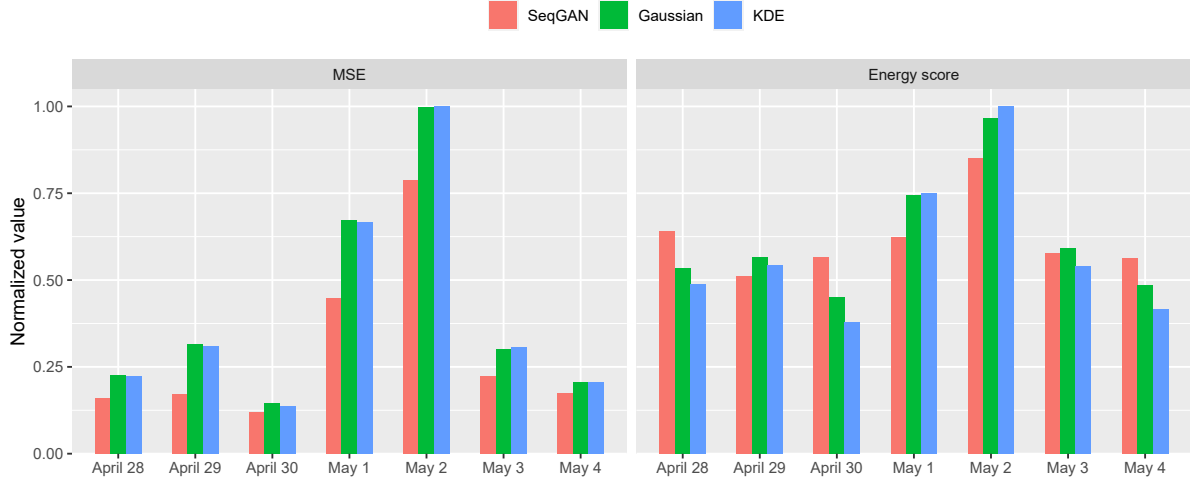


Figure 2.23: Comparison of models for the scenario generation, in terms of the MSE and the Energy score.

more interested in behavior matching, especially for microgrids associated with a wind farm that routinely sees large fluctuations. Therefore, we introduce the Brier score and the Variogram score. The model can be updated on a weekly basis, and therefore we only evaluate its performance over seven consecutive days. We consider 3 different wind farms in 2 different seasons. Sites #34804, #39977, and #29733 from the NERL data set are used, which are located in North Carolina, Kansas, and California, respectively. Based on the wind seasonal patterns reported by the U.S. Energy Information Administration [48], we consider one week in December (Case 1a) and one week in June (Case 1b) for site #34804, one week in December (Case 2a) and one week in April (Case 2b) for site #39977, and one week in December (Case 3a) and one week in May (Case 3b) for site #29733. Two weeks for each site are associated with peak and off-peak seasons.

The Brier score is an event-based and negatively oriented metric, which evaluates the performance of scenarios under a predefined event. The Brier score is defined as

$$S_{\text{Brier}} = \frac{1}{T} \sum_{t=1}^T [\mathbb{E}(g_t(\mathbf{Y}, \mathcal{E})) - g_t(\mathbf{x}, \mathcal{E})]^2, \quad (2.58)$$

where \mathcal{E} denotes the predefined event, and the function g_t indicates whether the event occurs in the sequence in time slot t . The Brier score depends on the selection of events. In the context of microgrid day-ahead scheduling, large ramps within a small time frame will result in significant financial losses. Therefore, we consider four events: a 10% change (relative to capacity) in 1 hour and a 20% change in 2 hours. The scores are given in Table 2.6.

We observe that scenarios generated by our method better and inherently match the behavioral properties of the wind farm in consideration. Consider the visual comparison in Fig. 2.22.

Table 2.6: Comparison of Models for the Scenario Generation Using the Brier Score.

Case	Event	SeqGAN	LSTM	KDE
1a	+10% in 1 hour	0.2148	0.2500	0.2240
	+20% in 2 hours	0.1866	0.2167	0.1960
	-10% in 1 hour	0.1745	0.1930	0.2151
	-20% in 2 hours	0.1617	0.2178	0.1917
1b	+10% in 1 hour	0.1842	0.1900	0.1906
	+20% in 2 hours	0.1291	0.1647	0.1494
	-10% in 1 hour	0.1597	0.1780	0.1867
	-20% in 2 hours	0.1151	0.1396	0.1460
2a	+10% in 1 hour	0.1621	0.1799	0.1788
	+20% in 2 hours	0.1299	0.1598	0.1460
	-10% in 1 hour	0.1556	0.1709	0.1843
	-20% in 2 hours	0.1468	0.1788	0.1556
2b	+10% in 1 hour	0.1518	0.1762	0.1689
	+20% in 2 hours	0.1087	0.1335	0.1340
	-10% in 1 hour	0.1588	0.1579	0.1828
	-20% in 2 hours	0.1333	0.1371	0.1415
3a	+10% in 1 hour	0.1548	0.1550	0.1660
	+20% in 2 hours	0.1134	0.1362	0.1249
	-10% in 1 hour	0.1424	0.1432	0.1642
	-20% in 2 hours	0.1216	0.1331	0.1297
3b	+10% in 1 hour	0.1175	0.1395	0.1581
	+20% in 2 hours	0.0885	0.1017	0.1165
	-10% in 1 hour	0.1103	0.1157	0.1685
	-20% in 2 hours	0.0800	0.1060	0.1260

The best scores are highlighted in bold.

The scenarios generated by the vanilla LSTM prove to be slightly smooth due to overfitting, therefore underestimating the variability. The KDE based scenarios cannot follow the correct pattern, thus affecting the performance.

The Variogram score is used to evaluate the time dependencies of scenario sets. It is a proper and negatively oriented multivariate score. The Variogram score captures time correlations

Table 2.7: Comparison of Models for the Scenario Generation Using the Variogram Score.

Case	$p = 1$			$p = 2$		
	SeqGAN	LSTM	KDE	SeqGAN	LSTM	KDE
1a	0.505	0.553	0.530	0.497	0.584	0.546
1b	0.346	0.350	0.388	0.278	0.287	0.306
2a	0.530	0.572	0.626	0.448	0.461	0.491
2b	0.506	0.588	0.554	0.421	0.538	0.457
3a	0.462	0.574	0.513	0.346	0.439	0.381
3b	0.349	0.389	0.432	0.324	0.363	0.424

compared with the Energy score. The Variogram score is defined as

$$S_{\text{Var}} = \sum_{t_1=1}^T \sum_{t_2=1}^T \left[|x_{t_1} - x_{t_2}|^p - \frac{1}{N} \sum_{n=1}^N |Y_{n,t_1} - Y_{n,t_2}|^p \right]^2, \quad (2.59)$$

where p is the order of the Variogram. The average daily Variogram scores are reported in Table 2.7. The SeqGAN based scenarios are much better than those generated by LSTM and KDE, indicating the advantage in generating sequences with realistic temporal correlations.

Microgrid Scheduling Analysis

Power system operation involves physical constraints related to time such as minimum start-up time. Statistical metrics may not be sufficient to evaluate the effectiveness of generated scenarios. Hence, we use the scenarios to perform a real day-ahead scheduling problem. The microgrid is assumed to be one region, where we use a 24-bus reliability test system. The system is modified to incorporate renewable uncertainty following [123]. The case study shows the effectiveness of the scenarios generated by SeqGAN on the day-ahead scheduling.

There are 6 wind farms with 200 MW capacity in the modified system. The generated scenarios on May 1 from the BPA data set are used to perform the analysis. We choose this date because the forecasted wind generation is around 50% capacity. We assume that the wind farms within one region share perfect positive correlation. Hence, we normalize the aggregated wind generation of all scenarios to $[0, 1]$ and consider the values to be the percentages of the total capacity. The computational efficiency is not an issue for such a small system. We use 100 scenarios to do the day-ahead scheduling. All the parameters are adopted from [123], where the generating units offer one block of price. Therefore, the day-ahead decisions are obtained by solving a two-stage stochastic mixed integer linear program. Day-ahead decisions of interest include on/off status and start-up/shutting-down signals. For simplicity, we ignore the uncertainties in load. Once the day-ahead decisions are determined and fixed, we perform economic

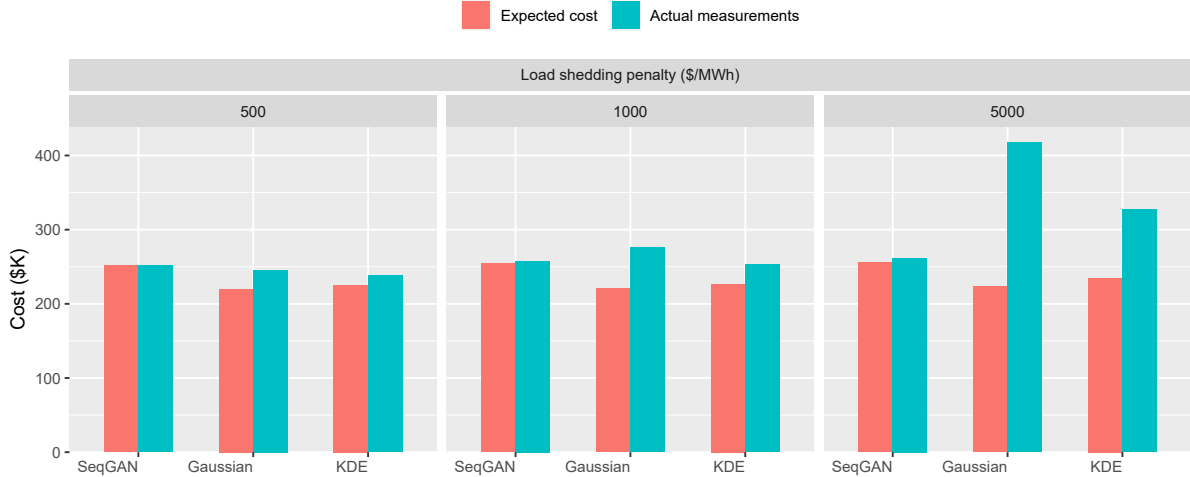


Figure 2.24: Comparison of scenarios generated by models for the scenario generation based on the expected and the actual costs.

dispatch according to the realization. We sample 400 sequences from the historical sequences randomly and use them as possible realizations. We take the average over all realizations as our actual cost associated with the day-ahead decisions. Simulation results are averaged over 5 runs since the realizations are sampled randomly. For each realization, we assume that 5% of load can be shedded by other programs such as demand response. The price of demand response is set to the offer price of the most expensive unit. The rest load shedding is subject to high penalty. Penalty for the wind curtailment is not applied, since the excess generation can be sold to the main grid. If the generated scenarios can encapsulate all possible realizations, high penalties will not occur, and the actual measurements should be close to the expected cost returned by the optimization problem.

We consider three different cases where the load shedding penalty for each MW is set as \$500, \$1000, and \$5000. Simulation results are in Fig. 2.24 and Fig. 2.25. We observe that the scenarios generated by Gaussian distribution always lead to a higher actual measurement compared with that resulted by KDE. Parametric models cannot capture the complex temporal dynamics. Hence, the generated scenarios cannot encapsulate all the possible realizations and the expected cost is lower since it excludes some extreme events. However, the corresponding day-ahead decisions cannot meet the realizations with extreme events. High penalties are applied to shed the load and deteriorate the performance. Therefore, scenarios generated by KDE are much better. However, the scenarios produced by KDE cannot represent all possible realizations either. The expected cost and actual measurements for SeqGAN are closer. Moreover, the standard deviations of the actual measurement are much lower than those of the other two methods. A large standard deviation represents violations in some realizations, which shows that the scenarios generated by SeqGAN can inherently represent all possible realizations and provide robustness. When the load shedding is expensive (i.e., \$5000/MWh), we observe huge

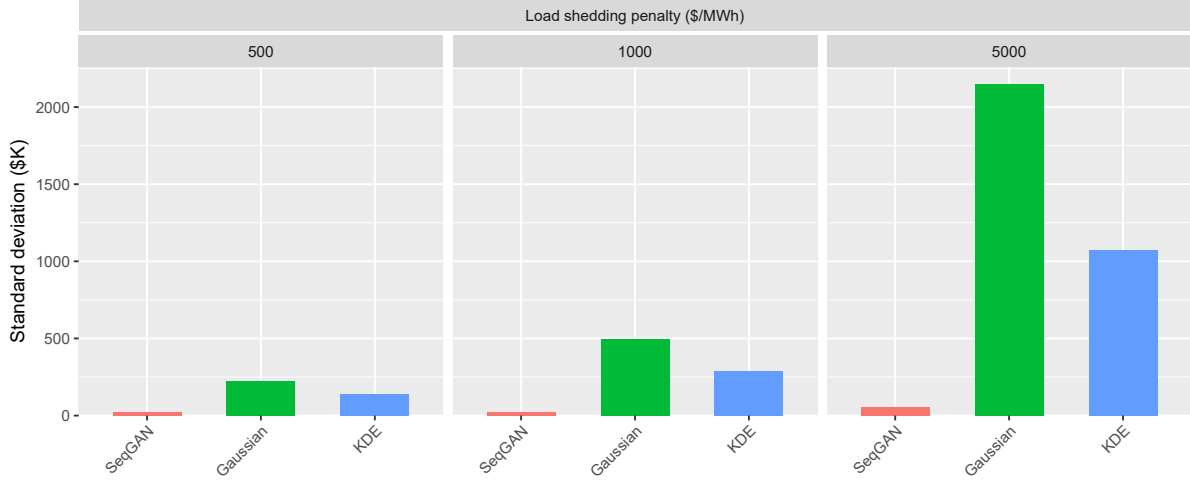


Figure 2.25: Comparison of scenarios generated by models for the scenario generation based on standard deviations of the actual costs.

differences in the actual measurements.

2.4 Mixed Autoencoder Based Fuzzy Clustering

In general, the essence of scenario reduction lies in finding a new scenario set with fewer number of scenarios that can keep the solution close to that generated by the original scenario set. However, two questions remain open for scenario reduction, i.e., how to perform scenario reduction, and how to tell which scenario reduction method provides scenarios with the best quality for a given problem. The proposed mixed autoencoder based fuzzy clustering (MAFC) adopts the concept “mixed autoencoders” [45, 46]. First, several deep autoencoders map time series in consideration to latent representations. Using the representations, another deep neural network (DNN) gives the degree of each time-series being in different patterns. Deep hypothesis spaces in autoencoders provide high generalization capability and capture the complex temporal dynamics. With membership functions, conventional methods of constructing centroids in c -means are extended to fuzzy time-series clustering. The architecture simultaneously learns feature representations and adjusts cluster assignments. The quality of our scenario reduction method is examined in two folds: similarity analysis and empirical analysis.

2.4.1 Problem Statement

Consider a scenario set $\mathcal{S} = \{\mathbf{s}^1, \dots, \mathbf{s}^N\}$, where N is the number of scenarios. Let T be the scheduling time horizon. Each scenario $\mathbf{s}^n \in \mathcal{S}$ is a time series of renewable generation, represented by $\mathbf{s}^n = (s_1^n, \dots, s_T^n)$. Moreover, each scenario \mathbf{s}^n is associated with a probability p^n , where $\sum_{n=1}^N p^n = 1$. Typically, the scenarios are with equal probability $1/N$.

When N is very large, it is numerically intractable to use all the N pairs of time series and probabilities to perform day-ahead scheduling. We have to reduce the number of scenarios to a small number, say K . If the reduced scenario set is constructed adequately, we expect to obtain nearly optimal day-ahead schedules. Let $\mathcal{C} = \{\mathbf{c}^1, \dots, \mathbf{c}^K\}$ be the reduced scenario set, where $\mathbf{c}^k = (c_1^k, \dots, c_T^k)$. Let P^k be the probability associated with \mathbf{c}^k , such that $\sum_{k=1}^K P^k = 1$.

We can reformulate the scenario reduction problem into a clustering task. Consider the problem of clustering a set of data points $\{\mathbf{s}^n \in \mathbb{R}^T, n = 1, \dots, N\}$ into K clusters, where the centroid of each cluster k is denoted by $\mathbf{c}^k \in \mathbb{R}^T$. The membership DNN in the proposed MAFC should output a vector of membership functions $\{u_k^n \in \mathbb{R}, k = 1, \dots, K\}$ for each \mathbf{s}^n , which represents the degree of time series \mathbf{s}^n being in each cluster k . Using membership functions, the probability P^k of each cluster k can be obtained.

We first describe the proposed MAFC architecture, as shown in Fig. 2.26. To capture the nonlinear nature and correlations within time series, we utilize K autoencoders to extract the features of each time-series. The latent representation can be interpreted as some useful information of the time series, for example, mean and covariance. Moreover, if the original scenarios maintain spatial correlations between different renewable generators, the latent representation is expected to include spatial information. Let the latent representation of autoencoder k be $\mathbf{z}_k \in \mathbb{R}^d$. Typically, the dimension of \mathbf{z} should be no more than the input, i.e., $d \leq T$. The latent embeddings of each autoencoder are further concatenated and fed into a membership DNN. The activation function of the membership DNN is selected to be softmax, and therefore, the output can be regarded as the degree u_k of being in each cluster k . At the same time, the decoders of autoencoders map \mathbf{z} to a reconstruction $\{\mathbf{X}_n \in \mathbb{R}^T, n = 1, \dots, N\}$. With u_k^n and the reconstruction, we build a centroid generator that outputs the centroid of each cluster k . Using the original scenario set \mathcal{S} and centroids, we calculate the reconstruction loss and update the network. Reconstruction loss is a data-dependent regularization for training the parameters and avoids capturing spurious data correlations. Moreover, it is assumed that the number of samples should be much greater than the scheduling time horizon, i.e., $N \gg T$. Otherwise, the model lacks generalization capability and will perform poorly. In the remainder of this section, we assume $N \gg T$ and set $d < T$.

2.4.2 Model Specifications

The MAFC is mathematically defined as follows. Let the parameter sets of the autoencoders and the membership DNN be $\theta_k, k = 1, \dots, K$ and θ_m , respectively. Let the concatenation of latent features for scenario \mathbf{s}^n be $\mathbf{z}^n = (\mathbf{z}_1^n, \dots, \mathbf{z}_K^n)$. \mathbf{z}^n is the input of the membership DNN, in which softmax is used as the activation function of the output layer. Let the values before the activation functions of the output layer of the membership DNN be $h^k(\mathbf{z}^n), k = 1, \dots, K$.

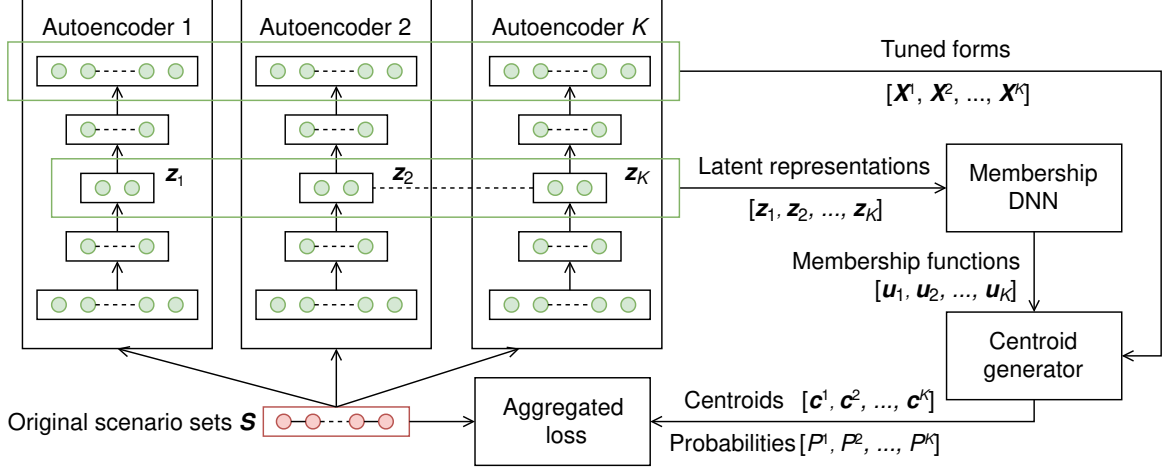


Figure 2.26: The mixed autoencoder based fuzzy clustering architecture.

The membership function for each cluster is given by

$$u_k^n(z^n; \theta_m) = \frac{e^{h^k(z^n)}}{\sum_{j=1}^K e^{h^j(z^n)}}, \quad k = 1, \dots, K, \quad (2.60)$$

where u_k^n represents the degree of scenario s^n being in cluster k . Let $\mathbf{u}_k = (u_k^1, \dots, u_k^N)$ collect the degrees of all time series $s^n \in \mathcal{S}$ being in cluster k . To obtain the centroid of each cluster, we adopt the method in the fuzzy c -means clustering algorithm. We introduce another tuple $\mathbf{X} \in \mathbb{R}^{K \times N \times T}$, and use $\mathbf{X}^k \in \mathbb{R}^{N \times T}$ to denote the output of autoencoder k with input \mathcal{S} . We feed \mathbf{u} and \mathbf{X} into the centroid generator, and it outputs K centroids (scenarios) $\mathbf{c}^k, k = 1, \dots, K$. Each time step in a time series can be obtained by

$$c_t^k = \frac{\sum_{n=1}^N (u_k^n)^m X_{n,t}^k}{\sum_{n=1}^N (u_k^n)^m}, \quad t = 1, \dots, T, \quad (2.61)$$

where m is a hyperparameter that controls the fuzziness of the clustering process. A higher m means a fuzzier clustering process. If $m = 1$, the problem becomes hard clustering. Typically, m is selected to be 2. Compared with the fuzzy c -means algorithm, which is one of the most widely used fuzzy clustering algorithms that allow elements to potentially belong to multiple clusters, the MAFC model has three different features. First, we need to perform the centroid construction for every time step. Second, the membership functions are determined by another deep neural network. The membership functions are conditioned on the latent representations and are expected to account for the pattern recognition. Moreover, the centroids are based on the outputs of decoders instead of the original scenarios.

Moreover, we also need the probabilities P^k of each cluster k . We consider the probability

of cluster k as the average of degrees of all time-series being in cluster k , which leads to

$$P^k = \frac{1}{N} \sum_{n=1}^N u_k^n, \quad k = 1, \dots, K. \quad (2.62)$$

Reconstruction loss is used to train the MAFC, which is a common choice in clustering tasks. Each autoencoder should be good at reconstructing instances which belong to that cluster. If the data set is properly clustered, we expect that all the time series assigned to the same cluster are similar, and the MAFC should result in a small reconstruction loss. The construction loss is defined as the probability distance between centroids \mathcal{C} and \mathcal{S} , given by

$$L_C(\mathcal{S}; \theta_m, \theta_1, \dots, \theta_K) = \sum_{k=1}^K P^k \sum_{n=1}^N \frac{1}{N} \|\mathbf{s}^n - \mathbf{c}^k\|_2^2, \quad (2.63)$$

where P^k and \mathbf{c}^k can be interpreted as a feature-driven degree of \mathbf{s}^n being in cluster k and a data-driven cluster k , respectively. The goal of this loss function is to minimize the distance between generated scenarios and scenarios in the original scenario set. Considering that a time series can be clustered into one cluster entirely, the probability weights ensure the distance to other clusters is not factored in.

We note a potential issue: there is no dominant membership assignment for each input \mathbf{s}^n . To tackle the issue, we adopt an additional loss function, named sample-wise entropy. Sample-wise entropy ensures that it will achieve its minimum only if the assignment \mathbf{u}^n of time-series \mathbf{s}^n is deterministic. In other words, there exists a $k' \in \{1, \dots, K\}$ that leads to $u_{k'}^n = 1$, and $u_k^n = 0$ for all $k \neq k'$. The formulation is given by

$$L_S(\mathcal{S}; \theta_m, \theta_1, \dots, \theta_K) = - \sum_{n=1}^N \sum_{k=1}^K (u_k^n)^m \log(u_k^n). \quad (2.64)$$

When $u_k^n \rightarrow 0$, we have $\lim_{u_k^n \rightarrow 0} -(u_k^n)^2 \log(u_k^n) = 0$. The function value of $-(u_k^n)^2 \log(u_k^n)$ over $u_k^n \in [0, 1]$ is shown in Fig. 2.27. Each individual element in the sample-wise entropy, i.e., $-(u_k^n)^2 \log(u_k^n)$, will reach its minimum when $u_k^n = 0$ or $u_k^n = 1$. Since the membership functions for each cluster are given by (2.60), we have $\sum_{k=1}^K u_k^n = 1$, $n = 1, \dots, N$. The sample-wise entropy guarantees that a scenario is associated with membership functions in which one is close to 1 and the rest are close to 0. Asymptotically, there exists a dominant label assignment for each scenario. Moreover, we observe from the experiment that without the sample-wise entropy, the parameters of the MAFC may stop at a local minimum where each scenario is assigned equal membership degrees to each cluster. The usage of sample-wise entropy can improve the performance of the model.

We use the weighted sum of L_C and L_S to train the MAFC, given by

$$L(\mathcal{S}; \theta_m, \theta_1, \dots, \theta_K) = L_C(\mathcal{S}; \theta_m, \theta_1, \dots, \theta_K) + \alpha L_S(\mathcal{S}; \theta_m, \theta_1, \dots, \theta_K). \quad (2.65)$$

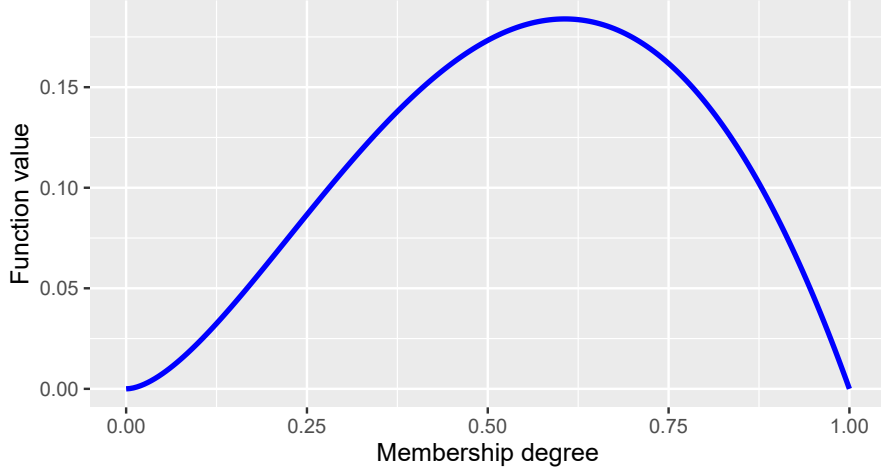


Figure 2.27: The value of each individual element in the sample-wise entropy.

Algorithm 2 Algorithm for training of the MAFC

Require:

Number of preserved scenarios K , K autoencoders, membership DNN, learning rate for *Adam*, maximum training epoch.

- 1: Initialize autoencoders and membership DNN with random parameters $\theta_k, k = 1, \dots, K$ and θ_m
 - 2: **while** the maximum epoch size has not been reached **do**
 - 3: Obtain latent representation \mathbf{z}_k for input \mathcal{S}
 - 4: Concatenate latent space: $\mathbf{z} = (\mathbf{z}_1, \dots, \mathbf{z}_K)$
 - 5: Obtain degrees $\mathbf{u} = (u_1, \dots, u_K)$ by (2.60)
 - 6: Construct centroid \mathbf{c} and probability vectors \mathbf{P} by (2.61) and (2.62), respectively, using \mathbf{u}
 - 7: Calculate aggregated loss L by (2.65) using \mathbf{c} , \mathbf{P} , and \mathbf{X}
 - 8: Take the gradient of L and update θ 's using *Adam*
 - 9: **end while**
-

In our experiment, α is adjusted every epoch and maintains the two terms at the same magnitude. It guarantees that both losses show close importance in calculating updating strategy. The parameters are then updated by an advanced gradient algorithm *Adam*. Algorithm 2 shows the process for training. The number of training epochs, batch size, and learning rate are set to 500, 64, and 0.001, respectively.

Note that we use symmetric topologies for encoders and decoders, and the topologies of all the autoencoders are unified. Table 2.8 lists the details about the topology, where all the layers are dense. The selection of K should depend on the complexity of the real system in consideration and the penetration of uncertainties.

Table 2.8: Topology of Networks Used in the Mixed Autoencoder Based Fuzzy Clustering.

Networks	Autoencoders		Membership DNN	
Layer	Dimension	Activation	Dimension	Activation
1	128	Sigmoid	128	Sigmoid
2	64	Sigmoid	64	Sigmoid
3	32	Sigmoid	32	Sigmoid
4	16	Sigmoid	K	Softmax

2.4.3 Case Studies

The proposed MAFC model is verified and compared with other scenario reduction techniques including simultaneous backward reduction (SBR) [38], k -Shape [124], global alignment kernels (GAK) [125], smoothed formulation of DTW (SoftDTW) [126], and k -means. To show that the latent space improves the results, we use kernel principal component analysis (PCA) to project 24-hour features to a lower dimensional space and perform clustering in the coefficient space of PCA using k -means. Moreover, we compare MAFC with vanilla mixed autoencoders in [45], where a DNN is used to derive the likelihood of each scenario being in each cluster, to show the effectiveness of fuzzy clustering. Generally, the cluster centroids produced by all the methods are not samples from the original set, although they live in the same space.

Data Description

We use wind power data from the Bonneville Power Administration (BPA) [120] and Elia [127]. The original data in the two data sets have resolutions of 5 and 15 minutes, respectively. We use the hourly average power in our study. Both data sets, with capacities of 4,450 MW and 3,667 MW, respectively, provide day-ahead forecasts and actual realizations. We consider the difference between the realized generation and the forecast generation as the forecast error. In this work, we perform scenario reduction with respect to the forecast error. We obtain the forecast errors for two years, i.e., 730 24-hour time series, fit the series using multivariate kernel density estimation, and sample out 2000 scenarios. Regarding the performance of scenario reduction, we only need to compare the preserved and original scenario sets. Therefore, we do not adopt advanced algorithms to generate the original scenario set.

To perform scenario reduction, we first need to define the number of scenarios in the preserved scenario set. It is constrained by the complexity of the power system in consideration and the computational power. We consider two cases for each data set, where 10 and 20 scenarios are preserved in the new scenario set. We label them as BPA-10, BPA-20, Elia-10, and Elia-20, respectively.

Table 2.9: Comparison of Methods for the Scenario Reduction Using the Cosine Distance Score.

Method	BPA-10	BPA-20	Elia-10	Elia-20
MAFC	0.885	0.888	0.896	0.896
SBR	1.009	1.023	0.924	0.944
k -Shape	0.998	0.999	0.986	1.002
GAK	0.915	0.914	0.951	0.960
SoftDTW	0.981	0.986	0.959	0.974
k -means	0.944	0.962	0.962	0.966
PCA	0.935	0.942	0.942	0.954
DNN	0.905	0.896	0.928	0.914

The best scores are highlighted in bold.

Statistical Analysis

To evaluate the quality of scenario reduction methods, we compare the new scenario sets generated by different methods, in terms of similarity and distance between time series. Moreover, we investigate the span of values in all the time series. This is important in power systems because day-ahead schedules generated by the new scenario set should be robust to all the possible realizations in the original scenario set. Here, we only show the spans visually, and additional analysis is conducted later.

Cosine distance is a similarity metric widely used to evaluate how similar two time series are. Mathematically, it measures the cosine of the angle between two vectors projected on a multi-dimensional space. For two time series \mathbf{s}^n and \mathbf{c}^k , the cosine distance between them is given by

$$D_c(\mathbf{s}^n, \mathbf{c}^k) = 1 - \frac{\mathbf{s}^n \cdot \mathbf{c}^k}{\|\mathbf{s}^n\|_2 \|\mathbf{c}^k\|_2}, \quad (2.66)$$

where $\mathbf{s}^n \cdot \mathbf{c}^k$ is the dot product of \mathbf{s}^n and \mathbf{c}^k . To factor in probabilities, we consider a score representing the expected cosine distance between the preserved and original scenario sets, which leads to

$$S_c(\mathbf{s}, \mathbf{c}) = \sum_{k=1}^K P^k \sum_{n=1}^N \frac{1}{N} D_c(\mathbf{s}^n, \mathbf{c}^k). \quad (2.67)$$

The scores of all the cases are reported in Table 2.9. Two vectors that are aligned in the same orientation will have a cosine distance measurement of 0. The scores of all the method are not close to 0 because the number of scenarios is dramatically reduced and the patterns in the original scenario set are different. However, the MAFC outperforms all the other methods

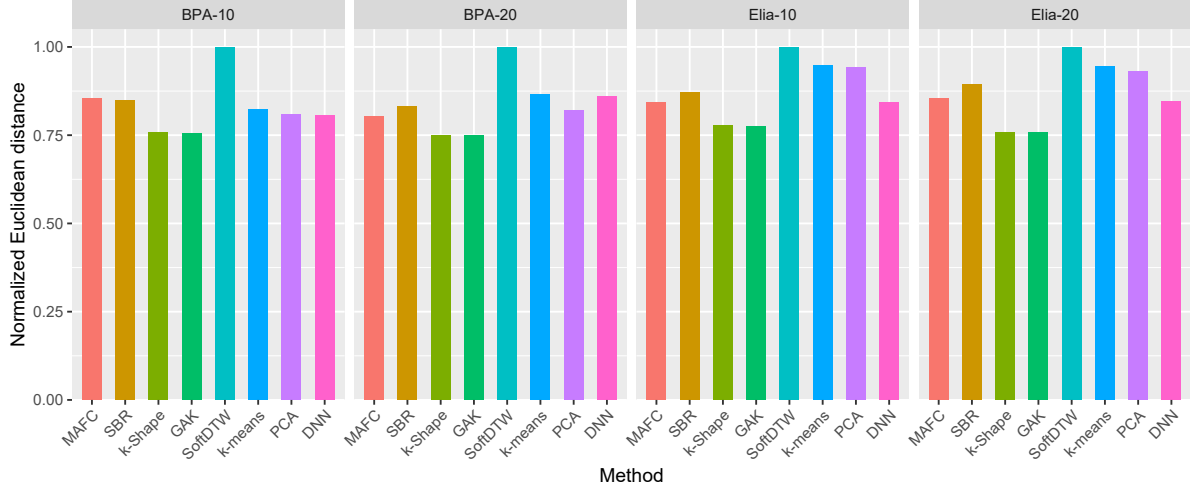


Figure 2.28: Comparison of methods for the scenario reduction using the Euclidean distance score.

in all the four cases, indicating the advantage in preserving scenarios with similar temporal correlations. The cosine distances of scenarios produced by the MAFC are slightly lower than 0.9. We also observe that, for a given data set, each method shows similar performance under different numbers of preserved scenarios. Moreover, the results of PCA and k -means indicate that the latent representation can give a better similarity. The scores of MAFC and DNN show that fuzzy clustering can better capture the complex patterns.

We are interested in behavior matching when finishing scenario reduction for renewable energy scenarios, especially for a system that routinely sees large fluctuations. There are many time-coupling constraints in a power system, for example, the minimum downtime. With correlations among each time-series in consideration, day-ahead schedules will be more robust and cost efficient for realizations.

On the other hand, cosine similarity only gives the similarity and ignores the Euclidean distance. The cost of realizations of intra-hour operation on the next day is associated with the deviation (in Euclidean space) between two scenario sets. In other words, we do not want a preserved scenario set that sacrifices Euclidean distance for cosine similarity. Therefore, we also examine the (probability) distance between two scenario sets. The metric in consideration is given by

$$S_e(\mathbf{s}, \mathbf{c}) = \sum_{k=1}^K P^k \sum_{n=1}^N \frac{1}{N} \|\mathbf{s}^n - \mathbf{c}^k\|_2^2. \quad (2.68)$$

Euclidean scores of all the cases are shown in Fig. 2.28. We observe that the scores of the MAFC are close to the minimum scores, and it does not sacrifice the performance in Euclidean space. Despite the numerous advantages of such probability metrics, it is not efficient in describing the consequence of very adverse scenarios. Due to small probabilities for those

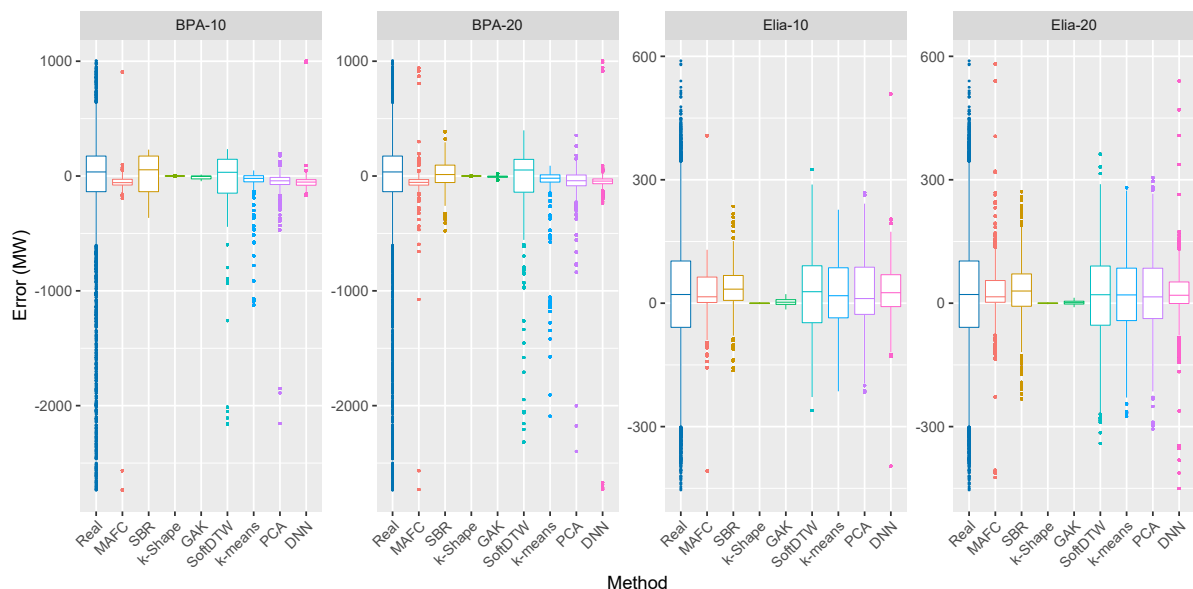


Figure 2.29: Box plots of values in scenarios generated by different methods for the scenario reduction, compared with the realized values in the original scenario set.

events, their impacts on (2.68) are eliminated.

To investigate the performance of scenario reduction techniques in extreme events, we graphically depict quartiles of values in all the time series. The results are shown in Fig. 2.29. Intuitively, more preserved scenarios give a better performance. If K is larger, the preserved scenario set tends to be the original set. Therefore, box plots associated with 20 scenarios are more similar to the box plot of real scenarios. Moreover, all the scenario reduction methods can generate a scenario set with values that match the majorities of those in the original scenario set. It coincides with the fact that all the Euclidean scores are close, as shown in Fig. 2.28. However, the box plots show the advantage of the MAFC in avoiding large loss of load in the next-day operations, i.e., the MAFC includes more extreme values. The day-ahead schedules obtained by the MAFC are expected to increase the robustness of the system, and better control the risks in realizations that are with high load shedding penalties but low probabilities.

Again, we use Energy score and Brier score to perform multivariate verification of scenarios and diagnose the preserved events in the new scenario set. The normalized Energy score is shown in Fig. 2.30. We observe that scenarios generated by the MAFC are superior when the number of scenarios in the preserved set is 10, while scenarios are slightly poorer than those produced by the DNN when the number is 20. The intuition behind the Energy score is to generate diverse yet representative scenarios. The first term is associated with the deviation from the expectation, and all the methods should give similar performance. However, our method shows more viability and improves the score by the second term.

The multivariate approach to forecast verification may permit to discriminate among various sets of trajectories, though it does not inform of their ability to mimic specific characteristics

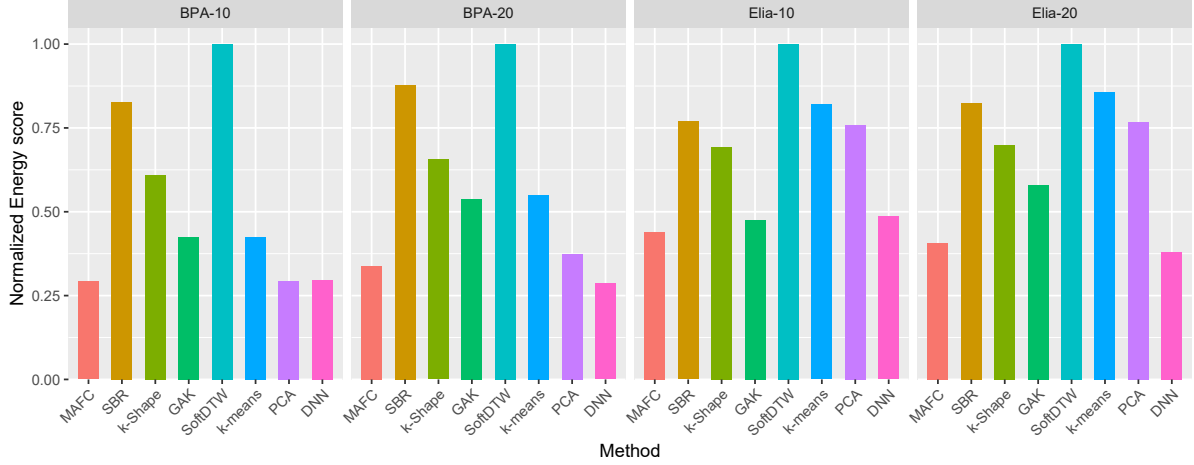


Figure 2.30: Comparison of methods for the scenario reduction using the Energy score.

of the stochastic process. It motivates us to adopt the Brier score, an event-based approach, which evaluates the performance of scenarios under a predefined event. The Brier score is also proper and negatively oriented. Let \mathcal{E} represent a predefined event, and the function $g_t(\mathbf{s}^n, \mathcal{E})$ indicate whether the event occurs in time slot t , in the scenario \mathbf{s}^n . The Brier score is defined as

$$S_B = \sum_{t=1}^T \left[\sum_{n=1}^N \frac{1}{N} g_t(\mathbf{s}^n, \mathcal{E}) - \sum_{k=1}^K P^k g_t(\mathbf{c}^k, \mathcal{E}) \right]^2. \quad (2.69)$$

The Brier score depends on the selection of events. In the context of day-ahead scheduling, extreme events will result in significant financial losses. Let $\mathbb{E}_t(\mathbf{s})$ and $\sigma_t(\mathbf{s})$ be the expected value and standard deviation in time slot t , in the scenario set \mathbf{s} . We define the first event \mathcal{E}_1 and its corresponding indicator function as follows:

$$g_t(\mathbf{s}^n, \mathcal{E}_1) = \begin{cases} 1, & \text{if } \mathbf{s}_t^n \notin [\mathbb{E}_t(\mathbf{s}) - \xi\sigma_t(\mathbf{s}), \mathbb{E}_t(\mathbf{s}) + \xi\sigma_t(\mathbf{s})], \\ 0, & \text{if } \mathbf{s}_t^n \in [\mathbb{E}_t(\mathbf{s}) - \xi\sigma_t(\mathbf{s}), \mathbb{E}_t(\mathbf{s}) + \xi\sigma_t(\mathbf{s})], \end{cases} \quad (2.70)$$

where ξ is a user-defined constant. For the BPA and Elia test cases, we set it to 1.86 and 1.96, respectively. The two values are selected by making $\mathbf{s}_t^n \in [\mathbb{E}_t(\mathbf{s}) - \xi\sigma_t(\mathbf{s}), \mathbb{E}_t(\mathbf{s}) + \xi\sigma_t(\mathbf{s})]$ with average probability 95%. Since we can curtail renewable generation at low costs, we are more interested in events associated with negative forecasting errors, i.e., realized generations are lower than forecasts, when generating scenarios of forecasting errors. Let \bar{R} be the capacity of renewable source. We consider the second event \mathcal{E}_2 where the sum of forecasts in four consecutive hours is lower than a threshold with respect to \bar{R} . The indicator function is defined as

$$g_t(\mathbf{s}^n, \mathcal{E}_2) = \begin{cases} 1, & \text{if } \sum_{i=0}^3 \mathbf{s}_{t+i}^n \leq -\xi\bar{R}, \\ 0, & \text{otherwise.} \end{cases} \quad (2.71)$$

Table 2.10: Comparison of Methods for the Scenario Reduction Using the Brier Score.

Event	Method	BPA-10	BPA-20	Elia-10	Elia-20
\mathcal{E}_1	MAFC	0.053	0.048	0.055	0.038
	SBR	0.063	0.063	0.060	0.058
	k -Shape	0.063	0.063	0.060	0.060
	GAK	0.063	0.063	0.060	0.060
	SoftDTW	0.065	0.038	0.063	0.022
	k -means	0.049	0.031	0.060	0.051
	PCA	0.060	0.057	0.060	0.054
	DNN	0.077	0.043	0.055	0.041
\mathcal{E}_2	MAFC	0.038	0.036	0.041	0.027
	SBR	0.053	0.053	0.060	0.044
	k -Shape	0.053	0.053	0.060	0.060
	GAK	0.053	0.053	0.060	0.060
	SoftDTW	0.063	0.031	0.047	0.014
	k -means	0.053	0.028	0.035	0.019
	PCA	0.043	0.041	0.030	0.005
	DNN	0.053	0.027	0.053	0.035

Again, to make the average probability of $\sum_{i=0}^3 \mathbf{s}_{t+i}^n \leq -\xi \bar{R}$ to be 5%, we set ξ to 0.32 and 0.2 for the BPA and Elia test cases, respectively. The Brier scores of both events for different methods are listed in Table 2.10. There exists no method that outperforms all the other methods for all the cases. However, we observe that deep learning based models (i.e., MAFC and DNN) and k -means based models (i.e., k -means and PCA) give better results. Scenarios produced by SBR, GAK, and k -Shape barely exhibit hallmark characteristics of renewable generation profiles, and the predefined events will not happen in the preserved sets. Therefore, their Brier scores are close to $T \times (5\%)^2$. Moreover, we observe that the more preserved scenarios, the better Brier scores. For example, the Brier scores of the MAFC are reduced from 0.053 in BPA-10 to 0.048 in BPA-20. All the Brier scores of the MAFC are lower than 0.06 (i.e., $24 \times (5\%)^2$), which indicates that scenarios maintained by the MAFC can capture some extreme events in the original scenarios, though the scores are not the best in some cases.

We report the computational time of every method in Table 2.11. The time includes both training and inference time. The results show that computational time is not an issue for the MAFC which adopts a deep learning structure. The MAFC generates a preserved scenario set in an acceptable time range. Computational efficiency is not addressed. From the perspective of system operators, the level of risk is more crucial. Since scenario reduction is used for day-ahead scheduling in our context, 362.8 seconds is considered as a reasonable value.

Table 2.11: Computational Time of Scenario Reduction Methods.

Method	MAFC	SBR	k -Shape	GAK	SoftDTW	k -means	PCA	DNN
Time (sec)	362.8	856.1	62.9	559.0	220.6	1.23	1.79	284.2

Empirical Analysis

Modern power systems are the largest man-made systems which involve complex physical constraints. Statistical analysis may not sufficiently characterize the error that arises from using a smaller set of scenarios to approximate the original set. Here, we also conduct an empirical study of a day-ahead unit commitment problem, to investigate the quality of the scenario reduction techniques.

We adopt two empirical criteria from [128], the objective error and the policy error. Let \mathbf{x} collect the decision variables and $f(\mathbf{x}; \mathcal{S})$ denote the objective function of the constrained optimization problem under scenario set \mathcal{S} . The objective error measures the difference in objective values:

$$e_o(\mathcal{S}, \mathcal{C}) = \left\| 1 - \frac{\max_{\mathbf{x}} f(\mathbf{x}; \mathcal{C})}{\max_{\mathbf{x}} f(\mathbf{x}; \mathcal{S})} \right\|, \quad (2.72)$$

whereas the policy error implies the error that is made when applying the decisions obtained by \mathcal{C} to the problem under \mathcal{S} :

$$e_p(\mathcal{S}, \mathcal{C}) = \left\| 1 - \frac{f(\arg \max_{\mathbf{x}} f(\mathbf{x}; \mathcal{C}); \mathcal{S})}{\max_{\mathbf{x}} f(\mathbf{x}; \mathcal{S})} \right\|. \quad (2.73)$$

There is no unit for both errors. The objective error measures the deviation between the objective value optimized by the preserved set and that obtained by the original set. This score examines the quality of scenario reduction techniques, in terms of succeeding in producing similar expectations. However, two decision sets are not necessarily the same even the two sets produce the same objective values. It motivates the use of policy error. A policy error of 0 implies that the preserved set can perfectly characterize the original set. In the intra-hour operation phase, the policy optimized by the preserved set can give identical costs, compared with the costs of the policy scheduled by the original set.

We also use a 24-bus reliability test system as our testing network. We normalize the aggregated wind generation of all the scenarios to $[0, 1]$ and consider the values to be the percentages of the total capacity. The expected percentage in the original scenario set \mathcal{S} is 58.6%. Six wind farms are included, and each has a capacity of 400 MW. In this work, we consider three blocks of load shedding. They can be implemented at low, medium, and high penalties with different capacities. An illustration of the scheme is given in Table 2.12, and the shedding percentage is with respect to the load at each bus.

Since the measures involve the specific optimization problem, we give the standard model of the stochastic unit commitment problem, which is formulated as a two-stage mixed integer

Table 2.12: Illustration of Load Shedding Blocks Used in the Empirical Analysis.

Shedding percentage	0-10%	10%-50%	50%-100%
Penalty (\$/MWh)	50	200	5000

linear program:

$$\min \sum_t \sum_{g \in \mathcal{G}} (C_g^{\text{NL}} u_{g,t} + C_g^{\text{SU}} y_{g,t} + C_g^{\text{SD}} z_{g,t}) + \sum_{s \in \mathcal{S}} p_s \sum_t \left(\sum_{g \in \mathcal{G}} C_g P_{g,t,s} + \pi^b \sum_{l \in \mathcal{L}} \Delta D_{l,t,s}^b \right) \quad (2.74a)$$

$$\text{s.t.} \quad y_{g,t} - z_{g,t} = u_{g,t} - u_{g,t-1}, \forall g, t, \quad (2.74b)$$

$$y_{g,t} + z_{g,t} \leq 1, \forall g, t, \quad (2.74c)$$

$$\sum_{\tau=t-UT_g+1}^t y_{g,\tau} \leq y_{g,t}, \forall t \geq UT_g, \quad (2.74d)$$

$$\sum_{\tau=t-DT_g+1}^t z_{g,\tau} \leq 1 - y_{g,t}, \forall t \geq DT_g, \quad (2.74e)$$

$$P_g^{\min} u_{g,t} \leq P_{g,t,s} \leq P_g^{\max} u_{g,t}, \forall g, t, s, \quad (2.74f)$$

$$RD_g \leq P_{g,t,s} - P_{g,t-1,s} \leq RU_g, \forall g, t, s, \quad (2.74g)$$

$$\begin{aligned} & \sum_{s \in \mathcal{W}} W_{w,t,s} + \sum_{g \in \mathcal{G}} P_{g,t,s} + \sum_{l \in \mathcal{L}} \Delta D_{l,t,s}^b \\ &= \sum_{l \in \mathcal{L}} D_{l,t,s} + \sum_{s \in \mathcal{W}} \Delta W_{w,t,s}, \forall t, s, b, \end{aligned} \quad (2.74h)$$

$$-\mathbf{PF}^{\max} \leq \mathbf{PTDF} \times \mathbf{I} \leq \mathbf{PF}^{\max}, \quad (2.74i)$$

$$\Delta W_{w,t,s} \leq \Delta W_{w,t,s}^{\max}, \forall w, t, s, \quad (2.74j)$$

$$\Delta D_{l,t,s}^b \leq \Delta D_{l,t,s}^{b,\max}, \forall l, t, s, b, \quad (2.74k)$$

where T is the scheduling time horizon; \mathcal{G} , \mathcal{L} , \mathcal{W} , and \mathcal{S} are the set of generating units, loads, wind farms, and scenarios, respectively; p_s denotes the probability of scenario s ; C_g^{NL} , C_g^{SU} , C_g^{SD} , C_g , and π^b denote the no-load cost, start-up cost, shut-down cost, offer price, and load shedding penalty of shedding block $b \in \mathcal{B}$, respectively; u , y , and z are binary variables, representing on/off status and start-up/shut-down signals; P is the power of generating unit, ΔD^b is the quantity of load shedding, W is the wind generation, and ΔW is the wind curtailment; UT and DT are the minimum up and down time; \mathbf{PF}^{\max} , \mathbf{PTDF} , and \mathbf{I} are the matrices of line capacity, power transfer distribution factor, and bus power injection, respectively. The maximum wind curtailment $\Delta W_{w,t,s}^{\max}$ is set to be the wind generation $W_{w,t,s}$.

Let \mathbf{x} and \mathbf{y} be the vectors of the first and second stage decisions, where \mathbf{x} includes all the binary variables in (2.74). In the first stage, we adopt the practice of the New York Independent

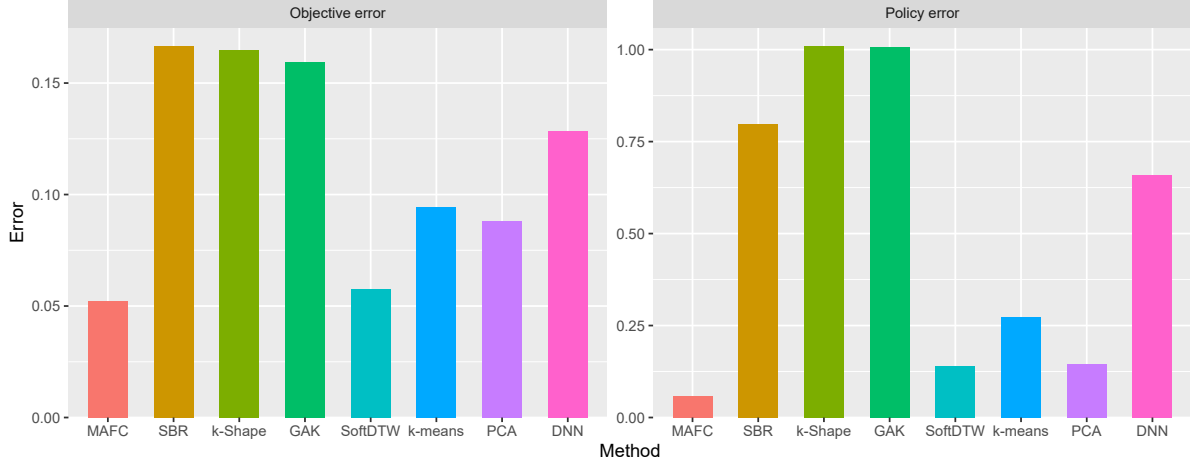


Figure 2.31: Comparison of different methods for the scenario reduction, in terms of the objective error and the policy error.

System Operator (NYISO), and apply a large penalty cost to load shedding [129]. Penalties of all the shedding blocks are set to \$5000/MW. In the second stage, the constraints are relaxed and we follow the three-block scheme as in Table 2.12. Note that we need to solve a set of optimal power flow problems when evaluating the policy error (2.73). That is, we first solve (2.74) using \mathcal{C} , then fix \mathbf{x}^* , and complete the realized dispatch for each $\mathbf{s}^n \in \mathcal{S}$.

The problem $\max_{\mathbf{x}} f(\mathbf{x}; \mathcal{S})$ is also solved by the extensive form in CPLEX. It takes 25 hours to finish and highlights the need of scenario reduction techniques. Here, we only consider BPA-10, and two scores are reported in Fig. 2.31. Regarding the objective error, it highly depends on the values of wind generation in the new scenario set. As shown in Figs. 2.28 and 2.29, all the methods reach fairly good performance. Therefore, all the objective errors are close to zero, but among which the MAFC gives the lowest error. On the other hand, the policy error measures the quality of the optimal decisions generated by the preserved set. Methods with lower cosine distances in Table 2.9 capture the inherent patterns better, and lead to comparably better solutions. One special case is GAK, whose performance is severely exacerbated by the lack of robustness. Moreover, we observe that the extreme events play a crucial role in determining the two errors, since there is no huge difference between the distances in Euclidean space. SoftDTW, k -means, PCA and DNN perform well in Fig. 2.29, and hence their performances are close to that of MAFC. The MAFC outperforms all the other methods and gives the lowest error, in terms of both measures. It highlights the ineffectiveness of the existing scenario reduction techniques targeting at minimizing probability distance. PCA is used to project the 24-hour features to a lower dimensional space, but the clustering task is also finished by k -means. By comparing the results of k -means and PCA, we find that clustering based on latent representations generates a better preserved scenario set, which could be a reason of better performance of the MAFC.

The operational costs are different under different realizations. It follows from the fact that

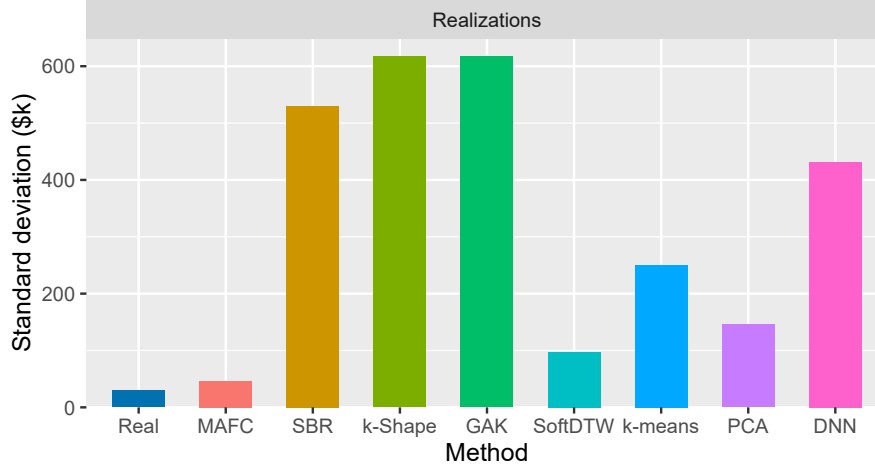


Figure 2.32: Comparison of the original scenario set and the preserved scenario sets generated by scenario reduction methods, in terms of the standard deviation of the realized cost.

wind generation in each scenario is non-identical. However, large penalties are applied in case large violations happen. We investigate the standard deviations of the realized costs for different methods. It can be interpreted as the risk of loss-of-load. The results are shown in Fig. 2.32. The MAFC method generates robust schedules that avoid load shedding and are close to the optimal schedules produced by the original scenario set. It shows the superiority of adding fuzziness by comparing the results of MAFC and DNN.

A perfect preserved scenario set should yield schedules that are exactly the same with those optimized by the original set. Let the number of different solutions optimized by \mathcal{C} and \mathcal{S} be $Z(\mathcal{S}, \mathcal{C})$, and the total number of decisions be Z' . We investigate the discrepancy between the decision sets generated by different methods and refer to this measure as policy stability. It is mathematically defined by

$$e_s(\mathcal{S}, \mathcal{C}) = 1 - \frac{Z(\mathcal{S}, \mathcal{C})}{Z'}. \quad (2.75)$$

Note that this measure is relevant given the large number of binary variables. The policy stability for each method is listed in Table 2.13. Amongst the six methods, the MAFC gives the highest policy stability. Moreover, the table reveals that the policy stability of MAFC, SoftDTW, k -means, and PCA are close, whereas those of SBR, GAK, k -Shape, DNN are similar. The observation coincides with the facts regarding the objective error, the policy error, and the standard deviation of the realized cost. Also, it shows that preserved scenarios using the MAFC can characterize original scenarios. Two scenario sets lead to almost identical schedules.

The penalty of load shedding has a huge impact on the realized cost. We also test the preserved scenario sets using different penalties. One block structure is adopted, where load shedding penalty is set to \$100/MWh, \$200/MWh, \$500/MWh, and \$2000/MWh, respectively.

Table 2.13: Comparison of Methods for the Scenario Reduction Using the Policy Stability.

Method	MAFC	SBR	k -Shape	GAK	SoftDTW	k -means	PCA	DNN
Stability (%)	98.8	94.4	94.6	94.8	97.9	97.7	97.8	95.3

Table 2.14: Comparison of Realized Costs under Different Penalties for the Scenario Reduction.

Penalties	100 (\$k)	200 (\$k)	500 (\$k)	2000 (\$k)
MAFC	178.1	188.1	219.4	369.2
SBR	188.4	222.7	325.7	840.8
k -Shape	195.3	237.8	365.2	1002
GAK	193.5	234.2	356.2	966.3
SoftDTW	187.4	195.7	223.7	345.4
k -means	176.8	193.0	241.9	485.9
PCA	175.3	188.5	228.0	425.3
DNN	184.1	215.2	308.6	775.2

The realized costs are summarized in Table 2.14. When the penalty is \$100/MWh and close to the fuel cost of conventional units, the realized costs of all the methods are similar. When the load shedding penalty is moderate, i.e., \$200/MWh and \$500/MWh, the realized cost of the MAFC shows superiority because the generated scenario set includes more adverse realizations. For other realizations with negative forecasting errors, the quantity of load shedding is not large, and will not increase the realized cost dramatically. However, when the penalty is very high, say, higher than \$2000/MWh, the realizations with negative forecasting errors play an important role in determining the realized costs, though the quantity of load shedding is still small. Therefore, SoftDTW gives the best realized cost, which aligns with the fact in Fig. 2.29 that majority of scenarios produced by SoftDTW are with negative forecasting errors. Energy imbalance can be compensated by reserves and demand response in modern power grid. In this regard, moderate penalty should be the most practical setting, and the MAFC can bring more financial benefits.

The previous analysis assumes that the original scenario set acts as the potential realizations on the next day. The preserved set is obtained based on the original scenario set as well. Therefore, it is necessary to validate the preserved set on other possible realizations to ensure generalization capability. We generate four new scenario sets and consider them as possible realizations. The numbers of scenarios in the four sets are 100, 200, 500, and 1000, respectively. The realized costs are shown in Fig. 2.33. We observe that the MAFC gives the lowest realized costs in all the test sets, which indicates that the new scenario set preserved by the MAFC has good generalization and the performance is guaranteed over all the possible realizations of uncertainties.

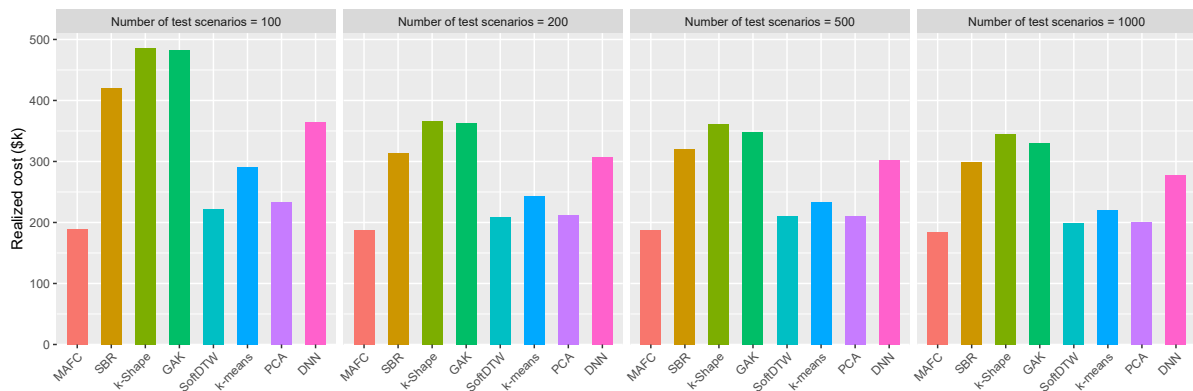


Figure 2.33: Comparison of the performance of different methods for the scenario reduction on four new scenario sets, in terms of the realized cost.

Table 2.15: Comparison of Different Selections of the Number of Preserved Scenarios.

K	3	5	10	20	50	100
Cost (\$k)	337.3	326.3	219.4	218.0	205.3	203.9
Time (sec)	2.750	4.499	10.05	21.68	99.35	292.5

It is worth investigating how to choose the number of scenarios K in the new scenario set. For a large power system, a large K may make the day-ahead scheduling problem too difficult to solve. On the other hand, if a small K is used, new scenarios may not capture the characteristic of possible evolution. For the 24-bus system, we evaluate some sets with different K , in terms of CPU time for solving unit commitment and realized costs. The load shedding penalty is set to \$500/MWh, and the results are listed in Table 2.15. We observe that when K reaches 10, the decrease in realized costs becomes small, while the CPU time increase about 30 times from $K = 10$ to $K = 100$. It is difficult to determine the optimal value of K . For a given system, one should make a trade-off based on the complexity of the system in consideration.

2.5 Conclusion and Discussion

To reduce uncertainty in the future power systems with high renewable penetration, the most intuitive way is to improve the forecasting techniques. Theoretically speaking, if accurate predictions are available, the uncertainty will be eliminated, and the optimal solution of power system scheduling and planning is associated with the deterministic realization. In other words, deterministic optimization can be used instead of applying intractable stochastic programs, and hence, integer variables (i.e., non-convexity) are trivial. Although accurate predictions are not available in general, it is still worth investigating better algorithms for the forecasting. Motivated by this, recent advances in deep learning are leveraged to perform short-term forecasting of renewable and net loads.

An attention temporal convolutional network is presented. The architecture is developed for the ultra-short-term spatio-temporal forecasting of renewable resources. It is verified on the wind speed and solar generation forecasting. Case studies reveal that predictions generated by the proposed method outperform those forecasted by the baselines, in terms of skill scores. With the use of convex combinations coupled with attention mechanisms, we can understand what is happening in the layers that are close to the output layer. The model needs no domain knowledge or feature selection, and hence, is general enough.

We observe that the time series predicted by the proposed structure cannot follow intra-minute ramping events accurately. For example, the intra-minute fluctuations of solar generation cannot be captured completely. It is a major drawback of this work since predictions made by the ATCN may complicate some tasks such as the voltage regulation. In future works, I will try to improve the capability of event following. Additionally, we still cannot understand what spatial and temporal signals are extracted by stacked dilated convolutional layers. For the renewable forecasting, the predictions will be used for the power system operation and are directly linked with potential financial losses. An understandable feature extraction that coincides with expert knowledge may be more reliable and well-founded. It is also worth investigating an interpretable feature extraction. Another limitation of this work is that the model is based on the assumption for the existence of correlations between geographically distributed time series. If the assumption does not hold, the performance will be deteriorated. Regarding the renewable forecasting, it is not always true, especially when the sites are located distantly.

The assumption of the existence of spatial correlations usually is not true in the case of net-load forecasting. It is not necessary for the net loads in different forecast zones to be spatially correlated. That being said, we still want to utilize off-site information. We propose a graph transformer network, wherein time series of each zone are processed individually. The graph transformer network can produce point predictions, quantiles, intervals, and scenarios. Predictions made by the model show state-of-the-art performance. Similarly, the model is general enough and can be used for different forecasting tasks. For example, forecasting of wind generation/speed and solar generation/irradiance. It allows feature selection for a complete graph, which is more appropriate for the forecasting tasks in power systems. Transformers in the GTrans ensure long-range persistence. However, the attention mechanisms still cannot be explained well, i.e., what information each head extracts.

Given the fact that perfect predictions are not obtainable, decision making under uncertainty is important. The performance of most of the methods, such as stochastic programming and robust optimization, highly relies on the uncertainty representations used. It motivates us to consider scenario generation, which generates scenarios that can be regarded as a set of potential realizations. Scenario generation is an important step for the day-ahead scheduling such as stochastic unit commitment, dynamic economic dispatch, or day-ahead trading of renewable generation. In this context, scenarios with high quality are desired. However, limited literature to date addresses this topic.

A scenario generation method is developed in this dissertation. The model, sequence generative adversarial network, uses the concept of generative adversarial networks coupled with reinforcement learning to guide the learning process of long short-term memory cells. It takes the advantage of long short-term memory cells to capture the complex temporal dynamics of weather. To jointly consider the fitness of each time slot and its future impact, Monte Carlo search is adopted to approximate the future impact. In contrast to the existing supervised methods, our model does not require any selection of features. Moreover, it is not prone to overfitting and misidentification of the patterns compared with the conventional time series models. The case studies show that the scenarios generated by our model can better characterize the variability of wind power when compared with those produced by Gaussian distribution, vanilla LSTM, and multivariate kernel density estimation. In future work, I will incorporate the spatial correlation which can be used by large scale systems and apply it to the decision-making process. Furthermore, I will extend the study to generate the long-term scenarios that can be used for expansion planning.

In some case, scenarios are already available, but the number of scenarios is large. In addition, some scenario generation methods cannot control the number of generated scenarios with guaranteed performance due to the law of large numbers. Many optimization problems in power systems include integer variables (i.e., non-convexities). If the number of scenarios is too large, the problem becomes intractable. In this regard, scenario reduction that reduces the number of scenarios yet without deteriorating the quality of scenarios is desired.

A mixed autoencoder based time-series clustering architecture is presented in this dissertation. The architecture is used to perform scenario reduction for stochastic scheduling. The model considers the scenario reduction problem as a time-series clustering task. Therefore, the new scenario set produced by the MAFC gives a better time-series similarity, without ceding the accuracy in Euclidean space. The results of a day-ahead unit commitment problem show that the scenarios generated by the proposed model outperform those produced by other methods and imply that the method provides quite a few practical economic values to system operators. However, we observe that the vanilla mixed autoencoders model also performs well when the number of preserved scenarios is large and the original scenarios do not show many fluctuations. The drawback is that the model only considers renewable energy. It is also worth extending the work to incorporate scenario reduction for multivariate time series such as correlated time series of renewable and load.

CHAPTER

3

INTEGRATED GAS AND POWER SYSTEMS

The large shift in electric generating resources with ongoing retirements of coal-fired and nuclear capacity coupled with growth in natural gas, wind, and solar resources brings new challenges to the power system planning, operation, and economics. This trend of high share of renewable energy requires more flexibility to follow the unpredictable variations, both in loads and renewable energy sources. In order to follow the realizations of uncertainties in real time, system operators use operating reserves, which are usually scheduled through the unit commitment. Nowadays, gas-fired units are widely used not only for the generation but also for the operating reserves because of the low natural gas price, and their fast start-up flexibility and ramp rates. The operational constraints and uncertainties in the gas network have a huge impact on the power system operation and economics. For example, when one pipeline suffers a contingency, it will influence the generation of gas-fired units. With the goal of developing renewable based energy systems, the integration of power and gas systems becomes necessary to realize efficient and secure operation of future energy systems. On the other hand, as the reliance on natural gas to meet electric generation requirements increases, additional planning measures and risks must be considered to better understand the implications of the complex interdependency between the natural gas system and the power system.

Moreover, the rapid development of power-to-gas (P2G) technology is promoting the integration of renewable energy and makes coupling between the power and gas systems deeper. P2G starts with converting electricity to hydrogen through water electrolysis, and it can further react with carbon dioxide that is captured from air to produce synthetic natural gas.

Due to the intermittent nature of renewable energy, curtailment happens in systems with high share of renewable energy. For example, this happens when solar power peaks during the day in California, or at night when wind power is greatest in Midwest. While those curtailments do not cause reliability issues, flexible balancing tools such as utility-scale energy storage are needed to increase renewable utilization. The combination of gas-fired units and P2G can act as storage and serve as a potential solution to renewable curtailment. Moreover, by means of the rapid response of polymer electrolyte membrane electrolysis, P2G can also offer auxiliary and regulatory power services of high value. In addition, P2G converts electricity to natural gas, and P2G can be regarded as an option of long-term storage since the natural gas can be easily stored. Due to the seasonal characteristic of renewable energy and load, P2G can absorb excess renewable generation in peak seasons, which can then be supplied to meet natural gas loads or stored to serve electric load in off-peak seasons using gas-fired generators.

In this chapter, we first propose an expansion co-planning model for integrated energy systems (IESs) where uncertainties in both systems are considered. A scenario based decomposition scheme called branch-and-price is presented to handle ample integer variables in the planning model. We then study transmission contingency-constrained unit commitment (CCUC) of an IES. Uncertainties both in contingencies and net loads are modeled by interval numbers, which reduces the computational burden compared with other uncertainty representations. We incorporate the risk preferences of decision makers in the framework to alleviate the conservativeness of solutions.

3.1 Multistage Stochastic Co-planning of Integrated Energy Systems

In this dissertation, we address two limitations of the existing works for the IES expansion planning. First, we consider the potential contribution of IES in some worldwide societal goals such as decarbonized economy and 100% renewable penetration. Second, the selection of scenarios is discussed. We adopt the multistage stochastic programming technique. The stochastic programming method encapsulates all possible realizations and hence is less conservative. Moreover, it allows the planner to make “wait-and-see” decisions. However, for a system on a large scale, the mixed integer program is difficult to solve. To make the problem tractable, we use branch-and-price algorithm.

3.1.1 Modeling Integrated Energy Systems Expansion Co-planning

The goal of IES expansion co-planning is to minimize the total investment and operation cost of IES over the planning periods T , while satisfying security constraints. The investment cost in consideration includes that of gas-fired generators, transmission lines, pipelines, and P2Gs. The operation cost consists of that of power and gas systems, in which the fuel cost of gas-fired generator is carried out by the total gas supply cost, and the carbon emission cost.

Let $g, l, p, t, st, a, i, b, c,$ and m be the index of generators, transmission lines, pipelines, years, stages, P2Gs, electric buses, load blocks, coupling buses, and gas nodes respectively. We have $1 \leq t \leq T$ and $1 \leq st \leq ST$. Let $\Omega_G^C, \Omega_G^E, \Omega_C^E, \Omega_L^C, \Omega_L^E, \Omega_P^C, \Omega_P^E, \Omega_A^C, \Omega_A^E, \mathcal{B}, \Omega_I, \Omega_M,$ and Ω_C be the set of candidate gas generators, existing gas generators, existing coal-fired generators, candidate transmission lines, existing transmission lines, candidate pipelines, existing pipelines, candidate P2Gs, existing P2Gs, load blocks, electric buses, gas nodes, and coupling buses, respectively. Let C^{inv} and DT be the investment cost of the corresponding candidate and the duration of load block. Let x be binary variables, representing the investment state. The objective function of IES expansion co-planning can be given by

$$\begin{aligned} \min \sum_{st=1}^{ST} \delta_{\mathbb{T}(st)} \left[\sum_{g \in \Omega_G^C} C_g^{\text{inv}} (x_{g,st} - x_{g,st-1}) + \sum_{l \in \Omega_L^C} C_l^{\text{inv}} (x_{l,st} - x_{l,st-1}) + \sum_{p \in \Omega_P^C} C_p^{\text{inv}} (x_{p,st} - x_{p,st-1}) \right. \\ \left. + \sum_{a \in \Omega_A^C} C_a^{\text{inv}} (x_{a,st} - x_{a,st-1}) \right] + \sum_{t=1}^T \delta_t \sum_{b \in \mathcal{B}} DT_{b,t} (EOC_{b,t} + GOC_{b,t} + COC_{b,t}), \quad (3.1) \end{aligned}$$

where δ_t and $\mathbb{T}(st)$ are the present value (i.e., discount factor) of year t and the first year in stage st , respectively.

The temporal variability of load and wind power is mainly due to meteorological fluctuations of seasons and hours of the day, we divided them into different load blocks. Let $f(\cdot)$ be the fuel cost function including carbon emission cost of coal-fired generators. P^{coal} and GL^S be the power of coal-fired generators and gas injection by gas supplies. The total operation cost follows as:

$$EOC_{b,t} = \sum_{i \in \Omega_I} f(P_{i,b,t}^{\text{coal}}), \quad (3.2)$$

$$GOC_{b,t} = \sum_{m \in \Omega_M} \pi_t^{\text{gas}} GL_{m,b,t}^S, \quad (3.3)$$

$$COC_{b,t} = \sum_{c \in \Omega_C} \pi_t^{\text{carbon}} (\epsilon_1 P_{c,b,t} - \epsilon_2 PT_{c,b,t}), \quad (3.4)$$

where π^{gas} and π^{carbon} are random variables, representing gas price and carbon emission price, respectively. ϵ_1 and ϵ_2 are carbon dioxide uncontrolled emission factors of gas-fired generator and the emission reduction factor of P2G. For the buses without coal-fired generator, we set $P_{i,b,t}^{\text{coal}} = 0$. For the nodes without gas supply, we set $GL_{m,b,t}^S = 0$. The fuel cost function is linearized. We use the average value $\epsilon_1 = 181$ kg/MWh, which is estimated by EIA. The CO_2 saving induced by P2G in kg/MWh is given by

$$\epsilon_2 = \frac{\text{molecular mass of } CO_2}{\text{molecular mass of } CH_4} \times \frac{1}{HHV_{CH_4}^{\text{mass}}}, \quad (3.5)$$

where $HHV_{CH_4}^{\text{mass}}$ is the higher heating value of methane with respect to its mass, taken as 0.0153. The resulting CO_2 emission reduction from production is $\epsilon_2 = 180$ kg/MWh.

The expansion co-planning model includes investments in generators, transmission lines, pipelines, and P2G. We use binary variables x 's to represent our decisions. Once a candidate is installed, we set its state x to be 1 for the remaining planning periods, which leads to the following constraints:

$$x_{g,st} \geq x_{g,st-1}, \forall g \in \Omega_G^C, \forall st, \quad (3.6)$$

$$x_{l,st} \geq x_{l,st-1}, \forall l \in \Omega_L^C, \forall st, \quad (3.7)$$

$$x_{p,st} \geq x_{p,st-1}, \forall p \in \Omega_P^C, \forall st, \quad (3.8)$$

$$x_{a,st} \geq x_{a,st-1}, \forall a \in \Omega_A^C, \forall st. \quad (3.9)$$

A large enough value M is used to make the constraint nonbinding, which leads to the following power flow constraints:

$$PL_{l,b,t} = B_l (\theta_{s(l),b,t} - \theta_{r(l),b,t}), \forall l \in \Omega_L^E, \forall b, t, \quad (3.10a)$$

$$- PL_l^{\max} \leq PL_{l,b,t} \leq PL_l^{\max}, \forall l \in \Omega_L^E, \forall b, t, \quad (3.10b)$$

$$- M(1 - x_{l,\mathbb{ST}(t)}) \leq PL_{l,b,t} - B_l (\theta_{s(l),b,t} - \theta_{r(l),b,t}) \leq M(1 - x_{l,\mathbb{ST}(t)}), \forall l \in \Omega_L^C, \forall b, t, \quad (3.10c)$$

$$- x_{l,\mathbb{ST}(t)} PL_l^{\max} \leq PL_{l,b,t} \leq x_{l,\mathbb{ST}(t)} PL_l^{\max}, \forall l \in \Omega_L^C, \forall b, t, \quad (3.10d)$$

where PL collects power flows in transmission lines with the maximum capacity PL^{\max} . Similarly, θ is the phase angle with the limits θ^{\min} and θ^{\max} . The function $\mathbb{ST}(t)$ returns the stage that year t belongs to.

Phase angle limits, capacities limits of generators, and capacities limits of P2G's are enforced by

$$\theta_i^{\min} \leq \theta_{i,b,t} \leq \theta_i^{\max}, \forall i \in \Omega_I, \forall b, t, \quad (3.11a)$$

$$P_g^{\min} \leq P_{g,b,t} \leq P_g^{\max}, \forall g \in \Omega_G^E \cup \Omega_G^C, \forall b, t, \quad (3.11b)$$

$$P_g^{\min} x_{g,\mathbb{ST}(t)} \leq P_{g,b,t} \leq P_g^{\max} x_{g,\mathbb{ST}(t)}, \forall g \in \Omega_G^C, \forall b, t, \quad (3.11c)$$

$$0 \leq PT_{a,b,t} \leq PT_a^{\max}, \forall a \in \Omega_A^E, \forall b, t, \quad (3.11d)$$

$$0 \leq PT_{a,b,t} \leq PT_a^{\max} x_{a,\mathbb{ST}(t)}, \forall a \in \Omega_A^C, \forall b, t. \quad (3.11e)$$

where PT is the power of P2Gs.

The nodal active power balance constraints are given by

$$P_{i,b,t} + P_{i,b,t}^{\text{wind}} - \sum_{s(l)=i} PL_{l,b,t} + \sum_{r(l)=i} PL_{l,b,t} = D_{i,b,t} + PT_{i,b,t} + \Delta P_{i,b,t}^{\text{wind}},$$

$$\forall i \in \Omega_I, \forall l \in \Omega_L^E \cup \Omega_L^C, \forall b, t, \quad (3.12)$$

where P^{wind} and D are random variables representing renewable generation and electric load. $P_{i,b,t}$ includes all the generation at bus i , i.e., both candidate and existing generators. $\Delta P_{i,b,t}^{\text{wind}}$

ensures that the renewable generation can be curtailed. $s(l)$ and $r(l)$ represent the sending and receiving buses of line l , respectively.

Regarding the gas system, we use the steady state model to describe constraints. The gas flow $GL_{m,b,t}^S$ from gas supply at node m is constrained by physical characteristics, which leads to

$$0 \leq GL_{m,b,t}^S \leq GL_m^{S,\max}, \forall m \in \Omega_M, \forall b, t. \quad (3.13)$$

We use Weymouth gas flow equations to represent the gas flow through each pipeline. The gas flows are modeled by

$$GL_{p,b,t}|GL_{p,b,t}| = \phi_p \left(\omega_{s(p),b,t}^2 - \omega_{r(p),b,t}^2 \right), \quad (3.14a)$$

$$-GL_p^{\max} \leq GL_{p,b,t} \leq GL_p^{\max}, \forall p \in \Omega_P^E, \forall b, t, \quad (3.14b)$$

$$-M(1 - x_{p,\text{ST}(t)}) \leq GL_{p,b,t}|GL_{p,b,t}| - C_p \left(\omega_{s(p),b,t}^2 - \omega_{r(p),b,t}^2 \right) \leq M(1 - x_{p,\text{ST}(t)}), \quad (3.14c)$$

$$-GL_p^{\max} x_{p,\text{ST}(t)} \leq GL_{p,b,t} \leq GL_p^{\max} x_{p,\text{ST}(t)}, p \in \Omega_P^C, \forall b, t, \quad (3.14d)$$

where GL is the gas flow in the pipeline, ω is the pressure at a gas node, and ϕ is coefficient that captures the characteristics of pipelines.

The nodal balance in gas systems describes that the gas injection equals the gas withdrawn including the compressor consumption τ_m at each node m , which is given by

$$\begin{aligned} GL_{m,b,t}^S + GT_{m,b,t} - \sum_{s(p)=m} GL_{p,b,t} + \sum_{r(p)=m} GL_{p,b,t} + GL_{m,b,t}^{\text{dis}} - GL_{m,b,t}^{\text{ch}} = \tau_{m,b,t} + D_{m,b,t}^{\text{gas}} \\ + GL_{g,b,t}, \forall m \in \Omega_M, \forall p \in \Omega_P^E \cup \Omega_P^C, \forall g \in \Omega_G^E \cup \Omega_G^C, \end{aligned} \quad (3.15)$$

where τ is the gas consumption by gas compressors, GT is the gas injected by P2Gs, and $GL_{m,b,t}^{\text{dis}}$ and $GL_{m,b,t}^{\text{ch}}$ are the discharging and charging rates of a gas storage. D^{gas} is a random variable, representing gas demand.

The state of charge SOC at each load block depends on the state of charge of the previous block, and if the block is the first block in year t , then it depends on the last block in year $t-1$. The model for gas storage is given by

$$0 \leq GL_{m,b,t}^{\text{dis}} \leq GL_m^{\text{dis},\max}, \forall m \in \Omega_M, \forall b, t, \quad (3.16a)$$

$$0 \leq GL_{m,b,t}^{\text{ch}} \leq GL_m^{\text{ch},\max}, \forall m \in \Omega_M, \forall b, t, \quad (3.16b)$$

$$SOC_{m,b,t} = SOC_{m,b-1,t} + \eta GL_{m,b,t}^{\text{ch}} - GL_{m,b,t}^{\text{dis}}/\eta, \forall m \in \Omega_M, \forall t, \forall b > 1 \quad (3.16c)$$

$$SOC_{m,1,t} = SOC_{m,|\mathcal{B}|,t-1} + \eta GL_{m,|\mathcal{B}|,t}^{\text{ch}} - GL_{m,|\mathcal{B}|,t}^{\text{dis}}/\eta, \forall m \in \Omega_M, \forall t, \forall b = 1, \quad (3.16d)$$

$$0 \leq SOC_{m,b,t} \leq SOC_{m,b,t}^{\max}, \quad (3.16e)$$

where $SOC_{m,b,t}$ is the state of charge of storage, in mcf, at bus m , in block b and year t .

The compressor is used to increase the pressures. The compression ratio is constrained by

the maximum compression ratio R , and some gases are consumed to increase pressure, which is modeled by

$$\omega_{m,b,t}^{\text{in}} \leq \omega_{m,b,t}^{\text{out}} \leq R_m \omega_{m,b,t}^{\text{in}}, \quad \forall m \in \Omega_M, \quad (3.17a)$$

$$H_{m,b,t} = E_m GL_{m,b,t}^C \left[\left(\frac{\omega_{m,b,t}^{\text{out}}}{\omega_{m,b,t}^{\text{in}}} \right) - 1 \right], \quad (3.17b)$$

$$\tau_{m,b,t} = \alpha_m + \beta_m H_{m,b,t} + \gamma_m H_{m,b,t}^2. \quad (3.17c)$$

where H is the heat rate of compressors, GL^C is the gas flow through compressors, and ω^{in} and ω^{out} are the pressures at the inlet and outlet of compressors. R , E , α , β , γ are constants, representing the maximum compression ratio and parameters of compressor, respectively.

Moreover, the pressure at each node needs to be bounded, which is given by

$$\omega_m^{\text{min}} \leq \omega_{m,b,t} \leq \omega_m^{\text{max}}, \quad \forall m \in \Omega_M, \quad \forall b, t. \quad (3.18)$$

It is obvious that the gas flow equations (3.14a) and (3.14c) are nonlinear. We use the incremental model to derive the piecewise linear approximation of gas flow equation [130]. Using $\Pi = \omega^2$ to replace the pressure squared, we have the new gas flow equation as follows:

$$GL_{p,b,t} |GL_{p,b,t}| = \phi_p (\Pi_{s(p),b,t} - \Pi_{r(p),b,t}). \quad (3.19)$$

Let \mathcal{Q} be the set of segments that are applied to linearize the left term, we introduce continuous variable κ_q and binary variable y_q for each segment $q \in \mathcal{Q}$. Continuous variables represent the length of each segment. Binary variables force that if a segment is chosen, all the other segments to its left must be chosen. The gas flow GL is approximated as:

$$GL = GL_1 + \sum_{q=1}^{|\mathcal{Q}|} (GL_{q+1} - GL_q) \kappa_q, \quad (3.20a)$$

$$\kappa_{q+1} \leq y_q, \quad y_q \leq \kappa_q, \quad \forall q \in \mathcal{Q} - 1, \quad (3.20b)$$

$$0 \leq \kappa_q \leq 1, \quad \forall q \in \mathcal{Q}. \quad (3.20c)$$

As for the nonlinear terms in (3.17), we adopt the method in [131]. We fit the gas consumption $\tau_{m,b,t}$ into polynomials of variables $GL_{m,b,t}^C$, $\omega_{m,b,t}^{\text{out}}$ and $\omega_{m,b,t}^{\text{in}}$ as the following equation:

$$\tau_{m,b,t} = \sigma_1 GL_{m,b,t}^C + \sigma_2 \omega_{m,b,t}^{\text{out}^2} + \sigma_3 \omega_{m,b,t}^{\text{in}^2} + \sigma_4 = \sigma_1 GL_{m,b,t}^C + \sigma_2 \Pi_{m,b,t}^{\text{out}} + \sigma_3 \Pi_{m,b,t}^{\text{in}} + \sigma_4. \quad (3.21)$$

We regard electric-driven compressors as electrical loads in the power system network. The power system and gas system are coupled by gas-fired generators and P2Gs. The model carries out the fuel cost of gas-fired generator by the cost of the gas supply. We use the higher heating

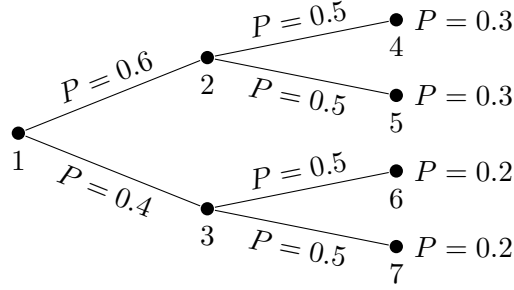


Figure 3.1: An example of scenario tree.

value of synthetic natural gas HHV_{SNG} , taken as 38.42 MJ/m^3 , to denote the conversion between electrical power flow and volumetric gas flow per hour, which leads to the two equations below:

$$GT_{a,b,t} = \eta^{\text{P2G}} PT_{a,b,t} / HHV_{\text{SNG}}, \forall a \in \Omega_A^E \cup \Omega_A^C, \quad (3.22a)$$

$$P_{g,b,t} = \eta^{\text{G2P}} GL_{g,b,t} HHV_{\text{SNG}}, \forall g \in \Omega_G^E \cup \Omega_G^C, \quad (3.22b)$$

where η^{P2G} and η^{G2P} are the efficiency of P2G and gas-fired generator, respectively.

3.1.2 Multistage Stochastic Program With Recourse

The investment strategies are subject to significant uncertainties. We consider the output of renewable, the increase of loads, gas price, and the emission cost of carbon as uncertainties. We assume that the increase of electric load and that of gas demand share perfect positive correlation, which reduces one random variable. We assume that the output of wind turbines follows a Weibull distribution, and others follow normal distribution. For numerical reasons, some methods should be applied to generate a discrete version of the underlying continuous distribution. The procedure of discretizing the continuous distribution is termed scenario generation. A scenario tree is a set of nodes and branches used in models of decision making under uncertainty. Every node in the tree represents a possible state of world at a particular time point and a position where a decision can be made [132]. The arcs represent realizations of uncertain variables. A path from the root node to a bottom node is defined as a multistage scenario, which describes a plausible realization of uncertainties over multiple horizons. Fig. 3.1 gives an example of three-stage scenario tree. There are four scenarios in this scenario tree. For example, path 1–2–4 is a scenario with probability 0.3. For each transition from any node to its successors, the realization follows the predefined distribution.

The Moment Matching Method for Scenario Generation

The moment matching method is a widely used method to generate scenarios. The idea of moment matching method is to match the statistical properties of generated scenarios with

those of the observed data process (underlying distribution). Following the notation presented by [133], define Γ as a set of statistical properties to be matched and Γ_i^{VAL} as the observed value of statistical property i from Γ . Let N be the number of random variables, T be the number of stages, Θ_t be the number of (conditional) outcomes in stage t , where $t \in \{1, \dots, T\}$. The tree in Fig. 3.1 has $T = 3$, $\Theta_1 = 1$, $\Theta_2 = 2$, and $\Theta_3 = 2$. Let \mathbf{y} be the outcome vector of dimension $N(\Theta_1 + \Theta_1\Theta_2 + \dots + \Theta_1\Theta_2\dots\Theta_T)$, \mathbf{p} be the probability vector of dimension $\Theta_1 + \Theta_1\Theta_2 + \dots + \Theta_1\Theta_2\dots\Theta_T$, and $f_i(\mathbf{y}, \mathbf{p})$ be the mathematical expression for statistical property i in Γ . We want to construct \mathbf{y} and \mathbf{p} so that the statistical properties of the discrete version match those of the underlying distribution. We can achieve this by solving the nonlinear and non-convex optimization problem:

$$\min_{\mathbf{y}, \mathbf{p}} \sum_{i \in \Gamma} (f_i(\mathbf{y}, \mathbf{p}) - \Gamma_i^{\text{VAL}})^2 \quad (3.23a)$$

$$\text{s.t.} \quad \mathbf{p}\mathbf{M} = 1, \quad (3.23b)$$

$$\mathbf{p} \succeq 0, \quad (3.23c)$$

where \mathbf{M} is a matrix of zeroes and ones, whose number of rows equals to the length of \mathbf{p} and number of columns equals to the number of nodes in the scenario tree. Each column in \mathbf{M} extracts a conditional realization of the underlying distribution. Since the optimization problem (3.23) is non-convex, the solution might be not globally optimal. We start with multiple start points and selected the solution with the smallest objective value. We enforce a lower bound for each probability to avoid peak realizations when we implement the process.

Selecting the Size of the Scenario Tree

Due to the exponential increase of computational complexity in the number of possible scenarios, multistage scenario generation approach places a greater emphasis on reducing the number of required samples. Moreover, too many scenarios may lead to over-specification. The number of scenarios generated by (3.23) depends on the number of stages as well as the number of statistical properties and outcomes in each stage. We fit the mean and variance of underlying distribution. While improved scenario trees may result from fitting more moments such as skewness and kurtosis, the authors of [134] indicate that the use of additional moment information provides minor improvement. Note that the number of uncertainties in consideration is 4. For all the outcomes of each node, we need to match 8 statistical properties. D probability-value pairs can match the first $2D - 1$ statistical properties exactly [135]. Hence, we set the number of outcomes of each node as 5.

Let us consider a 5-stage planning problem, the total number of scenarios is $5^4 = 625$, which may be too large for direct computation. To decrease the number of scenarios, we need to reduce its size. We are more interested in decisions now. Moreover, the current cost plays a more important role because of the discount factor. We can reduce the number of outcomes of

each node in future. For example, let $\Theta_2 = 5, \Theta_3 = 4, \Theta_4 = 3$, and $\Theta_5 = 2$, the total number of scenarios decreases to 120. To keep the problem tractable, we need to make a tradeoff between the size of scenario tree and the objective value in (3.23).

3.1.3 Multistage Stochastic Expansion Co-planning

The practical expansion planning problem involves a sequence of decisions that responds to outcomes that evolve over time. Given this insight, the two-stage stochastic programming method is not an appropriate one for the expansion planning problem since it fixes investment decisions. Let the decision horizon be $\mathcal{T} = \{1, \dots, |\mathcal{T}|\}$, we assume that the information is given by stochastic process $\{\xi_1, \dots, \xi_{|\mathcal{T}|}\}$. The decisions at each stage depend on all the previous decisions and outcomes of random variables, which allows the decision maker to make “wait-and-see” decisions. Let the vector of all decisions from stage 1 to stage t be $\tilde{\mathbf{x}}_t = \{\mathbf{x}_1, \dots, \mathbf{x}_t\}$ and the vector of random outcomes be $\tilde{\xi} = \{\xi_1, \dots, \xi_t\}$, a general multistage stochastic programming problem is given by

$$\begin{aligned} & \min \left\{ \mathbf{c}_1^\top(\xi_1)\mathbf{x}_1 + Q_1(\tilde{\mathbf{x}}_1) : \mathbf{W}_1\mathbf{x}_1 \leq h_1(\tilde{\xi}_1), \mathbf{x}_1 \in \mathbf{X}_1 \right\}, \\ Q_t(\tilde{\mathbf{x}}_t) &= \mathbb{E}_{\xi_{t+1}|\tilde{\xi}_t} \min \left\{ \mathbf{c}_{t+1}^\top(\xi_{t+1})\mathbf{x}_{t+1} + Q_{t+1}(\tilde{\mathbf{x}}_{t+1}) : \right. \\ & \quad \left. \mathbf{T}_{t+1}(\tilde{\xi}_{t+1})\tilde{\mathbf{x}}_t + \mathbf{W}_{t+1}\mathbf{x}_{t+1} \leq h_{t+1}(\tilde{\xi}_{t+1}), \mathbf{x}_{t+1} \in \mathbf{X}_{t+1} \right\}, \end{aligned} \quad (3.24)$$

where $t = 1, \dots, |\mathcal{T}| - 1$ with $Q_{|\mathcal{T}|+1} \equiv 0$. \mathbf{X}_t enforces the integrality requirement for some decision variables.

Nonanticipativity Constraints

Decision makers are not allowed to anticipate the outcome of future random events when making their decisions, so they need to enforce nonanticipativity. The program (3.24) implicitly includes nonanticipativity constraints, however, we need to keep the scenario tree structure, which is not easy to decompose. Let $|\mathcal{S}|$ be the number of scenarios, we assume that the random vector ξ is defined by a probability space (Ξ, \mathcal{S}) , where $\mathcal{S} = \{1, \dots, |\mathcal{S}|\}$, and $\Xi = (\xi^1, \dots, \xi^{|\mathcal{S}|})$ with probabilities $p^1, \dots, p^{|\mathcal{S}|}$. This allows us to decompose the model using scenarios. Let \mathcal{H}_t^s be the set of scenarios for which the realization of uncertainties is identical to the realization of uncertainties under scenario $s \in \mathcal{S}$ before stage $t \in \mathcal{T}$. We need to add the following constraints:

$$\mathbf{x}_{t'}^{s'} = \mathbf{x}_{t'}^s, \forall t' < t, \forall s' \in \mathcal{H}_t^s. \quad (3.25)$$

Fig. 3.2 gives an illustration of nonanticipativity constraints. For example, if $s = 4$, and $t = 3$, then $\mathcal{H}_3^4 = 3$ and $\mathcal{H}_2^4 = \{1, 2, 3\}$. The nonanticipativity constraints of this example are given by $\mathbf{x}_1^1 = \mathbf{x}_1^2 = \mathbf{x}_1^3 = \mathbf{x}_1^4$, $\mathbf{x}_2^1 = \mathbf{x}_2^2$, and $\mathbf{x}_2^3 = \mathbf{x}_2^4$. Note that for IES expansion problems, we only impose nonanticipativity constraints on investment decisions and the state of charge of gas storage.

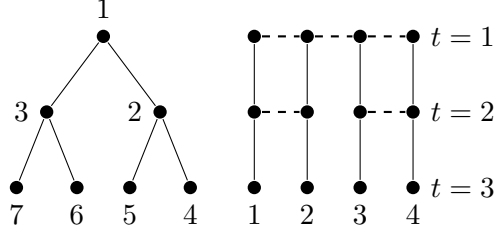


Figure 3.2: An illustration of nonanticipativity constraints.

Using nonanticipativity constraints, the stochastic mixed integer problem can be recast as a large-scale mixed integer problem:

$$\min \sum_{s \in \mathcal{S}} p^s \sum_{t=1}^{|\mathcal{T}|} \mathbf{c}_t^\top(\xi_t^s) \mathbf{x}_t(\xi_t^s) \quad (3.26a)$$

$$\text{s.t.} \quad \mathbf{W}_1 \mathbf{x}_1(\xi^s) \leq h_1(\xi_1^s), \quad \forall s \in \mathcal{S}, \quad (3.26b)$$

$$\begin{aligned} \mathbf{T}_t(\tilde{\xi}_t^s) \tilde{\mathbf{x}}_{t-1}(\xi^s) + \mathbf{W}_t \mathbf{x}_t(\xi^s) &\leq h_t(\tilde{\xi}_t^s), \\ \forall t \in \mathcal{T}, \forall s \in \mathcal{S}, \end{aligned} \quad (3.26c)$$

$$\mathbf{x}_{t'}(\xi^{s'}) = \mathbf{x}_{t'}(\xi^s), \quad \forall t' < t, \forall s' \in \mathcal{H}_t^s, \quad (3.26d)$$

$$\mathbf{x}_t(\xi^s) \in \mathbf{X}_t, \quad \forall t \in \mathcal{T}, \forall s \in \mathcal{S}, \quad (3.26e)$$

where p^s is the probability of scenario s . Compared with (3.24), (3.26) is in its extensive form, and nonanticipativity constraints are explicitly imposed by (3.26d).

Branch-and-Price Algorithm

The time complexity of branch and bound algorithm increases exponentially. The coupling elements in (3.26), i.e., nonanticipativity constraints, make the problem impossible to solve using the extensive form. Decomposition methods are needed for such a large-scale mixed integer problem, by which we can decompose the problem into several tractable pieces. We adopt the branch-and-price algorithm proposed in [57]. The branch-and-price algorithm consists of Dantzig-Wolfe decomposition, column generation, and branch-and-bound.

Let $(\mathbf{c}_t^s, h_t^s, \mathbf{T}_t^s, \mathbf{x}_{t,s}) = (\mathbf{c}_t^\top(\xi_t^s), h_t(\tilde{\xi}_t^s), \mathbf{T}_t(\tilde{\xi}_t^s), \mathbf{x}_t(\xi_t^s))$, we define

$$\psi_s := \left\{ \{x_{t,s}\}_{t=1}^{|\mathcal{T}|} : \mathbf{x}_{t,s} \in \mathbf{X}_{t,s}, \mathbf{T}_t^s \tilde{\mathbf{x}}_{t-1,s} + \mathbf{W}_t \mathbf{x}_{t,s} \leq h_{t,s}, \forall t \in \mathcal{T} \right\}. \quad (3.27)$$

Applying the mixed-integer finite basis theorem to the subset of ψ_s , there exists a finite set of its points $\mathcal{V}_s \subseteq \psi_s$ such that all points of ψ_s can be represented as a convex combination of

points in \mathcal{V}_s , whose index set is \mathcal{G}_s . We define the master problem as

$$\min_{\alpha} \quad \sum_{s \in \mathcal{S}} p^s \sum_{t \in \mathcal{T}, i \in \mathcal{G}_s} \mathbf{c}_t^s \mathbf{x}_{t,s}^i \alpha_s^i \quad (3.28a)$$

$$\text{s.t.} \quad \mathbf{x}_{t',s} = \sum_{i \in \mathcal{G}_s} \mathbf{x}_{t',s}^i \alpha_s^i, \quad \forall t' < t, \forall s' \in \mathcal{H}_t^s, \forall t, s, \quad (3.28b)$$

$$\sum_{i \in \mathcal{G}_s} \alpha_s^i = 1, \quad \forall s \in \mathcal{S}, \quad (3.28c)$$

$$\alpha_s^i \geq 0, \quad \forall s \in \mathcal{S}, \forall i \in \mathcal{G}_s, \quad (3.28d)$$

$$\mathbf{x}_{t,s} \in \mathbf{X}_t, \quad \forall t \in \mathcal{T}, \forall s \in \mathcal{S}, \quad (3.28e)$$

where p^s is the probability of scenario s . In the master problem, the decision variables are α 's, and $\mathbf{x}_{t,s}^i$'s are the solutions of scenario based subproblems. Again, constraints (3.28b) and (3.28c) are the nonanticipativity constraints and the convexity constraints, respectively. Moreover, (3.28e) denotes restrictions that require some or all the decision variables to be integer. We solve the linear programming (LP) relaxation of (3.28), i.e., relax (3.28c), and let dual variables associated with nonanticipativity constraints (3.28b) and convexity constraint (3.28c) be $\mu_{t,s}$ and λ_s , respectively. Note that the reduced cost of master problem variables α_s^i is given by $\sum_{t \in \mathcal{T}} (p^s \mathbf{c}_t^s + \mu_{t,s}) \mathbf{x}_{t,s}^i - \lambda_s$. The following pricing problem is used to verify the optimality of the master problem for scenario $s \in \mathcal{S}$:

$$\min \quad \mathbf{C}_s \cdot \mathbf{x}_s \quad (3.29a)$$

$$\text{s.t.} \quad \mathbf{x}_s \in \psi_s, \quad (3.29b)$$

where $\mathbf{C}_s = (p^s \mathbf{c}_1^s + \mu_{1,s}, \dots, p^s \mathbf{c}_{|\mathcal{T}|}^s + \mu_{|\mathcal{T}|,s})$. If the objective value is smaller than λ_s , it means that we can generate the corresponding column to the master problem since the column has negative reduced cost.

Note that the pricing problem (3.29) is a mixed integer problem. However, $|\mathcal{S}|$ problems are fully decomposed. Since we solve the LP relaxation of the master problem, general branching scheme should be applied to meet the integrality conditions. To avoid infeasibility of the master problem, a computed feasible solution is needed. We set all the investment decisions to be 1 and denote the solution by \mathbf{x}_s^0 . The branch-and-price scheme is summarized as follows.

Initialization. Set $\lambda_s = \infty$, $\mu_{t,s} = 0$ and $\mathcal{G}_s = \{0\}$, $\forall s \in \mathcal{S}, \forall t \in \mathcal{T}$. Set $UB = \infty$.

Step 1. $\forall s \in \mathcal{S}$, solve the pricing problem (3.29). If it indicates a negative reduced cost, add the column to the current master problem (3.28), and go to step 2. Otherwise, go to step 3.

Step 2. Solve the linear relaxation of the master problem (3.28), and update dual variables $\mu_{t,s}$ and λ_s to the pricing problem (3.29). Go back to step 1.

Step 3. Check the integrality conditions $\mathbf{x}_{t,s} \in \mathbf{X}_t, \forall t \in \mathcal{T}, \forall s \in \mathcal{S}$. If the conditions hold, go to step 5. Otherwise, go to step 4.

Step 4. Start the branching phase by defining two subproblems, and go back to step 1.

Step 5. If there is no more active node in the branching tree, then declare the incumbent solution and STOP. Otherwise, select an active node and go back to step 1.

Further Enhancement

Two fundamental difficulties arise when applying branch-and-price algorithm. First, conventional branching on variables may be ineffective because fixing variables can destroy the structure of the pricing subproblem. Second, column generation often converges slowly. Those two issues require us to make problem-specific enhancement.

To avoid infeasibility at the beginning, we need to first compute a feasible solution. For the IES expansion planning problem, the simplest way is to set all the investment decisions to be 1, i.e., enforce all the candidate investments. We observe that the selection of the feasible solution does not influence the computational efficiency of IES expansion co-planning problem.

In the column generation phase, we need to solve multiple scenario based subproblems. Each deterministic IES expansion co-planning problem is a mixed integer linear programming problem. For a system in real life, the subproblem itself can be difficult to solve. Note that it is not necessary to find the column with the most negative reduced cost. The first method is to generate near-optimal solutions using some heuristic algorithms. An alternative approach we apply in our experiments is to stop at some optimality gaps. We use CPLEX as our solver for subproblems. CPLEX applies branch-and-cut algorithm for mixed integer problems. However, we observe that it is time consuming to find the global optimal solution when the branching phase starts with the near-optimal solution. We stop the subproblems at a specific optimality gap and add the column to the master problem.

On the other hand, we only impose nonanticipativity constraints for the state of charge of gas storage and investment decisions, which makes the scale of master problem (3.28) small. Moreover, we solve the LP relaxation, which reduces the computation burden dramatically. In standard branch-and-price, only one column with highest reduced cost for all subproblems is added to the master problem. However, the computational efficiency of the master problem is not an issue here. In our experiment, we add the column for each subproblem to the master problem as long as it is associated with a negative cost.

Regarding the branching phase, we use rounding strategies. The expansion co-planning problem indeed is a binary problem. The branching leads to a specific value 0 or 1. Moreover, the advantage of branch-and-price algorithm is to find a better branching node and reduce the number of nodes in the branching tree. Given a fractional solution to (3.28), we perform rounding instead of continuing the branching phase. For all fractional values that are greater than or equal to 0.5, we round it to 1, whereas we round those that are less than 0.5 to 0. For some small integrated energy systems without nonanticipativity constraints on the storage, we observe that the optimal solution of LP relaxation for (3.28) is the integer programming solution. The reason might be the existence of totally unimodular matrices. Using rounding strategies, the solution is not guaranteed to be globally optimal anymore. The improved scheme is shown

Algorithm 3 Algorithm for the proposed branch-and-price

Require:

scenario sets \mathcal{S} , initial solution \mathbf{x}_s^0

- 1: **while** there exists any negative reduced cost **do**
- 2: **for** $s \in \mathcal{S}$ **do**
- 3: solve scenario based pricing problem (3.29) heuristically, using current $\mu_{t,s}$ and λ_s
- 4: stop branching at the optimality gap 5%
- 5: **if** the objective value is smaller than the current λ_s **then**
- 6: add the column to the master problem (3.28)
- 7: **end if**
- 8: **end for**
- 9: solve the master problem (3.28)
- 10: update dual variables $\mu_{t,s}$ and λ_s
- 11: **end while**
- 12: check the integrality conditions
- 13: **if** there exist fractional values **then**
- 14: perform the rounding strategy
- 15: **end if**

in Algorithm 3.

3.1.4 Case Studies

We use two cases to quantify the economic value of P2G in the long-term planning problem and verify the effectiveness of the branch-and-price algorithm. The small case is a 3-stage program based on a 6-bus power system coupled with a 6-node gas system, which focuses on the economic value of P2G. The large case is a 4-stage stochastic program based on a 118-bus power system [136] coupled with a 40-node gas system [137], which is compared with the extensive form solved by CPLEX (branch-and-cut), progressive hedging, and greedy algorithm. The scenarios are generated by MATLAB function *fmincon*.

6-Bus Test System

In this case, we consider a system as shown in Fig. 3.3. We set the capacities of the existing generators 1, 2 to 160 MW and the capacity of transmission lines to 100 MW and 120 MW, respectively. The parameters of candidate gas-fired generators and P2Gs are given in Table A.1. The parameters of candidate transmission lines and pipelines are given in Table A.2. Moreover, we set the tariffs on carbon emission as \$50 per tons of CO_2 . The scenarios tree generated by (3.23) is shown in Table A.3, where the number of outcomes of stages 2 and 3 are set as 5 and 2. The value used for wind generation is the unit value, where the base is 300 MW. The load is given in Table A.4.

The optimal solution of this case is given in Table 3.1. The multistage planning allows the planner to make decisions after the realization of random variables. For example, the evolu-

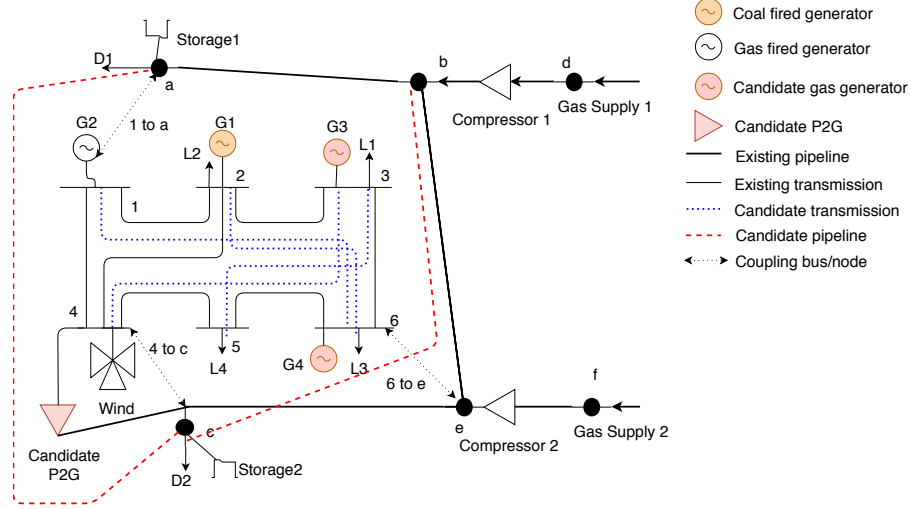


Figure 3.3: 6-bus power system coupled with a 6-node gas system.

Table 3.1: Investment Decisions for the 6-Bus Test System.

Scenario	Stage 1	Stage 2	Stage 3
1	P2G-3, Trans-2, Trans-3, Pipe-2	None	None
2			None
3		Gen-2	None
4			Trans-3, P2G-2
5		Gen-2	Pipe-1, Gen-1
6			None
7		Gen-2	None
8			None
9		Gen-2, Trans-1, P2G-1, P2G-2	Gen-1
10			None

tion of random variables in scenarios 5 and 6 is extreme. The 2-stage stochastic programming solution may lead to conservative decisions for other scenarios (e.g., scenarios 9 and 10). However, the multistage stochastic programming solution allows adaptive decisions. We solve a problem modeled by 2-stage stochastic programming, a problem modeled by 3-stage stochastic programming, and a problem with perfect information. The optimal objective values are \$588.86M, \$498.7M, and \$476.34M, respectively. The expected values of perfect information for 2-stage program and 3-stage program are \$112.52M and \$22.36M. It is obvious that the multistage program reduces the risk of uncertainty considerably

P2G can contribute to the system in two aspects. First, the P2G can reduce the tariff imposed for carbon emission. Second, the P2G can avoid the wind curtailment where it converts

Table 3.2: Sensitivity Analysis of Economic Value of P2G.

Carbon cost (\$/ton)	Wind (MW)	With P2G	Without P2G	Improvement
42	300	504.3	534.8	5.7%
50	300	498.7	535.9	6.9%
60	300	487.8	537.3	9.2%
123	300	412.6	546.0	24.4%
50	250	605.3	624.0	3%
50	350	414.2	484.7	14.5%

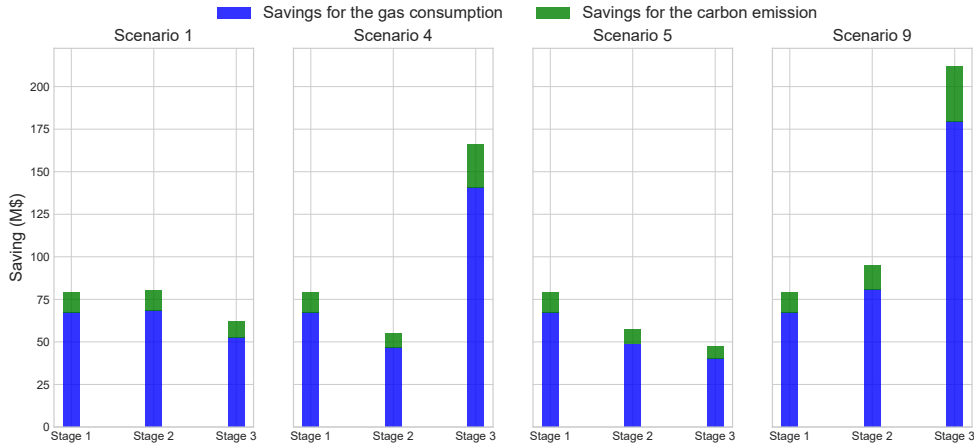


Figure 3.4: The savings contributed by the selected P2G in each stage.

the excess power into natural gas. The natural gas produced by P2G can be used to serve gas load or stored for future use. Hence, we conduct a sensitivity analysis using different prices of carbon emission and base generations to investigate the economic value of P2G. We use the prices of carbon given by EPA [52] and consider the base generation from 250 to 350 MW. As shown in Table 3.2, the economic value of P2G highly depends on the penetration of renewable energy. Higher penetration of renewable leads to curtailment in peak seasons such as the load block 4 in Table A.4. The excess generation can be converted into natural gas and reused in other seasons such as the load block 1. Moreover, the economic value depends on the price imposed by cap-and-trade market as well. Higher price means more environmental benefits induced by P2G. As shown in Table 3.2, the economic value of P2G is larger when the carbon cost is more expensive. In such cases, the system operators can sell carbon emission to others. On the other hand, the economic value of P2G increases as the available wind generation increases. More available wind power means more electricity is converted to natural gas.

To better illustrate the contribution of P2G, we show the savings contributed by P2G-3 in each stage for scenario 1, 4, 5 and 9. The results are given in Fig. 3.4.

For the 6-bus test system, we also test the proposed branch-and-price algorithm. Since the

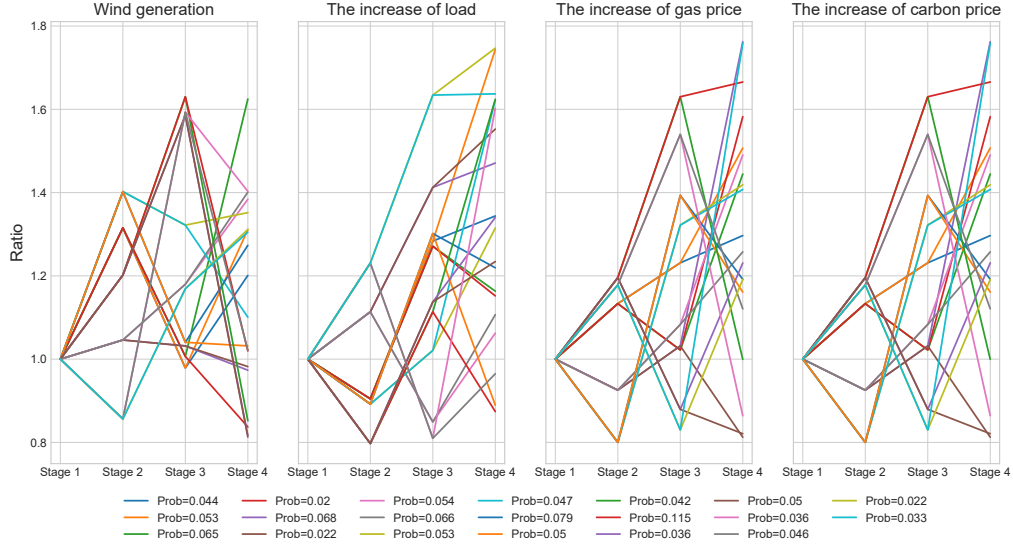


Figure 3.5: The evolution of all the uncertainties for the 20-scenario case.

size of the problem is small, we solve every subproblem optimally without early stop. It turns out that the solutions are exact.

118-Bus Test System

The solution validity and computational advantages of the proposed decomposition scheme are demonstrated through a case study on a 118-bus power system coupled with a 40-node gas system. The system consists of 118 electric buses, 186 transmission lines, and 54 generation units. There are 40 gas nodes, 40 pipelines, and 6 gas supplies. Two networks are also attached in Appendix A. The number of candidate generators, P2Gs, transmission lines, and pipelines in consideration are 8, 21, 15, and 8, respectively. Details about candidate sets are reported in Appendix A as well. We assume that each year consists of 4 load blocks. The total planning time horizon is 20 years. A 4-stage program is considered where each stage consists of 5 years. The generated scenarios are shown in Fig. 3.5. Note that the increase means the ratio between child and parent nodes.

The computational benefits of the proposed scheme are demonstrated through comparison against greedy algorithm, progressive hedging, and branch-and-cut algorithm. First, we choose to generate 20 scenarios. The number of outcomes at each stage is 1, 5, 2, 2, respectively. We set the penalty for the progressive hedging to \$2M. The numerical results are summarized in Table 3.3.

For the branch-and-cut, we terminate the program after 6 days and only give the best integer solution at that time. For the IES expansion co-planning problem, the extensive form (i.e., using branch-and-cut) cannot be solved within an acceptable time period. The results show that the decomposition method is necessary. Greedy algorithm makes the optimal choice at each step as

Table 3.3: Performance of Different Approaches under the 20-Scenario Case.

	CPU time (hours)	Objective value (\$M)
Greedy algorithm	0.04	5478.9
Progressive hedging	18.4	5361.8
Branch-and-cut	Stop at 150	5354.4
Branch-and-price	60.72	5327.5

Table 3.4: Performance of Different Approaches under the 60-Scenario Case.

	CPU time (hours)	Objective value (\$M)
Greedy algorithm	0.128	5927.4
Progressive hedging	fails to converge	
Branch-and-price	359.2	5787.9

it attempts to find the overall optimal way to solve the entire problem. It can solve the problem in a small amount of time. However, it ignores the future evolution of uncertainties and leads to worse investment decisions. Unlike the greedy algorithm where the problem is decomposed by stages (horizontal decomposition), both branch-and-price and progressive hedging decompose the problem by scenarios (vertical decomposition). For the IES expansion co-planning problem, the only coupling elements between scenarios are nonanticipativity constraints. However, there are many state sequential variables. Vertical decomposition methods fit the problem structure better. For the 20-scenario case, progressive hedging can converge, and the corresponding CPU time is less than that of branch-and-price. However, the objective value produced by progressive hedging is larger than that generated by branch-and-price. Note that progressive hedging is a heuristic technique for mixed integer problems. For the IES expansion co-planning problem, it is not time sensitive, and the decision maker is more interested in obtaining a lower cost. Branch-and-price outperforms progressive hedging since both of them can be solved within an acceptable time period.

However, based on the analysis in Section 3.1.2, 20 scenarios cannot encapsulate all possible evolution of uncertainties. We increase the number of scenarios and further compare branch-and-price algorithm with others. In this case, we generate 60 scenarios. The numbers of outcomes at each stage are 1, 5, 4, 3, respectively. We do not consider branch-and-cut in this case since it has to be terminated for the 20-scenario case. The computational performance is shown in Table 3.4. Greedy algorithm can obtain the suboptimal solution in a small amount of time. However, the relative gap of objective value is still large, which is not acceptable. Progressive hedging cannot converge in this case. We only try two settings where the penalty is set to \$1M and \$2M. It may converge for other selections of penalty. However, it shows the drawback of progressive hedging: the convergence is not guaranteed. In our experiment, we observe that the

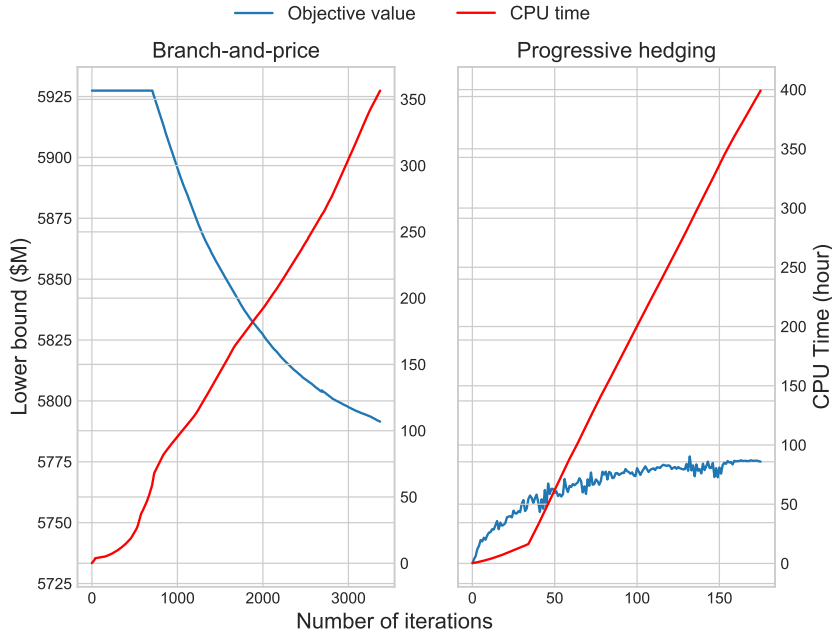


Figure 3.6: CPU time and bound versus iterations for branch-and-price and progressive hedging.

lower bound generated by progressive hedging oscillates between \$5774.6M and \$5775.0M.

To further compare the branch-and-price algorithm and progressive hedging, we show the evolution of CPU time and bound versus iterations. The results are presented in Fig. 3.6. The lower bound for branch-and-price in Fig. 3.6 denotes the LP relaxation of master problem (3.28). The algorithm requires a feasible solution to start. In our experiment, we use the solution obtained by greedy algorithm. We also try to use the solution where all investment decisions are set to 1. We observe little difference in the total CPU time between the two selections. For the case where all investment decisions are set to 1, the bound begins decreasing early. As shown in Fig. 3.6, the subproblems generate some useless columns into the master problem in the first 700 iterations. Techniques called dual stabilization can be applied to accelerate the convergence. For each subproblem, we use the near-optimal solution with 5% optimality gap. Compared with the time required to find global optimal solution, such a near-optimal solution saves much time. Moreover, current commercial solvers such as CPLEX can perform heuristic strategies before branching, which further accelerates the computation.

On the other hand, progressive hedging requires the global optimal solution for each subproblem, which makes the computation of each iteration slow. As shown in the Fig. 3.6, each iteration of progressive hedging takes longer CPU time than that of branch-and-price. Moreover, the penalty term introduces quadratic elements into the problem, which renders the subproblem difficult to solve. It takes 320 hours before oscillation in our experiment. The above highlights the shortcomings of progressive hedging.

3.2 Interval Based Transmission Contingency-Constrained Unit Commitment

We believe there are three main gaps when performing transmission contingency-constrained unit commitment (CCUC) for integrated power and gas systems: i) The existing CCUC methods for power systems are not directly applicable to CCUC for integrated energy systems. Moreover, additional efforts are needed to deal with the nonlinear and non-convex constraints in gas systems; ii) Scenario based CCUC such as chance-constrained optimization and risk at value may reflect the decision maker's attitude towards risk but can lead to more computational challenges; iii) P2G can also offer auxiliary and regulatory power services, which, however, is rarely examined in the existing literature on unit commitment. Unlike the scenario based methods where each scenario is associated with its probability, we use interval numbers to capture the stochastic nature of renewable energy and load. To schedule the generating units optimally, we need to compare interval numbers. To compare the interval numbers in the objective values, we introduce the preference ordering.

3.2.1 Contingency-Constrained Unit Commitment Model

The CCUC problem is formulated as a two-stage problem. In the first stage, the decision maker determines the on/off status of generating units, whereas the economic dispatch is solved in the second stage. The goal of unit commitment problem is to minimize the total production cost by selecting one set of unit commitment decisions for thermal units over the 24-hour scheduling horizon. The objective function includes start-up cost, shut-down cost, no load cost, fuel cost, total cost of gas supply, and penalties for load shedding. The fuel cost of gas-fired units is carried out by the cost of gas supply. Coal-fired generators are assumed to have linear day-ahead offer price.

Let $j, i, m, l, k, a, n, b, s, o, g$, and t be the index of gas nodes, power buses, pipelines, transmission lines, renewable generation, P2Gs, gas demands, electric loads, gas supplies, coal-fired units, generation units including coal-fired and gas-fired units, and time slots. The objective function can be formulated as:

$$\begin{aligned} \min \quad & \sum_{t=1}^T \left[\sum_{g=1}^G \left(C_g^{\text{NL}} u_{g,t} + C_g^{\text{U}} y_{g,t} + C_g^{\text{D}} z_{g,t} \right) \right. \\ & \left. + \sum_{o=1}^O C_o P_{o,t} + \pi \sum_{s=1}^S F_s^{\text{S}} + \pi^{\text{E}} \sum_{b=1}^B \Delta D_{b,t}^{\text{E}} + \pi^{\text{G}} \sum_{n=1}^N \Delta D_{n,t}^{\text{G}} \right], \end{aligned} \quad (3.30)$$

where u, y, z are binary variables, representing on/off status, start-up, and shut-down signals, respectively. They are associated with no-load costs C^{NL} , start-up costs C^{U} , shut-down costs C^{D} , respectively. P represents power of generators and P2Gs, F^{S} denotes gas injection by gas supplies, and ΔD^{E} and ΔD^{G} are the shedding quantity of electric load and gas demand.

Accordingly, C , π , π^E , and π^G are day-ahead offer prices of generators, gas price, penalties for electric load and gas demand shedding, respectively. The objective function is composed of two parts. The first part minimizes commitment based cost, including non-load, start-up, and shut-down costs. The second part optimizes fuel cost of coal-fired units, cost of gas supplies, and load shedding penalties in both networks.

The generator's state is represented by a binary variable. By incorporating the binary variables denoting start-up and shut-down signals, we have the following constraints:

$$y_{g,t} - z_{g,t} = u_{g,t} - u_{g,t-1}, \forall g, \forall t > 1, \quad (3.31a)$$

$$y_{g,t} - z_{g,t} = u_{g,t} - IS_g, \forall g, t = 1, \quad (3.31b)$$

$$y_{g,t} + z_{g,t} \leq 1, \forall g, \forall t, \quad (3.31c)$$

where IS is the initial on/off status of generators.

Moreover, the generators should operate within the minimum and maximum operating levels. Let RD and RU be ramp down and up rates of generators, and UT and DT be minimum up and down times of generators. The minimum up and down time constraints, and ramp rate constraints should be satisfied:

$$P_g^{\min} u_{g,t} \leq P_{g,t} \leq P_g^{\max} u_{g,t}, \forall g, \forall t, \quad (3.32a)$$

$$\sum_{\tau=t-UT_g+1}^t y_{g,\tau} \leq u_{g,t}, \forall t \geq UT_g, \quad (3.32b)$$

$$\sum_{\tau=t-DT_g+1}^t z_{g,\tau} \leq 1 - u_{g,t}, \forall t \geq DT_g, \quad (3.32c)$$

$$-RD_g u_{g,t} - RD_g^D z_{g,t} \leq P_{g,t} - P_{g,t-1}, \forall g, \forall t, \quad (3.32d)$$

$$P_{g,t} - P_{g,t-1} \leq RU_g u_{g,t} + RU_g^U y_{g,t}, \forall g, \forall t, \quad (3.32e)$$

where RD^D and RU^U are the shut-down and start-up generation limits.

We assume that the P2G also has its maximum operating level:

$$P_{a,t} \leq P_a^{\max}, \forall a, \forall t. \quad (3.33)$$

We use PTDF to describe the power flow in each transmission line. For better illustration, we introduce a slack variable to denote the injected power at each bus by

$$P_{i,t}^{\text{inj}} = \sum_{g \in \mathcal{G}(i)} P_{g,t} + \sum_{k \in \mathcal{K}(i)} (W_{k,t} - \Delta W_{k,t}) - \sum_{a \in \mathcal{A}(i)} P_{a,t} + \sum_{b \in \mathcal{B}(i)} (D_{b,t}^E - \Delta D_{b,t}^E), \forall i, \forall t, \quad (3.34)$$

where W and D^E are random variables, representing renewable generation and electric load. The electric load shedding ΔD^E and the renewable curtailment ΔW are considered as decision

variables. $\mathcal{K}(i)$, $\mathcal{B}(i)$, $\mathcal{A}(i)$, and $\mathcal{G}(i)$ are sets of renewable generation, electric loads, P2Gs, and generators at power bus i .

The power flow in each transmission line then can be calculated by

$$-PF_l^{\max} \leq \sum_{i=1}^I SF_{l,i} \times P_{i,t}^{\text{inj}} \leq PF_l^{\max}, \forall l, \forall t, \quad (3.35)$$

where SF is the power transfer distribution factors (PTDF) of power systems. The load and generation should be balanced in real time, which leads to:

$$\sum_{g=1}^G P_{g,t} + \sum_{k=1}^K (W_{k,t} - \Delta W_{k,t}) = \sum_{b=1}^B (D_{b,t}^E - \Delta D_{b,t}^E) + \sum_{a=1}^A P_{a,t}, \forall t. \quad (3.36)$$

The shedded load and wind curtailment is constrained by

$$\Delta W_{k,t} \leq W_{k,t}, \forall k, \forall t, \quad (3.37)$$

$$\Delta D_{b,t} \leq D_{b,t}, \forall b, \forall t. \quad (3.38)$$

A simplified steady state model of gas systems is adopted in this work. The physical constraints of each gas supplier are modeled by

$$F_s^{\min} \leq F_{s,t}^S \leq F_s^{\max}, \forall s, \forall t, \quad (3.39)$$

The gas flow in each pipeline can be calculated by

$$GF_{m,t} |GF_{m,t}| = \phi_m \left(\omega_{\mathcal{S}(m),t}^2 - \omega_{\mathcal{R}(m),t}^2 \right), \forall m, \forall t, \quad (3.40)$$

where GF denotes gas flow in pipelines and ω represents pressure at gas nodes. ϕ_m is a constant for each compressor. Similarly, the gas flow is constrained by the maximum capacity of its corresponding pipeline:

$$-GF_m^{\max} \leq GF_{m,t} \leq GF_m^{\max}, \forall m, \forall t. \quad (3.41)$$

The gas injection and demand should be balanced at each node, given by

$$\begin{aligned} \sum_{s \in \mathcal{SP}(j)} F_{s,t} + \sum_{a \in \mathcal{A}(j)} F_{a,t} + \sum_{\mathcal{R}(m)=j} GF_{m,t} &= \sum_{g \in \mathcal{G}(j)} F_{g,t} \\ &+ \sum_{\mathcal{S}(m)=j} GF_{m,t} + \sum_{n \in \mathcal{N}(j)} (D_{n,t}^G - \Delta D_{n,t}^G), \forall j, \end{aligned} \quad (3.42)$$

where F represents gas injection by P2Gs and gas consumption by gas-fired generators, GF is the gas flow in a pipeline, and D^G is a random variable denoting the gas demand. \mathcal{S} and \mathcal{R} return sending and receiving nodes of pipelines. $\mathcal{SP}(j)$, $\mathcal{A}(j)$, and $\mathcal{G}(j)$ are sets of gas supplies, P2Gs, and generators at gas node j , respectively. Gas storage is not considered in the model.

However, the model can be easily extended to incorporate storage by adding variables and constraints relating to operation of storage.

Higher heating value can be used to convert electrical power into volumetric gas flow and vice versa, as shown in the following:

$$F_{a,t} = \eta_a P_{a,t} \Delta T / HHV_{SNG}, \forall a, \forall t, \quad (3.43a)$$

$$P_{g,t} = \eta_g F_{g,t} \cdot HHV_{SNG} / \Delta T, \forall g, \forall t, \quad (3.43b)$$

where $\Delta T = 1$ since our model is based on each hour, and HHV_{SNG} is the higher heating value of synthetic natural gas.

3.2.2 Interval Based Uncertainty Representation

Uncertainties are modeled by interval numbers. The use of interval numbers assumes a vague uncertain set instead of a distribution. Compared with other uncertainty representations that are modeled in a stochastic fashion, i.e., with probabilities, vague set is easier to obtain. Especially, it is somehow difficult to specify the underlying distribution of contingencies. Uncertainties in our work come from two aspects: net generation and contingencies. The uncertain renewable generation and electric load varying within continuous ranges can be directly modeled by interval numbers.

Consider the wind farm $k \in \{1, \dots, K\}$ with predicted wind power as $W_{k,t}$ in time slot t . We assume that the corresponding uncertain wind power is $\tilde{W}_{k,t}$, where $W_{k,t} - W_{k,t}\epsilon_k \leq \tilde{W}_{k,t} \leq W_{k,t} + W_{k,t}\epsilon_k$. In other words, the realization of wind generation is within an interval $[W_{k,t}, \bar{W}_{k,t}]$, where $\underline{W}_{k,t} = W_{k,t} - W_{k,t}\epsilon_k$ and $\bar{W}_{k,t} = W_{k,t} + W_{k,t}\epsilon_k$. Similarly, we assume that the realization $\tilde{D}_{b,t}^E$ of load $b \in \{1, \dots, B\}$ is within an interval $[D_{b,t}^E, \bar{D}_{b,t}^E]$. We do not consider the uncertainty in gas demands since the gas contract is mainly on a daily or a monthly basis. The injected power at each bus in (3.34) can be reformulated by

$$P_{i,t}^{\text{inj}} = \sum_{g \in \mathcal{G}(i)} P_{g,t} + \sum_{k \in \mathcal{K}(i)} \left(\tilde{W}_{k,t} - \Delta W_{k,t} \right) - \sum_{a \in \mathcal{A}(i)} P_{a,t} - \sum_{b \in \mathcal{B}(i)} \left(\tilde{D}_{b,t}^E - \Delta D_{b,t}^E \right), \forall i, \forall t. \quad (3.44)$$

Similarly, load and generation in (3.36) should be replaced by interval numbers.

For the uncertainty introduced by contingencies, we adopt the method in [138]. Note that we focus on contingencies in transmission lines and pipelines. We first describe it using PTDF of power system and extend it to the gas system. In this dissertation, we consider $N-1$ contingency. Without contingencies, transmission constraints can be formulated as (3.35). However, for all L transmission lines, we need to ensure the solution robustness when any single outage happens. There are L discrete events for each time slot. Consider an interruption in transmission line l' . Let the corresponding new PTDF be $\mathbf{SF}^{l'}$. We can ensure the solution robustness by adding

the following constraint:

$$-PF_l^{\max} \leq \sum_{i=1}^I SF_{l,i}'' \times P_{i,t}^{\text{inj}} \leq PF_l^{\max}, \forall l, \forall t. \quad (3.45)$$

For all L possible interruptions in each time slot, we need $L \times T \times (L + 1)$ constraints as follows:

$$\begin{aligned} -PF_l^{\max} &\leq \sum_{i=1}^I SF_{l,i} \times P_{i,t}^{\text{inj}} \leq PF_l^{\max}, \forall l, \forall t, \\ -PF_l^{\max} &\leq \sum_{i=1}^I SF_{l,i}^1 \times P_{i,t}^{\text{inj}} \leq PF_l^{\max}, \forall l, \forall t, \\ &\vdots \\ -PF_l^{\max} &\leq \sum_{i=1}^I SF_{l,i}^L \times P_{i,t}^{\text{inj}} \leq PF_l^{\max}, \forall l, \forall t. \end{aligned}$$

To reduce the complexity, we can use intervals of PTDF to capture all possible cases. PTDFs are calculated offline, and each element is given by

$$SF_{l,i} = \min \left(\min_{l'} SF_{l,i}''', SF_{l,i} \right), \forall l, \forall i, \quad (3.46a)$$

$$\bar{SF}_{l,i} = \max \left(\max_{l'} SF_{l,i}''', SF_{l,i} \right), \forall l, \forall i, \quad (3.46b)$$

which establishes intervals $\tilde{SF}_{l,i} = [SF_{l,i}, \bar{SF}_{l,i}]$, $\forall l, i$. The set of transmission constraints then can be represented by the following interval based constraint:

$$-PF_l^{\max} \leq \sum_{i=1}^I \tilde{SF}_{l,i} \times P_{i,t}^{\text{inj}} \leq PF_l^{\max}, \forall l, \forall t, \quad (3.47)$$

which ensures that the resulting solution will be feasible for every possible uncertain contingency realization. It should hold for any given L and I , and it is irrelevant to the size of system in consideration.

It is worth mentioning that there is no PTDF matrix in gas systems. It should be noted that (3.40) is nonlinear. To derive the PTDF matrix for gas systems, we need some reformulations. Using $\Omega = \omega^2$ to replace the pressure squared, we have the new gas flow equation as follows:

$$GF_{m,t}|GF_{m,t}| = \phi_m \left(\Omega_{S(m),t} - \Omega_{\mathcal{R}(m),t} \right), \forall m, t, \quad (3.48)$$

which can be piecewise linearized using the incremental model [130]. As shown in Fig. 3.7, the gas flow function is linearized by one segment and three segments. Some works use one segment

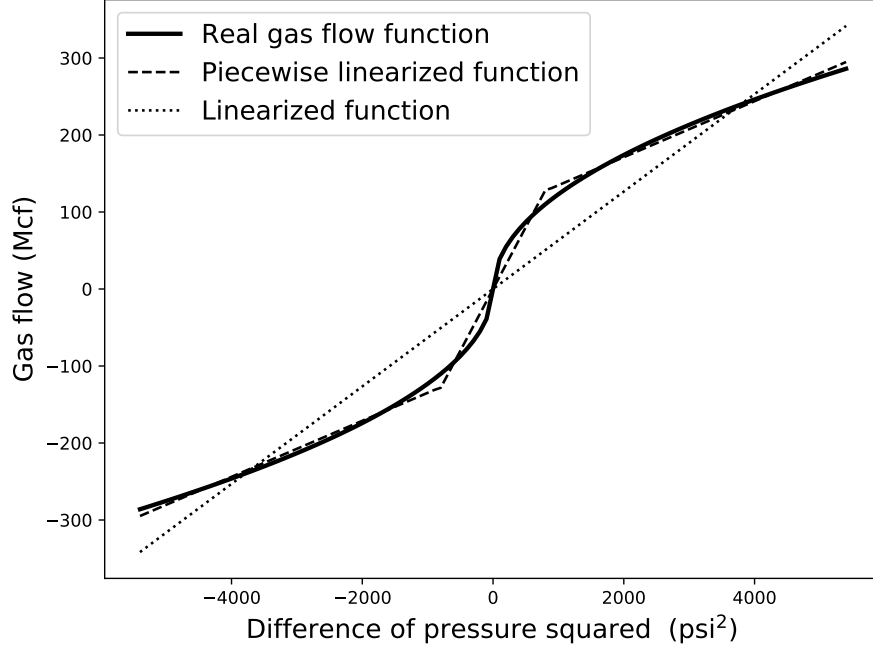


Figure 3.7: Illustration of piecewise linearized gas flow.

to linearize the gas flow equation using techniques such as Taylor series [139]. We start with one segment linearization and obtain the PTDF. Let the slope be Φ , post linearization we have the following new gas flow equation:

$$GF_{m,t} = \Phi_m (\Omega_{S(m),t} - \Omega_{R(m),t}), \forall m, \forall t. \quad (3.49)$$

We observe that only the difference of pressure squared matters. By selecting one gas node to be the slack node, the derivation of PTDF for gas systems is similar to that of power systems where only the difference of voltage angle matters.

Once the PTDF for gas systems is obtained, constraints (3.40)–(3.42) can be replaced by the following constraints:

$$-GF_m^{\max} \leq \sum_{j=1}^J GSF_{m,j} \times F_{j,t}^{\text{inj}} \leq GF_m^{\max}, \forall m, \forall t, \quad (3.50)$$

$$F_{j,t}^{\text{inj}} = \sum_{s \in SP(j)} F_{s,t} + \sum_{a \in A(j)} F_{a,t} - \sum_{g \in G(j)} F_{g,t} - \sum_{n \in N(j)} (D_{n,t}^G - \Delta D_{n,t}^G), \forall j, \forall t, \quad (3.51)$$

$$\sum_{s=1}^S F_{s,t} + \sum_{a=1}^A F_{a,t} = \sum_{g=1}^G F_{g,t} + \sum_{n=1}^N (D_{n,t}^G - \Delta D_{n,t}^G), \forall t. \quad (3.52)$$

PTDF of gas networks eliminates the dependency of gas flow on node pressures. Consider the piecewise linearization by three segments in Fig. 3.7, the slopes of each segment are 0.036,

0.1604, and 0.036, respectively. Let $\tilde{\Phi} = [0.036, 0.1604]$. The gas flow through pipeline m in time slot t satisfies

$$GF_{m,t} \in \tilde{\Phi}_m (\Omega_{\mathcal{S}(m),t} - \Omega_{\mathcal{R}(m),t}), \forall m, \forall t. \quad (3.53)$$

In other words, the gas flow $GF_{m,t}$ is within the interval number produced by the right-hand side. We notice that there are some slight mismatches only when the gas flow is small. In the real setting, the gas flow will not be close to zero. Using the interval arithmetic [140], we can obtain interval based $G\tilde{S}F^0$. The calculation is sensitive to the width of $\tilde{\Phi}_m$. To facilitate the implementation and avoid singularity when performing the inverse of interval matrix, we shrink the lower and upper bounds of $\tilde{\Phi}_m$ towards the slope produced by one segment linearization. The right-hand side in (3.53) can be replaced using PTDF and gas injection, which leads to

$$GF_{m,t} \in \sum_{j=1}^J G\tilde{S}F_{m,j}^0 \times F_{j,t}^{\text{inj}}, \forall m, \forall t. \quad (3.54)$$

Therefore, the following constraint ensures the solution robustness:

$$-GF_m^{\max} \leq \sum_{j=1}^J G\tilde{S}F_{m,j}^0 \times F_{j,t}^{\text{inj}} \leq GF_m^{\max}, \forall m, \forall t. \quad (3.55)$$

Unlike the transmission constraints in (3.45), the pipeline constraints involve interval numbers without contingencies. Similarly, we can calculate $G\tilde{S}F_{m,j}^{m'}$ for each contingency and obtain the final interval based PTDF by

$$G\underline{S}F_{m,j} = \min(\min_{m'} G\underline{S}F_{m,j}^{m'}, G\underline{S}F_{m,j}^0), \forall m, \forall j, \quad (3.56a)$$

$$G\bar{S}F_{m,j} = \max(\max_{m'} G\bar{S}F_{m,j}^{m'}, G\bar{S}F_{m,j}^0), \forall m, \forall j, \quad (3.56b)$$

which establishes intervals $G\tilde{S}F_{m,j} = [G\underline{S}F_{m,j}, G\bar{S}F_{m,j}]$. The set of pipeline constraints can be then represented by the following interval based constraint:

$$-GF_m^{\max} \leq \sum_{j=1}^J G\tilde{S}F_{m,j} \times F_{j,t}^{\text{inj}} \leq GF_m^{\max}, \forall m, \forall t. \quad (3.57)$$

3.2.3 Reformulation of Interval Based Constraints

In the new CCUC problem, interval numbers exist in (3.47), (3.57), and (3.44). Therefore, we call it an interval CCUC problem. The interval numbers in inequality constraints are used to ensure the solution robustness, i.e., there is no violation under any realization of uncertainty. However, the interval numbers in equality constraints make the objective value and some decision variables to be interval numbers. Here, we discuss the reformulation of interval inequality constraints first. Substitute the injected power (3.44) at each bus into (3.47), and rearrange the

left inequality:

$$\begin{aligned} & \sum_{i=1}^I \tilde{S}F_{l,i} \left(\sum_{g \in \mathcal{G}(i)} P_{g,t} + \sum_{b \in \mathcal{B}(i)} \Delta D_{b,t}^E \right) - \sum_{i=1}^I \tilde{S}F_{l,i} \left(\sum_{k \in \mathcal{K}(i)} \Delta W_{k,t} + \sum_{a \in \mathcal{A}(i)} P_{a,t} \right) \geq \\ & - PF_l^{\max} + \sum_{i=1}^I \tilde{S}F_{l,i} \left(\sum_{b \in \mathcal{B}(i)} \tilde{D}_{b,t}^E - \sum_{k \in \mathcal{K}(i)} \tilde{W}_{k,t} \right), \forall l. \end{aligned} \quad (3.58)$$

All the decision variables are non-negative. The boundary condition of the right-hand side can be expressed as:

$$\sum_{i=1}^I \tilde{S}F_{l,i} \sum_{b \in \mathcal{B}(i)} \tilde{D}_{b,t}^E - \sum_{i=1}^I \tilde{S}F_{l,i} \sum_{k \in \mathcal{K}(i)} \tilde{W}_{k,t} - PF_l^{\max}, \quad (3.59)$$

whereas the corresponding two boundary conditions of the left-hand side can be expressed as:

$$\sum_{i=1}^I \tilde{S}F_{l,i} \left(\sum_{g \in \mathcal{G}(i)} P_{g,t} + \sum_{b \in \mathcal{B}(i)} \Delta D_{b,t}^E - \sum_{k \in \mathcal{K}(i)} \Delta W_{k,t} + \sum_{a \in \mathcal{A}(i)} P_{a,t} \right), \quad (3.60a)$$

$$\sum_{i=1}^I \tilde{S}F_{l,i} \left(\sum_{g \in \mathcal{G}(i)} P_{g,t} + \sum_{b \in \mathcal{B}(i)} \Delta D_{b,t}^E - \sum_{k \in \mathcal{K}(i)} \Delta W_{k,t} + \sum_{a \in \mathcal{A}(i)} P_{a,t} \right), \quad (3.60b)$$

By the boundary conditions, we can ensure the solution robustness under any realization of uncertainty. A similar process can be applied to the right inequality and interval based pipeline constraints (3.57). Post the reformulation, the total number of power flow constraints is $2L \times T$, reducing from $L \times T \times (L + 1)$. Other inequality constraints do not include interval coefficients, and therefore, remain unchanged.

The complete interval CCUC model includes (3.30)–(3.33), (3.36)–(3.39), (3.51), (3.52), (3.57), (3.59), and (3.60). The above interval CCUC is an interval mixed integer linear programming problem. The unit commitment decisions are determined in the first stage, whereas other decisions are set in the second stage. The load and generation in (3.36) are interval numbers, which ensures that for any realization of load and renewable generation, the unit commitment decisions can serve the load. Therefore, the auxiliary services are considered inherently in this model. However, it makes the decision variables and objective values be interval numbers. This requires us to further reformulate constraints (3.32d) and (3.32e), where the decision variables in t are coupled with those in $t - 1$. Without loss of generality, we can consider the total net load in t by combining load and renewable generation as follows:

$$\tilde{d}_t = \sum_{b=1}^B \tilde{D}_{b,t}^E - \sum_{k=1}^K \tilde{W}_{k,t}, \forall t. \quad (3.61)$$

Let $\tilde{\mathbf{d}} = [\mathbf{d}, \bar{\mathbf{d}}]$ be the vector of independent intervals \tilde{d}_t and $\tilde{z}^*(\tilde{\mathbf{d}})$ be the corresponding objective value in (3.30). The following theorem characterizes the monotonicity of $\tilde{z}^*(\tilde{\mathbf{d}})$ with

respect to $\tilde{\mathbf{d}}$, the proof of which follows Theorem 4 in [141].

Theorem 1. For a given set of unit commitment decisions, the lower and upper bounds of \tilde{z}^* and generation decisions \tilde{P}_g^* for generator g can be obtained at $\underline{\mathbf{d}}$ and $\bar{\mathbf{d}}$, respectively.

It is worth mentioning that Theorem 1 will not hold if a high penalty for wind curtailment is applied.

We consider two sets of second stage decisions, denoted by \mathbf{x}^L and \mathbf{x}^U . The first set is associated with the lower bound of \tilde{z}^* where the net load is $\underline{\mathbf{d}}$. Another set is obtained at $\bar{\mathbf{d}}$. The ramp rate constraints (3.32d) and (3.32e) should hold for four cases: $P_{g,t}^L - P_{g,t-1}^U$, $P_{g,t}^L - P_{g,t-1}^L$, $P_{g,t}^U - P_{g,t}^L$, and $P_{g,t}^U - P_{g,t}^U$. The group of special ramp up/down constraints are added, which guarantees the feasibility of economic dispatch decisions under some extreme ramp realizations. The two sets of second stage decisions are decoupled in other constraints, but they need to hold independently. For example, the capacity constraints of P2G in (3.33) become:

$$P_{a,t}^L \leq P_a^{\max}, \forall a, \forall t, \quad (3.62a)$$

$$P_{a,t}^U \leq P_a^{\max}, \forall a, \forall t. \quad (3.62b)$$

3.2.4 Fuzzy Preference between Interval Numbers

The interval numbers in equality constraints make the objective value be an interval number, where we use two sets of decisions to obtain the lower and upper bounds. However, there arises one question relating to the comparison of any two interval numbers. For example, one can choose to start up a unit or curtail load for a system with net demand $[0, 10]$ units. Let the no-load cost be \$20, the fuel cost be \$2 per unit, and penalty for load shedding be \$5 per unit. The costs are $\$[20, 40]$ and $\$[0, 50]$ respectively. The midpoint (expected cost) of the first cost is larger, but the width (risk) is smaller. Moreover, the two sets of decisions only reflect the cost of minimum and maximum realizations without information about other possible realizations. We need to modify the objective function based on the lower and upper bounds. To compare such two interval numbers, we introduce fuzzy preference.

The approach on comparing two interval numbers for maximization problems is presented in [142]. We derive the approach for minimization problems as follows. To guide the analysis, we assume that less money is better than more money, less uncertainty is better than more uncertainty, and if less money is associated with more uncertainty, the decision maker must make a trade-off. Let $\mathbb{M}(\tilde{Z})$ be the midpoint of interval number \tilde{Z} and $\mathbb{W}(\tilde{Z})$ be the half-width. For any pair of interval numbers \tilde{A} and \tilde{B} , without loss of generality, we can assume that $\mathbb{M}(\tilde{A}) < \mathbb{M}(\tilde{B})$. We have $\mathbb{W}(\tilde{A}) \leq \mathbb{W}(\tilde{B})$ or $\mathbb{W}(\tilde{A}) > \mathbb{W}(\tilde{B})$. For a minimization problem, \tilde{A} is always the best choice when $\mathbb{W}(\tilde{A}) \leq \mathbb{W}(\tilde{B})$. We define the fuzzy set B' in $\psi = \{(\tilde{A}, \tilde{B}) \mid \mathbb{M}(\tilde{A}) < \mathbb{M}(\tilde{B}), \mathbb{W}(\tilde{A}) > \mathbb{W}(\tilde{B})\}$ with membership function $\mu_{B'}(\tilde{A})$ where $\mu_{B'}(\tilde{A}) \in [0, 1]$ by

$$\mu_{B'} = \max \left\{ 0, \frac{\mathbb{M}(\tilde{A}) + \mathbb{W}(\tilde{A}) - [\mathbb{M}(\tilde{B}) + \mathbb{W}(\tilde{B})]}{\mathbb{W}(\tilde{A}) - \mathbb{W}(\tilde{B})} \right\}. \quad (3.63)$$

If $\mu_{B'} = 1$, then \tilde{B} is definitely accepted, whereas \tilde{B} is definitely rejected if $\mu_{B'} = 0$. Otherwise, the selection depends on the optimistic degree of acceptance of \tilde{B} . Note that if the decision maker chooses a zero optimistic degree, the problem becomes robust optimization under interval uncertainty.

Let ξ denote the optimistic degree of the decision maker and \preceq denote “less than” relationship between two interval numbers. We have the following:

$$\tilde{A} \preceq \tilde{B}, \text{ if } \mu_{B'}(\tilde{A}) \leq \xi, \quad (3.64a)$$

$$\tilde{A} \succ \tilde{B}, \text{ if } \mu_{B'}(\tilde{A}) > \xi. \quad (3.64b)$$

Two sets of second stage decisions lead to the lower and upper bounds of the objective value for a given set of unit commitment decisions. However, the goal of CCUC is to select the set of unit commitment decisions, i.e., we need to reformulate the objective function based on (3.64) so that we can obtain the optimal unit commitment decisions through one optimization problem.

Theorem 2. For a CCUC problem, it is sufficient to minimize $(1 - \frac{\xi}{2})z(\mathbf{x}^U) + \frac{\xi}{2}z(\mathbf{x}^L)$. It produces the best interval defined by the relationship (3.64).

Proof. Let \mathbf{x}_1^* and \mathbf{x}_2^* be the solution of optimization problem

$$\begin{aligned} \min & \quad (1 - \frac{\xi}{2})z(\mathbf{x}^U) + \frac{\xi}{2}z(\mathbf{x}^L) \\ \text{s.t.} & \quad (\mathbf{x}^U, \mathbf{x}^L) \in \mathcal{X}. \end{aligned}$$

$\forall (\mathbf{x}_1, \mathbf{x}_2) \in \mathcal{X}$, we have the following:

$$\begin{aligned} (1 - \frac{\xi}{2})z(\mathbf{x}_1^*) + \frac{\xi}{2}z(\mathbf{x}_2^*) &\leq (1 - \frac{\xi}{2})z(\mathbf{x}_1) + \frac{\xi}{2}z(\mathbf{x}_2), \\ (1 - \frac{\xi}{2})\bar{z}^* + \frac{\xi}{2}z^* &\leq (1 - \frac{\xi}{2})\bar{z} + \frac{\xi}{2}z. \end{aligned}$$

Rearrange the equation, we have

$$\bar{z}^* - \bar{z} \leq \frac{\xi}{2}(\bar{z}^* - z^* - \bar{z} + z).$$

The membership function is defined on $\mathbb{W}(z^*) > \mathbb{W}(z)$, therefore we have

$$\frac{2(\bar{z}^* - \bar{z})}{(\bar{z}^* - z^* - \bar{z} + z)} \leq \xi.$$

We replace the midpoint and half-width in membership function (3.63) using the upper and

lower bounds, the membership function can be written as:

$$\mu_{z'}(z^*) = \frac{2(\bar{z}^* - \bar{z})}{(\bar{z}^* - z^* - \bar{z} + z)} \leq \xi.$$

Moreover, the inequality always holds for the case where $\mathbb{M}(z^*) < \mathbb{M}(z)$ and $\mathbb{W}(z^*) \leq \mathbb{W}(z)$. $\xi \in [0, 1]$, we have

$$(1 - \xi)\mathbb{M}(z^*) + \mathbb{W}(z^*) \leq (1 - \xi)\mathbb{M}(z) + \mathbb{W}(z).$$

By substituting the midpoint and half-width by the upper and lower bounds, we immediately obtain

$$\left(1 - \frac{\xi}{2}\right)\bar{z}^* + \frac{\xi}{2}z^* \leq \left(1 - \frac{\xi}{2}\right)\bar{z} + \frac{\xi}{2}z.$$

For the case where $\mathbb{M}(z^*) \geq \mathbb{M}(z)$, a similar proof follows by considering the membership function $\mu_{z^{*'}}(z)$. \square

Using Theorem 2, the objective function in (3.30) can be modified as follows:

$$\begin{aligned} \min \sum_{t=1}^T & \left[\sum_{g=1}^G \left(C_g^{\text{NL}} u_{g,t} + C_g^{\text{U}} y_{g,t} + C_g^{\text{D}} z_{g,t} \right) \right. \\ & + \left(1 - \frac{\xi}{2}\right) \left(\sum_{o=1}^O C_o(P_{o,t}^{\text{U}}) + \pi \sum_{s=1}^S F_s^{\text{S,U}} + \pi^{\text{E}} \sum_{b=1}^B \Delta D_{b,t}^{\text{E,U}} + \pi^{\text{G}} \sum_{n=1}^N \Delta D_{n,t}^{\text{G,U}} \right) \\ & \left. + \frac{\xi}{2} \left(\sum_{o=1}^O C_o(P_{o,t}^{\text{L}}) + \pi \sum_{s=1}^S F_s^{\text{S,L}} + \pi^{\text{E}} \sum_{b=1}^B \Delta D_{b,t}^{\text{E,L}} + \pi^{\text{G}} \sum_{n=1}^N \Delta D_{n,t}^{\text{G,L}} \right) \right]. \end{aligned} \quad (3.65)$$

The second line in (3.65) represents the cost under the upper bound and is associated with the term $(1 - \frac{\xi}{2})z(\mathbf{x}^{\text{U}})$ in Theorem 2, whereas the third line is corresponding to the cost under the lower bound. The optimistic decision maker prefers to minimize the expected cost whereas the pessimistic one cares more about the worst-case and tries to minimize the upper bound. When zero optimistic degree is chosen, the problem becomes robust optimization under box uncertainty. Regarding robust optimization with other uncertainty regions such as ball and polyhedral, interval optimization cannot be directly applied. This objective function also highlights the advantage of our method: one only needs to solve one deterministic mixed integer linear programming problem by mapping two extreme points instead of solving a large-scale stochastic optimization problem.

3.2.5 Case Studies

We verify the effectiveness of our interval CCUC model. First, we verify whether the reformulation of constraints in our model can ensure the solution robustness. Second, we investigate

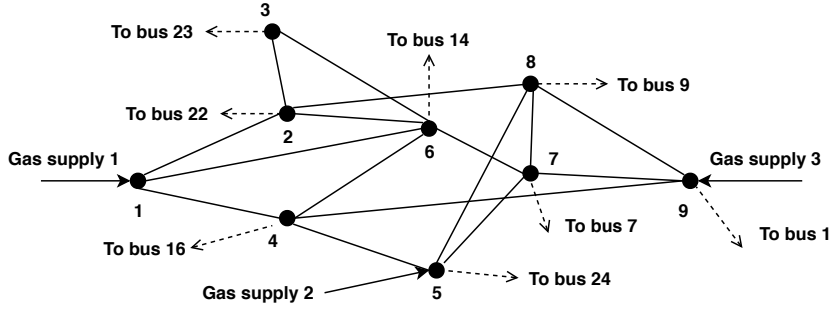


Figure 3.8: 9-node natural gas network.

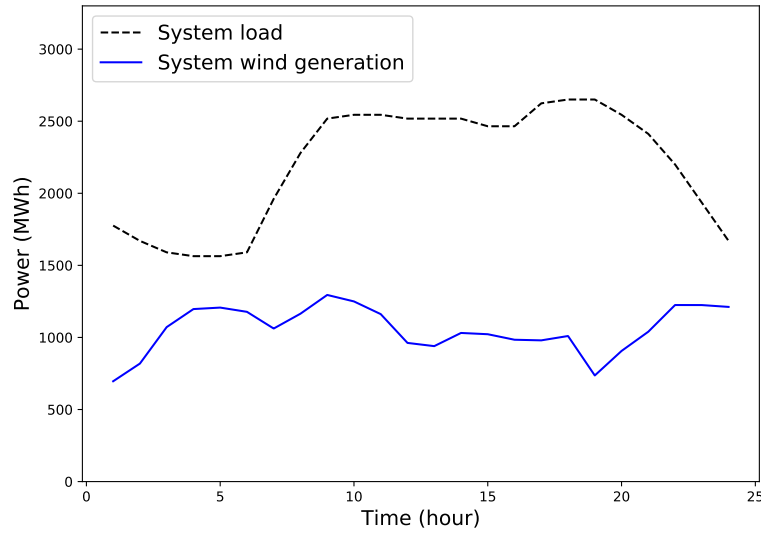


Figure 3.9: System demand and wind generation profile.

how the selection of slack nodes in the gas system and the optimistic degrees of decision maker influence the results. Third, we show the economic savings introduced by P2G. The calculation of interval PTDF for the gas system is implemented by Python library *Mpmath*.

A modified IEEE 24-bus electric system coupled with a 9-node natural gas network is used for the case study. The 24-bus power system is properly modified to accommodate six wind farms, and details about topology and data can be found in [123]. To avoid islanding, we add one transmission line between bus 2 and 7 with 50 MVA capacity. A 9-node natural gas network with 16 pipelines is modified from the 11-node network in [137]. As shown in Fig. 3.8, we assume that there are 3 gas supplies and two systems are coupled through 8 buses (dashed line). Two P2Gs are installed at bus 7 and bus 14 with capacity 200 MW and 350 MW, respectively. The efficiencies of gas-fired generators and P2Gs are set to 0.6 and 0.75. Forecast error of each wind farm is assumed to be within 20% (uncertainty level) of its forecast value, which leads to $\tilde{W} = [0.8W, 1.2W]$ whereas the uncertainty level of load is set to 5%. The expected wind penetration is set to 38%. The expected system load and wind profiles are given in Fig. 3.9.

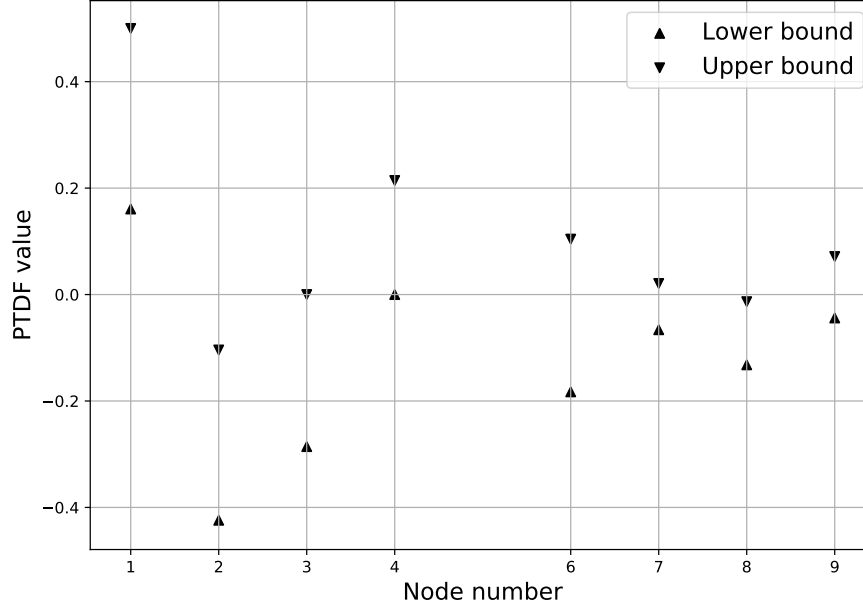


Figure 3.10: Interval based power transfer distribution factor of the pipeline from node 1 to 2.

It should be noted that the curve for wind is the total generation of six farms, i.e., the capacity of each single farm is 200 MW. The gas price, electric load shedding penalty, and gas demand shedding penalty are set to \$3.42/Mcf, \$5000/MW, and \$1500/Mcf, respectively.

To illustrate the interval PTDF for the natural gas system, intervals of PTDF of the pipeline connecting node 1 and 2 are given in Fig. 3.10. There are 16 possible contingencies for the gas system. Each contingency generates one interval. By combining 16 intervals with the interval PTDF generated by the case without contingency, we can obtain the final interval based PTDF. Node 5 is selected to be the slack node, and therefore, we leave it blank. The injection at the first node always tends to increase the gas flow in this pipeline because the underlying assumption is that the injection flows to node 5.

The interval based constraints are reformulated by the boundary conditions. It significantly reduces the problem size and guarantees that the system can survive with any loss of components. However, (3.59) and (3.60) introduce conservativeness because it ignores the correlation between the uncertain PTDF values. To examine the conservativeness and ensure that the model maintains the solution robustness, we evaluate the unit commitment decisions under different realizations. We include load shedding in our problem. To reflect the possible infeasibility, we set a large penalty. If the unit commitment decisions obtained from the model cannot meet some realizations, then, the load shedding occurs and increases the realized cost dramatically. Therefore, we first solve the CCUC problem and fix the unit commitment decisions. For each realization, we then solve an economic dispatch problem. In the dispatch problem, we replace interval PTDFs using the PTDF for the corresponding realization of contingencies. To make the problem feasible for our setting, we increase the capacity of transmission line between bus

Table 3.5: Realized Cost for Unit Commitment Decisions Obtained by the Proposed Model.

Contingency	$\epsilon = -0.2$	$\epsilon = -0.1$	$\epsilon = 0$	$\epsilon = 0.1$	$\epsilon = 0.2$
None	511.7	570.6	630.3	691.7	755.4
T_{7-8}	511.7	570.6	630.3	692.0	756.1
T_{16-17}	511.7	570.6	630.3	691.7	755.6
T_{19-20}	511.7	570.6	630.3	691.8	755.7
P_{2-3}	511.7	570.6	630.3	691.7	755.5

Table 3.6: CPU Time for 24-Bus System and 118-Bus System.

System	24-bus	118-bus
CPU time (sec)	3.82	13.04

14 and 16 to 1000 MW. The forecast error of net load, ϵ , is increased from -0.2 to 0.2 by 0.1. The CCUC problem gives an interval objective value as $\$[511.5, 766.7]k$. The results of each realization are shown in Table 3.5. Contingency type $T_{i,i'}$ denotes contingency for transmission line between bus i and i' , whereas $P_{j,j'}$ denotes contingency for pipeline between node j and j' . The unit of cost is $\$k$. We only show four types of contingencies, which are the worst cases. We observe that there is no violation for all the realizations because no load shedding occurs. This shows that the reformulation of interval inequality constraints still maintains the solution robustness. Moreover, the interval representation of PTDF for gas systems can successfully capture all possible contingencies.

We can immediately observe from Table 3.5 that Theorem 1 is correct. For any realization of contingency, the lowest economic dispatch cost happens at $\epsilon = -0.2$, i.e., the net load is lowest. When the net load is low, the economic dispatch costs under different contingencies are close to those under base case without contingency. Some constraints become binding if the net load is at $\epsilon = 0.2$ for the worst-case contingency. For a lower net load, those constraints are less severe and do not change the optimal solution. Compared with the interval objective value ($\$[511.5, 766.7]k$) produced by CCUC, the lower bound does not show conservativeness. The worst realization is $\$756.1k$ whereas the upper bound of interval objective value is $\$766.7k$. This shows that the reformulation of interval inequality constraints induces conservativeness.

We also test the proposed method on a 118-bus power system. The interval objective value is $\$[341.4, 509.5]k$, and the realizations lie in the range $\$[350.8, 476.9]k$. It shows that there is no violation on constraints for a large system. The CPU time for each system is reported in Table 3.6. The proposed model only needs to solve a problem including two extreme scenarios instead of solving a large-scale stochastic optimization problem. Therefore, solution can be obtained quickly even for a large system.

We assume that there exists a slack node in the gas system. Another issue needs to be addressed is that the influence of the selection of slack node. We change the slack node from node 1 to 9 and examine the lower and upper bounds for each case. If node 3 is selected to

Table 3.7: The Lower and Upper Bounds Produced by Selecting Different Slack Nodes.

Slack node	Lower bound (\$k)	Upper bound (\$k)
1	508.1	758.7
2	508.0	756.8
4	508.3	760.8
5	511.5	766.7
6	508.0	759.7
7	508.0	758.7
8	508.0	759.0
9	508.2	760.6

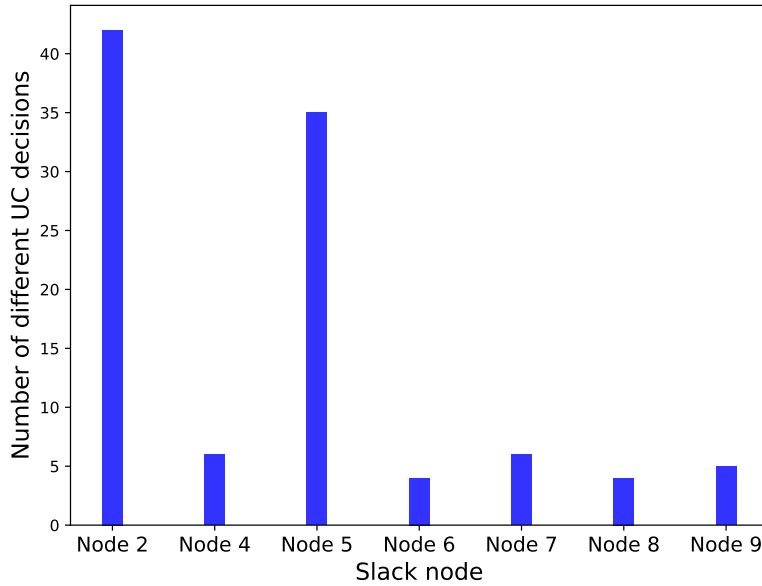


Figure 3.11: Number of different unit commitment decisions by selecting different slack nodes.

be the slack node, the calculation of PTFDF suffers singularity issue, and we omit this case. Other results are summarized in Table 3.7. It shows that the lower and upper bounds of cost change when the slack node changes. Most selections generate similar bounds, i.e., the cost is not sensitive to the selection of slack node.

Compared with the cost, the decision maker may be more interested in the change of unit commitment decisions. We investigate the unit commitment decisions under different selections of slack nodes. There are 12 generators in this system. The total number of binary variables is $12 \times 24 = 288$. We consider the case where node 1 is selected to be the slack node as the base case, and we show how many variables are different in other cases. As shown in Fig. 3.11, most cases generate similar unit commitment decisions.

To compare the interval numbers, we introduce the degree of optimism. As the degree

Table 3.8: Sensitivity Analysis of the Optimistic Degree.

Optimistic degree	Lower bound (\$)	Upper bound (\$)	Middle point (\$)
0	518,494	766,260	642,377
0.05	513,845	766,262	640,054
0.1	513,389	766,283	639,836
0.2	512,932	766,321	639,626
0.4	512,018	766,493	639,255
0.6	511,457	766,681	639,069
1	511,457	766,681	639,069

increases, the decision maker is less sensitive to the uncertainties and aims to minimize the mid-point of the cost interval (expected cost). The pessimistic decision maker cares more about the largest possible cost. When the decision maker tolerates no uncertainty (i.e., $\xi = 0$), the model becomes a worst-case optimization problem. Different degrees of optimism may lead to different sets of unit commitment decisions and different resulting cost intervals. Table 3.8 shows the sensitivity analysis of the optimistic degree. We change ξ from 0 to 1 and examine the lower and upper bounds. The monotonicity of both bounds and mid-point follows our analytical analysis. The lower bound and mid-point are decreasing (non-increasing) in ξ whereas the upper bound is increasing in ξ . One can verify that the width of intervals is increasing. The interval costs are the same for $\xi \in [0.6, 1]$, and we only list $\xi = 0.6$ and $\xi = 1$.

When $\xi = 0$, the decision maker only considers the worst realization, and the upper bound is the smallest. However, the set of unit commitment decisions produced by the worst realization leads to a higher cost for realizations with lower net load. By increasing the optimistic degree, the decision maker makes a tradeoff between cost uncertainty and expected cost. We observe that the interval cost is not sensitive to the optimistic degree. For our problem, the degree is only applied in the objective value, and our model ensures that the constraints will never be violated for any realization. Thus, the optimistic degree cannot fully represent the decision maker's attitude toward risk, and the resulting intervals are not sensitive to the selection of ξ . However, the model can be easily extended to the case where the decision maker allows violation of constraints. Moreover, if we increase the renewable penetration, the degree has more effects on the interval cost.

In consideration of P2G, the excess wind generation can be converted into natural gas. The produced natural gas can be used to serve gas demand or transmitted to supply gas-fired generator via gas system in case of congestion in transmission lines. Moreover, the unit commitment decisions are determined based on both maximum and minimum net load realizations. Without P2G, some generating units must be online to meet the worst case. However, those units are not necessary for the best case (i.e., the net load is at the minimum). By incorporating P2G in integrated energy systems, such reserves can be reduced. P2G can convert power in the worst realization whereas reduce its power to serve electric load quickly in the best realization. To

Table 3.9: Comparison of Operation Cost with and without the Use of P2G.

	Lower bound (\$)	Upper bound (\$)
With P2G	412,689	692,126
Without P2G	420,940	694,269

investigate this ability, we increase the capacity of each wind farm to 250 MW, which leads to 48% wind penetration. In the rest of the analysis, the optimistic degree is selected to be 1.

Table 3.9 shows the comparison of operation cost with and without the use of P2G. P2G reduces the operation cost by \$8,251 for the best case, whereas the saving is \$2,143 in the worst case. The power of P2G in the worst case is always 0. That means that the cost is reduced by shutting down some unnecessary units, which demonstrates that P2G offers auxiliary services directly. Regarding the best case, excess wind generation will be converted into natural gas, thus reducing the total gas supply. The reduced gas supply cost is \$3,127 in this case, and the economic saving brought by other abilities is \$5,124. It shows that auxiliary and regulatory power service offered by P2G can reduce more operation cost than that reduced by absorbing excess renewable generation. Over the above premises, the decision maker should consider this ability when doing unit commitment scheduling. To further investigate the economic value of P2G, we change the capacity of transmission line between bus 7 and 8 from 350 to 150 MVA. The change leads to wind curtailment due to congestion. The lower bounds for the case with and without use of P2G are \$423,713 and \$440,849. The upper bounds are \$704,534 and \$711,306. The reduced costs are \$17,136 and \$6,772. Compared with the results in Table 3.9, the values are larger. By reducing the line capacity, wind generation at bus 7 is subject to curtailment. In this setting, there exists wind curtailment even in the worst case because of transmission congestion. With the use of P2G, more curtailed generation is converted into natural gas. Therefore, we can observe a huge increase in the savings.

We split the total reduced cost into two categories: reduced gas supply cost and other reduced cost. Fig. 3.12 shows the values of each type in different cases. We also observe that the reduced gas supply cost only takes a small share. Again, it demonstrates that the reduced operation cost due to auxiliary and regulatory power service offered by P2G is not trivial and cannot be ignored. However, the savings decrease if we decrease the optimistic degree. By reducing the tolerance, say $\xi = 0$, the CCUC problem becomes a deterministic problem where reserves are not considered. Therefore, the only economic value of P2G is introduced by converting excess generation.

The operation of P2G is based on one important assumption: there exists excess renewable (or at least cheap) electric generation. We change the wind penetration and examine the economic value of P2G. The results are summarized in Table. 3.10. The P2G brings no economic value when the renewable penetration is low. For an integrated energy system with low renewable penetration, renewable curtailment rarely happens, and the power of P2G is always 0. However, if we impose transmission congestion by reducing the capacity of transmission line

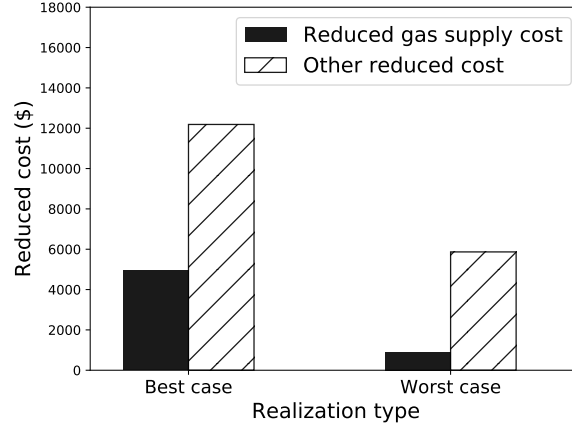


Figure 3.12: Illustration of the reduced cost.

Table 3.10: Change in Cost with Different Wind Penetration Levels

Penetration	With P2G (\$)	Without P2G (\$)
30%	[610.0, 841.5]	[610.0, 841.5]
40%	[497.3, 757.8]	[499.5, 757.8]
50%	[393.3, 676.5]	[403.7, 678.5]
60%	[304.0, 603.7]	[332.0, 606.4]
80%	[199.0, 475.1]	[250.8, 484.7]

between bus 7 and 8, P2G still brings some savings. For the integrated energy system in consideration, if the expected renewable penetration reaches 40%, P2G can reduce the operation cost in the best case. The reduced cost increases as the penetration increases. With the long-term goal of developing renewable source based energy systems, P2G can play an important role in realizing efficient and secure operation of the renewable-based integrated energy systems.

3.3 Conclusion and Discussion

The integration of natural gas and power systems is another promising method for improving renewable integration. First, fast start-up flexibility and ramp rates of gas-fired units make the gas-fired units suitable for providing the operating reserves. The flexibility can be used to hedge the renewable variability in the intra-hour operation. Besides, power-to-gas can offer auxiliary and regulator power service. From the perspective of long-term operation, power-to-gas provides a means of long-term storage. Due to the seasonal characteristic of renewable energy and load, power-to-gas can absorb excess renewable generation in peak seasons, which can then be supplied to meet natural gas loads or stored to serve electric load in off-peak seasons using gas-fired generators. The coupling of natural gas and power systems ensures that all the available renewable energy can be adopted. In this regard, the planning and scheduling of integrated natural gas and power systems is studied, in which the role of power-to-gas is

highlighted.

This dissertation first develops an expansion co-planning model for the integrated power and gas systems where uncertainties in both systems are considered. Moment matching is used to generate scenarios that can encapsulate all possible evolution of random variables. The selection of parameters for moment matching is discussed. A scenario based decomposition scheme called branch-and-price is applied to solve the problem, which relieve the computational difficulty.

Experimental results demonstrate that the proposed scheme outperforms the state-of-the-art methods. Most importantly, case studies show the economic value of power-to-gas technology in low-carbon oriented planning as well as the contribution of power-to-gas to renewable integration. However, some components in water and heat systems may also enhance the penetration of renewable energy. In future work, I will extend the model to accommodate the expansion of heat and water networks.

Next, we present an interval optimization framework of contingency-constrained unit commitment for the integrated power and gas system. Uncertainties from renewable generation, load, and contingencies are captured by interval numbers. An interval based power transfer distribution factor is introduced for the natural gas system. The model sheds light on how to optimally operate an integrated energy system with high renewable penetration satisfying $N - 1$ contingency criterion.

Experimental results demonstrate that the unit commitment decisions produced by the model can ensure solution robustness under any type of realization. The influence of selecting different hyper-parameters is carefully examined by sensitivity analysis. The case study shows that P2G can reduce the operation cost by offering auxiliary and regulator power service, and the savings are not trivial and should be considered when doing unit commitment scheduling. The use of P2G reduces renewable curtailment. However, the framework has some drawbacks which can be addressed in future work such as including physical constraints of pressure loss and compressors, and extending the method for radial (weak meshed) network. Most importantly, the probability of a contingency is low, but contingencies are included for the daily operation in this work. It is necessary to examine if the increased cost of considering contingencies, especially for pipeline contingencies, can hedge the potential financial losses when contingencies happen. On the other hand, the proposed method is not compared with other methods, which can be addressed in future work.

CHAPTER

4

ENERGY TRADING PARADIGMS

The rapid penetration of DERs is transforming the traditional centralized power grid management to a decentralized, active, and localized control paradigm. In this Chapter, we focus on two energy trading paradigms that can potentially enhance the renewable integration.

With the maturity of power-to-gas (P2G) technology, energy hubs become a key element in the vision of future energy networks. Energy hubs act as retailers of different energy carriers due to the emergence of the integrated energy system. Generally, energy hubs are equipped with storage of different energy sectors and can convert energy between different sectors promptly. Therefore, we first study the decision making problem of an energy hub, in which the energy hub optimally involves in the gas and electricity markets. When the renewable generation is high (i.e., the electricity price is low), the energy hub acts as a buyer in the electricity market and a seller in the gas market. When the renewable generation is low (i.e., the electricity price is high), the energy hub buys natural gas and sells electricity. In this way, the fluctuation of renewable generation can be hedged.

New regulations such as the recent FERC Order 2222 in the U.S. open the door to DERs in the wholesale markets. The development of platforms such as blockchain technology based paradigms provides a way for developing the markets of transactive energy that ensures transparency, choice, privacy and ease of use to the consumers. Over the past few years, there has been a significant interest in the economic mechanisms for transactive energy. The effectiveness of energy trading has been verified in works such as [74, 75]. We propose a continuous double auction (CDA) based mechanism for decentralized electricity trading, and again, study the optimal trading strategies.

4.1 Optimal Trading Strategies for Trading between Gas and Electricity Markets

An energy hub, which is considered as a unit where multiple energy carriers can be converted, conditioned, and stored, becomes a key element in future energy networks due to the emergence of the integrated energy system. Much is unknown about the management of energy hubs, for instance, how much energy to convert, how much energy to store, and how relevant it is to different factors such as prices. We answer these questions by formulating the trading decision making problem for energy hubs as a dynamic program.

The energy hubs own both the electric and gas storage. As for the energy conversion, the energy hubs have the options of converting electricity to natural gas, i.e., in P2G mode, and converting natural gas to electricity, i.e., in gas-to-power (G2P) mode. For example, P2G technology can convert electricity to natural gas whereas G2P mode can be achieved by generating electricity using gas fired generator. We assume that the energy hub is small enough compared to the market, so that the decisions would not affect the prices. The manager makes trading decisions over a finite horizon $t \in \mathbb{T} := \{0, 1, \dots, T\}$, and any energy left in the storage at the end of the scheduling horizon is worthless. We assume that the capacity of the storage and the capacity of the conversion are limited, but the line capacities of both energy carrier are large enough. Although only the electricity and gas markets are considered in this dissertation, the model can be extended to incorporate other energy sections such as water and heat.

4.1.1 Uncertainties and Variables

Modeling the Uncertainty

We consider the evolution of prices of natural gas and electricity as random processes. Wind generation depending on wind speed is also random. We model the prices as a mean-reverting process. Let P^G and P^E be the gas price and electricity price. Accordingly, we assume a discrete time version as the following equations:

$$P_{t+1}^G = P_t^G + k^G(\mu^G - P_t^G) + \hat{P}_{t+1}^G, \forall t, \quad (4.1)$$

$$P_{t+1}^E = P_t^E + k^E(\mu^E - P_t^E) + \hat{P}_{t+1}^E, \forall t, \quad (4.2)$$

where k^G and k^E are the mean-reversion rates which govern the speed of reversion to the mean price μ^G and μ^E respectively; The random variables \hat{P}_{t+1}^G and \hat{P}_{t+1}^E are i.i.d with distribution $\mathcal{N}(0, \sigma_G^2)$ and $\mathcal{N}(0, \sigma_E^2)$, which include noises in the evolution of prices.

Unlike the price model, a seasonality term is used to correct wind generation. We model the wind generation as the sum of an autoregressive process with order 1, i.e., AR(1), and a seasonality function $S(t)$:

$$W_{t+1} = \alpha_{\text{wind}}W_t + \hat{W}_{t+1} + S(t), \forall t, \quad (4.3)$$

where α_{wind} is a scalar, and $\hat{W}_{t+1} \sim \mathcal{N}(0, \sigma_{\text{wind}}^2)$ is an i.i.d term. The seasonality $S(t)$ is

$$S(t) = A + \gamma \cos[(t + \omega)2\pi/24], \forall t, \quad (4.4)$$

where A is a constant level, γ and ω are the magnitude and the phase shift of the hourly seasonality, respectively. It is worth noting that (4.1) and (4.2) can be converted to AR(1) process with $\alpha_1 = 1 - k$ and $\hat{P}_{t+1} \sim \mathcal{N}(\mu k, \sigma^2)$.

State Variables

State variables with subscript t are known in period t . The state of the problem in consideration includes:

- W_t : the wind generation produced in period t in MWh;
- P_t^G : the price of gas in period t in \$/mcf;
- P_t^E : the price of electricity in period t in \$/MWh;
- IG_t : the state of charge of the gas storage in period t in mcf.
- IE_t : the state of charge of the electric storage in period t in MWh.

Then, state S_t can be defined as $(W_t, P_t^G, P_t^E, IG_t, IE_t)$.

Decision Variables

Decision variables with subscript t are optimized in period t . Decision variables include:

- E_t : the quantity of electricity to sell or buy in period t in MWh.
- G_t : the quantity of gas to sell or buy in period t in mcf.
- A_t^{p2g} : the power of P2G or G2P in period t in MWh.

Although G2P and P2G are not the same equipment, they will never both be on at the same time due to the loss of energy during conversion. In order to reduce the decision space, we use one decision variable to denote their operation. If $A_t^{\text{p2g}} < 0$, the converter is operating in G2P mode; if $A_t^{\text{p2g}} \geq 0$, the converter is operating in P2G mode. Similarly, if the energy hub is selling energy, $E_t > 0$ or $G_t > 0$, and vice versa.

It should be noted that two equations of energy balance should be considered, which give the operation of storage:

$$A_t^e = W_t - A_t^{\text{p2g}} - E_t, \forall t, \quad (4.5)$$

$$A_t^g = F_t^{\text{p2g}} - G_t, \forall t, \quad (4.6)$$

where A_t^e and A_t^g are the charging rates of storage in MWh and mcf, respectively. F_t^{p2g} is the gas flow injection associated with the conversion of A_t^{p2g} . A control sequence $\{\pi_t(E_t, G_t, A_t^{\text{p2g}}), t \in \mathbb{T}\}$ is used to denote decisions.

4.1.2 Problem Formulation

Dynamic Equation

The wind generation and prices are determined by the random processes. The states of charge of gas storage and electric storage are determined by the charging or discharging rates. If $A_t^e < 0$ or $A_t^g < 0$, the storage is discharging. The transitions of storage are given below:

$$LE_{t+1}(S_t, \pi_t) = \begin{cases} \min \{IE_{\max}, IE_t + \eta_e A_t^e\} & \text{if } A_t^e \geq 0, \\ \max \{0, IE_t + \frac{1}{\eta_e} A_t^e\} & \text{if } A_t^e < 0, \end{cases} \quad (4.7)$$

$$LG_{t+1}(S_t, \pi_t) = \begin{cases} \min \{IG_{\max}, IG_t + \eta_g A_t^g\} & \text{if } A_t^g \geq 0, \\ \max \{0, IG_t + \frac{1}{\eta_g} A_t^g\} & \text{if } A_t^g < 0, \end{cases} \quad (4.8)$$

where IE_{\max} and IG_{\max} are the maximum capacities of electric storage and gas storage; η_e and η_g are the efficiencies of electric storage and gas storage. The state dynamic equation is given by:

$$S_{t+1} = T(S_t, \pi_t) = (W_{t+1}(W_t), P_{t+1}^G(P_t^G), P_{t+1}^E(P_t^E), LG_{t+1}(IG_t, \pi_t), LE_{t+1}(IE_t, \pi_t)). \quad (4.9)$$

Revenue to Go

In period t , the intermediate revenue is given by:

$$R(S_t, \pi_t) = E_t P_t^E + G_t P_t^G. \quad (4.10)$$

The decision variables are feasible if and only if all the following constraints hold:

$$-A_{g2p}^{\max} \leq A_t^{p2g} \leq A_{p2g}^{\max}, \quad (4.11a)$$

$$-A_e^{\max} \leq A_t^e \leq A_e^{\max}, \quad (4.11b)$$

$$-A_g^{\max} \leq A_t^g \leq A_g^{\max}, \quad (4.11c)$$

$$F_t^{p2g} = 3.412 \eta_{p2g} A_t^{p2g}, \quad \text{if } A_t^{p2g} \geq 0, \quad (4.11d)$$

$$F_t^{p2g} = \frac{3.412}{\eta_{p2g}} A_t^{p2g}, \quad \text{if } A_t^{p2g} < 0, \quad (4.11e)$$

where (4.11d) and (4.11e) give the conversion between the quantity of electricity and the quantity of gas.

Our goal is to maximize the total revenue over the time horizon \mathbb{T} . A feasible decision set Π will not change with states or actions. The total revenue can be defined as:

$$\max_{\pi \in \Pi} \sum_{t=0}^T \mathbb{E}[R(S_t, \pi_t) | S_0], \quad (4.12)$$

where S_0 is the initial state.

A recursive function can be formulated to solve the problem in a dynamic programming framework. The maximum revenue to go in period t given S_t can be obtained as:

$$J_t(S_t) = \max_{\pi_t \in \Pi} \{R(S_t, \pi_t) + \mathbb{E}[J_{t+1}(S_{t+1}) | (S_t, \pi_t)]\}, \quad (4.13)$$

where the boundary condition is: $J_{T+1}(S_{T+1}) = 0, \forall S_{T+1}$.

4.1.3 Optimal Policies

We assume the mean-revision rates of price models are less than 1. To ensure boundedness, we consider 95% of the values of the normal distribution that lie within two standard deviations, and scale the probability density by $\frac{1}{0.95}$. For the problem initialization, we assume the initial prices in period $t = 0$ are the mean price.

An Extreme Case

Lemma 3. For every period $t \in \mathbb{T}$, P_t^G and P_t^E are bounded, given μ , σ and k .

Proof. P_t^G is bounded by $\mu^G - 2t\sigma_G + 2(t-1)k\sigma_G$ and $\mu^G + 2t\sigma_G - 2(t-1)k\sigma_G$. In period $t = 1$, we have $P_1^G = P_0^G + \hat{P}_1^G$. Using the assumptions mentioned before, it turns to $P_1^G \in [\mu^G - 2\sigma_G, \mu^G + 2\sigma_G]$. Hence, the hypothesis holds for $t = 1$.

Suppose this hypothesis holds for all periods $1, \dots, t-1$. We next prove that for period t . P_{t-1}^G is bounded by $\mu^G - 2(t-1)\sigma_G - 2(t-2)k\sigma_G$ and $\mu^G - 2(t-1)\sigma_G + 2(t-2)k\sigma_G$. This leads to:

$$\begin{aligned} P_t^G &\geq \mu^G - 2(t-1)\sigma_G + 2(t-2)k\sigma_G + k[2(t-1)\sigma_G - 2(t-2)k\sigma_G] - 2\sigma_G \\ &\geq \mu^G - 2t\sigma_G + 2(t-1)k\sigma_G + 2(t-2)(1-k)\sigma_G \\ &\geq \mu^G - 2t\sigma_G + 2(t-1)k\sigma_G, \\ P_t^G &\leq \mu^G + 2(t-1)\sigma_G - 2(t-2)k\sigma_G + k[-2(t-1)\sigma_G + 2(t-2)k\sigma_G] + 2\sigma_G \\ &\leq \mu^G + 2t\sigma_G - 2(t-1)k\sigma_G - 2(t-2)(1-k)\sigma_G \\ &\leq \mu^G + 2t\sigma_G - 2(t-1)k\sigma_G. \end{aligned}$$

P_t^G is bounded, and it holds for all $t \in \mathbb{T}$. Similarly, P_t^E is bounded. \square

Lemma 3 implies that the largest deviation from the mean price in period t is bounded by a function of k and σ . The maximum deviation from the mean price happens in period $t = T$. This would lead to two extreme conditions that:

$$\begin{cases} P_T^G = \mu^G - 2T\sigma_G + 2(T-1)k\sigma_G, \\ P_T^E = \mu^E + 2T\sigma_E - 2(T-1)k\sigma_E, \end{cases}$$

and

$$\begin{cases} P_T^G = \mu^G + 2T\sigma_G - 2(T-1)k\sigma_G, \\ P_T^E = \mu^E - 2T\sigma_E + 2(T-1)k\sigma_E. \end{cases}$$

Theorem 4. There exists an optimal policy $\pi^* = (\pi_1^*, \dots, \pi_T^*)$ characterized by μ^G , σ_G , μ^E , and σ_E :

1. If $3.412/\eta_{p2g} [\mu^G + 2T\sigma_G - 2(T-1)k\sigma_G] \leq \mu^E - 2T\sigma_E + 2(T-1)k\sigma_E$, then $A_t^{*p2g} = -A_{g2p}^{\max}$, $\forall t \in \mathbb{T}$.
2. If $3.412\eta_{p2g} [\mu^G - 2T\sigma_G + 2(T-1)k\sigma_G] \geq \mu^E + 2T\sigma_E - 2(T-1)k\sigma_E$, then $A_t^{*p2g} = A_{p2g}^{\max}$, $\forall t \in \mathbb{T}$.

Proof. If $3.412/\eta_{p2g} [\mu^G + 2T\sigma_G - 2(T-1)k\sigma_G] \leq \mu^E - 2T\sigma_E + 2(T-1)k\sigma_E$, consider prices of two energy carriers using the same unit, which leads to $3.412/\eta_{p2g} \times P_t^G < P_t^E, \forall t$. Because $\mu^G + 2T\sigma_G - 2(T-1)k\sigma_G$ is the upper bound of deviation of the gas price, and $\mu^E - 2T\sigma_E + 2(T-1)k\sigma_E$ is the lower bound of deviation of the electricity price. In (4.5) and (4.6), as long as the right-hand side remains the same, the charging or discharging rate of storage would not change. Hence $\forall \epsilon > 0$, given two policies π_t^1 and π_t^2 with property that: $E_t^1 = E_t^2 - \epsilon$, $A_t^{1,p2g} = A_t^{2,p2g} + \epsilon$ and $G_t^1 = G_t^2 + \frac{3.412}{\eta_{p2g}}\epsilon$, the operation of storage is the same. This leads to that transition of these two policies, which will influence the expectation term, $T^1(S_t, \pi_t^1)$ and $T^2(S_t, \pi_t^2)$ is the same. The only difference of the revenue to go is the immediate revenue in period t .

$$\begin{aligned} R(S_t, \pi_t^2) &= E_t^2 \cdot P_t^E + G_t^2 \cdot P_t^G \\ &= (E_t^1 + \epsilon) \cdot P_t^E + (G_t^1 - \frac{3.412}{\eta_{p2g}}\epsilon) \cdot P_t^G \\ &= R(S_t, \pi_t^1) + \epsilon \cdot (P_t^E - \frac{3.412}{\eta_{p2g}}P_t^G) \\ &\geq R(S_t, \pi_t^1) + 0 \geq R(S_t, \pi_t^1). \end{aligned}$$

This shows that if we generate more electricity by converting gas to electricity, the revenue to go will increase. Based on the assumption that the transmission line capacity is large enough, the optimal policy π_t^* should be where $A_t^{*p2g} = -A_{g2p}^{\max}$. A similar proof can be conducted to prove the second threshold. \square

We say that the setting is an extreme case, when the highest price of one energy carrier is always lower than the lowest price of another energy carrier considering conversion efficiency. We can always make more money by converting more, which could be useful because the price of natural gas is usually about two or more times lower than the price of electricity for the same energy content in real life.

The Normal Case

Lemma 5. For every period $t \in \mathbb{T}$, J_t is non-increasing in A_t^{p2g} , if $P_t^{\text{E}} \geq 3.412/\eta_{\text{p2g}}P_t^{\text{G}}$, and the operation of storage keeps the same.

Proof. In the proof of Theorem 4, we have shown that as long as the increase or decrease of E_t and G_t is determined by A_t^{p2g} , the state transition keeps the same. Given two such policies π_t^1 and π_t^2 with the property mentioned before, then $\mathbb{E}[J_{t+1}(S_{t+1})|(S_t, \pi_t^1)] = \mathbb{E}[J_{t+1}(S_{t+1})|(S_t, \pi_t^2)]$. If we assume $A_t^{\text{p2g}} < 0$, the energy dynamic balance should hold during the energy conversion: $\frac{\partial E_t}{\partial A_t^{\text{p2g}}} = -\frac{\eta_{\text{p2g}}}{3.412} \frac{\partial G_t}{\partial A_t^{\text{p2g}}}$. This relationship maps the increase of gas we buy to the increase of electricity we sell using energy conversion. The increase of the power of the convertor will increase the quantity of gas, which leads to $\frac{\partial G_t}{\partial A_t^{\text{p2g}}} > 0$. By the chain rule, we can obtain the relation below:

$$\begin{aligned} \frac{\partial J_t}{\partial A_t^{\text{p2g}}} &= \frac{\partial R_t}{\partial E_t} \frac{\partial E_t}{\partial A_t^{\text{p2g}}} + \frac{\partial R_t}{\partial G_t} \frac{\partial G_t}{\partial A_t^{\text{p2g}}} + \frac{\partial \mathbb{E}}{\partial A_t^{\text{p2g}}} = P_t^{\text{E}} \frac{\partial E_t}{\partial A_t^{\text{p2g}}} + P_t^{\text{G}} \frac{\partial G_t}{\partial A_t^{\text{p2g}}} \\ &= (P_t^{\text{G}} - \frac{\eta_{\text{p2g}}}{3.412} P_t^{\text{E}}) \frac{\partial G_t}{\partial A_t^{\text{p2g}}} \leq 0, \end{aligned}$$

A similar proof can be conducted for $A_t^{\text{p2g}} \geq 0$. Thus, J_t is non-increasing in A_t^{p2g} . \square

Lemma 6. For every period $t \in \mathbb{T}$, J_t is non-decreasing in A_t^{p2g} , if $P_t^{\text{E}} \leq 3.412\eta_{\text{p2g}}P_t^{\text{G}}$, and the operation of storage keeps the same.

Proof. $\frac{\partial E_t}{\partial A_t^{\text{p2g}}} = -\frac{\eta_{\text{p2g}}}{3.412} \frac{\partial G_t}{\partial A_t^{\text{p2g}}}$ or $\frac{\partial E_t}{\partial A_t^{\text{p2g}}} = -\frac{1}{3.412\eta_{\text{p2g}}} \frac{\partial G_t}{\partial A_t^{\text{p2g}}}$, and since $0 < \eta_{\text{p2g}} < 1$, $P_t^{\text{G}} \geq \frac{1}{3.412\eta_{\text{p2g}}} P_t^{\text{E}} \geq \frac{1}{3.412} P_t^{\text{E}} \geq \frac{\eta_{\text{p2g}}}{3.412} P_t^{\text{E}}$ holds $\forall t \in \mathbb{T}$.

$$\begin{aligned} \frac{\partial J_t}{\partial A_t^{\text{p2g}}} &= \frac{\partial R_t}{\partial E_t} \frac{\partial E_t}{\partial A_t^{\text{p2g}}} + \frac{\partial R_t}{\partial G_t} \frac{\partial G_t}{\partial A_t^{\text{p2g}}} + \frac{\partial \mathbb{E}}{\partial A_t^{\text{p2g}}} = P_t^{\text{E}} \frac{\partial E_t}{\partial A_t^{\text{p2g}}} + P_t^{\text{G}} \frac{\partial G_t}{\partial A_t^{\text{p2g}}} \\ &= (P_t^{\text{G}} - \frac{\eta_{\text{p2g}}}{3.412} P_t^{\text{E}}) \frac{\partial G_t}{\partial A_t^{\text{p2g}}} \geq 0, \end{aligned}$$

or

$$\frac{\partial J_t}{\partial A_t^{\text{p2g}}} = (P_t^{\text{G}} - \frac{1}{3.412\eta_{\text{p2g}}} P_t^{\text{E}}) \frac{\partial G_t}{\partial A_t^{\text{p2g}}} \geq 0.$$

\square

Lemma 5 and 6 imply that we can obtain a higher revenue to go by decreasing or increasing the power of energy conversion, until some equality constraints become binding. Since we have assumed that the line capacities are large enough, A_t^{p2g} should reach its maximum or minimum.

Theorem 7. There exists an optimal policy $\pi^* = (\pi_1^*, \dots, \pi_T^*)$ characterized by two thresholds $\lambda_1 = 3.412\eta_{\text{p2g}}$ and $\lambda_2 = \frac{3.412}{\eta_{\text{p2g}}}$:

1. If $\frac{P_t^{\text{E}}}{P_t^{\text{G}}} \leq \lambda_1$, then $A_t^{\text{p2g}} = -A_{\text{g2p}}^{\text{max}}$;

2. If $\frac{P_t^E}{P_t^G} \geq \lambda_2$, then $A_t^{*p2g} = A_{p2g}^{\max}$;
3. If $\lambda_1 < \frac{P_t^E}{P_t^G} < \lambda_2$, then $A_t^{*p2g} = 0$.

Proof. The first two cases are the results of Lemma 5 and 6. As for the last case, the following proof is given:

$$\frac{\partial J_t}{\partial A_t^{p2g}} = \begin{cases} (P_t^G - \frac{1}{3.412\eta_{p2g}}P_t^E) \frac{\partial G_t}{\partial A_t^{p2g}} < 0, & \text{if } A_t^{p2g} \geq 0, \\ (P_t^G - \frac{\eta_{p2g}}{3.412}P_t^E) \frac{\partial G_t}{\partial A_t^{p2g}} > 0, & \text{if } A_t^{p2g} < 0. \end{cases}$$

Hence the maximum happens at where $A_t^{*p2g} = 0$. \square

Theorem 7 reduces one decision variable A_t^{*p2g} that needs to be determined, according to the realization of S_t . For every S_t and every t , by Theorem 7, the decision variables left are the optimal operation of electric and gas storage.

Lemma 8. For every period $t \in \mathbb{T}$, J_t is non-decreasing in IE_t and IG_t , given any $\mathbf{P}_t = (P_t^G, P_t^E)$ and W_t .

Proof. We prove J_t is non-decreasing in IE_t first. When $t = T$, since the boundary condition we defined is $J_{T+1}(S_{T+1}) = 0, \forall S_{T+1}$. The expectation term at $t = T$ is zero, which leads to: $J_T(S_T) = R(S_T, \pi_T)$. For $\pi_T^* = \arg \max_{\pi \in \Pi} R(S_T, \pi_T)$, $R_T^* = E_T^* P_T^E + G_T^* P_T^G$ holds. Using (4.5) and (4.6), we can conclude that $R_T^* = W_T P_T^E - A_T^{*p2g} P_T^E - A_T^{*e} P_T^E + F_T^{*p2g} P_T^G - A_T^{*g} P_T^G$. The storage should be on discharging mode at T . For A_T^e , we have $|A_T^e| \leq \min(A_e^{\max}, IE_T)$, and $|A_T^{*e}| = \min(A_e^{\max}, IE_T)$. Assume $\pi_T^* = \arg \max_{\pi \in \Pi} R(S_T, \pi_T)$ and $\pi_T'^* = \arg \max_{\pi \in \Pi} R(S_T', \pi_T)$, where the only difference of S_T and S_T' is IE_T and IE_T' , $|A_T^{*e}| \leq |A_T'^{*e}|$ holds. $R_T^* = W_T P_T^E - A_T^{*p2g} P_T^E - A_T^{*e} P_T^E + F_T^{*p2g} P_T^G - A_T^{*g} P_T^G \leq W_T P_T^E - A_T'^{*p2g} P_T^E - A_T'^{*e} P_T^E + F_T'^{*p2g} P_T^G - A_T'^{*g} P_T^G = R_T'^*$, i.e., in period T , the hypothesis holds.

Let us assume that the hypothesis holds for $T, T-1, \dots, t+1$, and

$$\pi_t^* = \arg \max_{\pi_t \in \Pi} R(S_t, \pi_t) + \mathbb{E}[J_{t+1}(S_{t+1})|S_t],$$

We consider a small variation $\epsilon > 0$ in IE_t , i.e., $IE_t' = IE_t + \epsilon$, if the storage is in discharging mode, there exists a new policy π_t with $A_t^e \in [A_t^{*e} - \epsilon, A_t^{*e}]$ that $IE_{t+1}(S_t', \pi_t) = LE_{t+1}(S_t', \pi_t) = \max(0, IE_t' + A_t^e) \geq \max(0, IE_t + A_t^{*e}) = IE_{t+1}(S_t, \pi_t^*)$. For the two different policies with different states, $A_t^e \leq A_t^{*e} \leq 0$ holds, which leads to $R(S_t', \pi_t) \geq R(S_t, \pi_t^*)$. We can conclude that if there is a variation, there exists a new policy that:

$$\begin{aligned} J_t(S_t', \pi_t) &= R(S_t', \pi_t) + \mathbb{E}[J_{t+1}(S_{t+1}')|S_t'] \geq R(S_t', \pi_t) + \mathbb{E}[J_{t+1}(S_{t+1})|(S_t, \pi_t^*)] \\ &\geq R(S_t, \pi_t^*) + \mathbb{E}[J_{t+1}(S_{t+1})|(S_t, \pi_t^*)] = J_t(S_t, \pi_t^*). \end{aligned}$$

For variation $\epsilon > 0$ in IE_t , we can always find a new policy that $J_t(S_t', \pi_t) \geq J_t(S_t, \pi_t^*)$. A similar process can be applied for the charging mode.

Let $\pi_t^* = \arg \max_{\pi_t^* \in \Pi} R(S_t', \pi_t) + \mathbb{E} [J_{t+1}(S_{t+1}) | S_t']$, $J_t(S_t', \pi_t^*) \geq J_t(S_t', \pi_t) \geq J_t(S_t, \pi_t^*)$, the hypothesis holds for t . J_t is non-decreasing in IE_t . A similar proof can be conducted to prove J_t is non-decreasing in IG_t . \square

For convenience, we change R_t into the following equation using equality constraint:

$$R_t^* = W_t P_t^E - A_t^{*p2g} P_t^E - A_t^{*e} P_t^E + F_t^{*p2g} P_T^G - A_t^{*g} P_T^G. \quad (4.14)$$

W_t can be regarded as known after the state realization, and Theorem 7 reduces one decision variable. The problem can be simplified into a new problem:

$$V_t(S_t) = \max_{A_e, t \in \mathbb{A}_e, A_g, t \in \mathbb{A}_g} \{-A_t^e P_t^E - A_t^g P_t^G + \mathbb{E}[V_{t+1} | S_t]\}. \quad (4.15)$$

Let us define the positive and negative parts of A_t^e and A_t^g as:

$$\begin{aligned} e_t^+ &= \max(0, A_t^e), \quad e_t^- = -\min(0, A_t^e); \\ g_t^+ &= \max(0, A_t^g), \quad g_t^- = -\min(0, A_t^g); \\ V_t(S_t) &= \max\{r(a_t, S_t) + \mathbb{E}[V_{t+1} | S_t]\}, \end{aligned}$$

where $r(a_t, S_t) = -e_t^+ P_t^E - g_t^+ P_t^G + e_t^- P_t^E + g_t^- P_t^G$; a_t is the collection of e_t^+ , e_t^- , g_t^+ and g_t^- .

Lemma 9. For every period $t \in \mathbb{T}$, V_t is concave in IE_t and IG_t , given any $\mathbf{P}_t = (P_t^G, P_t^E)$ and W_t .

Proof. We would use backward induction to prove IE_t first. For the terminal stage T , the expectation term is zero, and the discharging rate is limited by the rate capacity and IE_T , i.e., $e_T^- = \max(A_e^{\max}, IE_T)$. Since the expectation term is zero and the rest is affine, V_T is concave.

Assume V_t is concave for $t = T, T-1, \dots, t+1$, we need to prove $\frac{V_t^*(S_t^1) + V_t^*(S_t^2)}{2} \leq V_t^*(S_t^3)$, where $2 \cdot IE_t^3 | S_t^3 = IE_t^1 | S_t^1 + IE_t^2 | S_t^2$. Note that the feasible sets of our decision variables are convex sets because all constraints are affine, thus any convex combination of any two feasible decisions should be feasible too. Let $\pi_t^{*1} = \arg \max V_t(S_t^1)$ and $\pi_t^{*2} = \arg \max V_t(S_t^2)$, then $\pi_t^3 = \frac{\pi_t^{*1} + \pi_t^{*2}}{2}$ is feasible. All states excluding IE_{t+1} will not change associated with these three actions. Let S_{t+1}^3, S_{t+1}^2 and S_{t+1}^1 be the states of the next stage by applying π_t^3, π_t^{*1} and π_t^{*2} respectively. We have $S_{t+1}^3 = \frac{S_{t+1}^2 + S_{t+1}^1}{2}$, and by concavity in period $t+1$:

$$\begin{aligned} \mathbb{E}[V_{t+1}(S_{t+1}^1)] + \mathbb{E}[V_{t+1}(S_{t+1}^2)] &\leq 2\mathbb{E}[V_{t+1}(S_{t+1}^3)]; \\ r(\pi_t^{*1}, S_t^1) + r(\pi_t^{*2}, S_t^2) &= 2r(\pi_t^3, S_t^3); \\ \frac{V_t^*(S_t^1, \pi_t^{*1}) + V_t^*(S_t^2, \pi_t^{*2})}{2} &\leq V_t(S_t^3, \pi_t^3) \leq V_t^*(S_t^3, \pi_t^{*3}). \end{aligned}$$

$V_t(S_t)$ is concave in IE_t in period t , which means the lemma holds for t . In conclusion, V_t is concave in IE_t . A similar proof can be conducted to prove that V_t is concave in IG_t . \square

Lemma 9 implies that there exists a stationary policy for the revenue to go function in the Bellman equation. Using this, we observe that the optimal policy has a dual-threshold structure. In order to check the first order condition of V_t , we define $\bar{V}_{t+1}(S_{t+1}) = \mathbb{E}[V_{t+1}(S_{t+1})|(S_t, \pi_t)]$, which leads to the equation below:

$$V_t(S_t) = \max\{-e_t^+ P_t^E - g_t^+ P_t^G + e_t^- P_t^E + g_t^- P_t^G + \bar{V}_{t+1}(S_{t+1})\}. \quad (4.16)$$

Consider the optimality of concave function, the following first order necessary and sufficient condition should hold: $\frac{\partial V_t(S_t)}{\partial S_t} = 0$. We focus on IE_t and IG_t , let us rewrite the condition as $\frac{\partial V_t(IE_t)}{\partial IE_t} = 0$ and $\frac{\partial V_t(IG_t)}{\partial IG_t} = 0$. Since V_t is concave in IE_t and in IG_t , $\bar{V}_{t+1}(S_{t+1})$ is concave, we can obtain its right and left directional derivatives on IE_t and IG_t . Let $\partial_{IE}^+ \bar{V}_t(S_t)$ and $\partial_{IE}^- \bar{V}_t(S_t)$ to be two directional derivatives on IE , and $\partial_{IG}^+ \bar{V}_t(S_t)$ and $\partial_{IG}^- \bar{V}_t(S_t)$ to be two directional derivatives on IG .

Lemma 10. Given the current system state S_t , there is no electric or gas storage operation, i.e., $A_t^e = 0$ or $A_t^g = 0$, if the following conditions hold simultaneously:

$$\begin{cases} -P_t^E + \eta_e \partial_{IE}^+ \bar{V}_t(S_{t+1}) & \leq 0, \\ P_t^E + \frac{1}{\eta_e} \partial_{IE}^- \bar{V}_t(S_{t+1}) & \leq 0; \end{cases}$$

or

$$\begin{cases} -P_t^G + \eta_g \partial_{IG}^+ \bar{V}_t(S_{t+1}) & \leq 0, \\ P_t^G + \frac{1}{\eta_g} \partial_{IG}^- \bar{V}_t(S_{t+1}) & \leq 0. \end{cases}$$

Proof. We write the first-order conditions $\frac{\partial V_t(IE_t)}{\partial IE_t} = 0$ in terms of the action e_t^+ and e_t^- to maximize the right-hand side of the Bellman equation:

$$\begin{aligned} -P_t^E + \eta_e \partial_{IE}^+ \bar{V}_t(S_{t+1}) &\leq 0, & \text{if } e_t^+ &\geq 0, \\ -P_t^E + \eta_e \partial_{IE}^- \bar{V}_t(S_{t+1}) &\geq 0, & \text{if } e_t^+ &> 0, \\ P_t^E + \frac{1}{\eta_e} \partial_{IE}^- \bar{V}_t(S_{t+1}) &\leq 0, & \text{if } e_t^- &\geq 0, \\ P_t^E + \frac{1}{\eta_e} \partial_{IE}^+ \bar{V}_t(S_{t+1}) &\geq 0, & \text{if } e_t^- &> 0. \end{aligned} \quad (4.17)$$

Because we defined e_t^+ and e_t^- as $e_t^+ = \max(0, A_t^e)$, $e_t^- = -\min(0, A_t^e)$, $A_t^e = 0$ holds, if and only if $e_t^+ = 0$ and $e_t^- = 0$ hold simultaneously. Hence if $A_t^e = 0$ holds:

$$-P_t^E + \eta_e \partial_{IE}^+ \bar{V}_t(S_{t+1}) \leq 0, \quad (4.18)$$

$$P_t^E + \frac{1}{\eta_e} \partial_{IE}^- \bar{V}_t(S_{t+1}) \leq 0 \quad (4.19)$$

□

Lemma 10 shows that there exist two thresholds $k_t(S_t)$ and $h_t(S_t)$ that characterize an optimal policy. Let $k_t(S_t)$ be the maximum IE_t or IG_t that (4.19) holds, if (4.19) does not hold even for $IE_t = 0$ or $IG_t = 0$, then $k_t(S_t) = 0$; Similarly, let $h_t(S_t)$ be the minimum IE_t or IG_t that (4.18) holds, if (4.18) does not hold even for $IE_t = IE_{\max}$ or $IG_t = IG_{\max}$, then $k_t(S_t) = IE_{\max}$ or $k_t(S_t) = IG_{\max}$.

Theorem 11. There exists an optimal policy $\pi^* = (\pi_1^*, \dots, \pi_T^*)$ characterized by two thresholds $k_t^e(S_t)$ and $h_t^e(S_t)$ or $k_t^g(S_t)$ and $h_t^g(S_t)$.

1. If $IE_t \leq h_t^e(S_t)$ or $IG_t \leq h_t^g(S_t)$, then greedily charge the storage to $h_t^e(S_t)$ or $h_t^g(S_t)$, and $A_t^{*e} = \min\left(\frac{A_e^{\max}}{\eta_e}, \frac{h_t^e(S_t) - IE_t}{\eta_e}\right)$, $A_t^{*g} = \min\left(\frac{A_g^{\max}}{\eta_g}, \frac{h_t^g(S_t) - IG_t}{\eta_g}\right)$.
2. If $IE_t \geq k_t^e(S_t)$ or $IG_t \geq k_t^g(S_t)$, then greedily discharge the storage to $k_t^e(S_t)$ or $k_t^g(S_t)$ and $A_t^{*e} = \max(\eta_e A_e^{\max}, \eta_e(IE_t - k_t^e(S_t)))$, $A_t^{*g} = \max(\eta_g A_g^{\max}, \eta_g(IG_t - k_t^g(S_t)))$.

Proof. Let $IE_t' = h_t^e(S_t)$, $\forall IE_t \leq IE_t'$, by concavity we have $\partial_{IE}^+ \bar{V}_t(IE_t') \leq |\partial_{IE}^- \bar{V}_t(IE_t)|$, which leads to $-P_t^E + \eta_e \partial_{IE}^- \bar{V}_t(S_{t+1}) \geq 0$. Thus, $e_t^+ > 0$; $\forall IE_t \geq k_t^e(S_t)$, we have $P_t^E + \frac{1}{\eta_e} \partial_{IE}^+ \bar{V}_t(S_{t+1}) \geq 0$. Thus, $e_t^- > 0$. A similar proof can be conducted for the gas storage. \square

The thresholds above rely on the computation of the partial derivatives. Following the same approach of Theorem 4.1 in [143], it can be shown that the directional derivatives are piece-wise linear in IE_t or IG_t , $\forall t \in \mathbb{T}$.

To capture the impact of the power conversion, the following modification is needed for thresholds:

$$P_t^E = \min(P_t^E, 3.412\eta_{p2g}P_t^G), \quad P_t^G = \min(P_t^G, \frac{\eta_{p2g}}{3.412}P_t^E).$$

4.1.4 An Illustrative Example

We conduct some examples with different efficiencies to analyze the feasible region of the operation of the energy conversion.

Let η_{p2g} be the efficiency of the energy conversion if it works on P2G mode; η_{g2p} be the efficiency of the energy conversion if it works on G2P mode. As shown in Fig. 4.1, when the efficiencies of P2G and G2P are high, the region of no operation is small. The physical meaning of efficiency is energy loss. Consider the case where the efficiency is 1, there is no energy loss during energy conversion. Then, the threshold would be the same line. For that case, energy conversion will bring more economic values unless the prices in the same energy content are the same. The larger efficiency of G2P leads to a larger threshold of the G2P conversion. When the efficiency is low, which means the energy loss is high, a comparably lower gas price is required if we want to get benefits by buying gas, converting gas to electricity, and selling electricity. Similarly, when the efficiency of P2G is low, a comparably higher gas price is required if we want to get benefits by buying electricity, converting electricity to gas, and selling gas. Hence, a larger efficiency leads to a lower threshold of the P2G conversion.

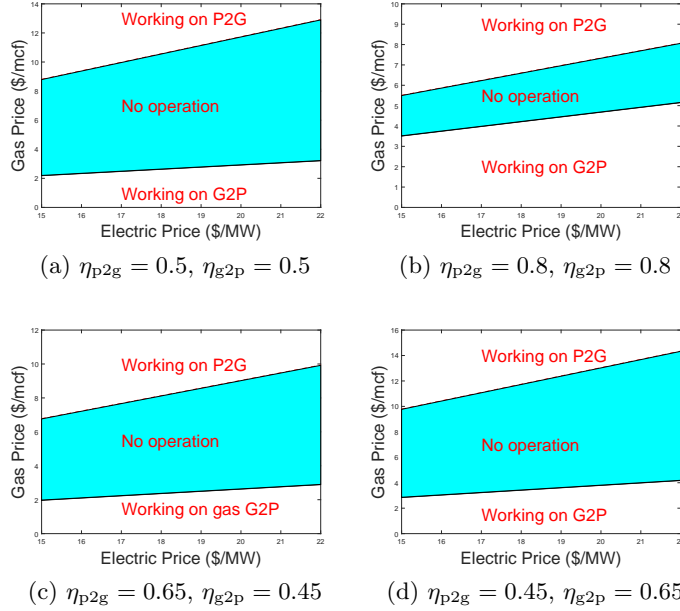


Figure 4.1: The feasible region of each operation in the normal case.

4.2 Optimal Trading Strategies for Transactive Energy

The current power distribution system is undergoing a transition from centralized markets to decentralized markets. However, the existing economic mechanism for decentralized markets has many disadvantages such as the ignorance of incomplete information, the lack of negotiation process, and the requirement of a high degree of synchronization between the prosumers. We propose a novel economic mechanism, based on continuous double auction (CDA). With respect to the incomplete information, an adaptive dynamic programming based strategy is used to adjust sequential strategies according to the market trends. Several results are established, which are then verified by sensitivity analysis.

4.2.1 Continuous Double Auction Model

A CDA is a marketplace where agents can transact continuously by submitting bids and asks at any time. A bid is a pair of price and quantity submitted by a buyer, and an ask is such a pair submitted by a seller. Unlike the spot market where the transactions are cleared one time, transactions occur in CDA whenever the highest bid price is at least as high as the lowest ask price. The current lowest ask price in the market is defined as the outstanding ask p_a , and the current highest bid price in the market is defined as the outstanding bid p_b . If a new ask arrives with a price lower than p_b , then the transaction is executed at p_b . If a new bid arrives with a price higher than p_a , then the transaction is executed at p_a . An illustrative example is shown in Table 4.1. (a), (b), (c), and (d) are buyers' and sellers' orders in the order book before

Table 4.1: An Illustrative Example of Continuous Double Auction.

(a)			(b)		
Buyer	Bid	Quantity	Seller	Ask	Quantity
b_1	98	3	s_1	100	2
b_2	97	2	s_2	101	1
b_3	96	4	s_3	102	2
b_4	95	1	s_4	103	3

(c)			(d)		
Buyer	Bid	Quantity	Seller	Ask	Quantity
b_1	97	1	s_1	100	2
b_2	96	4	s_2	101	1
b_3	95	1	s_3	102	2
b_4	94	3	s_4	103	3

new orders arrive, and buyers' and sellers' orders in the order book after new orders arrive, respectively. The price of new asks is 97 and the quantity is 4. Then, 3 units are transacted at 98, and the rest one is transacted at 97. We highlight the change in the table.

The CDA mechanism operates in various markets. The model in our work intends to encapsulate the essential features of the power distribution system. We assume the energy trading market is characterized by the following properties and protocols:

1. The selection of distributed ledger is reasonable. The smart contract can be executed automatically. The smart meter can learn the states, manage its behaviors by time, and programmable.
2. The prosumers know their own complete information and public information, but do not know other prosumers' information. Correlation among each prosumer's generation or utility function is ignored. The congestion issue is trivial for distributed energy trading.
3. All orders are for a bunch of quantity such as a single unit.

Note that (1) ensures that the market is electronic commerce and depends on smart agents. There are some correlations among each prosumer's preference in real life, e.g., demands tend to be high when the temperature is high. However, it is hard to quantify such factors since we have incomplete information. We will adopt a learning algorithm to estimate other's information which inherently captures correlations. The protocol in (3) eliminates the possibility of partial execution, and hence the need for rules governing it, which simplifies our problem. It will not influence the prosumers' strategy if the computational ability of agents is sufficient.

In the proposed mechanism, a CDA starts 5 minutes before the 5-minute delivery interval in consideration. The transactions are executed continuously until the delivery interval begins, and a smart contract is signed upon the completion of each transaction. As shown in Fig 4.2, the CDA for the delivery interval from t to $t + 5$ min, starts at $t - 5$ min and ends at t . A new

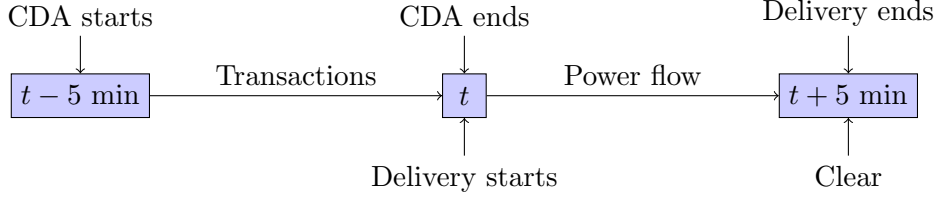


Figure 4.2: Timeline of CDA trading and physical delivery.

Table 4.2: Information Available to Each Prosumer.

Private information	Public information
Utility function Generation	Elasticities Incremental loss allocation Historical data

CDA starts at t for the next delivery interval. At $t + 5$ min, the system allocates the losses using incremental loss allocation method, and smart meters report the energy imbalance. If there is any imbalance, a penalty would be imposed. Then, the credits and payments are settled in the distributed ledger. A fixed charge will be imposed for each transaction since the system provides services such as voltage control and there are some operational costs for the distributed ledger.

When a CDA is complete, the system can learn the steady state properties of this CDA interval, in particular the elasticities of the underlying demand and supply functions can be obtained [144]. The system can calculate the incremental loss allocation coefficients of the past delivery interval based on the power flow analysis, which will be broadcast to the prosumers at the beginning of a new CDA period. Table 4.2 summarizes the information available to each prosumer. Historical data includes the information of the past transactions.

4.2.2 Optimal Trading Strategies

A prosumer can sell the generation or buy electricity during a CDA period. For simplicity, we discretize the 5-minute interval into M slots and assume that a prosumer will submit at most M bids or asks during a CDA period. Due to the fixed charge applied to each transaction, we assume the prosumers are less aggressive and can only act in one role during each CDA period. To determine the role, we first introduce a result from [144], which gives a formula of the expected price p of a random trade:

$$\hat{p} = \mathbb{E}(p) = \begin{cases} (\eta_S p_{\text{grid}}^{\max} - \eta_D p_{\text{grid}}^{\min}) / (1 + \eta_S - \eta_D), & \eta_S \neq \eta_D, \\ \eta \sinh(1/(2\eta)) (p_{\text{grid}}^{\max} + p_{\text{grid}}^{\min}), & \eta_S = \eta_D = \eta, \end{cases} \quad (4.20)$$

where η_S and η_D are the elasticities of the underlying supply and demand functions in the last CDA period, and p_{grid}^{\max} and p_{grid}^{\min} are the selling and buying prices of electricity from the grid. All these values are published by the system and are available to the prosumers at the beginning of each CDA period.

A utility function reflects the welfare obtained by consuming electricity, which is typically non-decreasing and concave. For each prosumer i , we assume that the utility takes the following form:

$$u_i(x_i) = b_i \ln(a_i x_i + 1), \quad (4.21)$$

where $a_i > 0$ and $b_i > 0$ are the parameters, and x_i is the consumption of power. Let the fixed rate for each transaction be γ . Since the prosumer can only act in one role, the total payoff can be defined by

$$R_i = b_i \ln(a_i x_i + 1) + \frac{(\hat{p} - \gamma)}{1 + K_i} (x_i^g - x_i)^+ - \frac{(\hat{p} + \gamma)}{1 - K_i'} (x_i^g - x_i)^-, \quad (4.22)$$

where x_i^g is the generation, K_i and K_i' are the coefficients of the incremental loss allocation of prosumer i for selling and buying, respectively. $Z^+ = \max(0, Z)$ and $Z^- = \max(0, -Z)$. Note that $K_i = -K_i'$, and $|K_i| < 1$. The prosumers are responsible for the energy losses, hence the prosumers use K_i to estimate the actual electricity that they deliver or receive for each transaction. The first order derivative of R_i is discontinuous at x_i^g , and is given by

$$\dot{R}_i = \begin{cases} a_i b_i / (a_i x_i + 1) - (\hat{p} - \gamma) / (1 + K_i), & x_i < x_i^g, \\ a_i b_i / (a_i x_i + 1) - (\hat{p} + \gamma) / (1 + K_i), & x_i > x_i^g. \end{cases} \quad (4.23)$$

Let the numerators of the two segments of the derivative of R_i be NL_i and NR_i , we have

$$NL_i(x_i) = a_i b_i (1 + K_i) - (\hat{p} - \gamma)(a_i x_i + 1), \forall x_i < x_i^g, \quad (4.24)$$

$$NR_i(x_i) = a_i b_i (1 + K_i) - (\hat{p} + \gamma)(a_i x_i + 1), \forall x_i > x_i^g, \quad (4.25)$$

Note that the denominators of the two segments are always positive. We can determine the role of prosumer i using the lemma below.

Lemma 12. If $NR_i(x_i^g) > 0$, the prosumer i acts as a buyer; If $NL_i(x_i^g) < 0$, the prosumer i acts as a seller; Otherwise the prosumer i consumes $x_i = x_i^g$.

Proof. Let us consider two affine functions NL_i and NR_i , $\forall x_i$. The intersection of NL_i and NR_i happens at $x_i = -1/a < 0$. We can conclude that $NL_i(x_i) > NR_i(x_i), \forall x_i > 0$. Let the directional derivatives of R_i at $x_i = x_i^g$ be $\partial^+ R_i(x_i^g)$ and $\partial^- R_i(x_i^g)$. If $NR_i(x_i^g) > 0$, then $\partial^+ R_i(x_i^g) > 0$. If the prosumer consumes more than x_i^g , the utility will increase, i.e., the prosumer should act as a buyer. If $NL_i(x_i^g) < 0$, then $\partial^- R_i(x_i^g) > 0$. If the prosumer consumes less than x_i^g , the utility will increase, i.e., the prosumer should act as a seller. \square

We adopt the belief functions $f_b(p)$ and $f_s(p)$ as [145] to measure the likelihood that the bid and ask prices will be accepted, respectively. Consider the H most recent transactions, and let $AG(p)$ be the number of transactions with prices that are no less than p in H transactions. The belief function of the seller is given by

$$f_s(p) = \begin{cases} AG(p)/H, & \forall p > p_b, \\ 1, & \forall p \leq p_b, \end{cases} \quad (4.26)$$

whereas the belief function of the buyer is given by

$$f_b(p) = \begin{cases} AL(p)/H, & \forall p < p_a, \\ 1, & \forall p \geq p_a, \end{cases} \quad (4.27)$$

where $AL(p)$ the number of transactions with prices that are no greater than p in H transactions. We use the points observed in H transactions as breakpoints to construct piecewise linear functions $f_s(p)$ and $f_b(p)$.

The market trend is crucial for dynamic markets. To analyze the market trend, we assume that the change is linear, which means all the trade points compose a line. We adopt the least squares technique to estimate the coefficients of linear function. Let $(h', p_{h'}), h' = 1, \dots, H'$ be the points, where H' is the number of transactions we selected, and $p_{h'}$ is the price of the transaction h' . We have the linear function:

$$p_{h'+1} = \theta_0 + \theta_1(h' + 1). \quad (4.28)$$

Let $\Delta_{h'} = p_{h'} - p_{h'-1}$. Solve $\hat{\theta}_1 \in \arg \min_{\theta} \sum_{h'=0}^{H'} (\Delta_{h'} - \theta_1)^2$, then $\hat{\theta}_1 = \left(\sum_{h'=0}^{H'} \Delta_{h'} \right) / H'$.

We use a discrete model to simulate the prosumer's decision making process. We assume that the prosumer will submit M sequences of bids or asks. Let $m \in [1, M]$ be the number of remaining stages, x be the excess electricity. Note that $x = x^g$, when $m = M$. We introduce a weighting factor λ to represent the influence of the market trends. We assume that the quantity of each transaction is 1 unit. The payoff-to-go of the seller at stage m can be expressed as:

$$S_m(x, \lambda) = \max_p f_s(\lambda p) [p - \gamma + S_{m-1}(x - 1 - K, \lambda)] + [1 - f_s(\lambda p)] S_{m-1}(x, \lambda). \quad (4.29)$$

The first term represents the intermediate payoff plus the payoff-to-go if the ask is accepted and the second term represents the payoff-to-go if the ask is not accepted. The corresponding payoff-to-go of the buyer can be given by

$$B_m(x, \lambda) = \max_p f_b(\lambda p) [-p - \gamma + B_{m-1}(x + 1 - K, \lambda)] + [1 - f_b(\lambda p)] B_{m-1}(x, \lambda). \quad (4.30)$$

For the boundary condition, we assume that any remaining electricity will be consumed by the

prosumer:

$$S_0(x) = B_0(x) = b \ln(ax + 1). \quad (4.31)$$

Note that in each stage m , the agent needs to update the belief function based on the information. The weighting factor λ is introduced to adjust the expectation of probability of executing the transaction.

To discuss how to update λ , we show some properties first. For notational convenience, we discard γ in our analytical proof since it is a constant and will not influence the result.

Lemma 13. Given any λ , $S_m(x, \lambda)$ and $B_m(x, \lambda)$ are increasing in x . Furthermore, $S_m(x, \lambda)$ and $B_m(x, \lambda)$ are increasing in m .

Proof. We prove this lemma by induction. As for the boundary condition $m = 0$, $S_0(x) = B_0(x) = b \ln(ax + 1)$, it obviously holds for both functions. We assume that $S_m(x, \lambda)$ is increasing in x holds for $m - 1$, and $x_1 < x_2$, we have

$$\begin{aligned} S_{m-1}(x_1) &< S_{m-1}(x_2), \\ S_m(x_2, \lambda) &\geq f_s(\lambda p^*(x_1)) [p^*(x_1) + S_{m-1}(x_2 - 1 - K, \lambda)] + (1 - f_s(\lambda p^*(x_1))) S_{m-1}(x_2, \lambda) \\ &> f_s(\lambda p^*(x_1)) [p^*(x_1) + S_{m-1}(x_1 - 1 - K, \lambda)] + (1 - f_s(\lambda p^*(x_1))) S_{m-1}(x_1, \lambda) \\ &= S_m(x_1, \lambda). \end{aligned}$$

Lemma 13 holds for m . $S_m(x, \lambda)$ is increasing in x . The other claims can be proved similarly. \square

Intuitively, the more generation available and the more time that is left, the higher payoff of the prosumer.

Theorem 14. Given any λ , the optimal trading price p_m^* for both seller and buyer decreases in x . Furthermore, the optimal trading price p_m^* for seller increases in m , but the optimal trading price p_m^* for buyer decreases in m .

Proof. Let $p_m(x)$ be the value of p that maximizes (4.29) or (4.30). Because we use natural logarithm to represent the prosumers' utility, which is strictly concave, we can conclude that $S_0(x + 1) - S_0(x) \geq S_0(x + 2) - S_0(x + 1)$ holds for all $x \geq 0$. Without loss of generality, we can assume $K = 0$. The proof follows similarly for any K . We use f instead of f_s for notational convenience. First, we show that the following sets of inequalities hold:

$$S_{m+1}(x + 1) - S_{m+1}(x) \geq S_m(x + 1) - S_m(x), \quad x, m \geq 0, \quad (4.32)$$

$$S_{m+1}(x) - S_m(x) \geq S_{m+2}(x) - S_{m+1}(x), \quad x, m \geq 0, \quad (4.33)$$

$$S_m(x + 1) - S_m(x) \geq S_m(x + 2) - S_m(x + 1), \quad x, m \geq 0. \quad (4.34)$$

This can be proved by induction. Since the inequalities are true when $x + m = 0$, we assume that they are true whenever $x + m < k$. Now consider $x + m = k$, we first show (4.32) is true.

We have proved that $S_m(x)$ is increasing in m , then (4.32) is valid when $x = 0$. Now, for some \bar{p} , we have

$$\begin{aligned} S_{m+1}(x) &= f(\lambda\bar{p})\bar{p} + f(\lambda\bar{p})S_m(x-1) + [1 - f(\lambda\bar{p})]S_m(x), \\ S_{m+1}(x) - S_m(x) &= f(\lambda\bar{p})\bar{p} + f(\lambda\bar{p})[S_m(x-1) - S_m(x)]. \end{aligned}$$

By definition, we have

$$\begin{aligned} S_{m+1}(x+1) &\geq f(\lambda\bar{p})\bar{p} + f(\lambda\bar{p})S_m(x) + [1 - f(\lambda\bar{p})]S_m(x+1), \\ S_{m+1}(x+1) - S_m(x+1) &\geq f(\lambda\bar{p})\bar{p} + f(\lambda\bar{p})[S_m(x) - S_m(x+1)]. \end{aligned}$$

We have assumed (4.34) for $x-1$ and m is true, which leads to $S_m(x) - S_m(x+1) \geq S_m(x-1) - S_m(x)$. Therefore, we have

$$\begin{aligned} S_{m+1}(x+1) - S_m(x+1) &\geq f(\lambda\bar{p})\bar{p} + f(\lambda\bar{p})[S_m(x-1) - S_m(x)], \\ S_{m+1}(x+1) - S_m(x+1) &\geq S_{m+1}(x) - S_m(x). \end{aligned}$$

If we follow the same approach, we can prove (4.33) using inequality (4.32) for $x-1$ and m . We can combine (4.34) and (4.32) for x and $m-1$ into one inequality, and follow the similar approach. We have

$$S_{m+1}(x+1) + S_{m-1}(x+1) \geq S_m(x+2) + S_m(x).$$

The inequality (4.33) for $x+1$ and $m-1$ gives

$$S_m(x+1) - S_{m-1}(x+1) \geq S_{m+1}(x+1) - S_m(x+1).$$

Therefore, we have $2S_m(x+1) \geq S_m(x+2) + S_m(x)$, which is (4.34) for x and m . To establish the monotonicity of $p_m(x)$ with respect to x and m , we consider the modularity of $S_m(x)$:

$$\begin{aligned} \frac{\partial^2}{\partial x \partial p} \{f_s(\lambda p)p + f_s(\lambda p)S_{m-1}(x-1-K) + [1 - f(\lambda p)]S_{m-1}(x)\} \\ = \lambda f'_s(\lambda p) \frac{\partial}{\partial x} [S_{m-1}(x-1-K) - S_{m-1}(x)]. \end{aligned}$$

The belief function of seller is decreasing, i.e., $f'_s(\lambda p) \leq 0$, and $\lambda \geq 0$. We can conclude that if $S_{m-1}(x-1-K) - S_{m-1}(x)$ increases in x , then the function is submodular, and $p_m(x)$ decreases in x . If $S_{m-1}(x-1-K) - S_{m-1}(x)$ decreases in m , then the function is supermodular, and $p_m(x)$ increases in m . The inequality (4.34) implies that $S_{m-1}(x-1-K) - S_{m-1}(x)$ increases in x , and the inequality (4.32) implies that $S_{m-1}(x-1-K) - S_{m-1}(x)$ decreases in m . One can prove the other claim following the same approach. \square

If the generation (plus or minus the quantity that has been transacted) is high, the buyer

and seller tend to bid and ask low, respectively. The objective of a buyer is to make a tradeoff between the final utility and the energy cost. Since we have assumed a natural logarithm function as our utility function, the incremental utility of a buyer may be small if the buyer has enough generation. In other words, the more generation, the fewer incentives the buyer has to buy energy. It is intuitive for such a buyer to submit a bid with lower price. If the bid is not accepted, the influence is low because the incremental utility is low. Furthermore, if the price of bid is high, it may deteriorate the final utility because the incremental utility cannot cover the payment. Similarly, selling electricity will not influence the seller's utility a lot, but increase the seller's payoff intermediately. Theorem 14 also shows that our bidding strategy inherently considers the time pressure.

Proposition 15. Given any x , $B_m(x, \lambda)$ is increasing in λ , and $S_m(x, \lambda)$ is decreasing in λ .

Proof. It is obvious that the proposition holds for the boundary $m = 0$. We assume that the proposition holds for $m - 1$, we use induction to prove m . Let $\lambda_2 \bar{p} = \lambda_1 p_1^*$ and $0 < \lambda_1 < \lambda_2$, we have $\bar{p} < p_1^*$ and

$$\begin{aligned} B_m(x, \lambda_2) &\geq -f_b(\lambda_2 \bar{p}) \bar{p} + f_b(\lambda_2 \bar{p}) B_{m-1}(x+1-K, \lambda_2) + [1 - f_b(\lambda_2 \bar{p})] B_{m-1}(x, \lambda_2) \\ &\geq -f_b(\lambda_2 \bar{p}) p_1^* + f_b(\lambda_2 \bar{p}) B_{m-1}(x+1-K, \lambda_1) + [1 - f_b(\lambda_2 \bar{p})] B_{m-1}(x, \lambda_1) \\ &= B_m(x, \lambda_1). \end{aligned}$$

The other claim can be proved similarly. □

The probability of accepting an ask with the same price will increase if the market trend is increasing. The belief function of seller is monotonically decreasing, a smaller λ should be applied. On the other hand, the probability of accepting a bid with the same price will decrease if the market trend is increasing. The belief function of the buyer is monotonically increasing, a smaller λ should be applied as well. Let $\lambda_0 = 1$, then for a prosumer, the λ_m at each sequence is

$$\lambda_m = \lambda_{m-1} - \hat{\theta}/\hat{p}. \quad (4.35)$$

4.2.3 An Illustrative Example

Here, we first validate Theorem 14. Then, we show that the change of total revenue and the change of trading strategy under different market trends follow the analytical solution. A comparison between our strategy and zero intelligence (ZI) strategy is conducted to show the effectiveness of our strategy. It is worth mentioning that the unit of price and payoffs depends on the currency of selected blockchain platform. In this section, we omit all the units of price and payoffs. The unit of generation is MW.

We consider 200 watts as one trading unit and set the parameters as $a = 2$, $b = 75$, $K = 0.05$, and $\gamma = 0$. To validate Theorem 14, we fix the belief function and λ . Fig. 4.3 shows the optimal submitted prices under different stages and quantities of excess electricity. The optimal ask

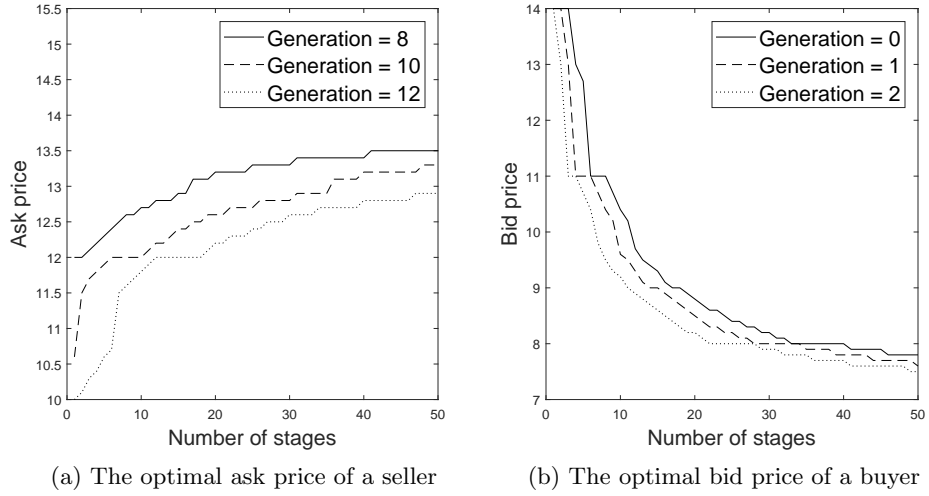


Figure 4.3: The optimal submitted price under different stages and quantities of excess electricity.

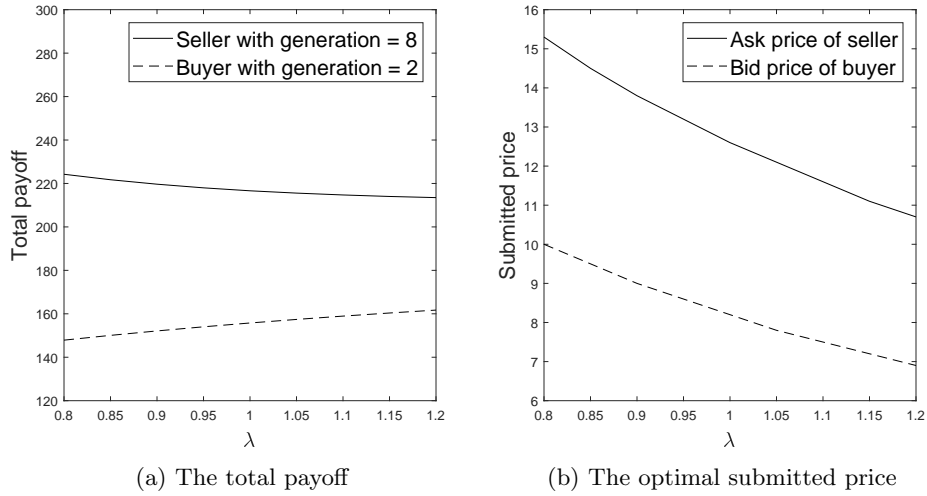


Figure 4.4: The total payoff and the optimal submitted price under different market trends.

price of the seller is decreasing in the quantity of excess electricity and increasing in stages, which corresponds to our analytical results.

Fig. 4.4 shows the change in the total payoff and that of the optimal submitted price under different market trends. We fix the excess electricity and set the stage number to 20. A larger λ indicates a decreasing market trend, which leads to a larger payoff for the buyer and a smaller payoff for the seller. The seller tends to sell the surplus electricity as soon as possible, and the buyer wants to buy the electricity they need at the end of CDA since the market trend is decreasing. Therefore, the ask and bid prices are decreasing in λ .

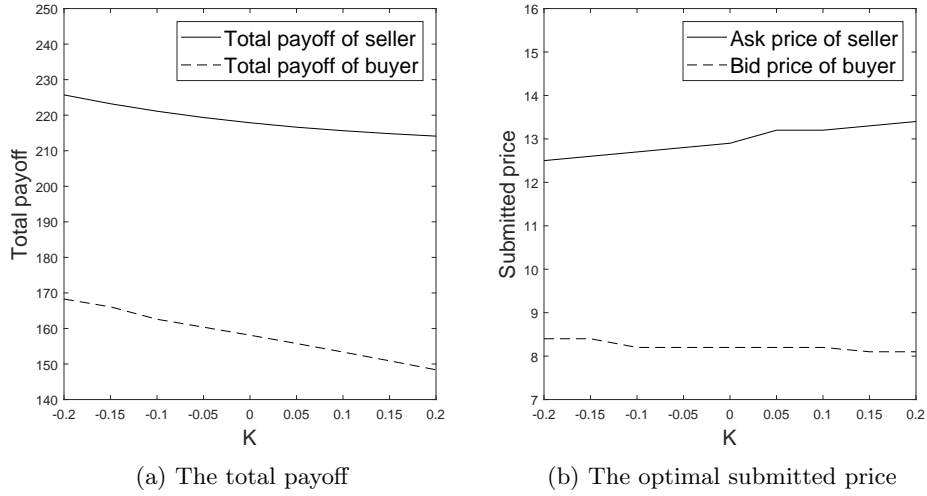


Figure 4.5: The total payoff and the optimal submitted price under different loss allocation coefficients.

Fig. 4.5 shows the change in the total payoff and submitted price under different incremental loss allocation coefficients. If $K < 0$, the seller will deliver less than 1 unit electricity for each transaction, and the buyer will receive more than 1 unit electricity for each transaction. It is intuitive that the total payoffs are higher when $K < 0$. Moreover, the prosumers are likely to complete more transactions in this setting. Hence, the submitted prices are lower for sellers, and those are higher for buyers. From the perspective of the power system operation, the transactions between the prosumers with negative K are favorable since it will decrease the total loss.

To compare our strategy and ZI strategy, we assume the others' bids and asks arrive randomly, and the prosumer using our strategy submits 5 sequential bids or asks. The arrivals of asks and bids are given in Fig. 4.6. The optimal bids of a buyer at each sequence are 10.8, 11.4, 11.4, 12.3, and 5. The second and fourth bids are executed at price 11.4 and 11.97. The buyer cannot improve utility by buying more, then submits a bid with buying price of grid at the last sequence. The optimal asks of a seller at each sequence are 12.1, 12.4, 12, 11.7, and 20. The first and fourth sequence are executed at price 12.1 and 11.7. Similarly, the seller has no incentive to sell at the last sequence, hence submits the ask with selling price of grid. It is worth mentioning that the price of the second ask is higher than the price of the first ask, because the first ask is executed, and the generation left is lower. Since the ZI strategy generates bids or asks randomly, we conduct 5000 trials and calculate the average value. The final utility of seller and buyer using our strategy are 135.82 and 131.3, respectively. The final average utility using ZI strategy are 133.06 and 128.02, respectively. Obviously, our strategy is better than ZI strategy.

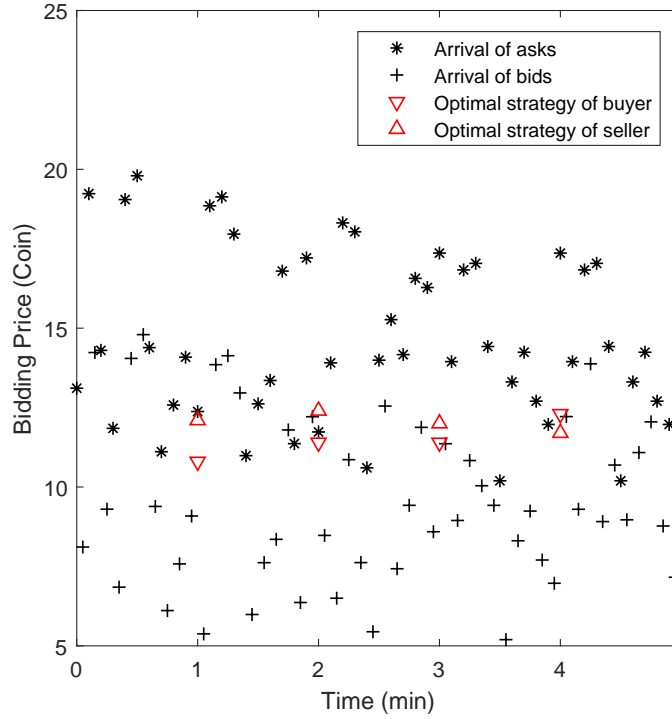


Figure 4.6: An illustrative example of auction process.

4.3 Conclusion and Existing Technical Challenges

We first study the optimal operation of a profit-maximizing energy hub equipped with the energy conversion and the energy storage through a dynamic programming formulation. We propose the two-threshold policies of the energy conversion and the energy storage, respectively. The optimal operation of the energy conversion depends on the efficiency of the conversion process. Moreover, the expected revenue is a concave function of the state of charge of the storage, which leads to a stationary policy for the operation of the energy storage. The properties shed some lights on how different energy sectors should be converted, conditioned, and stored, which provides some insights on the enhancement of renewable integration.

Moreover, we propose a local electricity market. The CDA based economic mechanism encourages peer-to-peer trading in distribution power systems, in which risks of renewable penetration are hedged locally. The proposed mechanism incorporates the negotiation process between each prosumer and captures the allocation of losses. Moreover, we analyze the prosumer's optimal strategy using dynamic programming. The proposed strategy can learn the recent market information and make adaptive decisions. We analytically show that the optimal policy depends on the market trends, the generation left, and the bidding sequence left.

However, there exist many technical challenges in the current work. Regarding the trading between different energy sectors, the time spans of different markets are different. For example,

in the gas markets, current cleared price is for the delivery of natural gases one week later. Moreover, the effectiveness of such a trading scheme highly depends on the efficiency of energy conversion device. As for the CDA framework, we simply use the coefficients of the incremental loss allocation to allocate the losses. However, the coefficients are not well-defined for the peer-to-peer trading setting. It is important to establish a local market where loss allocation meets some certain properties for each player.

CHAPTER

5

SUSTAINABLE COMMUNITY AND DYNAMIC MICROGRID

The desire for a green, efficient, and sustainable energy supply results in a tense dynamic situation accompanying the rapid growth of solar energy in the world. Customer-sited solar photovoltaic (PV) systems portend a potentially disruptive change in the customer-utility relationship. We observe that a zero-energy community (ZEC) is a good solution to the PV development planning in a deregulated environment. A ZEC, which offsets all of its energy use from renewables available within the community environment, reduces the transmission line losses, is more independent and self-sufficient, and has more controls over energy decisions. That have been said, utilities worry about a baseload death spiral. Rooftop solar in conjunction with net metering decreases rate-based revenue, while not necessarily reducing utility costs for two reasons: 1) rooftop solar owners still rely on the grid when solar is not delivering at night or on cloudy days, and 2) net metering transactions, in practice, rely on infrastructure owned, operated, and maintained by the utilities. Such conflicts of interest urge a negotiation process to find a win-win solution. To make the most of the multi-benefits of a ZEC, it needs to be appropriately planned using a new business model and regimes that ensure an efficient and symmetric benefit allocation. On the above premises, we focus on cooperative planning for ZEC based PV-storage systems.

The penetration of distributed solar coincides with the deployment of electric vehicles, storage, and other controllable loads, which are considered as distributed energy resources (DERs). During grid outages, it is desirable for DERs to participate in effective and efficient critical service restoration to enhance grid resiliency, especially when power support from the

upstream transmission system is not available. Dynamic microgrids with adaptive boundaries can be formed, in which distributed generation serves critical service facilities. In other words, increased penetration of DERs, especially solar at a community level, can provide additional resiliency and improve the reliability of the distribution system. In this chapter, we examine this ability.

5.1 Sustainable Community Based PV-Storage Planning

We consider a ZEC with a set of end users, which are allowed to invest in PV and storage. The load serving entity (LSE) offers net metering to the community with a capacity limit. The time-of-use (TOU) pricing scheme is adopted. Without cooperative planning, each household installs a PV-storage system optimally based on the individual consumption pattern. Intuitively, they will try to charge their storage at off-peak hours and sell back the electricity to the grid at peak hours. Some papers assume that the power from storage cannot be sold back. However, we apply the capacity limit, as it is the current practice followed by the utilities. Moreover, we assume that the end users have no incentive to share the consumption patterns with the LSE under the non-cooperative framework. The payoff of the LSE is the difference between the wholesale market price and the TOU rate times the energy consumption. In cooperative planning, the LSE and the end users optimally determine the size of PV-storage systems. We assume a fixed lifetime for investments, and hence, the cost based on per unit can be leveled to an annual base. The entitlement is allocated based on the amount of money each player pays for enforcement. For storage, the end users can charge their partitions or rent the LSE's partition with a fixed holding cost. The end users can use the PV generation to serve their demand, store it to their storage partitions, or the LSE's storage partition. The LSE can use its PV generation to serve households' demand or sell it back to the grid. The uncertainties are addressed by a two-stage stochastic program. The first stage decisions are the investments, whereas the second stage decisions are the operation schedules. To allocate the surplus introduced by the cooperation, we consider a bargaining game, in which the optimal allocation is obtained by the Nash bargaining solution (NBS).

5.1.1 Non-cooperative Benchmark

We describe the non-cooperative model first. Its results serve as the disagreement outcomes in the bargaining game. In this non-cooperative planning benchmark, each player determines the optimal capacity of PV and storage based on private information.

Storage and PV Investment Costs

We assume that each end user $i \in \mathcal{I}$, where $\mathcal{I} = \{1, \dots, I\}$, needs to decide the capacity of solar power $PV_i \in [0, PV_i^{\max}]$ in kW, and the capacity of storage $S_i \in [0, S_i^{\max}]$ in kWh, where PV_i^{\max} and S_i^{\max} are the maximum capacities allowed for the deployment of end user i .

The capacities should be constrained by physical constraints such as available area of roof. The capital recovery factor is used to convert the capital investment costs of storage and PV into a series of equal annualized costs. Let c_i^{PV} and c_i^{S} denote the investment cost of PV per kW and storage per kWh. Let n_1 and n_2 be the lifetime of PV and storage, respectively. The annual investment costs are given by

$$A_i^{\text{PV}} = c_i^{\text{PV}} \times \frac{d(d+1)^{n_1}}{(1+d)^{n_1} - 1}, \quad (5.1a)$$

$$A_i^{\text{S}} = c_i^{\text{S}} \times \frac{d(d+1)^{n_2}}{(1+d)^{n_2} - 1}, \quad (5.1b)$$

where d is the discount rate. We assume that the investment cost covers all expenditures. The installed capacity of PV determines the solar generation based on the realizations of insolation for each day. For end user i , the total annualized investment costs are given by

$$A_i = A_i^{\text{PV}} PV_i + A_i^{\text{S}} S_i. \quad (5.2)$$

The model can be easily extended to include power rating cost of storage by adding one decision variable.

Given the first stage decisions PV_i and S_i , each end user needs to schedule the operations of PV and storage optimally. Let $\mathcal{T} = \{1, \dots, T\}$ be the operation time horizon and Ω be the set of scenarios. We assume that the realizations of individual consumption and insolation are random variables. For scenario $\omega \in \Omega$ and time slot $t \in \mathcal{T}$, we consider a corresponding realization of insolation $r_{\omega,t}$. We normalize $r_{\omega,t}$ to $[0, 1]$ and the solar generation in scenario ω and time slot t can be written as

$$P_{i,\omega,t}^{\text{PV}} = r_{\omega,t} \times PV_i. \quad (5.3)$$

We assume that all the end users come from the same community. Therefore, insolation shares perfect positive correlation amongst each user. Let the consumption of user i be $D_{i,\omega,t}$. The energy should be balanced in real time, which leads to

$$P_{i,\omega,t}^{\text{PV}} + P_{i,\omega,t}^{\text{dis}} + P_{i,\omega,t}^+ = D_{i,\omega,t} + P_{i,\omega,t}^{\text{ch}} + P_{i,\omega,t}^- + \Delta P_{i,\omega,t}^{\text{PV}}, \quad (5.4)$$

where $P_{i,\omega,t}^{\text{dis}}$ and $P_{i,\omega,t}^{\text{ch}}$ are the power discharged from and charged into the storage, $\Delta P_{i,\omega,t}^{\text{PV}}$ is the curtailed solar generation, and $P_{i,\omega,t}^-$ and $P_{i,\omega,t}^+$ are the generation sold to and bought from the LSE. Total generation sold to the LSE should be constrained by the capacity limit of net metering by

$$\sum_{t \in \mathcal{T}} P_{i,\omega,t}^- \leq CAP_i, \quad (5.5)$$

where CAP_i is the capacity limit of net metering.

Let $SOC_{i,\omega,t}$ be the state of charge of the storage, for which the following constraints should be satisfied:

$$S_i \geq SOC_{i,\omega,t}, \quad (5.6a)$$

$$SOC_{i,\omega,t} = SOC_{i,\omega,t-1} + P_{i,\omega,t}^{\text{ch}}\eta - P_{i,\omega,t}^{\text{dis}}/\eta, \quad (5.6b)$$

where η is the charging/discharging efficiency of the storage.

Let the probability of scenario ω be p_ω , and the retail rate of electricity in time slot t be λ_t . Assume that the TOU rate structure is applied and there is no uncertainty in the retail rates. The individual optimization problem for user i is given by

$$\max \quad \lambda_t \sum_{\omega \in \Omega} p_\omega \sum_{t \in \mathcal{T}} \left(P_{i,\omega,t}^- - P_{i,\omega,t}^+ \right) - A_i \quad (5.7a)$$

$$\text{s.t.} \quad (5.2), (5.3), (5.4), (5.5), (5.6). \quad (5.7b)$$

We denote the objective value in (5.7a) by d_i , which is the total payoff of user i .

Payoffs of the LSE

In this non-cooperative planning benchmark, the LSE's payoff in each hour is the difference between the wholesale market price and the TOU rate times the energy consumption. The wholesale market prices are regarded as random variables. Let the wholesale market price in scenario ω and time slot t be $\pi_{\omega,t}$. The mathematical formulation is given by

$$d_0 = \sum_{\omega \in \Omega} p_\omega \sum_{t \in \mathcal{T}} (\lambda_t - \pi_{\omega,t}) \sum_{i \in \mathcal{I}} \left(P_{i,\omega,t}^+ - P_{i,\omega,t}^- \right). \quad (5.8)$$

After solving (5.7), the payoff of the LSE can be numerically calculated.

5.1.2 Cooperative Planning Framework

Next, we consider the cooperative PV-storage planning for the entire community. The LSE and the end users optimally determine the size of PV and storage. The entitlement is allocated based on the amount of money each player pays for the enforcement. When the end users use the LSE's storage partition, a holding cost is applied.

Modeling the End Users

Under cooperative planning, each end user is allowed to make private investment. For the shared investment, the partition of each player is proportional to the money invested by the player. We assume that the annualized capital costs are the same for both private and shared investments. Mathematically, we can consider private and shared enforcement as one decision variable by summing up the quantities. The new payoff function of end user i can be written

as:

$$\sum_{\omega \in \Omega} p_{\omega} \sum_{t \in \mathcal{T}} \left[\lambda_t \left(P_{i,\omega,t}^- - P_{i,\omega,t}^+ \right) - \gamma SOC_{i,\omega,t}^U \right] - A_i, \quad (5.9)$$

where γ is the holding cost, and $SOC_{i,\omega,t}^U$ is the power stored in the LSE's storage in scenario ω at time slot t . A new set of storage constraints should be satisfied:

$$SOC_{i,\omega,t}^U = SOC_{i,\omega,t-1}^U + P_{i,\omega,t}^{\text{ch,U}} \eta - P_{i,\omega,t}^{\text{dis,U}} / \eta, \quad (5.10)$$

where $P_{i,\omega,t}^{\text{ch,U}}$ and $P_{i,\omega,t}^{\text{dis,U}}$ are the power charged to and discharged from the LSE's storage, respectively.

Moreover, the power balance equation should incorporate the LSE's storage, which is given by

$$P_{i,\omega,t}^{\text{PV}} + P_{i,\omega,t}^+ = D_{i,\omega,t} + P_{i,\omega,t}^- + P_{i,\omega,t}^{\text{ch}} - P_{i,\omega,t}^{\text{dis}} + \Delta P_{i,\omega,t}^{\text{PV}} + P_{i,\omega,t}^{\text{ch,U}} - P_{i,\omega,t}^{\text{dis,U}}. \quad (5.11)$$

Constraints (5.2), (5.3), (5.5), (5.6) remain unchanged.

Modeling the LSE

Without cooperation, the LSE can only obtain revenue from selling electricity to the end users. However, it can increase its revenue by offering storage service or selling electricity to the wholesale market if the LSE and the end users perform cooperative planning. We assume that the LSE needs to determine the capacity of the PV system $PV_0 \in [0, PV_0^{\text{max}}]$ and that of the storage $S_0 \in [0, S_0^{\text{max}}]$. Using the capital recovery factor in (5.1), the total annualized investment costs are given by

$$A_0 = A_0^{\text{PV}} PV_0 + A_0^{\text{S}} S_0. \quad (5.12)$$

The payoff comes from two aspects: selling electricity and storage service. For the first part, we need to consider power balance because the LSE invests in PV in this case, which is given by

$$r_{\omega,t} \times PV_0 + P_{0,\omega,t}^{\text{ex}} = \sum_{i \in \mathcal{I}} \left(P_{i,\omega,t}^+ - P_{i,\omega,t}^- \right), \quad (5.13)$$

where $P_{0,\omega,t}^{\text{ex}}$ is the power that the LSE exchanges with the main grid. When $P_{0,\omega,t}^{\text{ex}} > 0$, it means that the LSE is buying power from wholesale market. Therefore, the first part of payoff can be given by

$$\sum_{\omega \in \Omega} p_{\omega} \sum_{t \in \mathcal{T}} \left[\lambda_t \sum_{i \in \mathcal{I}} \left(P_{i,\omega,t}^+ - P_{i,\omega,t}^- \right) - \pi_{\omega,t} P_{0,\omega,t}^{\text{ex}} \right]. \quad (5.14)$$

For the storage service, the LSE charges holding costs to the end users. It can be written as

$$\sum_{\omega \in \Omega} p_{\omega} \sum_{t \in \mathcal{T}} \gamma \sum_{i \in \mathcal{I}} SOC_{i,\omega,t}^U, \quad (5.15)$$

in which the total charged partition of storage is constrained by the investment:

$$\sum_{i \in \mathcal{I}} SOC_{i,\omega,t}^U \leq S_0. \quad (5.16)$$

Let u_0^1 and u_0^2 denote (5.14) and (5.15), respectively, The optimization problem of the LSE is given by

$$\max \quad u_0 = u_0^1 + u_0^2 - A_0 \quad (5.17a)$$

$$\text{s.t.} \quad (5.12), (5.13), (5.16). \quad (5.17b)$$

5.1.3 Solution Methodology

Nash Bargaining Solution

The challenge of community based PV-storage expansion planning is that the end users and the LSE are rational decision makers and aim to optimize their benefits. We adopt the NBS, a solution concept from cooperative game theory, where the goals of Pareto efficiency and symmetry are achieved. The bargaining game can model the cooperative agreements between the end users and the LSE. It helps players choose the right strategies considering the allocation of surplus. Our bargaining game consists of the following elements [146]:

- A set of players that include I end users and one LSE. All the players negotiate with each other to find the globally optimal agreements.
- A set of payoff functions.
- A set of disagreement payoffs.

Let $d_i, \forall i \in \mathcal{I}$ be the optimal payoffs of the end users without cooperation, which can be obtained by solving (5.7). Let d_0 be the corresponding payoff of the LSE, given by (5.8). It is worth mentioning that we need to solve a set of optimization problems to obtain the set of $d_i, \forall i \in \mathcal{I} \cup \{0\}$. Let \mathcal{X} be the feasible region of decision variables in the cooperative problem. We denote the set of possible payoffs by set \mathcal{V} , given by

$$\mathcal{V} = \left\{ (v_0, \dots, v_i) \mid v_i = u_i(x), \forall i, \forall x \in \mathcal{X} \right\}, \quad (5.18)$$

where $u_i, \forall i \in \mathcal{I}$ is given by (5.9) and u_0 is given by (5.17). Note that p_ω, λ_t , and $r_{\omega,t}$ are parameters associated with scenarios. For any given γ , u_i is linear. In other words, the utility functions for the end users and the LSE are convex. Let $\mathbf{d} = \{d_0, d_1, \dots, d_I\}$, and a bargaining problem be a pair $(\mathcal{V}, \mathbf{d})$. We say that a vector of payoffs $(v_i^*, \forall i \in \mathcal{I} \cup \{0\})$ is an NBS if it

solves the following optimization problem:

$$\max \quad \prod_{i \in \mathcal{I} \cup \{0\}} (v_i - d_i) \quad (5.19a)$$

$$\text{s.t.} \quad v \in \mathcal{V}, \quad (5.19b)$$

$$v_i > d_i, \quad \forall i \in \mathcal{I} \cup \{0\}. \quad (5.19c)$$

Note that all the constraints are affine, and therefore the feasible region of possible outcomes is convex. The NBS can be applied to find a unique, fair, and Pareto-optimal solution for the community based PV-storage expansion planning problem.

As problem (5.19) maximizes the objective, a concave function is desired from a computational perspective. The NBS-based problem can be reformulated as follows:

$$\max \quad \sum_{i \in \mathcal{I} \cup \{0\}} \ln(v_i - d_i) \quad (5.20a)$$

$$\text{s.t.} \quad v \in \mathcal{V}, \quad (5.20b)$$

$$v_i > d_i, \quad \forall i \in \mathcal{I} \cup \{0\}. \quad (5.20c)$$

Post reformulation we have a convex problem (5.20) given a fixed holding cost. Gradient based methods can be used to solve the problem. In our experiments, the primal-dual interior-point method is applied.

McCormick Envelopes

The holding cost γ is also a decision variable in (5.20), which leads to bilinear terms and makes the problem non-convex. If the players want to negotiate the holding cost as well, certain reformulations are needed. We relax the bilinear terms via McCormick envelopes. Consider the following optimization problem:

$$\min_{x,y} \quad xy \quad (5.21a)$$

$$\text{s.t.} \quad x^L \leq x \leq x^U, \quad (5.21b)$$

$$y^L \leq y \leq y^U. \quad (5.21c)$$

By replacing xy by W and introducing new inequality constraints, we can create the following convex problem:

$$\min_{x,y} W \tag{5.22a}$$

$$\text{s.t} \quad x^L y + y^L x - x^L y^L \leq W, \tag{5.22b}$$

$$x^U y + y^U x - x^U y^U \leq W, \tag{5.22c}$$

$$x^U y + y^L x - x^U y^L \geq W, \tag{5.22d}$$

$$x^L y + y^U x - x^L y^U \geq W. \tag{5.22e}$$

We replace all the bilinear terms in (5.20) using (5.22) to convexify the problem. Note that the relaxed problem gives an upper bound for the original problem. Gradient based method can then be applied to obtain the optimal solution. In our problem, the bilinear term only exists in the objective function, and it is replaced by its convex underestimators and overestimators. The reformulation does not change the feasible region. Therefore, the solution obtained from the relaxed problem is always feasible for the original problem.

5.1.4 Scenario Generation

We use a three-phase approach to generate the scenarios. In the first phase, we use CNN to obtain the time-series point forecast of the uncertain parameters. Then, we obtain the probability distribution function for the prediction error. Finally, we sample the error distribution to generate different scenarios.

To generate the scenarios, we begin with developing a CNN model to obtain the point forecast of the uncertainty at every time slot of the future. The approach of using CNN is appropriate over the conventional machine learning approaches from the aspect of feature engineering. The traditional machine learning algorithms require a strong detailed feature set to make meaningful predictions. Sophisticated statistical methodologies are required to select related features, which is difficult and time consuming. On the contrary, the CNN architecture can automatically achieve feature engineering. Hence, we have used CNN for the point forecasting application since CNN can enhance the performance of the tasks with less or no feature engineering.

After having the point forecast value for every uncertain parameter, the error between the actual value and the forecast is calculated by taking the difference between the two. Then, a probability density function is obtained with the help of KDE using the error values for each random variable. The resulting distributions for 6 random variables, i.e., wholesale locational marginal price (LMP), solar insolation, and the load of four residential houses, are shown in Fig. 5.1. After having obtained the error distribution, we build a continuous multivariate joint probability distribution describing the forecast errors.

We use the concept of Monte Carlo sampling to sample the multivariate KDE. This is a com-

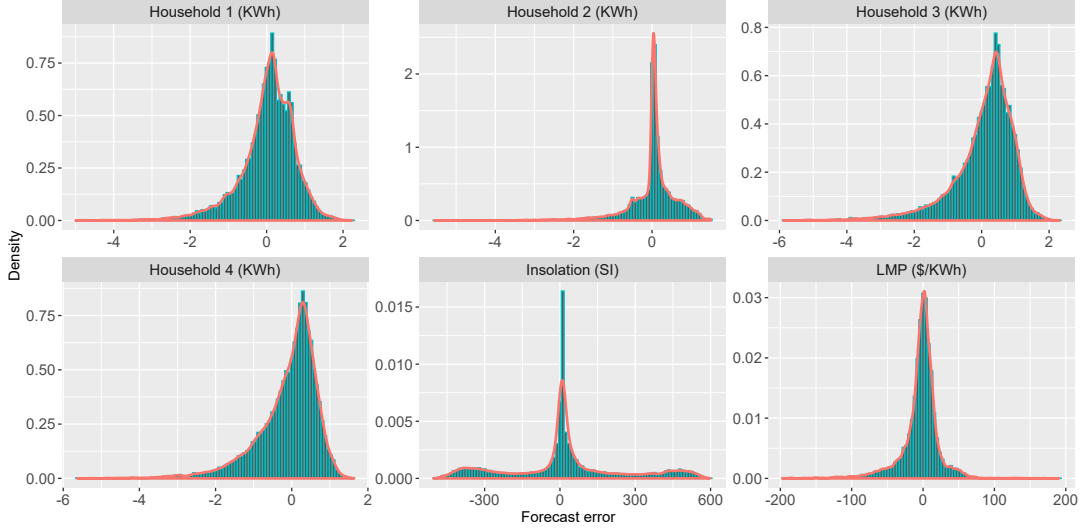


Figure 5.1: Probability density function for forecast errors.

mon procedure used in sampling distributions to generate scenarios for stochastic programming. A single sample from the multivariate KDE gives $I + 2$ different error values, each corresponding to its respective random variable. We draw Ω i.i.d. random vectors s_ω by sampling $\hat{f}_{\mathbf{H}}(\mathbf{x})$, where $s_\omega = (\Delta D_{1,\omega}, \dots, \Delta D_{I,\omega}, \Delta \pi_\omega, \Delta r_\omega)$. Thus, the load demand, wholesale LMP, and solar insolation for each scenario can be presented as follows:

$$D_{i,\omega,t} = D_{i,t}^{\text{forecast}} + \Delta D_{i,\omega}, \forall i, \forall t, \forall \omega, \quad (5.23)$$

$$\pi_{\omega,t} = \pi_t^{\text{forecast}} + \Delta \pi_\omega, \forall t, \forall \omega, \quad (5.24)$$

$$r_{\omega,t} = r_t^{\text{forecast}} + \Delta r_\omega, \forall t, \forall \omega, \quad (5.25)$$

where $D_{i,\omega,t}$, $\pi_{\omega,t}$, and $r_{\omega,t}$ are the consumption of residence i , wholesale LMP, and solar insolation in scenario ω in time t , respectively. $D_{i,t}^{\text{forecast}}$, π_t^{forecast} , and r_t^{forecast} are the forecasted values of load for household i , LMP, and solar insolation in time t , respectively. $\Delta D_{i,\omega}$, $\Delta \pi_\omega$, and Δr_ω are the corresponding forecast errors for each scenario ω . We assume a single error value per scenario for all the time instances corresponding to the random variable.

The use of KDE guarantees that the fitting is exact, and the sample paths are generated from the underlying distribution. The investment decisions are sensitive to scenarios used to perform optimization. Therefore, KDE ensures a data-driven solution that factors in the meteorological and geographical factors for the specific community.

5.1.5 Case Studies

we consider a cooperative game between one LSE and four households. We consider a 48-hour operation horizon in the second stage, where the coefficients in the objective function are

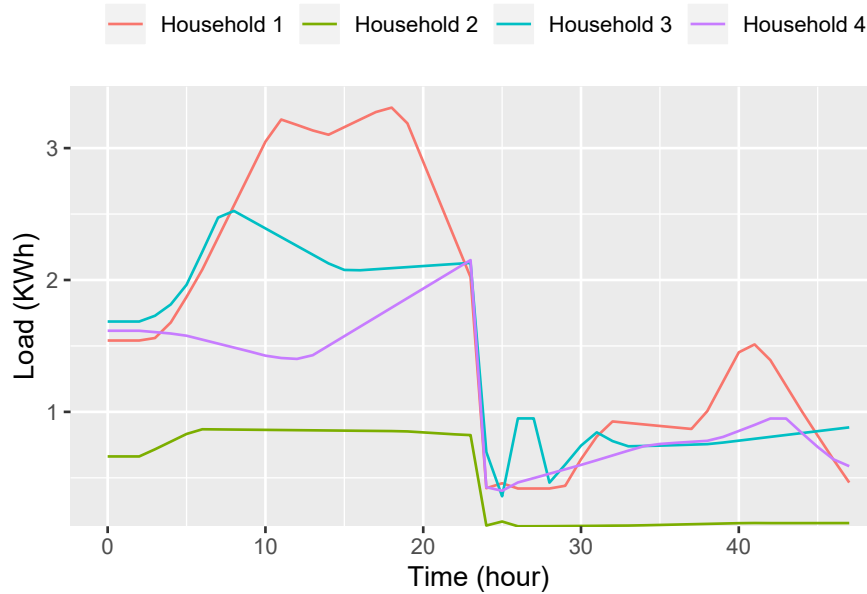


Figure 5.2: Expected consumption for each household.

scaled by $365/2$ to reflect the cost for the entire year. The first 24 hours represent the heating season, while the remainder characterizes the cooling season. The expected consumption for each household is shown in Fig. 5.2. Insolation is normalized and there is no unit for it. Only two days are used due to the limit of computational power and memory. Specification of heating and cooling seasons captures the seasonality. Moreover, we use the average of all the days in each season, and different scenarios are used to capture the daily variations. We generate 15 scenarios for this work. Similar to the load, the TOU rate, LMP, and insolation follow two schemes, which are given in Fig. 5.3.

We first assume that no uncertainty exists and verify that the cooperation can increase the payoffs for each player. Non-cooperative framework is used to benchmark the advantages of the proposed business model. Players are generally rational and selfish. In this sense, such planning problems cannot be optimized in a centralized way by the LSE, where the goal is to achieve the maximum total social welfare. The centralized optimization problem may deteriorate payoffs of some players and discourage their participation. The results are summarized in Table 5.1. In this case, γ is fixed at $\$0.10/\text{kWh}$. The households buy power from the LSE, and hence, the corresponding payoffs are negative. We immediately observe that cooperation can increase revenues for everyone. However, the results show minor improvements since there is no uncertainty.

Under this setting, the LSE does not invest in PV, and the households do not invest in storage in both non-cooperative and cooperative frameworks. Investments of PV are listed in Fig. 5.4. The storage invested by the LSE is 0.783 MWh. Without cooperation, each household determines its optimal investment. The PV generation usually hits its maximum when the TOU

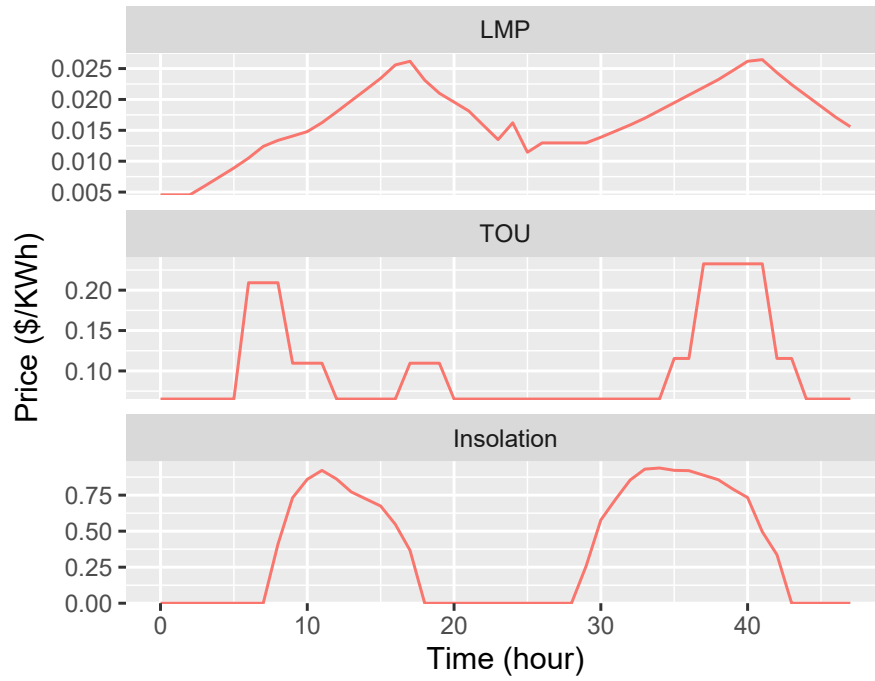


Figure 5.3: Expected LMP, insolation, and TOU rate.

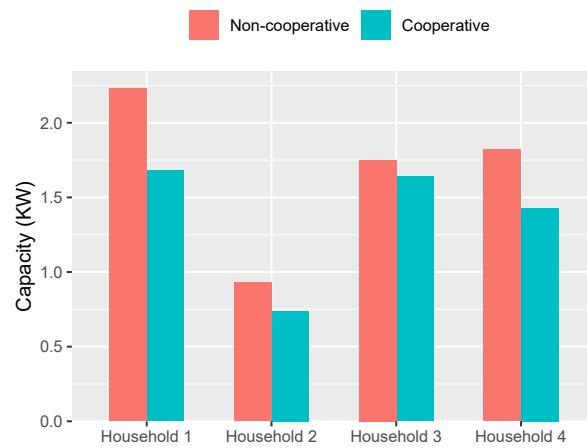


Figure 5.4: Investment decisions without uncertainty.

Table 5.1: Payoffs of Each Player without Uncertainty.

Household	Non-cooperation (\$)	Cooperation (\$)
1	-1126.55	-1125.66
2	-273.64	-273.56
3	-937.08	-936.45
4	-703.44	-702.62
LSE	1705.81	1711.96

Table 5.2: Investment Decisions for Different Selections of γ .

Household		$\gamma = 0.01$	$\gamma = 0.03$	$\gamma = 0.1$	N-C
1	PV	2.032	2.081	2.2789	2.466
	storage	0	0	0	0
2	PV	0.936	1.032	1.196	1.273
	storage	0	0	0	0
3	PV	1.335	1.463	1.635	1.823
	storage	0	0	0	0
4	PV	1.380	1.467	1.566	1.749
	storage	0	0	0	0
LSE	PV	0	0	0	0
	storage	6.964	6.879	6.574	0

rate and the LMP are high, due to which the LSE’s revenue decreases. If the players are allowed to collaborate, the households can buy energy at lower rates and store it in the LSE’s storage. Hence, for this case, the invested capacity of PV is lower, as shown in Fig. 5.4. However, the LSE needs to install storage to offer such a service. By doing so, households can increase their revenue by reducing investment costs. The LSE can increase its payoffs by buying less power from household via net metering at higher rates. This is a win-win solution. Moreover, the NBS guarantees the Pareto optimality of strategies.

Intuitively, households will not use the storage if the holding cost is high. Therefore, the invested capacities in PV are close to those without cooperation. On the other hand, if there is cheap storage available to the end users, they will store the electricity during off-peak hours and use it during peak hours. Therefore, the total invested capacity of PV is increasing in γ . Such trend leads to the need for more storage capacity when γ is low. Table 5.2 shows that the invested capacity of shared storage is decreasing in γ . The units of invested PV and storage are kW and kWh, respectively. N-C means non-cooperative framework.

Moreover, we observe from Table 5.3, in which “diff” denotes the increased payoff compared with the non-cooperative framework, that more surplus is allocated to the LSE. In this sense, the LSE is willing to negotiate with the end users and cooperate.

In the previous analysis, we fix γ . However, the holding cost should be a bargaining element in the cooperative ZEC expansion planning. The (Pareto) optimal holding cost obtained by the bargaining process is zero. We fix $\gamma = 0$ and compare the two cases. The comparison is shown

Table 5.3: Payoffs (\$) for Different Selections of γ .

Household		$\gamma = 0.01$	$\gamma = 0.03$	$\gamma = 0.1$	N-C
1	payoffs	-2068.11	-2068.16	-2068.03	-2068.20
	diff	0.09	0.04	0.16	N/A
2	payoffs	-1175.49	-1175.55	-1175.44	-1175.57
	diff	0.08	0.03	0.13	N/A
3	payoffs	-1775.45	-1775.50	-1775.38	-1775.54
	diff	0.09	0.04	0.16	N/A
4	payoffs	-1359.97	-1360.02	-1359.90	-1360.06
	diff	0.09	0.04	0.16	N/A
LSE	payoffs	512.33	512.05	526.76	511.52
	diff	0.80	0.52	15.23	N/A

Table 5.4: Comparison of Outcomes under Fixed γ and Bargaining Dependent γ .

	Household	Fixed $\gamma = 0$	Optimal γ
1	PV (kW)	1.88848069	1.88848076
	storage (kWh)	0	0
	payoffs (\$)	-2034.00	-2034.00
2	PV (kW)	0.834158309	0.834158356
	storage (kWh)	0	0
	payoffs (\$)	-1141.38	-1141.38
3	PV (kW)	1.29068449	1.29068448
	storage (kWh)	0	0
	payoffs (\$)	-1741.34	-1741.34
4	PV (kW)	1.30832018	1.30832017
	storage (kWh)	0	0
	payoffs (\$)	-1325.86	-1325.86
LSE	PV (kW)	0	0
	storage (kWh)	6.48597607	6.48597664
	payoffs (\$)	725.15	725.15

in Table 5.4. The payoffs of the non-cooperative framework are the same as those in Table 5.3. If the holding cost is determined via the bargaining process, the allocation is fair. The increased payoffs for each household are \$34.20, \$34.20, \$34.20, and \$34.20, respectively. It highlights the advantage of NBS. In our experiments, the relaxation is tight. The reason is that the optimal fixed cost γ is 0, and it is the lower bound of the envelope, where the convex underestimator, the convex overestimator, and the original objective function are the same. Intuitively, the LSE has no incentive to install storage since $\gamma = 0$. However, the LSE can gain profits by installing a PV system and selling excess electricity to the wholesale market. If a non-cooperative approach is used, the LSE has no information about the residential PV-storage systems and residential demands. Due to the lack of this information, the LSE will not be able to size its PV-storage system optimally. As long as the payoffs can outweigh the loss suffered from offering free

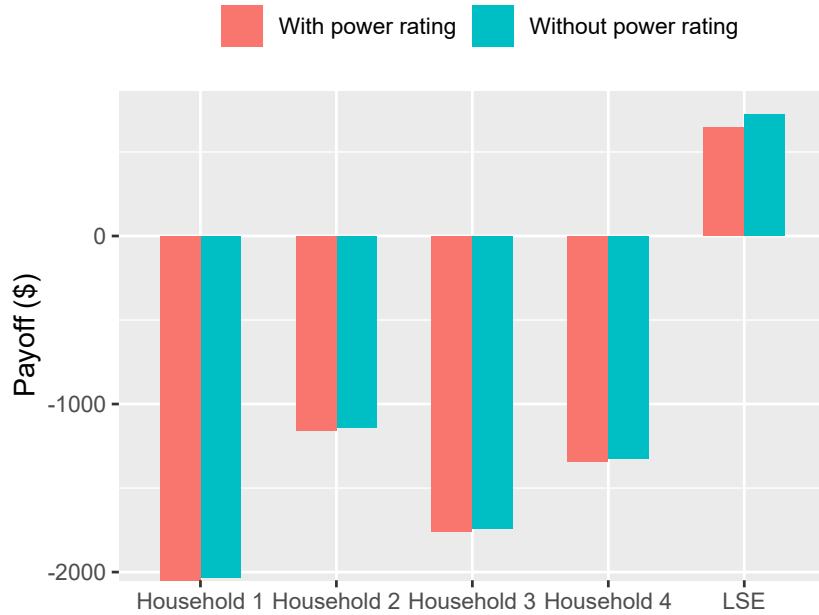


Figure 5.5: Comparison of payoffs for cases with and without investment of power rating.

storage service, the LSE will still want to cooperate.

As mentioned earlier, our model can be easily extended to incorporate the investment of power rating for storage. A new decision variable should be added following the same spirit used for the other two investment decisions. We consider the investment cost for power rating as \$800/kW, and compare the results with and without the investment of that. γ is considered as a decision variable. The comparison of the payoffs is shown in Fig. 5.5.

5.1.6 Conclusion

A novel business model where utility and households within a community cooperatively deploy solar and storage is presented. The Nash bargaining solution allocates the potential increase in payoffs. To capture the meteorology and geography of the local community within the uncertainty, a CNN based scenario generation method is used. The numerical results demonstrate that the utility and every household in the community can increase their payoffs and adopt more renewable energy by cooperative planning, which sheds light on the future customer-utility relationship. The case study also shows that the Nash bargaining solution leads to a good allocation of surplus and guarantees a win-win outcome.

The current problem formulation is not computationally efficient. In real life, there might be hundreds of households. It is necessary to investigate distributed optimization approach for the problem in consideration. Also, I will consider TOU rates as variables (i.e., dynamic pricing) in the bargaining process, which can provide valuable insights into the utility rate making process.

5.2 Critical Service Restoration via Dynamic Microgrids

Although there are remarkable ongoing efforts in grid resiliency enhancement using dynamic microgrids and DERs, most of the works solve the underlying problems in a centralized manner. Centralized optimization may sacrifice the privacy of DER owners. Moreover, it requires that the operator is able to solve a complicated problem promptly, which is not always the case under emergencies. Mixed binary second-order cone programs on a large scale can be computationally prohibitive, while linear models may not characterize the physical dynamics adequately. In this regard, distributed optimization approaches are widely adopted to tackle problems in the distribution system. However, binary variables representing on/off statuses of switches may change the structure of well-studied problems in the distribution network. Those methods are not directly applicable to critical service restoration problems with dynamic microgrids. The problem in consideration needs a distributed optimization technique that is compatible with binary variables.

Besides problems in power systems, mixed-integer optimization is a pivotal tool for the formulation and solution of many problems in other fields. For example, warehouse management and vehicle routing in operations research [147], and clustering and image segmentation in computer vision [148]. Extensive works are proposed to solve mixed-integer optimization problems efficiently. Again, most of the existing works require the system operator to gather all the information and be able to solve complex problems, and hence, they are not ideal methods for the critical service restoration problem and cannot leverage the specific structure of the problem in consideration.

In this dissertation, we investigate a distributed optimization based solution with guaranteed performance. First, the critical service restoration problem is formulated as a mixed-integer second-order cone program. A heuristic distributed optimization approach that is based on column generation is proposed to enhance computational efficiency. The heuristic method is shown to converge after finite iterations with a bounded optimality gap. The case study compares the proposed algorithm with the centralized optimization approach and alternating direction method of multiplier technique. Numerical results highlight the necessity of distributed optimization and effectiveness of the proposed approach.

5.2.1 Problem Formulation

Notations and Assumptions

Consider a distribution network as a graph $\mathcal{G} = (\mathcal{I}, \mathcal{E})$ where $\mathcal{I} = (1, \dots, I)$ represents the set of buses and \mathcal{E} denotes the set of distribution lines connecting the buses in \mathcal{I} . We index buses and edges by i and (i, j) , respectively, where (i, j) indicates pointing from i to j . Let \mathcal{I}_L denote load buses without net generation. For each bus $i \in \mathcal{I}$, let $V_i = |V_i|e^{i\theta_i}$ be its complex voltage, and we define $v_i := |V_i|^2$ as its magnitude squared. Meanwhile, P_i^G , Q_i^G , P_i^L , and Q_i^L represent the active generation, reactive generation, active consumption, and reactive consumption at bus

i , respectively. Let $z_{ij} = r_{ij} + \mathbf{i}x_{ij}$ and $S_{ij} = P_{ij} + \mathbf{i}Q_{ij}$ be the complex impedance and branch power flow from bus i to bus j . Note $z_{ij} = z_{ji}$ and $S_{ij} \neq -S_{ji}$. Let L_{ij} be complex branch current, and $l_{ij} := |L_{ij}|^2$ be the magnitude of complex branch current squared. We consider a projection of all the decision variables to the space of $\{P_i^G, Q_i^G, P_i^L, Q_i^L, v_i, \forall i \in \mathcal{I}\}$ and $\{P_{ij}, Q_{ij}, l_{ij}, \forall (i, j) \in \mathcal{E}\}$. Resulting decision variables are non-negative. Moreover, the lower and upper bounds of a variable Z are denoted by \underline{Z} and \bar{Z} , respectively.

To achieve the goal of serving critical infrastructures by distributed generation, several dynamic microgrids that feature adjustable topologies and boundaries are needed, which requires system operators to optimize on/off statuses of switches and the direction of flows in each edge. We first define a set of binary variables $\{\beta_{ij}, \forall (i, j) \in \mathcal{E}\}$ to represent the flow directions. In the rest of this work, we refer this set as *direction indicators*. Moreover, another set of binary variables $\{y_i, \forall i \in \mathcal{I}\}$ is used to define if bus i is energized or not. If $y_i = 1$, it means bus i is energized. We define $\mathbb{B} := \{0, 1\}$. If all the flows in an edge are zeros, then the switch of that line should be open.

The following assumptions are made throughout this paper:

- A1) Generation, consumption, voltage at each bus, and flows in each line are bounded.
- A2) Line resistances and reactances are strictly positive, i.e., lines are passive and inductive.
- A3) The second-order cone programming (SOCP) relaxations of branch flows are exact.
- A4) There exists, at least, limited communication between the coordinator and buses under emergencies. Moreover, the coordinator is assumed to be able to solve easy-to-handle problems, e.g., small linear programming (LP) tasks.

In practice, A1 and A2 are mild. Congestion is usually not included in the studies of distribution networks. We can assume that upper bounds are large numbers. A3 holds for a radial network under some assumptions as shown in [149], or one can check the sufficient condition of exactness for a given system as in [150]. Moreover, a brief discussion on tackling inexact cases is included later, and we also verify the exactness in the numerical results.

Critical Service Restoration Model

Critical service restoration seeks to maximize total weighted served energy, where critical loads are associated with larger weights, while meeting various operational constraints. The objective function can be given by

$$\sum_{i \in \mathcal{I}} f_i = \sum_{i \in \mathcal{I}} (\pi_i P_i^L + \pi'_i Q_i^L), \quad (5.26)$$

where π_i and π'_i are weights of active and reactive powers at bus i . In practice, weights of reactive power are usually not considered, i.e., $\pi'_i = 0$. In (5.26), we consider the consumption at each bus as decision variables, which implicitly assumes that system operators can disconnect every

bus or have methods to shed loads at a certain cost (e.g., demand response). Recent installation of smart meters allows for remote disconnection of customer supply by system operators.

The critical service restoration problem can be formulated as the following mixed-integer second-order program:

$$\max \sum_{i \in \mathcal{I}} f_i \quad (5.27a)$$

$$\text{s.t.} \quad \sum_{(i,j) \in \mathcal{E}} P_{ij} - \sum_{(k,i) \in \mathcal{E}} (P_{ki} - r_{ki} l_{ki}) = P_i^G - P_i^L, \forall i \in \mathcal{I}, \quad (5.27b)$$

$$\sum_{(i,j) \in \mathcal{E}} Q_{ij} - \sum_{(k,i) \in \mathcal{E}} (Q_{ki} - x_{ki} l_{ki}) = Q_i^G - Q_i^L, \forall i \in \mathcal{I}, \quad (5.27c)$$

$$-M(1 - \beta_{ij}) \leq v_i - v_j - 2r_{ij}P_{ij} - 2x_{ij}Q_{ij} + z_{ij}^2 l_{ij} \leq M(1 - \beta_{ij}), \forall (i, j) \in \mathcal{E}, \quad (5.27d)$$

$$l_{ij} v_i = P_{ij}^2 + Q_{ij}^2, \forall (i, j) \in \mathcal{E}, \quad (5.27e)$$

$$0 \leq P_{ij} \leq \bar{P}_{ij} \beta_{ij}, \forall (i, j) \in \mathcal{E}, \quad (5.27f)$$

$$0 \leq Q_{ij} \leq \bar{Q}_{ij} \beta_{ij}, \forall (i, j) \in \mathcal{E}, \quad (5.27g)$$

$$0 \leq l_{ij} \leq \bar{l}_{ij} \beta_{ij}, \forall (i, j) \in \mathcal{E}, \quad (5.27h)$$

$$0 \leq P_i^G \leq \bar{P}_i^G y_i, \forall i \in \mathcal{I}, \quad (5.27i)$$

$$0 \leq P_i^L \leq \bar{P}_i^L y_i, \forall i \in \mathcal{I}, \quad (5.27j)$$

$$0 \leq Q_i^G \leq \bar{Q}_i^G y_i, \forall i \in \mathcal{I}, \quad (5.27k)$$

$$0 \leq Q_i^L \leq \bar{Q}_i^L y_i, \forall i \in \mathcal{I}, \quad (5.27l)$$

$$v_i y_i \leq v_i \leq \bar{v}_i y_i, \forall i \in \mathcal{I}. \quad (5.27m)$$

$$\sum_{(j,i) \in \mathcal{E}} \beta_{ji} = y_i, \forall i \in \mathcal{I}_L, \quad (5.27n)$$

$$y_i \in \mathbb{B}, \forall i \in \mathcal{I}, \beta_{ij} \in \mathbb{B}, \forall (i, j) \in \mathcal{E}. \quad (5.27o)$$

Constraints (5.27b)-(5.27e) adopt DistFlow model from [151], in which voltages and current angles are eliminated. For the angle recovery, we refer to [149]. Big M is used in (5.27d), which ensures that the constraint is not binding when $\beta_{ij} = 0$. (5.27f)-(5.27h) ensure that the flows in (i, j) will be zero when the direction indicator $\beta_{ij} = 0$. (5.27i)-(5.27l) constrain generation and consumption by generation capacity and actual demand. Voltage squared is bounded by (5.27m). (5.27n) assumes that load nodes can be energized by one path only, and generation buses can be self-energized. Moreover, (5.27o) imposes integral requirements. Note that we do not impose any constraint on the substation, hence, the program is general enough to model the case where the main grid is down.

Since we assume lines are passive and inductive, one can prove that, for each line, the flows at least in one direction must be zero at minima. Therefore, we add a cut (5.28) to accelerate computation.

$$\beta_{ij} + \beta_{ji} \leq 1, \forall (i, j) \in \mathcal{E}. \quad (5.28)$$

For non-convex constraint (5.27e), we adopt SOCP relaxation, which is given by

$$-(l_{ij} + v_i)^2 + (l_{ij} - v_i)^2 + 4P_{ij}^2 + 4Q_{ij}^2 \leq 0, \forall (i, j) \in \mathcal{E}. \quad (5.29)$$

The model can incorporate other considerations that are modeled by linear constraints. By adding time indexes, a multi-period problem can be formulated. Moreover, objective function can be augmented to include other benefits.

Distributed Formulation

In case of emergencies, system operators may have limited computational power and require time-efficient solution, which motivates us to decompose the problem into small pieces and follow a distributed scheme. We define a set of slack variables $\mathbf{c}_i = \{(P_{ij}^i, Q_{ij}^i, l_{ij}^i, \beta_{ij}^i, v_j^i), \forall (i, j) \in \mathcal{E}\}$ to represent the coupling decision variables optimized at bus i . Moreover, we have a set of individual variables $\mathbf{x}_i = \{P_i^G, Q_i^G, P_i^L, Q_i^L, v_i, y_i\}$. Let $(\mathbf{c}_i, \mathbf{x}_i)$ collect slack variables and individual variables at bus i . We denote the constraint set of $(\mathbf{c}_i, \mathbf{x}_i)$ over (5.29) by \mathcal{F}_s^i whereas that over other linear constraints by \mathcal{F}_p^i . Problem (5.27) is reformulated as:

$$\mathbf{CP}: \quad \max \quad \sum_{i \in \mathcal{I}} f_i(\mathbf{c}_i, \mathbf{x}_i) \quad (5.30a)$$

$$\text{s.t.} \quad (\mathbf{c}_i, \mathbf{x}_i) \in \mathcal{F}_p^i, \forall i \in \mathcal{I}, \quad (5.30b)$$

$$(\mathbf{c}_i, \mathbf{x}_i) \in \mathcal{F}_s^i, \forall i \in \mathcal{I}, \quad (5.30c)$$

$$\mathbf{c}_{ij} - \mathbf{c}_j = 0, \forall (i, j) \in \mathcal{E}, \quad (5.30d)$$

$$\mathbf{c}_{ij} - \mathbf{c}_i = 0, \forall (i, j) \in \mathcal{E}, \quad (5.30e)$$

$$y_i, \forall i \in \mathcal{I}, \beta_{ij}^i \in \mathbb{B}, \forall (i, j) \in \mathcal{E}, \quad (5.30f)$$

where (5.30d) and (5.30e) are interpreted as consensus constraints. \mathbf{c}_{ij} is the agreed value of coupling elements. It guarantees the solution of CP equals to that of (5.27). By relaxing the consensus constraints, the problem can be decomposed into subproblems at each bus. Note β_{ij}^i 's must converge to binaries, which may limit the adaptability of some conventional distributed optimization approaches or make them merely heuristics. Let f^{CP} be the optimal objective value of CP.

5.2.2 Solution Methodology

Here, we first introduce basics of an exact algorithm, named branch-and-price. Then, based on the algorithm, we develop a heuristic for CP.

Dantzig-Wolfe Reformulation and Branch-and-Price

Representing a bounded polyhedron by its extreme points is the basic construct of Dantzig-Wolfe decomposition in linear programming [152]. Branch-and-price adopts the same spirit due

to discrete nature of integer variables. Here, we show the feasible region of CP can be regarded as a bounded polyhedron, given any fixed values of binary variables.

Lemma 16. Given any fixed values of binary variables and any $\epsilon > 0$, there exists a set of linear constraints $\mathcal{F}_{ap} := \cup_i \mathcal{F}_{ap}^i$ that approximates $\mathcal{F}_s := \cup_i \mathcal{F}_s^i$ such that $|f^{\text{CP}} - f^{\text{AP}}| \leq \epsilon$, where f^{AP} is the optimal objective value of the approximated problem (AP).

Proof. See [153]. □

Note AP approximates problem (5.27) under A3.

Lemma 17. Given any fixed values of binary variables, the feasible region of AP is a polytope, i.e., $\mathcal{F}_{ap} \cup \mathcal{F}_p$ is a bounded polyhedron, under A1.

Proof. The constraints are linear, and therefore it is a polyhedron. All the variables are bounded, $\exists M > 0$, such that $\|(\mathbf{c}_i, \mathbf{x}_i)\| \leq M, \forall (\mathbf{c}_i, \mathbf{x}_i) \in \mathcal{F}_{ap}^i \cup \mathcal{F}_p^i$. □

Given Lemmas 16 and 17, the feasible region under any fixed values of binary variables can be represented by extreme points. The number of combinations of binary variables is also finite, and therefore, the feasible region of AP can be represented by finite points. The problem over those finite points is called *master problem*. However, most points are not useful and make the problem too large. In practice, a *restricted master problem* (RMP) with a base set is considered. By generating meaningful columns into the base set, the solution of RMP equals to that of the master problem, and therefore, that of AP and that of CP with ϵ accuracy. For the proof of equivalence between RMP, the master problem, and AP, we refer to [58].

The RMP of critical service restoration problems is constructed as follows. Let the set of extreme points added at k -th iteration from the subproblem at bus i be $\mathbf{c}_{i,k}$. Note $\mathbf{x}_{i,k}$ is not added. Define the corresponding objective value as $u_{i,k} := f_i(\mathbf{c}_{i,k}, \mathbf{x}_{i,k})$. RMP at K -th iteration is written as:

$$\max_{\alpha_{i,k}, \mathbf{c}_{ij}} \quad \sum_{k=0}^K \sum_{i \in \mathcal{I}} u_{i,k} \alpha_{i,k}, \quad (5.31a)$$

$$\text{s.t.} \quad \mathbf{c}_{ij} - \sum_{k=0}^K (\mathbf{c}_{i,k} \alpha_{i,k}) = 0, \quad \forall (i, j) \in \mathcal{E}, \quad \forall i \in \mathcal{I}, \quad (5.31b)$$

$$\sum_{k=0}^K \alpha_{i,k} = 1, \quad \forall i \in \mathcal{I}, \quad (5.31c)$$

$$\mathbf{c}_{ij} \in \mathcal{C}, \quad \forall (i, j) \in \mathcal{E}, \quad \alpha_{i,k} \geq 0, \quad \forall i, k, \quad (5.31d)$$

where (5.31d) denotes restrictions that require some coupling elements to be binaries, and convexity constraint (5.31c) comes from the fact that all the points in the original feasible region can be represented by the convex combination of extreme points. We solve the linear programming (LP) relaxation of RMP, i.e., relax (5.31d). Let dual variables associated with consensus

constraint (5.31b) and convexity constraint (5.31c) be $\boldsymbol{\mu}_i$ and λ_i , respectively. Subproblems are augmented and considered as pricing problems. The following subproblem is solved for every bus to generate a meaningful column into RMP for the next iteration:

$$U_{i,K+1} = \max \quad f_i(\mathbf{c}_i, \mathbf{x}_i) - \boldsymbol{\mu}_i^\top \mathbf{c}_i \quad (5.32a)$$

$$\text{s.t.} \quad (\mathbf{c}_i, \mathbf{x}_i) \in \mathcal{F}_p^i, \mathcal{F}_s^i, \quad (5.32b)$$

$$y_i, \beta_{ij}^i, \beta_{ji}^i \in \mathbb{B}, \forall j \in \mathcal{N}(i), \quad (5.32c)$$

where $\mathcal{N}(i)$ is the set of neighbors of bus i . If $U_{i,K+1} > \lambda_i$, the solution in this pricing problem indicates a positive increased revenue of RMP. Then, $\mathbf{c}_{i,K+1}$ should enter the base set. When there are no positive ones for all the pricing problems, integrality check and branching procedure should be done. However, RMP may be infeasible at the beginning, i.e., when the base set is empty. The following lemma provides a way to generate a feasible initial base set.

Lemma 18. $(\mathbf{c}_i, \mathbf{x}_i) = \mathbf{0}, \forall i \in \mathcal{I}$ is a feasible solution to CP.

Remark 1. Branch-and-price can solve the critical service restoration problem in a distributed manner, with an exact solution (with ϵ accuracy), under A3. The exactness of SOCP relaxation only guarantees the existence of a good polyhedron approximation for the feasible region of problem (5.27). Therefore, any good polyhedron approximation to (5.27e) should work. The region defined by (5.27e) is a quadratic equation intersected with bounded polyhedron, which has been shown that the exact convex hull is second-order cone representable in [154]. It allows us to apply branch-and-price. The columns added into RMP are not necessarily with the highest increased revenue. Heuristics maintaining the equality while with optimality gap are also acceptable.

A Modified Distributed Optimization Approach

Branch-and-price can find a better branching node compared with branch-and-bound, but branching is still time consuming. There are remarkable ongoing efforts on the enhancement of implementing branch-and-price, e.g., rounding at the root node. In this work, we want to leverage the special structure of the critical service restoration problem. First, the problem can be considered as a two-stage problem: determining the direction of power flows in each line, and then, optimizing dispatches. For an energized load bus i , $y_i = 1$. Second, integer variables are binaries. The two features above motivate us to solve a pure binary problem, fix the values of binary variables, and recover continuous variables. To do so, we first show that the recovery of continuous variables is always feasible. In the rest of this work, we refer the process for the recovery of continuous variables as *recovery problem*.

Lemma 19. Given any fixed values of binary variables, the optimal solution set of the recovery problem is nonempty and compact, under A1.

Proof. Let $\boldsymbol{\gamma}$ collect all the continuous variables. Consider the following recovery problem:

$\max_{\gamma \in \Gamma} \sum_{i \in \mathcal{I}} f_i(\gamma)$, where $\Gamma = \{\gamma | \gamma \in \cup_i \mathcal{F}_s^i(\beta_{ij}, y_i), \gamma \in \cup_i \mathcal{F}_p^i(\beta_{ij}, y_i)\}$. One can verify that Γ is nonempty for a selection of $\{\beta_{ij}, \forall (i, j) \in \mathcal{E}, y_i, \forall i \in \mathcal{I}\}$ by setting all the variables excluding some voltages to zero. Under A1, Γ is bounded. Moreover, the set is the intersection of the level set of continuous functions and hyperplanes, which indicates it is closed. We conclude that Γ is compact. Each function f_i is linear, the optimal value $\sum_{i \in \mathcal{I}} f_i(\gamma^*)$ is finite, and γ^* is nonempty by Weierstrass extreme value theorem. $\gamma^* \subseteq \Gamma$, then γ^* is bounded since Γ is bounded. $\gamma^* = \Gamma \cap \{\gamma \in \mathbb{R}^{|\mathcal{I}|} | \sum_{i \in \mathcal{I}} f_i(\gamma) \leq \sum_{i \in \mathcal{I}} f_i(\gamma^*)\}$, which indicates that γ^* is closed, and therefore compact. \square

Lemma 19 guarantees that we can always find feasible and optimal dispatches for any selection of β_{ij} 's. If solving such a centralized SOCP problem is still computational demanding for system operators under emergencies or the privacy of DER owners is required to be preserved, it can be reformulated into a form that is easy to decompose as (5.30). Methods such as column generation via Dantzig-Wolfe decomposition and conventional ADMM can solve it in a distributed manner.

The procedure of selecting β_{ij} 's is given as follows. Consider the following modified restricted master problem:

$$\text{MRMP:} \quad \max_{\alpha_{i,k}, \beta_{ij}, \beta_{ji}} \sum_{k=0}^K \sum_{i \in \mathcal{I}} u_{i,k} \alpha_{i,k}, \quad (5.33a)$$

$$\text{s.t.} \quad \beta_{ij} - \sum_{k=0}^K (\beta_{ij,k}^i \alpha_{i,k}) = 0, \quad \forall (i, j) \in \mathcal{E}, \quad (5.33b)$$

$$\beta_{ij} - \sum_{k=0}^K (\beta_{ij,k}^j \alpha_{j,k}) = 0, \quad \forall (i, j) \in \mathcal{E}, \quad (5.33c)$$

$$\beta_{ji} - \sum_{k=0}^K (\beta_{ji,k}^i \alpha_{i,k}) = 0, \quad \forall (i, j) \in \mathcal{E}, \quad (5.33d)$$

$$\beta_{ji} - \sum_{k=0}^K (\beta_{ji,k}^j \alpha_{j,k}) = 0, \quad \forall (i, j) \in \mathcal{E}, \quad (5.33e)$$

$$\sum_{k=0}^K \alpha_{i,k} = 1, \quad \forall i \in \mathcal{I}, \quad (5.33f)$$

$$\beta_{ij}, \beta_{ji} \in \mathbb{B}, \quad \forall (i, j), \quad \alpha_{i,k} \geq 0, \quad \forall i, k. \quad (5.33g)$$

Again, let μ_{ij}^i, μ_{ji}^i collect dual variables of consensus constraint (5.33b), (5.33d), and λ_i repre-

sents that of (5.33f). The modified pricing problem for bus i is given by

$$\max \quad f_i(\mathbf{c}_i, \mathbf{x}_i) - \sum_{j \in \mathcal{N}(i)} (\mu_{ij}^i \beta_{ij}^i + \mu_{ji}^i \beta_{ji}^i) \quad (5.34a)$$

$$\text{s.t.} \quad (\mathbf{c}_i, \mathbf{x}_i) \in \mathcal{F}_p^i, \mathcal{F}_s^i, \quad (5.34b)$$

$$y_i, \beta_{ij}^i, \beta_{ji}^i \in \mathbb{B}, \forall j \in \mathcal{N}(i), \quad (5.34c)$$

where $\mathcal{N}(i)$ is the set of neighbors of bus i . Similarly, if the pricing problem indicates a positive increased revenue, the column should be added into MRMP.

Theorem 20. The solution of LP relaxation of MRMP meets the integrality requirement already, i.e., $\beta_{ij}^*, \beta_{ji}^* \in \mathbb{B}, \forall (i, j) \in \mathcal{E}$.

Proof. For the ease of explanation, we first give the canonical form of the relaxed MRMP. $\beta := \{(\beta_{ij}, \beta_{ji}), \forall (i, j) \in \mathcal{E}\}$, and $\alpha := \{(\alpha_{i,k}), \forall i \in \mathcal{I}, \forall k \in \{0, \dots, K\}\}$. Let $\hat{\mathbb{B}}$ be the convex hull of \mathbb{B} . We have $\beta \in \hat{\mathbb{B}}^{2|\mathcal{E}|}$ and $\alpha \in \hat{\mathbb{B}}^{|\mathcal{I}| \times K}$. The relaxed MRMP can be written as $\max_{(\beta, \alpha) \in \mathcal{A}} \mathbf{u}^\top [\beta, \alpha]$, where $\mathcal{A} = \{(\beta, \alpha) | \mathbf{A}[\beta, \alpha]^\top = \mathbf{b}, (\beta, \alpha) \in \hat{\mathbb{B}}^{2|\mathcal{E}| + |\mathcal{I}| \times K}\}$. Obviously, $\mathbf{b} = [\mathbf{0}^{4|\mathcal{E}|}, \mathbf{1}^{|\mathcal{I}|}]^\top$, whose elements are integers. If matrix \mathbf{A} is totally unimodular, then \mathcal{A} has integer vertices and leads to integral solutions. Let the order of \mathbf{A} be $M \times N$. It is sufficient to show every subset $\mathcal{R} \subseteq \{1, \dots, M\}$ of rows can be divided into two sets \mathcal{R}_1 and \mathcal{R}_2 that $a^n = \sum_{m \in \mathcal{R}_1} a_{m,n} - \sum_{m \in \mathcal{R}_2} a_{m,n} \in \{-1, 0, 1\}, \forall n \in \{1, \dots, N\}$, where $a_{m,n}$ is a coefficient of \mathbf{A} (Chapter 19 in [155]). Consider the following partition rule: (5.33b) and (5.33d) are always in a partition; and (5.33c) and (5.33e) are always in another partition, which ensures the requirement for column associated with β_{ij} 's hold. Since we have (5.28), then $-\beta_{ij,k}^i - \beta_{ji,k}^i \in \{0, -1\}$, which also holds if one row is not in \mathcal{R} . For column n relating to $\alpha_{i,k}$, when $-\beta_{ij,k}^i - \beta_{ji,k}^i = 0$, the allocation will not make any change. When $-\beta_{ij,k}^i - \beta_{ji,k}^i = -1$, we add two rows to \mathcal{R}_1 if current $a^n = 1$ and to \mathcal{R}_2 if current $a^n = -1$. If $a^n = 0$, we skip the two rows and allocate other pairs first until all the current a^n 's are 0. The value of a^n is always changed by 1, and we can keep the a^n 's of all the columns relating to a node (i.e., $\alpha_{i,k}, \forall k$) in $\{0, -1\}$ or $\{0, 1\}$. Therefore, (5.33f) can be allocated in the end according to values a^n 's for this node, and there always exists such a partition for every subset of rows. \square

Remark 2. MRMP removes the dependency of $\alpha_{i,k}$'s on consensus constraints of continuous variables. It ensures that the feasible region of MRMP has integer vertices. The new pricing problem assumes that all the other variables are projected to the space of direction indicators. However, the information returned by MRMP excludes the ‘‘price’’ of the consensus of continuous coupling variables, which may lead to suboptimality post the recovery.

Let ψ_k be the base set of MRMP at iteration k . Algorithm 4 concludes the proposed distributed optimization approach for selecting direction indicators. Let $\mathcal{B}_k = \{\beta_{ij,k}, \forall (i, j) \in \mathcal{E}\}$ be the set of direction indicators added to ψ_{k-1} at iteration k , we show the finiteness of Algorithm 4.

Algorithm 4 Algorithm for selecting direction indicators.

Require:

- Initial base set ψ_0 , graph \mathcal{G}
- 1: Add ψ_0 to MRMP, set $\boldsymbol{\mu} = \mathbf{0}$, $k = 0$, and $\boldsymbol{\lambda} = \mathbf{0}$
 - 2: **while** any pricing problem indicates a positive increase **do**
 - 3: $\psi_{k+1} = \psi_k$
 - 4: **for** $i \in \mathcal{I}$ **do**
 - 5: solve decoupled pricing problems (5.34) using $\boldsymbol{\mu}, \boldsymbol{\lambda}$;
 - 6: **if** $f_i(\mathbf{c}_i, \mathbf{x}_i) - \sum_{j \in \mathcal{N}(i)} (\mu_{ij}^i \beta_{ij}^i + \mu_{ji}^i \beta_{ji}^i) > \lambda_i$ **then**
 - 7: add the column $(\beta_{ij}^i, \forall j \in \mathcal{N}(i))$ to ψ_{k+1}
 - 8: **end if**
 - 9: **end for**
 - 10: solve MRMP over ψ_{k+1} , $k = k+1$
 - 11: update $\boldsymbol{\mu}, \boldsymbol{\lambda}$
 - 12: **end while**
-

Theorem 21. Given a graph \mathcal{G} , Algorithm 4 terminates after adding finite columns. In the worst case, it takes $\prod_{i \in \mathcal{I}} 3^{|\mathcal{N}(i)|}$ iterations to stop.

Proof. \mathcal{B}_k consists of a combination of direction indicators, which implies that the total number of possible \mathcal{B}_k is finite. For each bus i , it has $|\mathcal{N}(i)|$ neighbors. For each undirected edge (i, j) , there are three combinations: $\beta_{ij} = \beta_{ji} = 0$, $\beta_{ij} = 1 \wedge \beta_{ji} = 0$, and $\beta_{ij} = 0 \wedge \beta_{ji} = 1$, given constraint (5.28). Therefore, the number of possible selections at node i is $3^{|\mathcal{N}(i)|}$. For the entire \mathcal{G} , the number of total combinations is $\prod_{i \in \mathcal{I}} 3^{|\mathcal{N}(i)|}$. At iteration k , we either terminate the while loop or add a combination \mathcal{B}_k of the feasible region of CP into MRMP. Since the number of possible \mathcal{B}_k in CP is shown to be $\prod_{i \in \mathcal{I}} 3^{|\mathcal{N}(i)|}$, it is sufficient to show that each combination is added to MRMP at most once. If the above is true, Algorithm 1 must terminate after, at most, $\prod_{i \in \mathcal{I}} 3^{|\mathcal{N}(i)|}$ iterations.

First recall that we optimally solve MRMP at iteration $k - 1$ and update dual variables, which means that there exists no $\mathcal{B}_l \in \psi_{k-1}, \forall l \in \{0, \dots, k-1\}$ with positive increased revenue. However, for each subset (solution of the subproblem at bus i) of \mathcal{B}_k , we solve a pricing problem and \mathcal{B}_k only includes that subset when $f_i(\mathbf{c}_i, \mathbf{x}_i) - \sum_{j \in \mathcal{N}(i)} (\mu_{ij}^i \beta_{ij}^i + \mu_{ji}^i \beta_{ji}^i) > \lambda_i$. It indicates each subset is with a positive increased revenue. Therefore, \mathcal{B}_k has a positive increased revenue, and it is not a subset of the base set ψ_{k-1} before. Each combination will be added once. \square

Remark 3. MRMP merely relaxes the consensus on continuous variables in RMP. RMP is equivalent to the master problem, AP, and CP. CP is a mixed-integer SOCP problem. Hence, the complexity of MRMP still exponentially increases with respect to the number of buses in a graph.

Now we want to study the performance of direction indicators selected by Algorithm 1. Let the set of all the $\prod_{i \in \mathcal{I}} 3^{|\mathcal{N}(i)|}$ combinations of \mathcal{B}_k be \mathcal{V} . We have $\psi_k \subseteq \mathcal{V}$ and $\mathcal{B}_k \subset \mathcal{V}, \forall k \in$

$\{0, \dots, \prod_{i \in \mathcal{I}} 3^{|\mathcal{N}^{(i)}|}\}$. The recovery problem can be regarded as a function over the solution of MRMP, whereas MRMP can be interpreted as a set function over the base set ψ_k . We define another set function that represents the objective value of the recovery problem under the base set ψ_k . In other words, there exists a set function $V : 2^{|\mathcal{V}|} \rightarrow \mathbb{R}$ that assigns each base set ψ_k a scalar $V(\psi_k)$, which represents the optimal objective value of recovery problem under the current base set. Recall that f^{CP} and f^{AP} represent the optimal objective value of CP and AP, respectively.

Theorem 22. Let ψ be the base set when Algorithm 1 terminates. Given any $\delta > 0$, we have $(1 - \frac{1}{e})f^{CP} - \delta < V(\psi) \leq f^{CP} + \delta$.

Proof. By Lemma 16, it is sufficient to show $(1 - \frac{1}{e})f^{AP} < V(\psi) \leq f^{AP}$. Given (5.26), f^{AP} is non-negative. $V(\psi)$ may be suboptimal, which leads to $V(\psi) \leq f^{AP}$. Next, we show set function V is monotone and submodular. Let \mathcal{B}_k^* be the optimal solution corresponding to $V(\psi_k)$. Without loss of generality, we consider two subsets of \mathcal{V} : $\psi_{l1} \subseteq \psi_{l2} \subseteq \mathcal{V}$. If $\mathcal{B}_{l2}^* \in \psi_{l1}$, $V(\psi_{l1}) = V(\psi_{l2})$. On the other hand, if $\mathcal{B}_{l2}^* \notin \psi_{l1}$, $V(\psi_{l1}) \leq V(\psi_{l2})$, otherwise $\mathcal{B}_{l1}^* \in \psi_{l2}$ will contradict that \mathcal{B}_{l2}^* is the optimal solution. To conclude, $V(\psi_{l1}) \leq V(\psi_{l2})$ and V is monotone. We show submodularity by discrete derivative: $V(\psi_{l1} \cup \mathcal{B}) - V(\psi_{l1}) \geq V(\psi_{l2} \cup \mathcal{B}) - V(\psi_{l2})$, $\forall \mathcal{B} \in \mathcal{V} \setminus \psi_{l2}$. When $\mathcal{B} \neq \mathcal{B}_{l2+B}^*$, the right hand side is zero, at least, equality should hold due to monotonicity. When $\mathcal{B} = \mathcal{B}_{l2+B}^*$, we have $V(\psi_{l1} \cup \mathcal{B}) = V(\psi_{l2} \cup \mathcal{B})$, but $V(\psi_{l1}) \leq V(\psi_{l2})$. Therefore $V(\psi_{l1} \cup \mathcal{B}) - V(\psi_{l1}) \geq V(\psi_{l2} \cup \mathcal{B}) - V(\psi_{l2})$ and V is submodular. By the nature of maximization in each pricing problem, a column with the most positive increased revenue to CP is added into MRMP, given current base set, i.e., $V(\psi_{k-1} \cup \mathcal{B}_k) - V(\psi_{k-1}) \geq V(\psi_{k-1} \cup \mathcal{B}) - V(\psi_{k-1})$, $\forall \mathcal{B} \in \mathcal{V}$. It is worth noting that this is only true when ψ_{k-1} is generated by MRMP. Now, consider the sequence of columns generated by the original RMP and pricing problems as $\mathbf{v}^* := (\mathbf{v}_1^*, \dots, \mathbf{v}_L^*)$, where L is the number of iterations required by RMP. Let $K + 1$ be the number of iterations required by MRMP. We have

$$\begin{aligned}
V(\mathbf{v}^*) &\leq V(\mathbf{v}^* \cup \psi_K) && \text{(by monotonicity)} \\
&= V(\psi_K) + \sum_{l=1}^L [V(\psi_K \cup \{\mathbf{v}_1^*, \dots, \mathbf{v}_l^*\}) - V(\psi_K \cup \{\mathbf{v}_1^*, \dots, \mathbf{v}_{l-1}^*\})] \\
&\leq V(\psi_K) + \sum_{l=1}^L [V(\psi_K \cup \mathbf{v}_l^*) - V(\psi_K)] && \text{(by submodularity)} \\
&\leq V(\psi_K) + \sum_{l=1}^L [V(\psi_K \cup \mathcal{B}_{K+1}) - V(\psi_K)] && \text{(by pricing)} \\
&= V(\psi_K) + L(V(\psi_{K+1}) - V(\psi_K)).
\end{aligned}$$

Note $V(\mathbf{v}^*) = f^{AP}$ since RMP is exact (with ϵ accuracy), and let $f^{AP} - V(\psi_K) = \delta_K$, we have $\delta_K \leq L(\delta_K - \delta_{K+1})$, $\delta_{K+1} \leq (1 - 1/L)^{K+1} \delta_0$, and $\delta_0 = f^{AP} - V(\psi_0)$. Since we start with an initial feasible solution as stated in Lemma 18, $V(\psi_0)$ is a constant and equals to 0 in our case.

Table 5.5: Parameters of Critical Loads.

Node number	9	17	27	30	37	46	66	79	87	94	101
P (kW)	92	39	40	20	20	105	20	40	40	20	40
Q (kVar)	32	19	20	10	10	75	10	20	20	10	20

Then, we have $f^{AP} - V(\psi_{K+1}) \leq (1 - 1/L)^{K+1} f^{AP}$ and $V(\psi_{K+1}) \geq [1 - (1 - 1/L)^{K+1}] f^{AP}$. We can add columns into MRMP and RMP even if they cannot improve the problem. Therefore, we reconstruct the master problem and have $L = K + 1$. By Bernoulli inequality, we have $V(\psi) > (1 - \frac{1}{e}) f^{AP}$. \square

Remark 4. The gap coincides with the well-known $(1 - 1/e)$ bound in the greedy algorithm. The critical service restoration problem in consideration can be formulated as assigning each load bus to generation buses by steps, where greedy algorithm can work. Unlike greedy algorithm that horizontally decomposes the problem, our method exhibits a vertical decomposition scheme, and is solved “greedily”. Moreover, one may obtain a tighter bound for a specific critical service restoration problem using curvature of V as discussed in [156] and references therein. However, the curvature will change over different settings, e.g., different available solar generation.

5.2.3 Case Studies

The proposed algorithm is implemented for two critical service restoration problems on the modified 123-node test feeder and the modified European low voltage test feeder [157], respectively. We focus on verifying the correctness and effectiveness of the proposed algorithm under different settings in the 123-node test feeder case. We formulate a multi-period problem using the European low voltage test feeder and compare with the modified ADMM and centralized optimization with early stop. Powers in both feeders are normalized to per unit values by 100 kVA. For all the branches, we assume that a remote-controlled switch is available. Restricted master problem and pricing problems are solved by CPLEX.

The Modified 123-Node Test Feeder

11 critical loads are included. The proposed restoration method is demonstrated by four cases: 1) there are 5 community PVs, and the main grid is down; 2) there are 5 community PVs, and the main grid is down, where all the loads are with identical weights; 3) there are 10 community PVs, and the main grid is down; 4) there are 5 community PVs, and lines 18-13 and 52-152 are at fault. The topology with 5 community PVs is shown in Fig. 5.6. The location and demand of each critical load are listed in Table 5.5. The capacity and siting of solar generation are given in Table 5.6. In case 1, 3, 4, we set $\pi = 10, \pi' = 2$ and $\pi = 500, \pi' = 100$ for non-critical and critical loads, respectively. In case 2, all the loads are with weights $\pi = 10, \pi' = 2$.

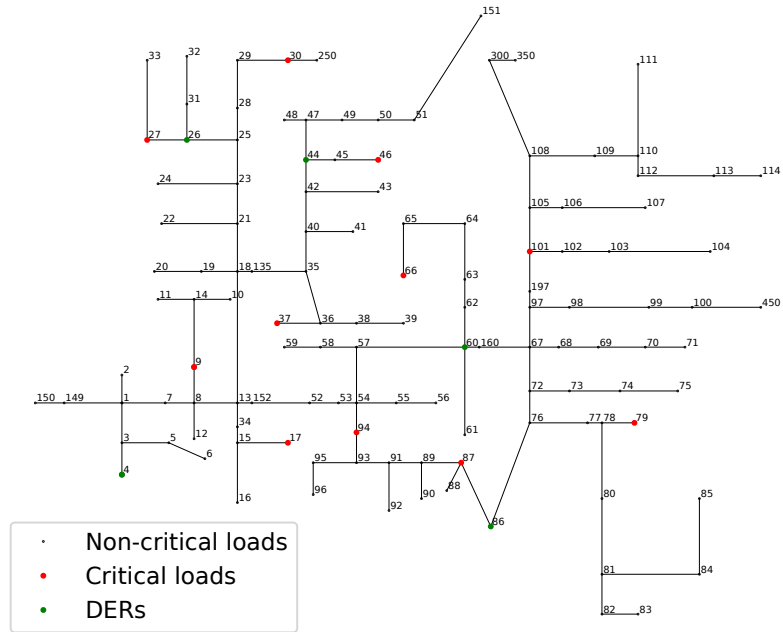


Figure 5.6: IEEE 123-node distribution system with 11 critical loads and 5 community PVs.

Table 5.6: Parameters of Community-Level Solar.

All the cases			Case 3 only		
Node	\bar{P}^G (kW)	\bar{Q}^G (kVar)	Node	\bar{P}^G (kW)	\bar{Q}^G (kVar)
4	145.33	64.25	15	165.33	134.25
26	226.23	86.52	21	165.33	134.25
44	129.52	89.02	35	165.33	134.25
60	201.63	152.69	53	169.52	149.02
86	92.63	54.56	99	165.33	134.25

It implicitly assumes that there is no critical load, and the problem becomes a load restoration problem.

The total computational time of the proposed method consists of time for the recovery problem, time for generating the initial feasible solution, total time for solving MRMP's, total time for solving pricing problems. The pricing problem of each node can be solved locally, and therefore, we consider the slowest one at each iteration as the computational time of solving pricing problems at that iteration. By summing up all the slowest ones, we have the total time required for solving pricing problems. Similarly, we consider the sum of CPU time for solving MRMP at each iteration as the total time for solving MRMP's. In the remaining analysis, we label time for the recovery problem, time for generating the initial feasible solution, total time

Table 5.7: Comparison between the Proposed Method and the Centralized Optimization.

	Computational time (sec)					Objective value				
	Proposed method					Centralized optimization	Exactness	Proposed method	Centralized optimization	Relative optimality gap
	Time-F	Time-M	Time-P	Time-R	Total time					
Case 1	0.0156	0.0010	0.7813	0.2311	1.0290	4.8599	Yes	1849.61	2023.56	9.42%
Case 2	0.0070	0.0080	1.1757	0.2259	1.4166	76.1741	Yes	79.32	86.45	8.99%
Case 3	0.0079	0.0090	1.0214	0.2114	1.2497	8.4938	No	2492.62	2534.41	1.68%
Case 4	0.0069	0.0098	0.0569	0.2253	0.2989	4.9564	Yes	1864.82	1928.97	3.44%

for solving MRMP's, total time for solving pricing problems as $Time-R$, $Time-F$, $Time-M$, and $Time-P$, respectively.

The comparison between the proposed restoration method and centralized optimization approach, in terms of computational time and the optimal objective values, is shown in Table 5.7. The solution of case 3 is inexact, and those of other cases are all exact. Since our method is merely a heuristic, the total computational time is expected to be less than that of centralized optimization approach. Moreover, if the recovery problem is also solved in a distributed manner, DERs are not required to report all of their statuses to system operators. CPLEX solves mixed-integer programs using branch-and-cut method. When we select identical weights for all the loads in case 2, it is not easy to generate useful cuts for accelerating computation, and therefore, the CPU time in case 2 is much larger. However, our method can find a set of near-optimal direction indicators quickly in case 2. Time-R is quite close for all the cases because it solves similar problems. Our method can converge in all the cases, and corresponding recovery problems are feasible. It indicates the critical service restoration problem can be solved using a 2-stage scheme, and our method can work. On the other hand, the actual bounds are much tighter than the theoretical bound. As we mentioned in Remark 4, one can prove a tighter bound for a specific critical service restoration problem using curvature of the set function. For most of the cases, our method is expected to give a near-optimal solution. In particular, compared with other cases, our method gives a better solution in case 3, where the available solar generation can meet the demands of critical loads. Similarly, a relatively greater result is obtained in case 4, where substation can serve some critical loads.

The Modified European Low Voltage Test Feeder

The topology of the modified system is shown in Fig. 5.7. There are 906 buses in this feeder, and we add 12 critical loads and 17 DERs. Moreover, some lines are added, and we assume every bus is with loads. We set $\pi = 10$, $\pi' = 2$ and $\pi = 500$, $\pi' = 100$ for non-critical and critical loads, respectively. The case, where the power support from the upstream transmission system is not available, is considered. The original load file has time resolution of 1 minute. We take the average of each 10-minute interval, and hence each hour is associated with 6 time steps. At the beginning of each hour, we allow the system to change its topology and form new microgrids. The main grid is assumed to be recovered in 3 hours, so we solve 3 independent problems.

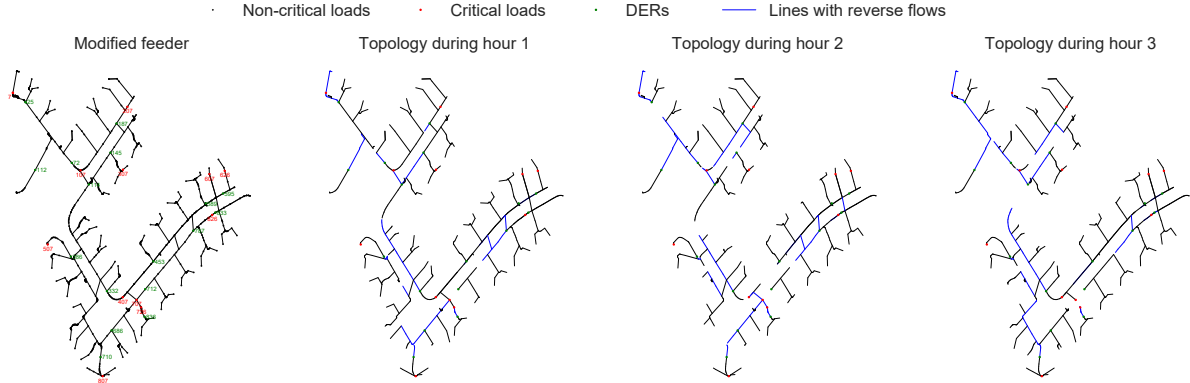


Figure 5.7: Modified European low voltage test feeder.

Table 5.8: Comparison between Three Methods

Method	Hour 1		Hour 2		Hour 3	
	Time (sec)	Objective value	Time (sec)	Objective value	Time (sec)	Objective value
Prop.	7.52	2198.58	9.17	4468.89	7.21	4915.50
ADMM	14.1	2154.68	17.8	4434.28	17.3	4869.82
CO	612	2259.34	1002	5079.16	1141	5360.40

Given different forecasts of DERs and loads for the hour in consideration, the optimization gives three different adaptive topologies, which are visualized in Fig. 5.7. Blue lines denote lines with reverse flows. For example, flows are from bus 2 to bus 1 if line 1-2 is blue. In different hours, different dynamic microgrids that feature adjustable topologies and boundaries can use their distributed generation to serve one or more critical service facilities within them as much as possible.

We compare the result produced by the proposed approach with those generated by centralized optimization with early stop and modified ADMM. The centralized optimization spends excessive time on branching when the incumbent solution generates a near-optimal objective value. Therefore, we stop the branching and report the incumbent solution when the optimality gap is less than 2%. Regarding the ADMM, we solve mixed-integer SOCP problems in subproblems, and binary variables converge to binaries successfully. The comparison is listed in Table 5.8, where CO and Prop. denote centralized optimization method and the proposed method, respectively. The optimality gaps of solutions generated by the proposed method with respect to those produced by the centralized optimization are 2.69%, 12.01%, and 8.29%, respectively. Since we stop centralized optimization at optimality gap 2%, the gaps are all within the theoretical bound. However, the CPU time of centralized optimization is much larger. For hour 3, it takes about 20 minutes. This time depends on the realization of load and DERs. Besides, CPU time may be larger in case where time resolution of load is 1 minute. Regarding ADMM, since we solve mixed-integer programs in the subproblems, it can converge to binaries.

However, it merely serves as a heuristic. The computational time of ADMM is larger than that of the proposed method, while the corresponding objective value is lower than that generated by the proposed method.

The solutions in Table 5.8 are not exact, and one may argue centralized mixed-integer linear programming is more computationally efficient than mixed-integer SOCP. We compare the centralized optimization model and the proposed method using the linearized DistFlow model, in which losses are neglected, and the problem becomes a mixed binary linear program. The objective values produced by the proposed method are 2191.20, 4290.41, and 4853.29, whereas those yielded by centralized optimization are 2271.98, 4845.60, and 5178.94, respectively. The theoretical bound holds for every hour, and the overall optimality gap is 7.82%. Our algorithm takes 0.91 sec, 1.09 sec, and 0.72 sec for each hour, respectively. Regarding the CPU time of centralized optimization approach, the first hour takes 1255.72 sec. However, both the second and third hours take longer than 3600 sec. It highlights the necessity of distributed optimization approach. Under emergencies, it is not practical to spend larger than 1 hour for the computation. Especially, at the beginning of emergencies, we should restore critical loads within a small time range.

5.2.4 Conclusion

This work studies the critical service restoration problem using dynamic microgrids coupled with distributed energy resources. The problem is a mixed-integer second-order cone program, which is further reformulated into a form that is easy to decompose. We propose a heuristic algorithm to solve the problem in a distributed manner, which is shown to converge after finite iterations with a bounded optimality gap. A numerical study verifies the correctness and effectiveness of the proposed method. Moreover, it shows that the DER can improve the resiliency.

However, the proposed scheme merely generates a near-optimal solution. In future work, distributed optimization approaches that produce an exact solution will be studied. On the other hand, the proposed approach requires a few communications between central coordinator and nodes. Moreover, it is assumed that the coordinator can process some easy-to-handle problems, which may be not practical when a big grid outage happens. It is also worth investigating a fully decentralized algorithm with near-optimal solutions.

BIBLIOGRAPHY

- [1] T. Hong, P. Pinson, Y. Wang, R. Weron, D. Yang, and H. Zareipour, “Energy forecasting: A review and outlook,” *IEEE Open Access Journal of Power and Energy*, vol. 7, pp. 376–388, 2020.
- [2] J. Tastu, P. Pinson, P. Trombe, and H. Madsen, “Probabilistic forecasts of wind power generation accounting for geographically dispersed information,” *IEEE Transactions on Smart Grid*, vol. 5, no. 1, pp. 480–489, 2014.
- [3] R. Girard and D. Allard, “Spatio-temporal propagation of wind power prediction errors,” *Wind Energy*, vol. 16, no. 7, pp. 999–1012, 2013.
- [4] X. G. Agoua, R. Girard, and G. Kariniotakis, “Short-term spatio-temporal forecasting of photovoltaic power production,” *IEEE Transactions on Sustainable Energy*, vol. 9, no. 2, pp. 538–546, 2018.
- [5] C. Yang, A. A. Thatte, and L. Xie, “Multitime-scale data-driven spatio-temporal forecast of photovoltaic generation,” *IEEE Transactions on Sustainable Energy*, vol. 6, no. 1, pp. 104–112, 2015.
- [6] Y. Zhao, L. Ye, P. Pinson, Y. Tang, and P. Lu, “Correlation-constrained and sparsity-controlled vector autoregressive model for spatio-temporal wind power forecasting,” *IEEE Transactions on Power Systems*, vol. 33, no. 5, pp. 5029–5040, 2018.
- [7] X. G. Agoua, R. Girard, and G. Kariniotakis, “Probabilistic models for spatio-temporal photovoltaic power forecasting,” *IEEE Transactions on Sustainable Energy*, vol. 10, no. 2, pp. 780–789, 2019.
- [8] A. Tascikaraoglu, B. M. Sanandaji, G. Chicco, V. Cocina, F. Spertino, O. Erdinc, N. G. Paterakis, and J. P. S. Catalo, “Compressive spatio-temporal forecasting of meteorological quantities and photovoltaic power,” *IEEE Transactions on Sustainable Energy*, vol. 7, no. 3, pp. 1295–1305, 2016.
- [9] M. Khodayar and J. Wang, “Spatio-temporal graph deep neural network for short-term wind speed forecasting,” *IEEE Transactions on Sustainable Energy*, vol. 10, no. 2, pp. 670–681, 2019.
- [10] M. Khodayar, S. Mohammadi, M. E. Khodayar, J. Wang, and G. Liu, “Convolutional graph autoencoder: A generative deep neural network for probabilistic spatio-temporal solar irradiance forecasting,” *IEEE Transactions on Sustainable Energy*, vol. 11, no. 2, pp. 571–583, 2020.
- [11] J. F. Toubreau, T. Morstyn, J. Bottieau, K. Zheng, D. Apostolopoulou, Z. De Grve, Y. Wang, and F. Vallee, “Capturing spatio-temporal dependencies in the probabilistic forecasting of distribution locational marginal prices,” *IEEE Transactions on Smart Grid*, vol. 12, no. 3, pp. 2663–2674, 2021.
- [12] S. Woo, J. Park, J. Park, and L. Manuel, “Wind field-based short-term turbine response forecasting by stacked dilated convolutional lstms,” *IEEE Transactions on Sustainable Energy*, vol. 11, no. 4, pp. 2294–2304, 2020.

- [13] J. Liang and W. Tang, “Ultra-short-term spatio-temporal forecasting of renewable resources: An attention temporal convolutional network based approach,” submitted to *IEEE Transactions on Smart Grid*, under revision.
- [14] T. Hong and S. Fan, “Probabilistic electric load forecasting: A tutorial review,” *International Journal of Forecasting*, vol. 32, no. 3, pp. 914–938, 2016.
- [15] J. Olauson *et al.*, “Net load variability in nordic countries with a highly or fully renewable power system,” *Nature Energy*, vol. 1, p. 16175, 2016.
- [16] H. Shaker, H. Zareipour, and D. Wood, “Impacts of large-scale wind and solar power integration on california’s net electrical load,” *Renewable and Sustainable Energy Reviews*, vol. 58, pp. 761–774, 2016.
- [17] M. Sun, T. Zhang, Y. Wang, G. Strbac, and C. Kang, “Using bayesian deep learning to capture uncertainty for residential net load forecasting,” *IEEE Transactions on Power Systems*, vol. 35, no. 1, pp. 188–201, 2020.
- [18] Y. Wang, N. Zhang, Q. Chen, D. S. Kirschen, P. Li, and Q. Xia, “Data-driven probabilistic net load forecasting with high penetration of behind-the-meter PV,” *IEEE Transactions on Power Systems*, vol. 33, no. 3, pp. 3255–3264, 2018.
- [19] H. Shaker, H. Zareipour, and D. Wood, “A data-driven approach for estimating the power generation of invisible solar sites,” *IEEE Transactions on Smart Grid*, vol. 7, no. 5, pp. 2466–2476, 2016.
- [20] S. Sepasi, E. Reihani, A. M. Howlader, L. R. Roose, and M. M. Matsuura, “Very short term load forecasting of a distribution system with high PV penetration,” *Renewable Energy*, vol. 106, pp. 142–148, 2017.
- [21] P. Kobylinski, M. Wierzbowski, and K. Piotrowski, “High-resolution net load forecasting for micro-neighbourhoods with high penetration of renewable energy sources,” *International Journal of Electrical Power & Energy Systems*, vol. 117, p. 105635, 2020.
- [22] M. Khodayar, G. Liu, J. Wang, O. Kaynak, and M. E. Khodayar, “Spatiotemporal behind-the-meter load and pv power forecasting via deep graph dictionary learning,” *IEEE Transactions on Neural Networks and Learning Systems*, 2020.
- [23] J. Liang and W. Tang, “Attention mechanism based probabilistic day-ahead net load forecasting with behind-the-meter solar,” working article.
- [24] X.-Y. Ma, Y.-Z. Sun, and H.-L. Fang, “Scenario generation of wind power based on statistical uncertainty and variability,” *IEEE Transactions on Sustainable Energy*, vol. 4, no. 4, pp. 894–904, 2013.
- [25] M. Yang, S. Fan, and W.-J. Lee, “Probabilistic short-term wind power forecast using componential sparse bayesian learning,” *IEEE Transactions on Industry Applications*, vol. 49, no. 6, pp. 2783–2792, 2013.
- [26] H. Bludszuweit, J. A. Dominguez-Navarro, and A. Llombart, “Statistical analysis of wind power forecast error,” *IEEE Transactions on Power Systems*, vol. 23, no. 3, pp. 983–991, 2008.

- [27] C. Wan, Z. Xu, P. Pinson, Z. Y. Dong, and K. P. Wong, “Probabilistic forecasting of wind power generation using extreme learning machine,” *IEEE Transactions on Power Systems*, vol. 29, no. 3, pp. 1033–1044, 2014.
- [28] J. M. Morales, R. Minguez, and A. J. Conejo, “A methodology to generate statistically dependent wind speed scenarios,” *Applied Energy*, vol. 87, no. 3, pp. 843–855, 2010.
- [29] D. Lee and R. Baldick, “Load and wind power scenario generation through the generalized dynamic factor model,” *IEEE Transactions on Power Systems*, vol. 32, no. 1, pp. 400–410, 2017.
- [30] Y. Lin, M. Yang, C. Wan, J. Wang, and Y. Song, “A multi-model combination approach for probabilistic wind power forecasting,” *IEEE Transactions on Sustainable Energy*, vol. 10, no. 1, pp. 226–237, 2019.
- [31] Z. Wang, W. Wang, C. Liu, Z. Wang, and Y. Hou, “Probabilistic forecast for multiple wind farms based on regular vine copulas,” *IEEE Transactions on Power Systems*, vol. 33, no. 1, pp. 578–589, 2018.
- [32] D. Saez, F. Avila, D. Olivares, C. Canizares, and L. Marin, “Fuzzy prediction interval models for forecasting renewable resources and loads in microgrids,” *IEEE Transactions on Smart Grid*, vol. 6, no. 2, pp. 548–556, 2015.
- [33] W. Xie, P. Zhang, R. Chen, and Z. Zhou, “A nonparametric bayesian framework for short-term wind power probabilistic forecast,” *IEEE Transactions on Power Systems*, vol. 34, no. 1, pp. 371–379, 2019.
- [34] L. Yu, W. Zhang, J. Wang, and Y. Yu, “SeqGAN: Sequence generative adversarial nets with policy gradient,” in *Thirty-First AAAI Conference on Artificial Intelligence (AAAI)*, 2017, pp. 2852–2858.
- [35] J. Liang and W. Tang, “Sequence generative adversarial networks for wind power scenario generation,” *IEEE Journal on Selected Areas in Communications*, vol. 38, no. 1, pp. 110–118, 2020.
- [36] J. Dupacova, N. Grove-Kuska, and W. Romisch, “Scenario reduction in stochastic programming: An approach using probability metrics,” *Mathematical Programming*, vol. 95, no. 3, pp. 493–511, 2003.
- [37] H. Heitsch and W. Romisch, “Scenario tree modeling for multistage stochastic programs,” *Mathematical Programming*, vol. 118, no. 2, pp. 371–406, 2009.
- [38] —, “Scenario reduction algorithms in stochastic programming,” *Computational Optimization and Applications*, vol. 24, no. 2, pp. 187–206, 2003.
- [39] Y. Feng and S. M. Ryan, “Solution sensitivity-based scenario reduction for stochastic unit commitment,” *Computational Management Science*, vol. 13, no. 1, pp. 29–62, 2016.
- [40] Z. Li and Z. Li, “Linear programming-based scenario reduction using transportation distance,” *Computers & Chemical Engineering*, vol. 88, pp. 50–58, 2016.
- [41] Z. Li and C. A. Floudas, “Optimal scenario reduction framework based on distance of uncertainty distribution and output performance: I. single reduction via mixed integer linear optimization,” *Computers & Chemical Engineering*, vol. 70, pp. 50–66, 2014.

- [42] J. Li, F. Lan, and H. Wei, “A scenario optimal reduction method for wind power time series,” *IEEE Transactions on Power Systems*, vol. 31, no. 2, pp. 1657–1658, 2016.
- [43] Y. Wang, Y. Liu, and D. S. Kirschen, “Scenario reduction with submodular optimization,” *IEEE Transactions on Power Systems*, vol. 32, no. 3, pp. 2479–2480, 2017.
- [44] J. Hu and H. Li, “A new clustering approach for scenario reduction in multi-stochastic variable programming,” *IEEE Transactions on Power Systems*, vol. 34, no. 5, pp. 3813–3825, 2019.
- [45] S. E. Chazan, S. Gannot, and J. Goldberger, “Deep clustering based on a mixture of autoencoders,” 2019. [Online]. Available: <https://arxiv.org/abs/1812.06535>
- [46] D. Zhang, Y. Sun, B. Eriksson, and L. Balzano, “Deep unsupervised clustering using mixture of autoencoders,” 2017. [Online]. Available: <https://arxiv.org/abs/1712.07788>
- [47] J. Liang and W. Tang, “Scenario reduction for stochastic day-ahead scheduling: A mixed autoencoder based time-series clustering approach,” *IEEE Transactions on Smart Grid*, vol. 12, no. 3, pp. 2652–2662, 2021.
- [48] EIA. (2018) Annual energy outlook 2018. [Online]. Available: <https://www.eia.gov/outlooks/aeo/>
- [49] T. Ding, Y. Hu, and Z. Bie, “Multi-stage stochastic programming with nonanticipativity constraints for expansion of combined power and natural gas systems,” *IEEE Transactions on Power Systems*, vol. 33, pp. 317–328, 2018.
- [50] B. Odetayo, M. Kazemi, J. MacCormack, and A. Seifi, “A chance constrained programming approach to the integrated planning of electric power generation natural gas network and storage,” *IEEE Transactions on Power Systems*, vol. 33, pp. 6883–6893, 2018.
- [51] R. Bent, S. Blumsack, P. Hentenryck, C. Sanchez, and M. Shahriari, “Robust co-optimization planning of interdependent electricity and natural gas systems with a joint $n-1$ and probabilistic reliability criterion,” *IEEE Transactions on Power Systems*, vol. 33, pp. 6397–6409, 2018.
- [52] EPA. (2017) The social cost of carbon. [Online]. Available: <https://19january2017snapshot.epa.gov/climatechange/social-cost-carbon>
- [53] S. Clegg and P. Mancarella, “Integrated modeling and assessment of the operational impact of power-to-gas (p2g) on electrical and gas transmission networks,” *IEEE Transactions on Power Systems*, vol. 4, pp. 1234–1244, 2015.
- [54] T. Estermann, M. Newborough, and M. Sterner, “Power-to-gas systems for absorbing excess solar power in electricity distribution networks,” *International Journal of Hydrogen Energy*, vol. 190, pp. 13 950–13 959, 2016.
- [55] P. Falugi, I. Konstantelos, and G. Strbac, “Planning with multiple transmission and storage investment options under uncertainty: A nested decomposition approach,” *IEEE Transactions on Power Systems*, vol. 33, pp. 3559–3572, 2018.
- [56] J. Qiu, Z. Dong, J. Zhao, Y. Xu, Y. Zheng, C. Li, and K. Wong, “Multi-stage flexible expansion co-planning under uncertainties in a combined electricity and gas market,” *IEEE Transactions on Power Systems*, vol. 30, pp. 2119–2129, 2015.

- [57] G. Lulli and S. Sen, “A branch-and-price algorithm for multistage stochastic integer programming with application to stochastic batch-sizing problems,” *Management Science*, vol. 50, pp. 786–796, 2004.
- [58] F. Vanderbeck, “On Dantzig-Wolfe decomposition in integer programming and ways to perform branching in a branch-and-price algorithm,” *Operations Research*, vol. 48, no. 1, pp. 111–128, 2000.
- [59] F. Vanderbeck and L. Wolsey, “An exact algorithm for ip column generation,” *Operations Research Letters*, vol. 19, pp. 151–159, 1996.
- [60] J. Liang and W. Tang, “Stochastic multistage co-planning of integrated energy systems considering power-to-gas and the cap-and-trade market,” *International Journal of Electrical Power & Energy Systems*, vol. 119, p. 105817, 2020.
- [61] C. Posada, G. Morales, P. Duenas, and O. Sanchez, “Dynamic ramping model including intraperiod ramp-rate changes in unit commitment,” *IEEE Transactions on Sustainable Energy*, vol. 8, pp. 43–50, 2017.
- [62] M. Hermans, K. Bruninx, and E. Delarue, “Impact of ccgt start-up flexibility and cycling costs toward renewables integration,” *IEEE Transactions on Sustainable Energy*, vol. 9, pp. 1469–1476, 2018.
- [63] Q. Wang, J. Watson, and Y. Guan, “Two-stage robust optimization for $n-k$ contingency-constrained unit commitment,” *IEEE Transactions on Power Systems*, vol. 28, pp. 2366–2375, 2013.
- [64] C. Zhao and R. Jiang, “Distributionally robust contingency-constrained unit commitment,” *IEEE Transactions on Power Systems*, vol. 33, pp. 94–102, 2018.
- [65] D. Pozo and J. Contreras, “A chance-constrained unit commitment with an $n-k$ security criterion and significant wind generation,” *IEEE Transactions on Power Systems*, vol. 28, pp. 2842–2851, 2013.
- [66] D. Tejada, O. Sanchez, and A. Ramos, “Security constrained unit commitment using line outage distribution factors,” *IEEE Trans. Power Syst.*, vol. 33, pp. 329–337, 2018.
- [67] NERC. (2017) Special reliability assessment: Potential bulk power system impacts due to severe disruptions on the natural gas system. [Online]. Available: <https://www.nerc.com/pa/RAPA/ra/Reliability>
- [68] J. Liang and W. Tang, “Interval based transmission contingency-constrained unit commitment for integrated energy systems with high renewable penetration,” *International Journal of Electrical Power & Energy Systems*, vol. 119, p. 105853, 2020.
- [69] A. Najafi, H. Falaghi, J. Contreras, and M. Ramezani, “A stochastic bilevel model for the energy hub manager problem,” *IEEE Transactions on Smart Grid*, vol. 8, no. 5, pp. 2394–2404, 2017.
- [70] A. Dolatabadi, B. Mohammadi-ivatloo, M. Abapour, and S. Tohidi, “Optimal stochastic design of wind integrated energy hub,” *IEEE Transactions on Industrial Informatics*, vol. 13, no. 5, pp. 2379–2388, 2017.

- [71] J. Liang and W. Tang, "Optimal trading strategies for energy hubs equipped with power-to-gas technology," in *2018 North American Power Symposium (NAPS)*, 2018, pp. 1–6.
- [72] National Institute of Standards and Technology (NIST). (2017) Transactive energy: An overview. [Online]. Available: <https://www.nist.gov/engineering-laboratory/smart-grid/hot-topics/transactive-energy-overview>
- [73] E. Mengelkamp, J. Garttner, K. Rock, S. Kessler, L. Orsini, and C. Weinhardt, "Designing microgrid energy markets: A case study: The brooklyn microgrid," *Applied Energy*, vol. 218, pp. 870–880, 2014.
- [74] Y. Wang, W. Saad, Z. Han, H. V. Poor, and T. Basar, "A game-theoretic approach to energy trading in the smart grid," *IEEE Transactions on Smart Grid*, vol. 5, no. 3, pp. 1439–1450, 2014.
- [75] W. Tushar, C. Yuen, D. B. Smith, and H. V. Poor, "Price discrimination for energy trading in smart grid: A game theoretic approach," *IEEE Transactions on Smart Grid*, vol. 8, no. 4, pp. 1790–1801, 2017.
- [76] H. A. Mostafa, R. El Shatshat, and M. M. A. Salama, "A correlated equilibrium game-theoretic approach for multiple participants electric distribution systems operation," *IEEE Transactions on Smart Grid*, vol. 7, no. 1, pp. 32–42, 2016.
- [77] H. Wang, T. Huang, X. Liao, H. Abu-Rub, and G. Chen, "Reinforcement learning for constrained energy trading games with incomplete information," *IEEE Transactions on Cybernetics*, vol. 47, no. 10, pp. 3404–3416, 2017.
- [78] D. Friedman and J. Rust, *The double auction market: Institutions, theories and evidence*. Cambridge, 1993.
- [79] J. Wang, N. Z. Q. Wang, and Y. Chi, "A novel electricity transaction mode of microgrids based on blockchain and continuous double auction," *Energies*, vol. 10, p. 1971, 2017.
- [80] J. Liang and W. Tang, "Optimal trading strategies in continuous double auctions for transactive energy," in *2019 North American Power Symposium (NAPS)*, 2019, pp. 1–6.
- [81] R. Darghouth, G. Barbose, and R. Wiser, "Customer-economics of residential photovoltaic systems (part 1): The impact of high renewable energy penetrations on electricity bill savings with net metering," *Energy Policy*, vol. 67, pp. 290 – 300, 2014.
- [82] E. L. Ratnam, S. R. Weller, and C. M. Kellett, "Scheduling residential battery storage with solar pv: Assessing the benefits of net metering," *Applied Energy*, vol. 155, pp. 881 – 891, 2015.
- [83] J. Warrick. (2015) Utilities wage campaign against rooftop solar. [Online]. Available: <https://www.washingtonpost.com>
- [84] P. Shamsi, H. Xie, A. Longe, and J. Joo, "Economic dispatch for an agent-based community microgrid," *IEEE Transactions on Smart Grid*, vol. 7, no. 5, pp. 2317–2324, 2016.
- [85] P. Tian, X. Xiao, K. Wang, and R. Ding, "A hierarchical energy management system based on hierarchical optimization for microgrid community economic operation," *IEEE Transactions on Smart Grid*, vol. 7, no. 5, pp. 2230–2241, 2016.

- [86] L. Che, X. Zhang, M. Shahidehpour, A. Alabdulwahab, and A. Abusorrah, "Optimal interconnection planning of community microgrids with renewable energy sources," *IEEE Transactions on Smart Grid*, vol. 8, no. 3, pp. 1054–1063, 2017.
- [87] D. Kalathil, C. Wu, K. Poolla, and P. Varaiya, "The sharing economy for the electricity storage," *IEEE Transactions on Smart Grid*, vol. 10, no. 1, pp. 556–567, 2019.
- [88] W. Tushar, B. Chai, C. Yuen, S. Huang, D. B. Smith, H. V. Poor, and Z. Yang, "Energy storage sharing in smart grid: A modified auction-based approach," *IEEE Transactions on Smart Grid*, vol. 7, no. 3, pp. 1462–1475, 2016.
- [89] P. Chakraborty, E. Baeyens, K. Poolla, P. P. Khargonekar, and P. Varaiya, "Sharing storage in a smart grid: A coalitional game approach," *IEEE Transactions on Smart Grid*, vol. 10, no. 4, pp. 4379–4390, 2019.
- [90] J. Liang, A. Shirsat, and W. Tang, "Sustainable community based pv-storage planning using the nash bargaining solution," *International Journal of Electrical Power & Energy Systems*, vol. 118, p. 105759, 2020.
- [91] Y. Li, J. Xiao, C. Chen, Y. Tan, and Y. Cao, "Service restoration model with mixed-integer second-order cone programming for distribution network with distributed generations," *IEEE Transactions on Smart Grid*, vol. 10, no. 4, pp. 4138–4150, 2019.
- [92] H. Sekhavatmanesh and R. Cherkaoui, "Distribution network restoration in a multiagent framework using a convex OPF model," *IEEE Transactions on Smart Grid*, vol. 10, no. 3, pp. 2618–2628, 2019.
- [93] L. Che and M. Shahidehpour, "Adaptive formation of microgrids with mobile emergency resources for critical service restoration in extreme conditions," *IEEE Transactions on Power Systems*, vol. 34, no. 1, pp. 742–753, 2019.
- [94] S. Poudel and A. Dubey, "Critical load restoration using distributed energy resources for resilient power distribution system," *IEEE Transactions on Power Systems*, vol. 34, no. 1, pp. 52–63, 2019.
- [95] Q. Peng and S. H. Low, "Distributed optimal power flow algorithm for radial networks, I: Balanced single phase case," *IEEE Transactions on Smart Grid*, vol. 9, no. 1, pp. 111–121, 2018.
- [96] B. Zhang, A. Y. S. Lam, A. D. Domnguez-Garca, and D. Tse, "An optimal and distributed method for voltage regulation in power distribution systems," *IEEE Transactions on Power Systems*, vol. 30, no. 4, pp. 1714–1726, 2015.
- [97] A. Abel Hafez, W. A. Omran, and Y. G. Hegazy, "A decentralized technique for autonomous service restoration in active radial distribution networks," *IEEE Transactions on Smart Grid*, vol. 9, no. 3, pp. 1911–1919, 2018.
- [98] A. Sharma, D. Srinivasan, and A. Trivedi, "A decentralized multi-agent approach for service restoration in uncertain environment," *IEEE Transactions on Smart Grid*, vol. 9, no. 4, pp. 3394–3405, 2018.

- [99] A. Kargarian and Y. Fu, “System of systems based security-constrained unit commitment incorporating active distribution grids,” *IEEE Transactions on Power Systems*, vol. 29, no. 5, pp. 2489–2498, 2014.
- [100] A. Ahmadi-Khatir, A. J. Conejo, and R. Cherkaoui, “Multi-area unit scheduling and reserve allocation under wind power uncertainty,” *IEEE Transactions on Power Systems*, vol. 29, no. 4, pp. 1701–1710, 2014.
- [101] J. Liang, W. Tang, and X. Lu, “Toward distributed optimization for critical service restoration with distributed energy resources,” in *2020 59th IEEE Conference on Decision and Control (CDC)*, 2020, pp. 2628–2633.
- [102] C. Lea, R. Vidal, A. Reiter, and G. D. Hager, “Temporal convolutional networks: A unified approach to action segmentation,” in *14th European Conference on Computer Vision (ECCV)*, 2016, pp. 47–54.
- [103] S. Bai, J. Z. Kolter, and V. Koltun, “An empirical evaluation of generic convolutional and recurrent networks for sequence modeling,” 2018. [Online]. Available: <https://arxiv.org/abs/1803.01271>
- [104] Y. Chen, Y. Kang, Y. Chen, and Z. Wang, “Probabilistic forecasting with temporal convolutional neural network,” *Neurocomputing*, vol. 399, pp. 491–501, 2020.
- [105] A. Vaswani, N. Shazeer, N. Parmar, J. Uszkoreit, L. Jones, A. N. Gomez, L. Kaiser, and I. Polosukhin, “Attention is all you need,” in *Proceedings of the 30th Advances in Neural Information Processing Systems (NIPS)*, 2017, pp. 5998–6008.
- [106] T. Salimans and D. P. Kingma, “Weight normalization: A simple reparameterization to accelerate training of deep neural networks,” in *Proceedings of the 30th International Conference on Neural Information Processing Systems (NIPS)*, 2016, p. 901909.
- [107] K. K. Thekumparampil, C. Wang, S. Oh, and L.-J. Li, “Attention-based graph neural network for semi-supervised learning,” 2018. [Online]. Available: <https://arxiv.org/abs/1803.03735>
- [108] T. N. Kipf and M. Welling, “Semi-supervised classification with graph convolutional networks,” in *Proceedings of the 5th International Conference on Learning Representations (ICLR)*, 2017.
- [109] National Renewable Energy Laboratory, “Wind integration national data set toolkit.” [Online]. Available: <https://www.nrel.gov/grid/wind-integration-data.html>
- [110] —, “Solar power data for integration studies.” [Online]. Available: <https://www.nrel.gov/grid/solar-power-data.html>
- [111] T. Gneiting and A. E. Raftery, “Strictly proper scoring rules, prediction, and estimation,” *Journal of the American Statistical Association*, vol. 102, no. 477, pp. 359–378, 2007.
- [112] D. Bahdanau, K. Cho, and Y. Bengio, “Neural machine translation by jointly learning to align and translate,” in *Proceedings of the 3rd International Conference on Learning Representations (ICLR)*, 2015.

- [113] K. Xu, J. Ba, R. Kiros, K. Cho, A. Courville, R. Salakhudinov, R. Zemel, and Y. Bengio, “Show, attend and tell: Neural image caption generation with visual attention,” in *Proceedings of the 32nd International Conference on Machine Learning (ICML)*, vol. 37, 2015, pp. 2048–2057.
- [114] P. Velickovic *et al.*, “Graph attention networks,” in *Proceedings of the 6th International Conference on Learning Representations (ICLR)*, 2018.
- [115] D. P. Kingma and M. Welling, “Auto-encoding variational bayes,” in *Proceedings of the 2nd International Conference on Learning Representations (ICLR)*, 2014.
- [116] K. He, X. Zhang, S. Ren, and J. Sun, “Deep residual learning for image recognition,” in *2016 IEEE Conference on Computer Vision and Pattern Recognition (CVPR)*, 2016, pp. 770–778.
- [117] J. L. Ba, J. R. Kiros, and G. E. Hinton, “Layer normalization,” 2018. [Online]. Available: <https://arxiv.org/abs/1607.06450>
- [118] C. Doersch, “Tutorial on variational autoencoders,” 2021. [Online]. Available: <https://arxiv.org/abs/1606.05908>
- [119] F. Wiese, I. Schlecht, W.-D. Bunke, C. Gerbaulet, L. Hirth, M. Jahn, F. Kunz, C. Lorenz, J. Mhlenpfordt, J. Reimann, and W.-P. Schill, “Open power system data–frictionless data for electricity system modelling,” *Applied Energy*, vol. 236, pp. 401 – 409, 2019.
- [120] Bonneville Power Administration (BPA). Wind generation and total load in the BPA balancing authority. [Online]. Available: <https://transmission.bpa.gov/Business/Operations/Wind/>
- [121] P. Pinson and R. Girard, “Evaluating the quality of scenarios of short-term wind power generation,” *Applied Energy*, vol. 96, pp. 12–20, 2012.
- [122] A. Staid, J.-P. Watson, R. J.-B. Wets, and D. L. Woodruff, “Generating short-term probabilistic wind power scenarios via nonparametric forecast error density estimators,” *Wind Energy*, vol. 20, no. 12, pp. 1911–1925, 2017.
- [123] C. Ordoudis, P. Pinson, G. Morales, and M. Zugno, “An updated version of the IEEE RTS 24-bus system for electricity market and power system operation studies,” Technical University of Denmark, Tech. Rep., 2016.
- [124] J. Paparrizos and L. Gravano, “*k*-shape: efficient and accurate clustering of time series,” in *ACM SIGMOD International Conference on Management of Data (SIGMOD)*, 2015.
- [125] M. Cuturi, “Fast global alignment kernels,” in *International Conference on Machine Learning (ICML)*, 2011.
- [126] M. Cuturi and M. Blondel, “Soft-dtw: a differentiable loss function for time-series,” in *International Conference on Machine Learning (ICML)*, 2017.
- [127] Elia. Wind-power generation data. [Online]. Available: <https://www.elia.be/en/grid-data/power-generation>
- [128] N. Lohndorf, “An empirical analysis of scenario generation methods for stochastic optimization,” *European Journal of Operational Research*, vol. 255, no. 1, pp. 121–132, 2016.

- [129] G. Zhang, X. Guo, M. Swider, and M. Marwali, “Transmission constraint relaxation and pricing in the new york electricity market,” in *2018 North American Power Symposium (NAPS)*, 2018, pp. 1–6.
- [130] C. Posada and P. Martin. (2015) Gas network optimization: a comparison of piecewise linear models. [Online]. Available: http://www.optimization-online.org/DB_FILE/2014/10/4580.pdf.
- [131] S. Wu, R. Mercade, E. Boyd, and L. Scott, “Model relaxation for the fuel cost minimization of steady-state gas pipeline networks,” *Mathematical and Computer Modelling*, vol. 31, pp. 197–220, 2000.
- [132] Y. Feng and S. Ryan, “Scenario construction and reduction applied to stochastic power generation expansion planning,” *Computers & Operations Research*, vol. 40, 2013.
- [133] U. Rubasheuski, J. Oppen, and D. Woodruff, “Multistage scenario generation by the combined moment matching and scenario reduction method,” *Operations Research Letters*, vol. 42, pp. 374–377, 2014.
- [134] J. Birge and F. Louveaux, *Introduction to stochastic programming*. Springer, 2011.
- [135] K. Hoyland and S. Wallace, “Generating scenario trees for multistage decision problems,” *Management Science*, vol. 47, pp. 295–307, 2001.
- [136] I. Pena, C. B. Martinez-Anido, and B. Hodge, “An extended iee 118-bus test system with high renewable penetration,” *IEEE Transactions on Power Systems*, vol. 33, no. 1, pp. 281–289, 2018.
- [137] M. Schmidt. (2017) A library of gas network instances. [Online]. Available: <http://gaslib.zib.de/>
- [138] Y. Yu, L. P., E. Litvinov, and D. Schiro, “Transmission contingency-constrained unit commitment with high penetration of renewables via interval optimization,” *IEEE Transactions on Power Systems*, vol. 32, pp. 1410–1421, 2017.
- [139] L. Bai, F. Li, T. Jiang, and H. Jia, “Robust scheduling for wind integrated energy systems considering gas pipeline and power transmission n1 contingencies,” *IEEE Transactions on Power Systems*, vol. 32, pp. 1582–1584, 2017.
- [140] R. Moore, R. Kearfott, and M. Cloud, *Introduction to interval analysis*. SIAM, 2009.
- [141] T. Ishizaki, M. Koike, N. Ramdani, Y. Uede, T. Masuta, T. Oozeki, T. Sadamoto, and J. Imura, “Interval quadratic programming for day-ahead dispatch of uncertain predicted demand,” *Automatica*, vol. 64, pp. 163 –173, 2016.
- [142] A. Sengupta and T. Pal, “On comparing interval numbers,” *European Journal of Operational Research*, vol. 127, pp. 28–43, 2000.
- [143] Y. Xu and L. Tong, “Optimal operation and economic value of energy storage at consumer locations,” *IEEE Transactions on Automatic Control*, vol. 62, no. 2, pp. 792–807, 2017.
- [144] H. Luckcock, “A steady-state model of the continuous double auction,” *Quantitative Finance*, vol. 3, no. 5, pp. 385–404, 2003.

- [145] G. Tesauro and J. L. Bredin, “Strategic sequential bidding in auctions using dynamic programming,” in *Proceedings of the First International Joint Conference on Autonomous Agents and Multiagent Systems: Part 2*, 2002, p. 591598.
- [146] K. Dehghanpour and H. Nehrir, “An agent-based hierarchical bargaining framework for power management of multiple cooperative microgrids,” *IEEE Transactions on Smart Grid*, vol. 10, no. 1, pp. 514–522, 2019.
- [147] S. Nadarajah and A. A. Cire, “Network-based approximate linear programming for discrete optimization,” *Operations Research*, vol. 68, no. 6, pp. 1767–1786, 2020.
- [148] B. Wu and B. Ghanem, “ l_p -box admm: A versatile framework for integer programming,” *IEEE Transactions on Pattern Analysis and Machine Intelligence*, vol. 41, no. 7, pp. 1695–1708, 2019.
- [149] M. Farivar and S. H. Low, “Branch flow model: relaxations and convexification—part I,” *IEEE Transactions on Power Systems*, vol. 28, no. 3, pp. 2554–2564, 2013.
- [150] L. Gan, N. Li, U. Topcu, and S. H. Low, “Exact convex relaxation of optimal power flow in radial networks,” *IEEE Transactions on Automatic Control*, vol. 60, no. 1, pp. 72–87, 2015.
- [151] M. E. Baran and F. F. Wu, “Optimal capacitor placement on radial distribution systems,” *IEEE Transactions on Power Delivery*, vol. 4, no. 1, pp. 725–734, 1989.
- [152] C. Barnhart, E. L. Johnson, G. L. Nemhauser, M. W. P. Savelsbergh, and P. H. Vance, “Branch-and-price: column generation for solving huge integer programs,” *Operations Research*, vol. 46, no. 3, pp. 316–329, 1998.
- [153] A. Ben-Tal and A. Nemirovski, “On polyhedral approximations of the second-order cone,” *Mathematics of Operations Research*, vol. 26, no. 2, pp. 193–205, 2001.
- [154] A. Santana and S. Dey, “The convex hull of a quadratic constraint over a polytope,” *SIAM Journal on Optimization*, vol. 30, no. 4, pp. 2983–2997, 2018.
- [155] A. Schrijver, *Theory of linear and integer programming*. New York, NY: John Wiley & Sons, 1998.
- [156] M. Sviridenko, J. Vondrk, and J. Ward, “Optimal approximation for submodular and supermodular optimization with bounded curvature,” *Mathematics of Operations Research*, vol. 42, no. 4, pp. 1197–1218, 2017.
- [157] K. P. Schneider *et al.*, “Analytic considerations and design basis for the IEEE distribution test feeders,” *IEEE Transactions on Power Systems*, vol. 33, no. 3, pp. 3181–3188, 2018.

APPENDIX

APPENDIX

A

PARAMETERS AND TOPOLOGIES FOR THE EXPANSION CO-PLANNING PROBLEM

A.1 Parameters of the Small System

Table A.1: Candidate Sets of Generators and P2Gs.

Name	Bus	Capacity (MW)	Investment cost (\$M)
Gen-1	3	100	96
Gen-2	6	80	77
P2G-1	4	60	60
P2G-2	4	40	40
P2G-3	4	50	50

Table A.2: Candidate Sets of Lines.

from	to	Capacity (MW)	Diameter (inch)	Cost (\$M)
1	6	100	N/A	32
2	6	150	N/A	32
3	4	50	N/A	12
2	5	100	N/A	32
a	c	N/A	2.16	32.8
b	c	N/A	2.16	32.8

Table A.3: Evolution of Random Variables.

Probability	Increase of gas price	Increase of carbon price	Increase of load	Wind generation
0.1667	0.79, 0.75	0.75, 0.95	0.80, 1.01	1.16, 1.00
0.0848	0.79, 1.12	0.75, 0.60	0.80, 0.67	1.16, 1.79
0.0690	1.09, 1.00	0.97, 0.89	1.09, 1.03	0.98, 0.80
0.0505	1.09, 1.50	0.97, 1.33	1.09, 1.46	0.98, 1.43
0.0802	0.95, 1.33	1.14, 1.58	1.02, 1.40	0.69, 0.47
0.1265	0.95, 0.89	1.14, 1.05	1.02, 0.98	0.69, 0.92
0.1049	1.16, 1.51	1.21, 1.57	1.14, 1.47	0.81, 1.11
0.0781	1.16, 0.98	1.21, 1.02	1.14, 1.01	0.81, 0.58
0.1101	1.30, 1.12	1.22, 1.64	1.25, 1.67	1.41, 2.02
0.1293	1.30, 1.71	1.22, 1.09	1.25, 1.17	1.41, 1.11

Table A.4: 4-Block Load Duration Curve and Wind Profile.

Block	1	2	3	4
Duration (hours)	87	2541	4380	1752
Load (MW)	446	350	270	230
Wind (MW)	282	255	300	450

A.2 Parameters of the Large System

The topologies of 118-bus power system and 40-node gas system are shown in Fig. A.1 and Fig. A.2, respectively.

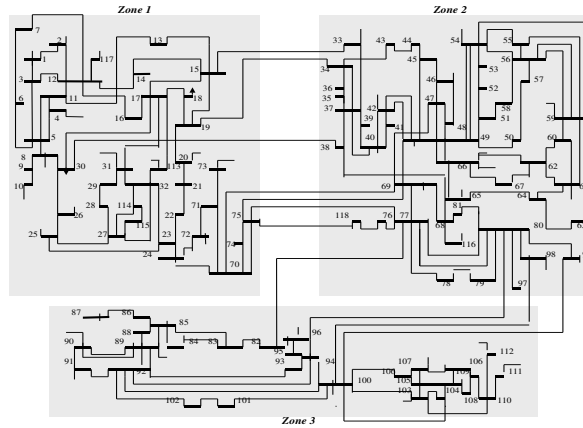


Figure A.1: Topology of 118-bus power system.

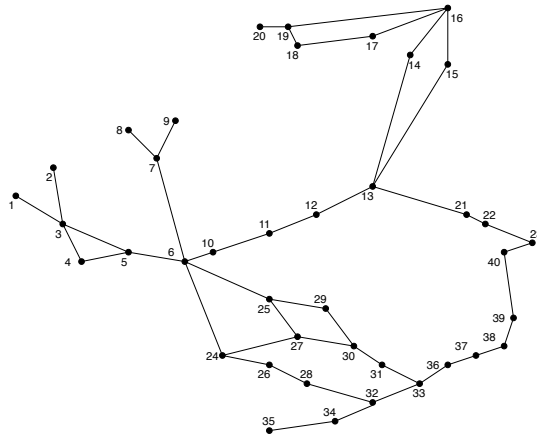


Figure A.2: Topology of 40-node gas system.

Moreover, the coupling buses/nodes are listed in Table A.5.

The candidate sets of gas-fired generator, P2G, transmission line, and pipelines in the large test system are reported in Tables A.6, A.7, A.8, and A.9, respectively.

Table A.5: The Coupling Buses/Nodes in the Test System.

Number	Bus	Node	Number	Bus	Node
1	10	4	10	70	6
2	12	8	11	73	5
3	25	3	12	87	34
4	37	18	13	89	35
5	38	11	14	91	28
6	46	13	15	99	14
7	59	15	16	100	29
8	61	24	17	110	36
9	65	17	18	116	21

Table A.6: Candidate Set of Gas Generators.

Candidate generator	Bus number	Node number	Capacity (MW)	Investment cost (\$M)
1	10	4	200	192
2	12	8	100	96
3	25	3	150	144
4	37	18	200	192
5	38	11	150	144
6	73	5	100	96
7	99	14	100	96
8	100	29	200	192

Table A.7: Candidate Set of P2Gs.

Candidate P2G	Bus number	Node number	Capacity (MW)	Investment cost (\$M)
1	10	4	100	100
2	10	4	175	175
3	10	4	250	250
4	25	3	100	100
5	25	3	175	175
6	25	3	250	250
7	65	17	100	100
8	65	17	200	200
9	65	17	300	300
10	73	5	50	50
11	73	5	100	100
12	73	5	150	150
13	99	14	100	100
14	99	14	175	175
15	99	14	250	250
16	46	13	100	100
17	46	13	175	175
18	46	13	250	250
19	12	8	100	100
20	12	8	175	175
21	12	8	250	250

Table A.8: Candidate Set of Transmission Lines.

Line number	From bus	To bus	Flow limit (MW)	Investment cost (\$M)
1	20	34	500	45
2	24	85	500	45
3	30	117	300	20
4	33	54	175	7
5	37	73	500	45
6	59	66	175	7
7	65	80	175	7
8	79	96	500	45
9	91	100	300	20
10	99	111	500	45
11	107	112	175	7
12	69	15	300	20
13	49	29	500	45
14	10	91	300	20
15	65	51	175	7

Table A.9: Candidate Set of Pipelines.

Pipeline number	From node	To node	Diameter (inch)	Investment cost (\$M)
1	2	8	2.62467	8
2	4	35	2.62467	50
3	5	24	2.62467	22.5
4	11	17	2.62467	50
5	12	29	2.62467	22.5
6	24	35	2.62467	22.5
7	29	36	2.62467	22.5
8	29	40	2.62467	50